Development and Deployment of Renewable and Sustainable Energy Technologies

Jae Sung Jung

Dissertation submitted to the faculty of the Virginia Polytechnic Institute and State University in partial fulfillment of the requirements for the degree of

Doctor of Philosophy
in
Electrical Engineering

Kwa-Sur Tam, Co-Chair
Robert P. Broadwater, Co-Chair
Amos L. Abbott
Inyoung Kim
Sean McGinnis

February 17 2014
Blacksburg, VA

Keywords: Distributed Energy Resource, Plug-in Electric Vehicle, Solar Generation, Wind Generation, Energy Storage System, DER Adoption, Local Steady-State Impact Study, Quasi Steady-State Impact Study, Wind Characteristics, Wind Spectral Analysis, Distribution Control, PV Coordinated Control, PV Centralized Control

Development and Deployment of Renewable and Sustainable Energy Technologies

Jae Sung Jung

ABSTRACT

Solar and wind generation are one of the most rapidly growing renewable energy sources, and is regarded as an appealing alternative to conventional power generated from fossil fuel. This is leading to significant levels of distributed renewable generation being installed on distribution circuits. Although renewable generation brings many advantages, circuit problems are created due to its intermittency, and overcoming these problems is a key challenge to achieving high penetration.

It is necessary for utilities to understand the impacts of Photovoltaic (PV) generation on distribution circuits and operations. An impact study is intended to quantify the extent of the issues, discover any problems, and investigate alternative solutions. In this manner, system wide and local impact study are proposed in the dissertation.

1) System wide impact study

This study considers system effects due to the addition of Plug-in Hybrid Vehicles (PHEV) and Distributed Energy Resource (DER) generation. The DER and PHEV are considered with energy storage technology applied to the residential distribution system load. Two future year scenarios are considered, 2020 and 2030. The models used are of real distribution circuits located near Detroit, Michigan, and every customer load on the circuit and type of customer are modeled. Monte Carlo simulations are used to randomly select customers that receive PHEV, DER, and/or storage systems. The Monte Carlo simulations provide not only the expected average result, but also its uncertainty.

2) Local impact study

Analysis of high PV penetration in distribution circuits using both steady-state and quasi steady-state impact studies are presented. The steady-state analysis evaluates impacts on the

distribution circuit by comparing conditions before and after extreme changes in PV generation at three extreme circuit conditions, maximum load, maximum PV generation, and when the difference between the PV generation and the circuit load is a maximum. The quasi steady-state study consists of a series of steady-state impact studies performed at evenly spaced time points for evaluating the spectrum of impacts between the extreme impacts. Results addressing the impacts of cloud cover and various power factor control strategies are presented. PV penetration levels are limited and depend upon PV generation control strategies and the circuit design and loading. There are tradeoffs in PV generation control concerning circuit voltage variations, circuit losses, and the motion of automated utility control devices. The steady state and quasi steady-state impact studies provide information that is helpful in evaluating the effect of PV generation on distribution circuits, including circuit problems that result from the PV generation.

In order to fully benefit from wind power, accurate wind power forecasting is an essential tool in addressing this challenge. This has motivated researchers to develop better forecast of the wind resources and the resulting power. As a solution for wind generation, frequency domain approach is proposed to characterize and analyze wind speed patterns in the dissertation.

3) Frequency Domain Approach

This study introduces the frequency domain approach to characterize and analyze wind speed patterns. It first presents the technique of and the prerequisite conditions for the frequency domain approach. Three years of wind speed data at 10 different locations have been used. This chapter demonstrates that wind speed patterns during different times and at different locations can be well characterized by using the frequency domain approach with its compact and structured format. We also perform analysis using the characterized dataset. It affirms that the frequency domain approach is a useful indicator for understanding the characteristics of wind speed patterns and can express the information with superior accuracy.

Among the various technical challenges under high PV penetration, voltage rise problems caused by reverse power flows are one of the foremost concerns. The voltage rises due to the PV generation. Furthermore, the need to limit the voltage rise problem limits PV generators from injecting more active power into the distribution network. This can be one of the obstacles to high penetration of PVs into circuits. As a solution for solar generation, coordinated control of automated devices and PV is proposed in the dissertation.

4) Coordinated Automated Device and PV Control

A coordinating, model-centric control strategy for mitigating voltage rise problems due to PV penetration into power distribution circuits is presented. The coordinating control objective is to maintain an optimum circuit voltage distribution and voltage schedule, where the optimum circuit operation is determined without PV generation on the circuit. In determining the optimum circuit voltage distribution and voltage schedule, the control strategy schedules utility controls, such as switched capacitor banks and voltage regulators, separate from PV inverter controls. Optimization addresses minimizing circuit losses and motion of utility controls. The coordinating control action provides control setpoints to the PV inverters that are a function of the circuit loading or time-of-day and also the location of the PV inverter. Three PV penetration scenarios are considered, 10%, 20%, and 30%. Baselines with and without coordinating controls for circuit performance without PV generation are established, and these baselines are compared against the three PV penetration scenarios with and without coordinating control. Simulation results are compared and differences in voltage variations and circuit losses are considered along with differences in utility control motion. Results show that the coordinating control can solve the voltage rise problem while minimizing circuit losses and reducing utility control motion. The coordinating control will work with existing PV inverter controls that accept control setpoints without having to modify the inverter controls.

5) Coordinated Local and Centralized PV Control

Existing distribution systems and their associated controls have been around for decades. Most distribution circuits have capacity to accommodate some level of PV generation, but the question is how much can they handle without creating problems. It proposes a Configurable, Hierarchical, Model-based, Scheduling Control (CHMSC) of automated utility control devices and photovoltaic (PV) generators. In the study here the automated control devices are assumed to be owned by the utility and the PV generators and PV generator controls by another party. The CHMSC, which exists in a hierarchical control architecture that is failure tolerant, strives to maintain the voltage level that existed before introducing the PV into the circuit while minimizing the circuit loss and reducing the motion of the automated control devices. This is accomplished using prioritized objectives. The CHMSC sends control signals to the local controllers of the automated control devices and PV controllers. To evaluate the performance of the CHMSC, increasing PV levels of adoption are analyzed in a model of an actual circuit that has significant existing PV penetration and automated voltage control devices. The CHMSC control performance is compared with that of existing, local control. Simulation results presented demonstrate that the

CHMSC algorithm results in better voltage control, lower losses, and reduced automated control device motion, especially as the penetration level of PV increases.

Dedication

The dissertation is dedicated to my father who has inspired me. He always taught me that the most successful persons are those who retain enthusiasm for the mission, and are able to do their best without regret. It is also dedicated to my mother who supported me from the beginning of my studies and offered unconditional love and encouragement throughout the course of this dissertation. Whenever I felt frustrated, she urged me on. As a result, I finally have a chance to introduce my dissertation. I also dedicate this work to my brother and his wife. He took care of my family in my stead so that I could concentrate on my studies.

Acknowledgement

It is a pleasure to thank the many people who made this dissertation possible. Without their aid and support, the completion of Doctor of Philosophy would have been much more difficult.

I must first to express my gratitude towards my advisor, Dr. Robert P. Broadwater. His leadership, support, attention to detail, hard work, and scholarship have set an example I hope to match someday. Furthermore, he served as a true mentor by providing knowledgeable advice on all aspect of academic life.

I am deeply grateful to my Co-Adviser Dr. Kwa-Sur Tam for his great influence on the way I approach not only my research but also other challenges in life. We had many invaluable conversations on the Philosophy of Research. He is a great mentor for technology development.

Also, I would like to thank Dr. Amos L. Abbott, Dr. Inyoung Kim, and Dr. Sean McGinnis who sit on my advisory committee for my dissertation and I gained a great deal of relevant knowledge which is the foundation for my research.

I was particularly fortunate to have all my friends, roommates and colleagues for study and life at Virginia Tech. And I benefitted greatly from the Electrical Distribution Design (EDD) Inc. for providing the great equipment and wonderful environment for my research. I recognize that this research would not have been possible without the financial assistance and technical assistance of EDD, National Renewable Energy Laboratory (NREL), DTE and PEPCO Energy Company and I express my profound gratitude to this company.

Needless to say, this entire exercise would be at most a dream were it not for my family. Their love and support made this entire endeavor worthwhile.

Table of Contents

List of Figures

List of Tables

Chapter 1 : Introduction

1.1. Background

Solar and wind generation are one of the most rapidly growing renewable energy sources, and is regarded as an appealing alternative to conventional power generated from fossil fuel. This is leading to significant levels of distributed renewable generation being installed on distribution circuits. Although renewable generation brings many advantages, circuit problems are created due to its intermittency, and overcoming these problems is a key challenge to achieving high penetration.

It is necessary for utilities to understand the impacts of renewable generation on distribution circuits and operations. An impact study is intended to quantify the extent of the issues, discover any problems, and investigate alternative solutions. By evaluating projected impacts with the current distribution system model, new plans can be developed to appropriately encourage the addition of distributed resources and load shifting to manage anticipated capacity issues. This could allow the utility to avoid or defer costly system/equipment upgrades, otherwise needed to meet the increased demands.

Impact study can be divided into two categories; system wide and local study. System wide impact study addresses the expected growth impacts if new technologies are introduced into the current distribution circuit including Plug-in Hybrid Vehicles (PHEV), Distributed Energy Resource (DER) generation, and energy storage systems. This study deals with the uncertainties about new technology including its location, size, characteristics and etc.

On the other hand, local impact study addresses the expected impacts of new technologies in the current distribution circuit. It is more feasible study because the native loading and Photovoltaic (PV) data are available and further, its location and characteristics of PV generation are usually known in realistic circuit.

For tackling this challenge obtained from impact study, wind power forecasting is essential tool for wind generation. Research in the area of wind power forecasting has been devoted to the development of good and reliable wind power forecasting and many different approaches have been employed. Furthermore, precise wind forecasting tool results in a cost reduction to integrate wind power into the existing electricity supply system. This has motivated researchers to develop better forecast of the wind resources and the resulting power.

Among the various technical challenges under high PV penetration, one of the major research challenges is directed towards optimized control of high penetration of PV generation within the existing power system. In power distribution circuit that contains high level of penetration of PV generation but has insufficient number of storage system, a sudden change of PV generation could limit PV generators from injecting more active power into the distribution network, resulting in tackling the high penetration of PVs into circuits. Control algorithm is required to dispatch real and reactive power of PV generators while keeping its output voltage, current, or power factor at desired level.

1.2. Dissertation Objective

Figure 1-1 shows the objectives of this dissertation. The first objective is to analyze the impact of renewable generation on distribution circuits and operations and the second is to propose the solution for utilizing the high penetration of wind and solar generation.

For the first objective, system wide and local impact studies are proposed in the dissertation. System wide impact study addresses the expected growth impacts if new technologies are introduced into the current distribution circuit including PHEV, DER generation, and energy storage systems. For the system wide impact study, DER adoption analysis is proposed in this dissertation. However, simulating one time point is not sufficient to evaluate the uncertainty of future PHEV load and DER generation. Therefore, Monte Carlo simulation is used to evaluate adoption patterns of residential customers. The Monte Carlo simulation provides not only the expected average result, but also its uncertainty.

For the local impact study, DER impact study is proposed in this dissertation. It addresses the expected impacts of new technologies in the current distribution circuit. In this manner, both local steady-state and quasi steady-state PV impact studies are presented. The steady-state impact study investigates impacts at extreme circuit conditions and the quasi steady-state represents a series of steady-state studies over a set of time varying values. Thus, the quasi steady-state study evaluates a spectrum of impacts.

For the second objective, frequency domain approach for wind generation and control algorithm for PV generation are proposed. The frequency domain approach characterizes and analyzes wind speed by using the pure data obtained by separating such noises. This benefit enables the improvement of forecasting accuracy.

Furthermore, optimal coordinated control of automated devices and PV generators is proposed as a centralized control. The main objective of the control is to maintain the voltage level that existed before introducing the PV into the circuit. For this, the control of automated devices is coordinated with the

control of PV generators. Then, the coordinated local and centralized control of automated devices and PV generators is proposed. The optimal control set-points obtained from centralized control are sent to the corresponding local controller of automated devices and PVs.

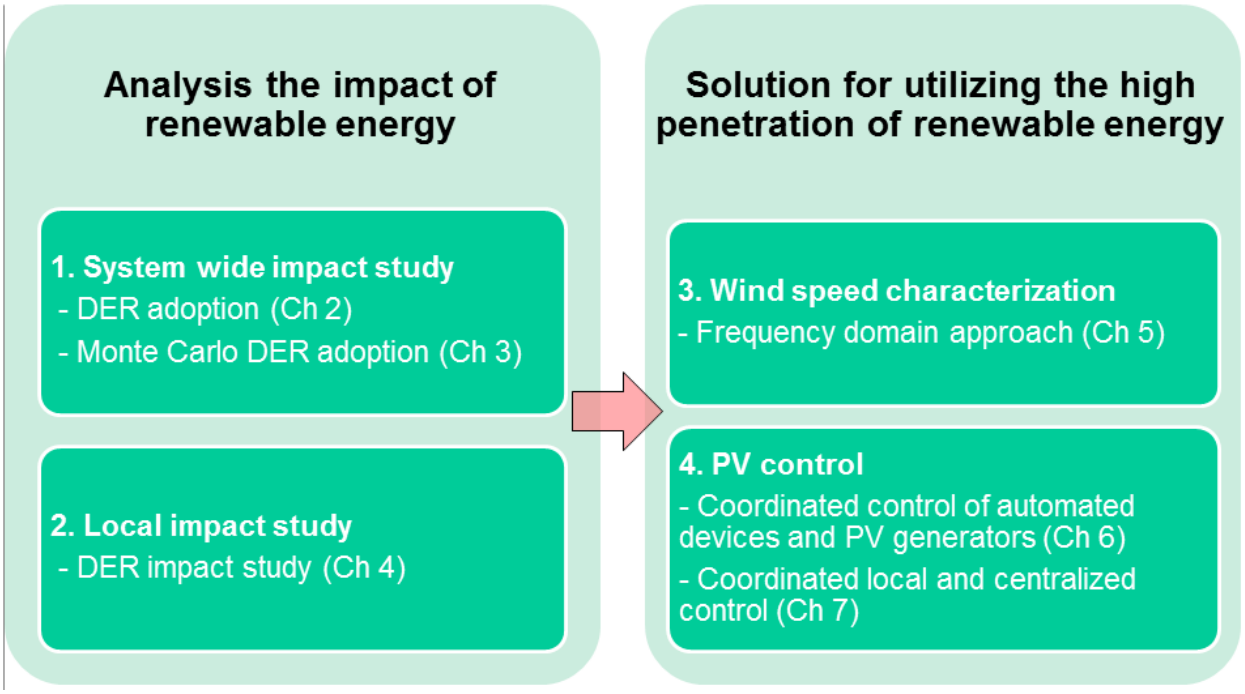

Figure 1-1 Objectives of the dissertation

1.3. Dissertation Outline

- *Chapter 2*

This study considers potential system effects from the addition of Plug-in Electric Vehicle (PEV) load to individually metered residential customers together with a concurrent market adoption of DER and energy storage technologies to offset the associated load growth. To evaluate various renewable energy source conditions, a prototypical circuit is evaluated in Detroit, Los Angeles, and Orlando locations for both summer and winter loading conditions. Various load adoption scenarios are simulated by randomly assigning specified loading to target customer classes on the circuit.

- *Chapter 3*

This chapter considers system effects due to the addition of PHEV and DER generation. The DER and PHEV are considered with energy storage technology applied to the residential distribution system load. Two future year scenarios are considered, 2020 and 2030. The models used are of real distribution

circuits, and every customer load on the circuit and type of customer are modeled. Monte Carlo simulations are used to randomly select customers that receive PHEV, DER, and/or storage systems. The Monte Carlo simulations provide not only the expected average result, but also its uncertainty. The adoption scenarios are investigated for both summer and winter loading conditions.

- *Chapter 4*

Analysis of high PV penetration in distribution circuits using both steady-state and quasi steady-state impact studies are presented. The steady-state analysis evaluates impacts on the distribution circuit by comparing conditions before and after extreme changes in PV generation at three extreme circuit conditions, maximum load, maximum PV generation, and when the difference between the PV generation and the circuit load is a maximum. The quasi steady-state study consists of a series of steady-state impact studies performed at evenly spaced time points for evaluating the spectrum of impacts between the extreme impacts. Results addressing the impacts of cloud cover and various power factor control strategies are presented. PV penetration levels are limited and depend upon PV generation control strategies and the circuit design and loading. There are tradeoffs in PV generation control concerning circuit voltage variations, circuit losses, and the motion of automated utility control devices. The steady state and quasi steady-state impact studies provide information that is helpful in evaluating the effect of PV generation on distribution circuits, including circuit problems that result from the PV generation.

- *Chapter 5*

This study introduces the frequency domain approach to characterize and analyze wind speed patterns. It first presents the technique of and the prerequisite conditions for the frequency domain approach. Three years of wind speed data at 10 different locations have been used. This chapter demonstrates that wind speed patterns during different times and at different locations can be well characterized by using the frequency domain approach with its compact and structured format. We also perform analysis using the characterized dataset. It affirms that the frequency domain approach is a useful indicator for understanding the characteristics of wind speed patterns and can express the information with superior accuracy.

- *Chapter 6*

A coordinating, model-centric control strategy for mitigating voltage rise problems due to PV penetration into power distribution circuits is presented. The coordinating control objective is to maintain an optimum circuit voltage distribution and voltage schedule, where the optimum circuit operation is

determined without PV generation on the circuit. In determining the optimum circuit voltage distribution and voltage schedule, the control strategy schedules utility controls, such as switched capacitor banks and voltage regulators, separate from PV inverter controls. Optimization addresses minimizing circuit losses and motion of utility controls. The coordinating control action provides control setpoints to the PV inverters that are a function of the circuit loading or time-of-day and also the location of the PV inverter. Three PV penetration scenarios are considered, 10%, 20%, and 30%. Baselines with and without coordinating controls for circuit performance without PV generation are established, and these baselines are compared against the three PV penetration scenarios with and without coordinating control. Simulation results are compared and differences in voltage variations and circuit losses are considered along with differences in utility control motion. Results show that the coordinating control can solve the voltage rise problem while minimizing circuit losses and reducing utility control motion. The coordinating control will work with existing PV inverter controls that accept control setpoints without having to modify the inverter controls.

- *Chapter 7*

Existing distribution systems and their associated controls have been around for decades. Most distribution circuits have capacity to accommodate some level of PV generation, but the question is how much can they handle without creating problems. This chapter proposes a Configurable, Hierarchical, Model-based, Scheduling Control (CHMSC) of automated utility control devices and photovoltaic (PV) generators. In the study here the automated control devices are assumed to be owned by the utility and the PV generators and PV generator controls by another party. The CHMSC, which exists in a hierarchical control architecture that is failure tolerant, strives to maintain the voltage level that existed before introducing the PV into the circuit while minimizing the circuit loss and reducing the motion of the automated control devices. This is accomplished using prioritized objectives. The CHMSC sends control signals to the local controllers of the automated control devices and PV controllers. To evaluate the performance of the CHMSC, increasing PV levels of adoption are analyzed in a model of an actual circuit that has significant existing PV penetration and automated voltage control devices. The CHMSC control performance is compared with that of existing, local control. Simulation results presented demonstrate that the CHMSC algorithm results in better voltage control, lower losses, and reduced automated control device motion, especially as the penetration level of PV increases.

- *Chapter 8*

Overall conclusion and future work.

1.4. Glossary

In this dissertation, the following abbreviations and terms are used:

ADF: the Augmented Dickey-Fuller test.

AIC: Akaike Information Criterion.

ANN: Artificial Neural Networks.

CHMSC: Configurable, Hierarchical, Model-based, Scheduling Control

CPR: Clean Power Research.

CV: Coefficient of Variation.

DER: Distributed Energy Resource.

DFT: Discrete Fourier Transform.

DOE: The U.S. Department of Energy.

EPRI: Electric Power Research Institute.

IBMY: In My Backyard.

IDFT: Inverse Discrete Fourier Transform.

IEEE: Institute of Electrical and Electronics Engineering.

MAPE: Mean Absolute Percentage Error.

NCDC: National Climatic Data Center.

NREL: National Renewable Energy Laboratory.

NWP: Numerical Weather Prediction.

PEV: Plug-in Electric Vehicle.

PFUR: Phase power Flow Unbalance Rate.

PHEV: Plug-in Hybrid Vehicles.

PV: Photovoltaic.

PVUR: Phase Voltage Unbalance Rate.

SBC: Schwarz Bayesian Criterion.

UR: Uncertainty Range.

Chapter 2 : Evaluation of DER Adoption in the Presence of New Load Growth and Energy Storage Technologies

2.1. Introduction

Analysis of concurrent growth or adoption of electric vehicles, DER, and energy storage technologies is presented in this chapter. In particular, PEV, customer owned solar generation, customer owned wind generation, and utility owned battery storage are considered. An objective is to evaluate adoption levels of solar and wind generation supplemented with battery storage that will offset the adoption of electric vehicle loads.

Monte Carlo simulation is used to randomly place DER generation units at locations throughout a prototypical circuit. The simulation provides customer arrival home and plug-in time models, including automated charging during early morning hours.

Technology adoption is modeled as a function of customer billing class. The same billing class can be modeled to adopt different types of PEVs and/or DERs at different adoption levels. Adoption of multiple PEVs by a single customer may be modeled, such as for commercial classes that are expected to employ more than one PEV.

Solar data was imported via the internet from the In My Backyard (IMBY) application from the National Renewable Energy Lab (NREL) [1]. For a given solar generation location and size, the NREL interface provides hourly generation data for an entire year, and 8760 hours of generation from year 2004 are used in the analysis hear. For the wind generation, wind speed data is obtained using U.S Local Climatological Data from the National Climatic Data Center (NCDC) [2]. The wind power used in this analysis is calculated by the wind turbine power equation. For each hour of analysis, customer loads are estimated from averaged hourly SCADA measurements, hourly customer kWHr load data, and monthly kWHr load data processed by load research statistics to create hourly loading estimates for each customer [3, 4].

A distribution circuit with 1404 residential, 30 commercial and small industrial class customers are used in the analysis. The circuit is used to analyze both summer and winter conditions for three selected

cities, Detroit, Michigan, Los Angeles, California, and Orlando, Florida. Of particular interest is what levels of DER adoption and battery storage would be needed to offset the adoption of the PEV loads.

A base case where just PEV adoption is considered is used to establish feeder load characteristics due to the new PEV loads along with primary overloads that are caused by the new PEV loads. The study then proceeds to evaluate how DER adoption levels and battery storage strategies could compensate for the PEV loads to help manage feeder overloads. The results of summer and winter analysis are presented for Detroit, Los Angeles, and Orlando locations with various adoption scenarios. Analysis results are then considered followed by a comparison between the results obtained from Detroit, Los Angeles, and Orlando. Findings of the study are summarized.

2.2. Simulation Assumptions and Profile

2.2.1. Native Load Profile

The sample system used for this study has a substation serving 1404 individually metered residential customers. From an available set of residential load measurements, two groups of January and July load profiles are selected to evaluate the seasonal effects for summer and winter months. Figure 2-1 presents a percent loading profile during winter and summer, respectively. These load profiles shows a baseline condition before DER adoption with near-peak conditions occurring from the hours of 4 PM through 11 PM and no overloaded distribution transformers.

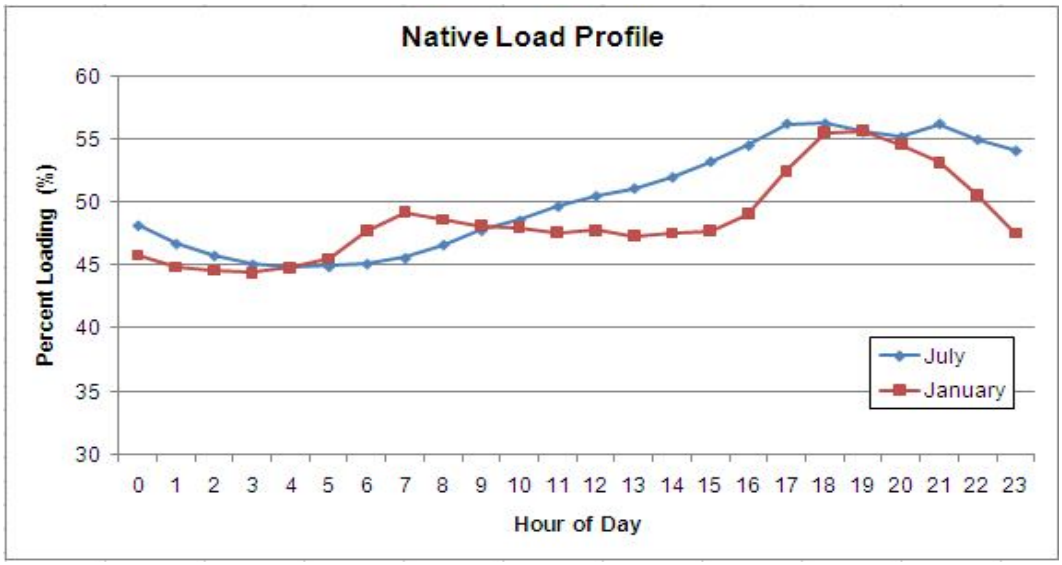

Figure 2-1 Native Percent Loading during Summer and Winter

2.2.2. PEV Load Profile

Since PEV automobile technology is new to the mass market, information on how consumers will utilize this new technology is not available.

In this study the batteries of the PEV are assumed to be charged only at residential homes. It is also assumed that the battery is fully discharged when PEV charging of 8kWh occurs once a day. This assumption provides the worse case scenario. There are two likely voltages at residential locations, 120V and 240V [5]. This study uses a 120V charging scenario as illustrated in Figure 2-2, supplied by a 120V/15A circuit charging at an essentially constant demand of around 2kW for five hours. Choosing 120V instead of 240V charging results in overloads occurring earlier and provides the worse case scenario. In the simulation for a given consumer the charging is a function of arrival time as discussed below.

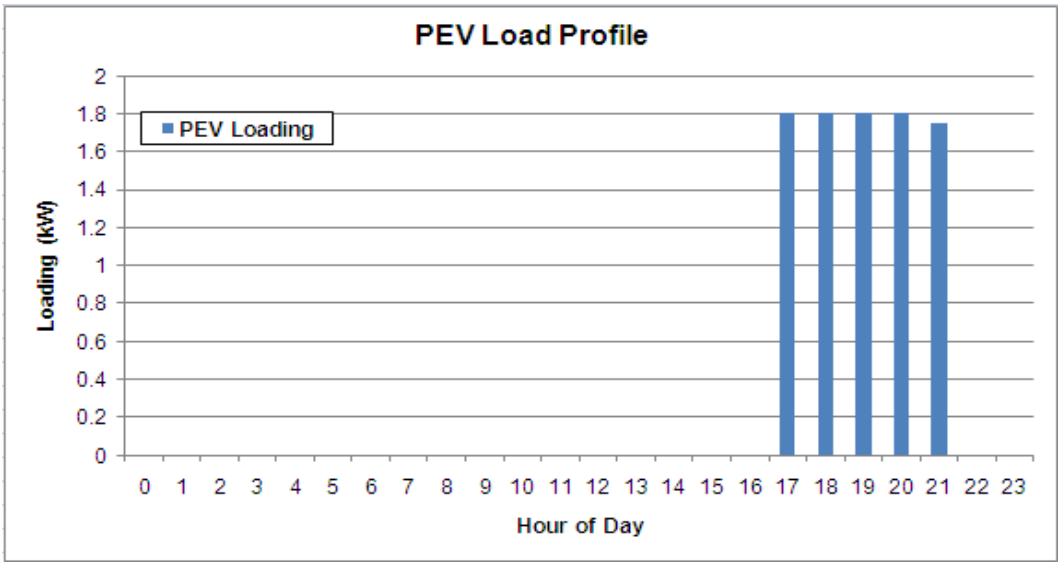

Figure 2-2 Typical 120V/15A Charging Profile for PEV

2.2.3. Solar Generation Profile

To analyze potential solar benefits of customer owned solar generation, a 2kW solar PV array for distributed generation is assumed. The study considers the solar incidence for the defined geographical locations in July and January. The solar generation back to the grid is based on data from the IMBY tool from NREL for the average solar incidence for two 1kW panels per installation.

2.2.4. Wind Generation Profile

For the assessment of wind energy potential, a 2kW wind turbine for distributed generation is assumed. The hourly mean wind speed is obtained from the NCDC for the defined geographical locations in July and January 2010 [2]. Then, the wind power produced is calculated by using wind speed:

$$P_{wind} = \frac{1}{2} \cdot \rho \cdot A \cdot v^3 \cdot c_p \qquad (2\text{-}1)$$

where ρ is the air density, A is the area cleared by the rotor, v is the wind speed, and c_p is the efficiency of the turbine. In this study, the wind power is calculated at 15°C and 1 atm pressure which is 1.225 kg/m^3 air density contained in 3.5 m rotor with 45% efficiency.

2.2.5. Storage Profile

The study also considers battery storage in combination with renewable energy, which stores the renewable energy production for later retrieval with 80% efficiency. While the real-time renewable

energy configuration produces more total energy, it has effectively no impact on the peak residential demands without control. However, when coupled with a storage system, the renewable energy generation is able to significantly influence peak characteristics, especially during the peak growth scenario driven by an emerging PEV market. In this study it is assumed that the storage system stores renewable energy production and returns to the system during the 7 hour near-peak duration from 5 PM to 12 PM.

2.3. Case Studies

2.3.1. Simulation Methodology

The distribution circuit to be analyzed is shown in Figure 2-3. This circuit has 1404 residential, 30 commercial, and small industrial customers with 90%, 9% and 1% of the total load, respectively.

Figure 2-3 Distribution Circuit to be Analyzed

This study utilizes a relatively conservative PEV adoption rate of one percent per year for residential customers over the next ten year period. It assumes the typical PEV owner would tend to initiate recharging upon returning home from the work. Thus, knowing the pattern of people arriving home from work will provide a probability distribution of when PEV charging will begin. By applying a Monte Carlo simulation to the census data and relating travel time to miles traveled [6], a profile of people arriving

home from work and the average number of miles people travel to and from work was obtained. The profile developed is in Figure 2-4 and shows the distribution of arrival times at home. This also assumed to represent the distribution of when PEVs will begin charging.

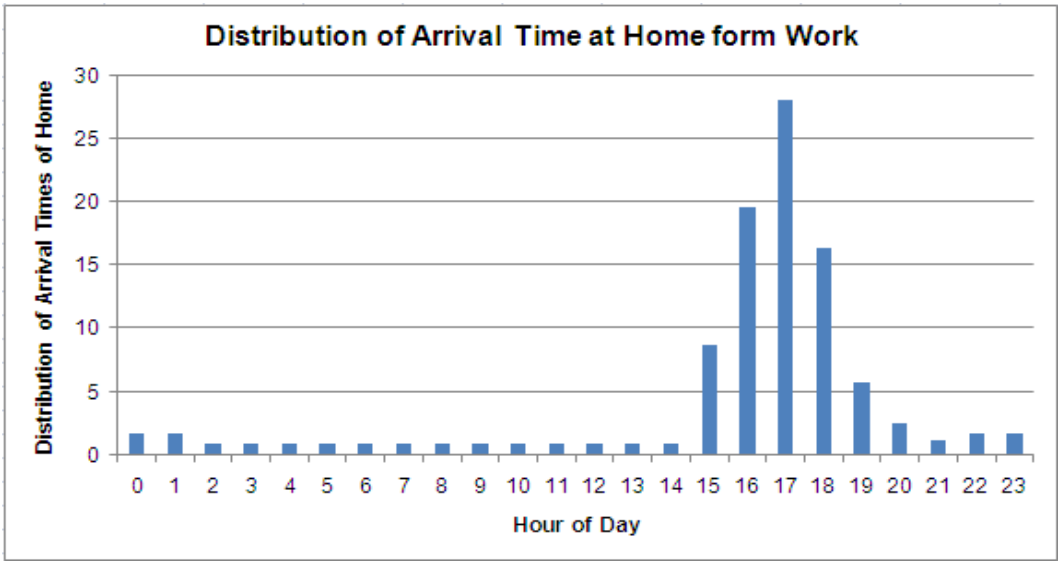

Figure 2-4 Distribution of Arrival Times at Home from Work

The study considers an aggressive ten year renewable energy (solar, wind) adoption rate of 3% per year, to analyze potential renewable energy source benefits with 30% of the residential customers having a 2kW renewable energy system for distributed generation. The generation impacts are also analyzed with storage system adoption rates of 3% per year over the same period. The storage systems could be provided by and controlled by the utility

Figure 2-5 presents the outline of the DER adoption algorithm. After the selection of a seasonal load profile and adoption levels of the customer class, the DER adoptions are randomly placed. This process is repeated until the selected adoption levels have been reached. System impacts are then analyzed in terms of induced component overloads and low-voltage conditions.

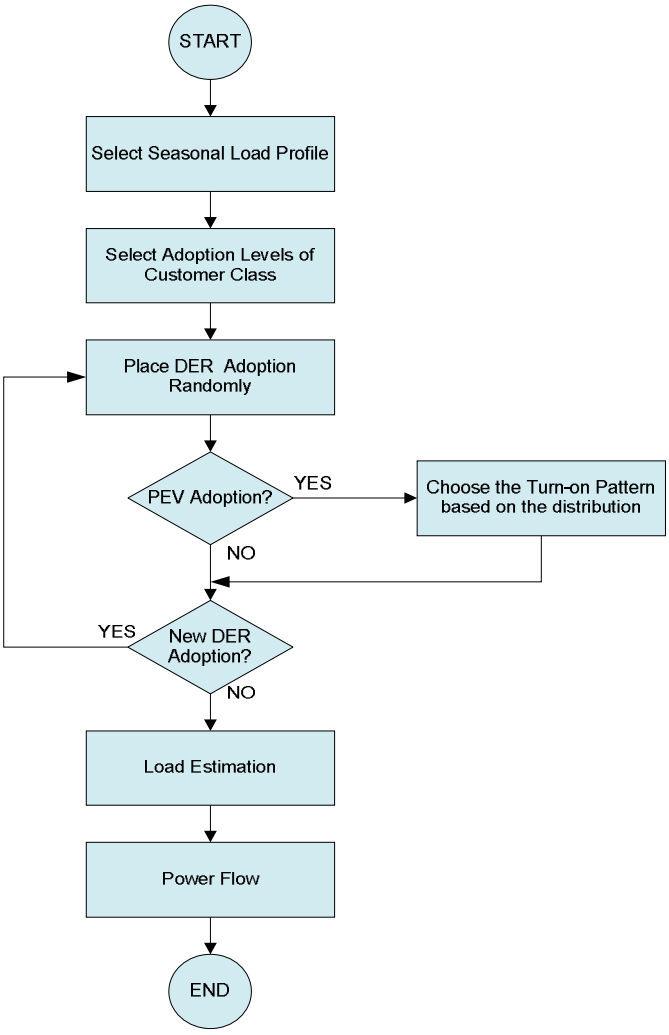

Figure 2-5 Flowchart of DER Adoption Analysis

The investigation analyzes the inherent variation in the performance of renewable energy resources by evaluating the same prototypical circuit during winter and summer loading conditions at three distinct geographic locations: northern (Detroit), middle (Los Angeles), and southern (Orlando), with the scenarios shown in **Error! Reference source not found.**.

Table 2-1 Scenarios of DER Adoption Analysis

	PEV	Solar Gen.	Storage (Solar)	Wind Gen.	Storage (Wind)
Base	×	×	×	×	×
Case 1	10 %	×	×	×	×
Case 2	10 %	30 %	×	×	×
Case 3	10 %	×	30 %	×	×

Case 4	10 %	×	×	30 %	×
Case 5	10 %	×	×	×	30 %
Case 6	10 %	10 %	×	10 %	×

2.3.2. Solar Generation

The resulting solar generation profile is shown in Figure 2-6 for each location in January and July. In this figure solar production is represented as negative load. This component data is then used to define the solar and storage components modeled per installation for the DER adoption analysis.

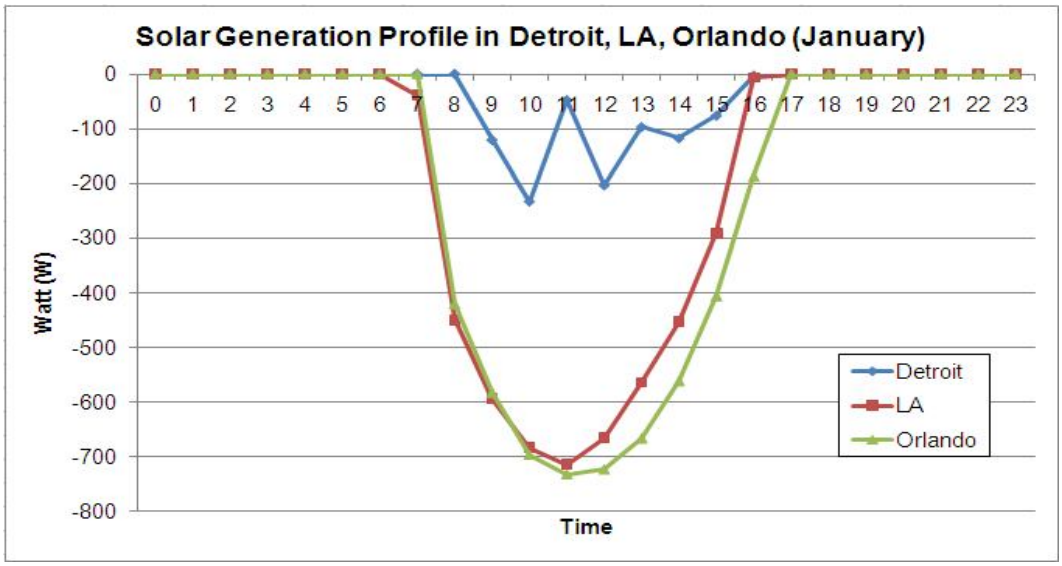

(a) Solar Generation Profile in January

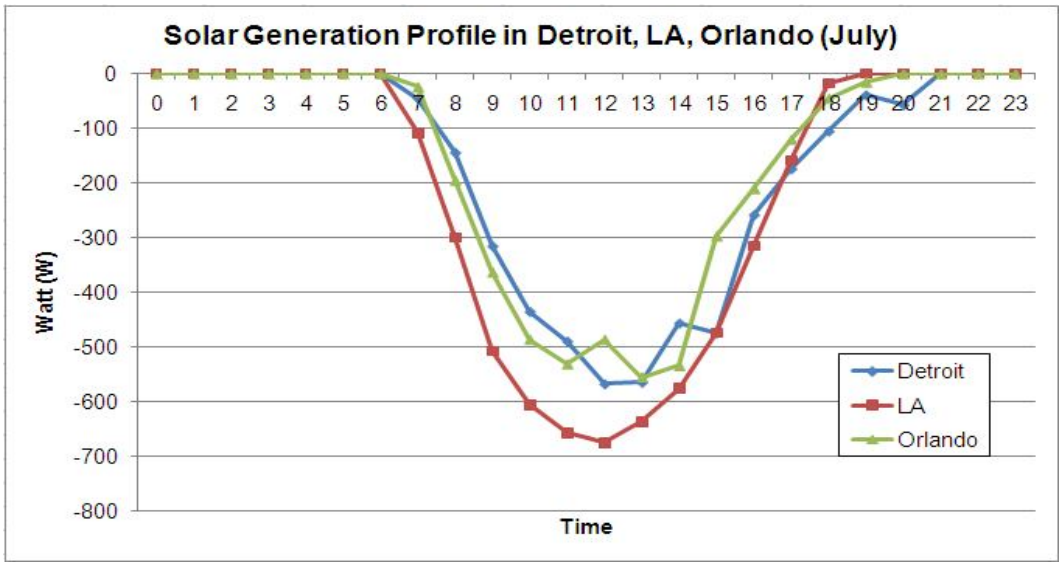

(b) Solar Generation Profile in July

Figure 2-6 Solar Generation Comparison by Location (2kW PV Array)

It was found that similar solar generation is produced during the summer in LA (5.0kWh), Detroit (4.1kWh), and Orlando (3.9kWh). In winter, comparable results are obtained between LA (4.5kWh) and Orlando (5.0kWh), while in Detroit (0.8kWh) there is noticeably less generation over the same period [7]. Furthermore, Orlando produces slightly more solar energy during winter than summer which provides a different pattern from the other two cities.

2.3.3. Wind Generation

Figure 2-7 compares the wind generation profile for each location in January and July. The figure shows the estimated negative load produced by wind generation. These results indicate that wind generation fluctuates more than solar generation but can produce energy during both day and night.

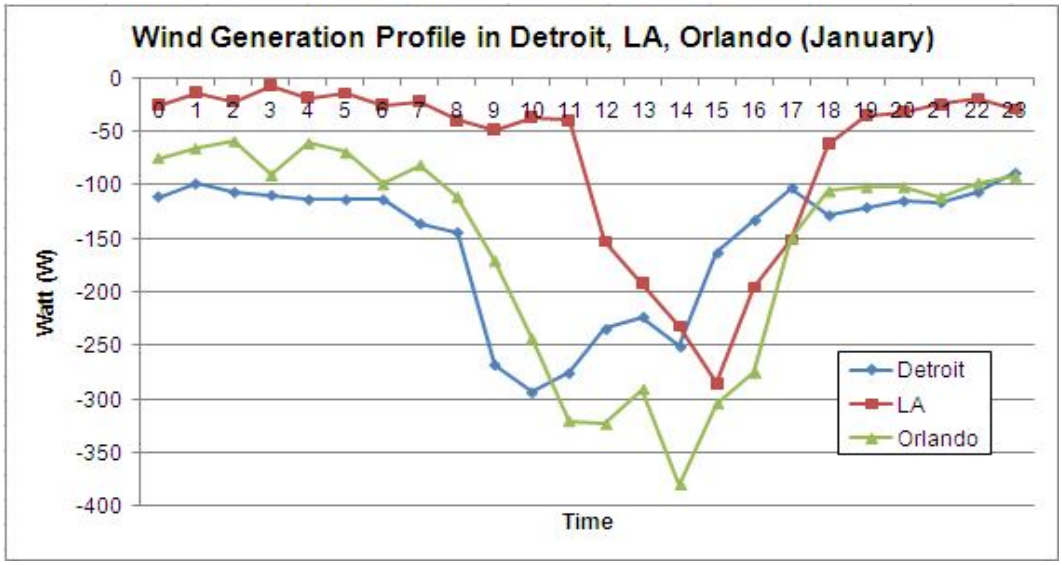

(a) Wind Generation Profile in January

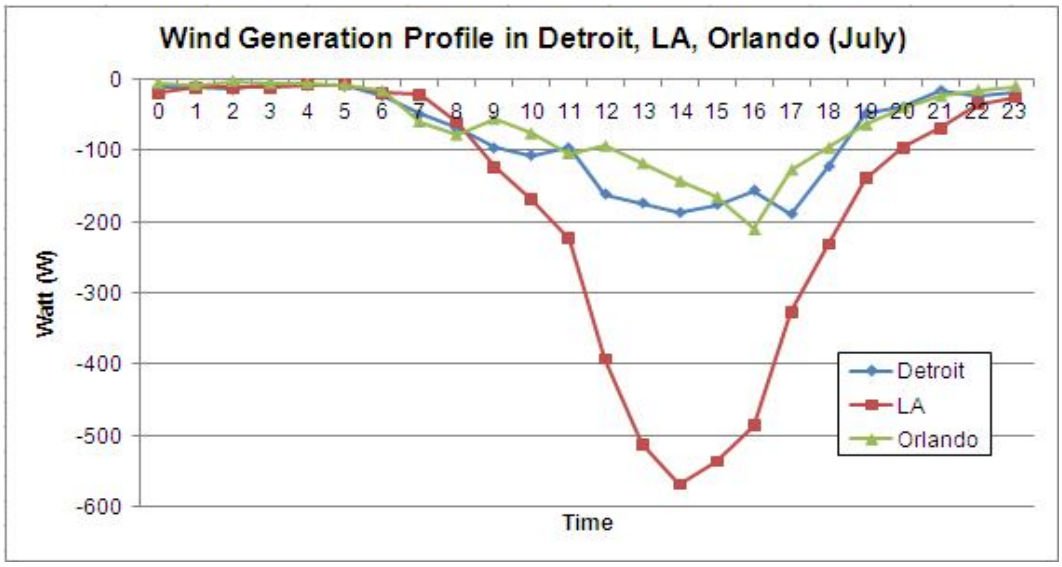

(b) Wind Generation Profile in July

Figure 2-7 Wind Generation Comparison by Location (2kW Wind Turbine)

It was found that Detroit (3.7kWh) and Orlando (3.8kWh) produce more wind generation than LA (1.7kWh) for the winter period. However, LA (4.1kWh) has more wind generation during summer than Detroit (1.8kWh) and Orlando (1.6kWh). A similar pattern is observed between Detroit and Orlando for wind generation. Note that smaller amounts of wind generation are observed in the three selected cities because of the lack of wind resources in large cities.

2.3.4. Reference Case

To understand the capability of DER generation and storage technology in offsetting a growing PEV market demand and induced overload conditions, a reference case is considered. Figure 2-8 shows the current flow for the prototypical circuit, measured at the substation, with 10% residential PEV adoption in January and July as a reference case. As expected, the majority of additional PEV loading is delivered in the near-peak period, and thus the peak current magnitude increases, resulting in system overloading conditions.

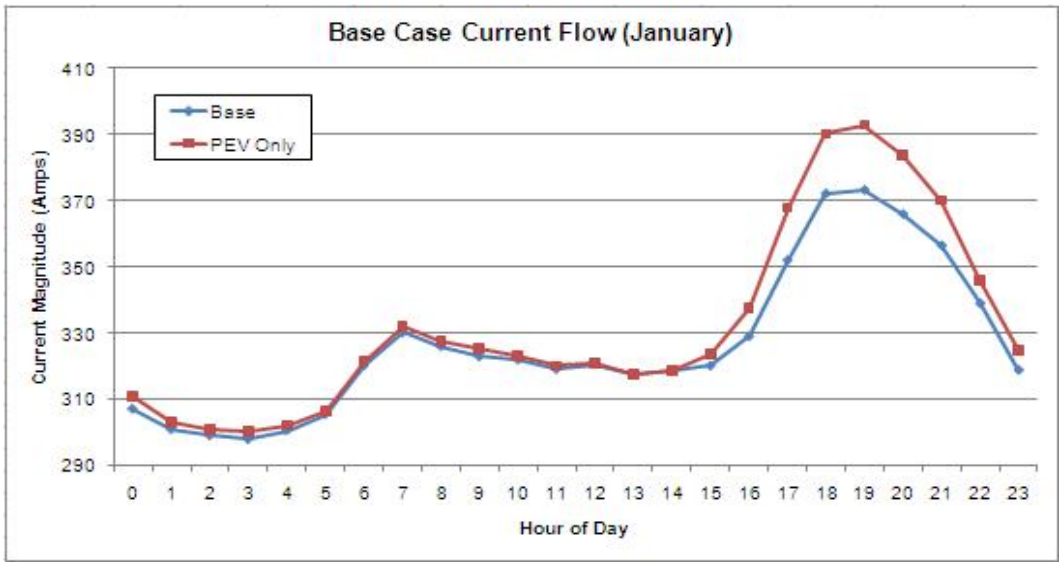

(a) System Current Flow in January

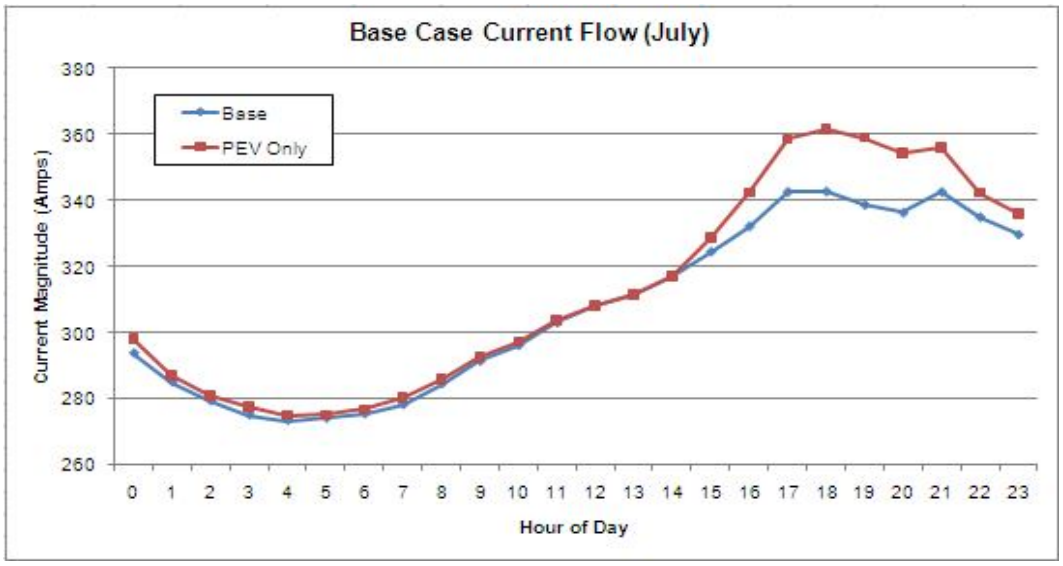

(b) System Current Flow in July

Figure 2-8 System Current Flow for Base Case by DER Adoption

Figure 2-9 shows that the charging scheme has a substantial influence on the number of overloaded components resulting from the PEV introduction. From 2 to 10 percent PEV adoption rates, the number of induced component overloads is seen to vary from around 1 to 2 for January, while ranging from around 1 to 6 for July.

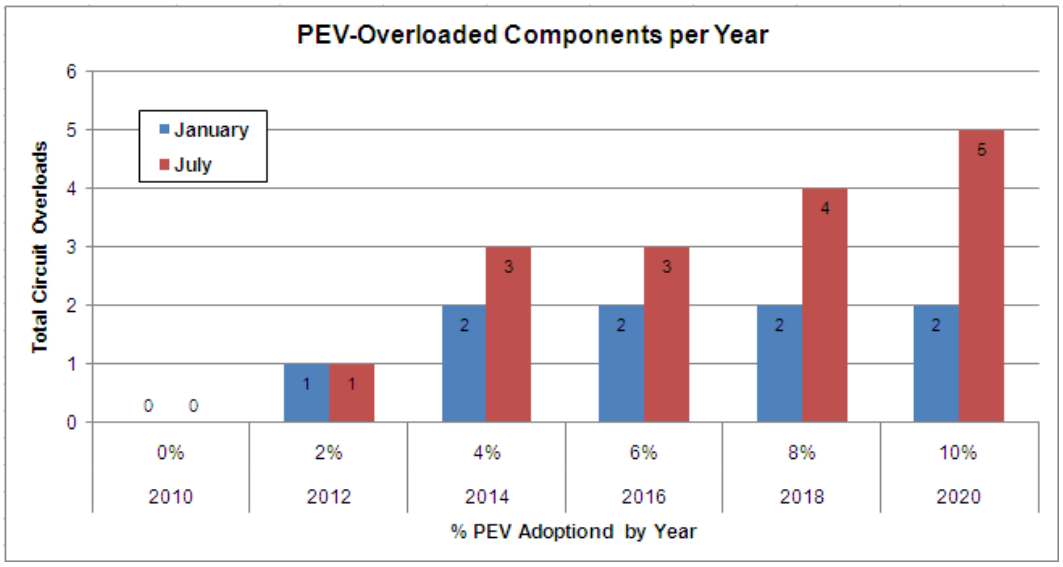

Figure 2-9 Number of PEV-Induced Overloaded Components

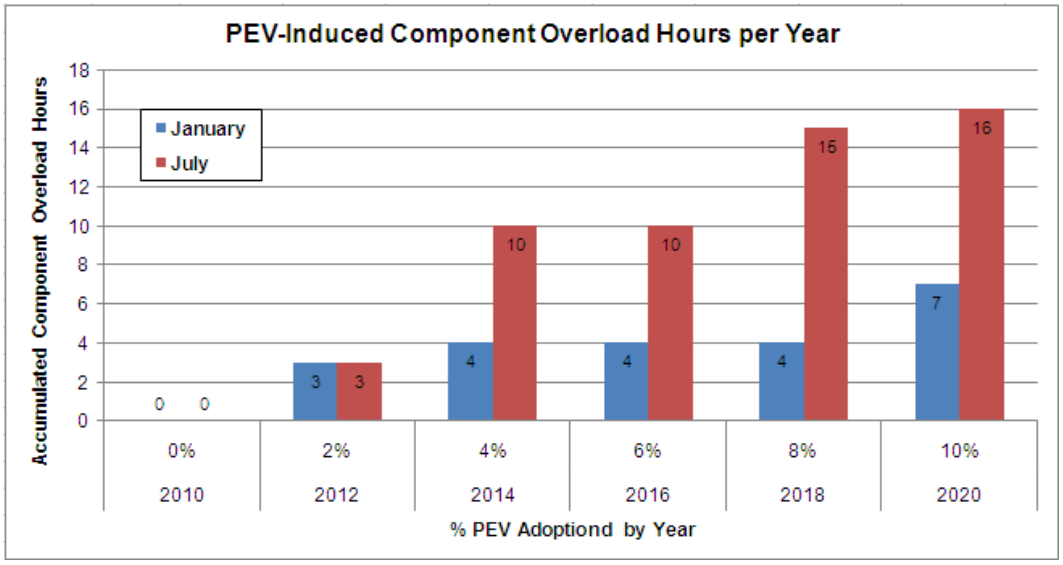

Figure 2-10 Accumulated Component Overload Hours

However, the range in the cumulative overloaded component hours for the same PEV adoptions varies from 3 to 7 hours for January and from 3 to 16 hours for July as indicated in Figure 2-10. Thus, more components are overloaded and remain in the overloaded state for a longer time period during summer.

2.4. Test Results

2.4.1. Detroit Case

Figure 2-11 and Figure 2-12 show results of the start-of-circuit current flow comparisons among the various scenarios of **Error! Reference source not found.** considered in January and July in Detroit. As illustrated in Figure 2-11, during winter, none of the DER generation scenarios coupled with PEV growth causes the current level to fall below the base system peak demand. The impact from solar generation is notably less during the winter but the wind generation helps offset the new PEV loads.

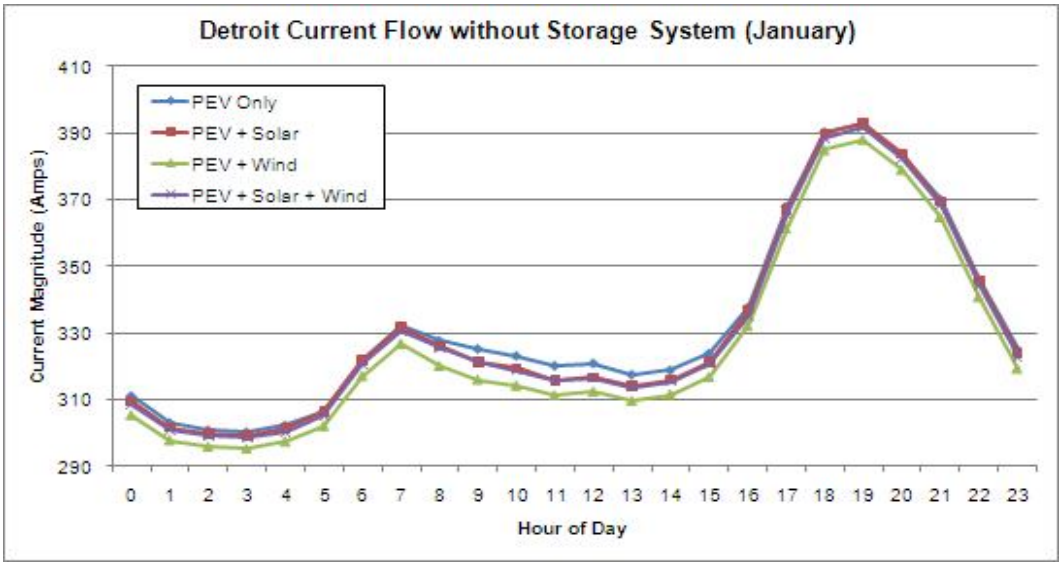

(a) System Current Flow without Storage System

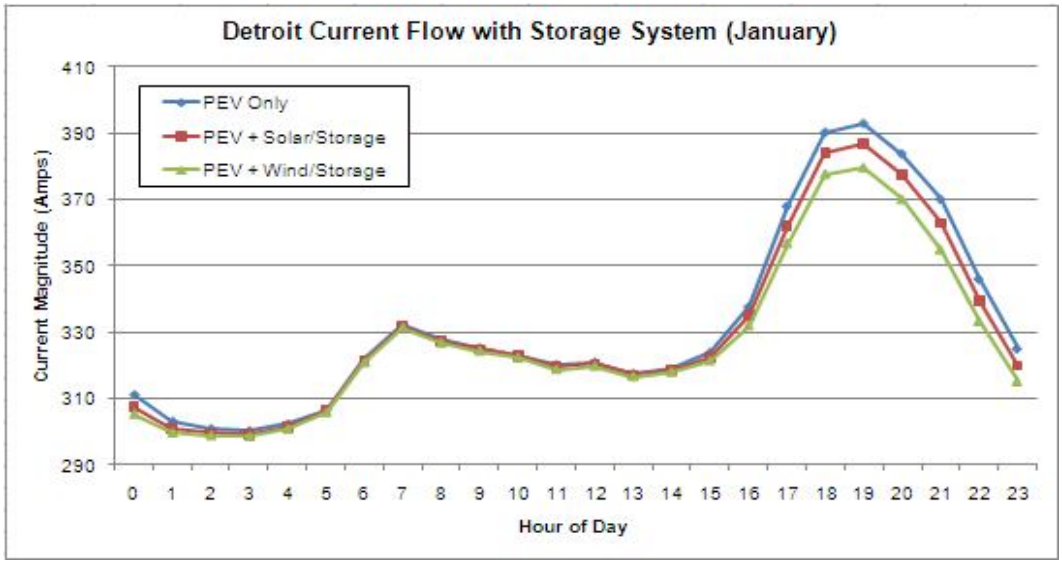

(b) System Current Flow with Storage System

Figure 2-11 System Current Flow for Detroit by DER Adoption in January

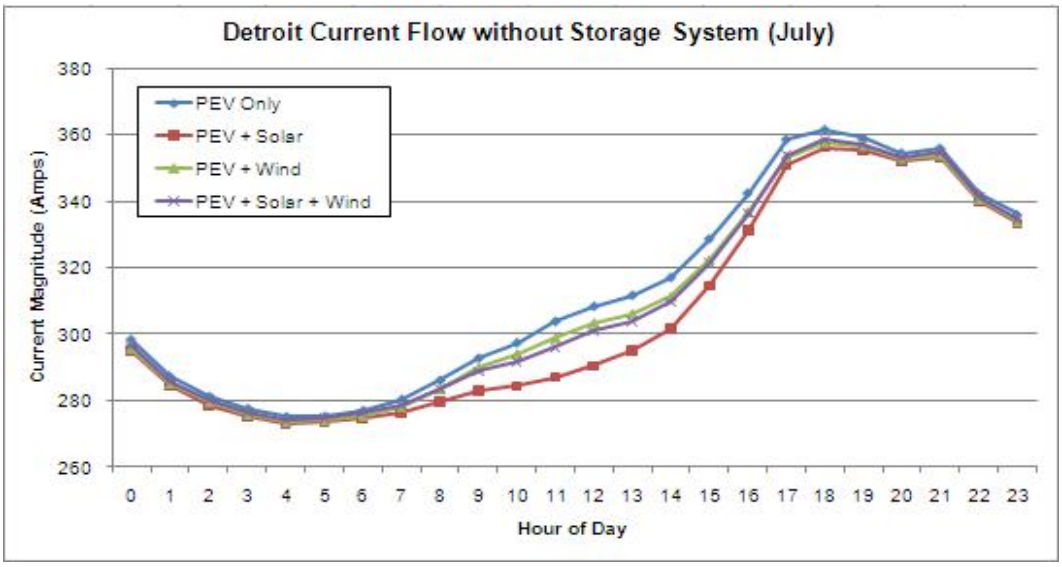

(a) System Current Flow without Storage System

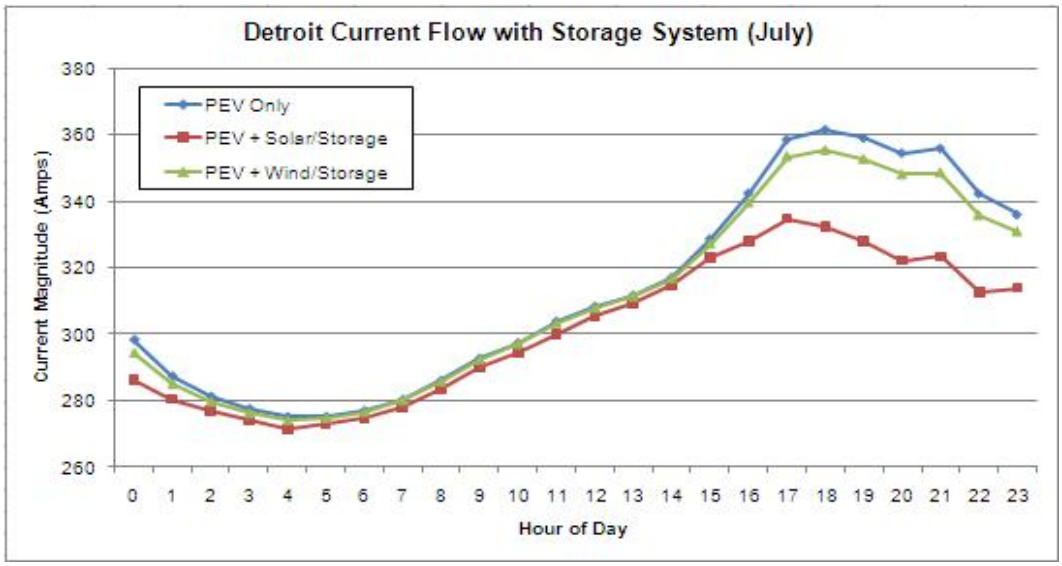

(b) System Current Flow with Storage System

Figure 2-12 System Current Flow for Detroit by DER Adoption in July

Figure 2-12 shows that for case 2, solar generation during summer, results in midday demand dips but has little impact on peak demands. With the projected PEV recharging occurring during the existing peak, the solar-storage combination is able to clip the increased peak demand to a level below that of the base system. However, for case 4, wind generation, only shows marginal improvements.

2.4.2. Los Angeles Case

Figure 2-13 and Figure 2-14 show the current flow for Los Angeles, measured at the substation, with the various scenarios considered in January and July. For cases 2 and 4 during the winter period, shown in Figure 2-13, standalone solar and wind generation level out the midday demand but have little impact on peak demand. With the combination of wind and solar generation for case 6, similar results are obtained. However, when coupled with the storage system, the solar generation reduced peak current flow in the system by approximately 7%. However, wind generation had little effect on peak demand.

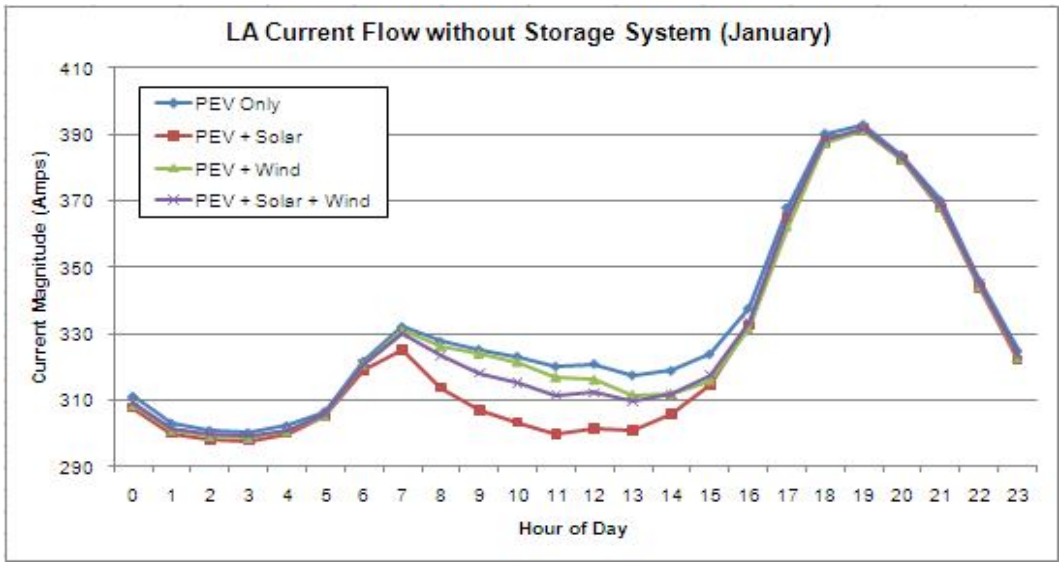

(a) System Current Flow without Storage System

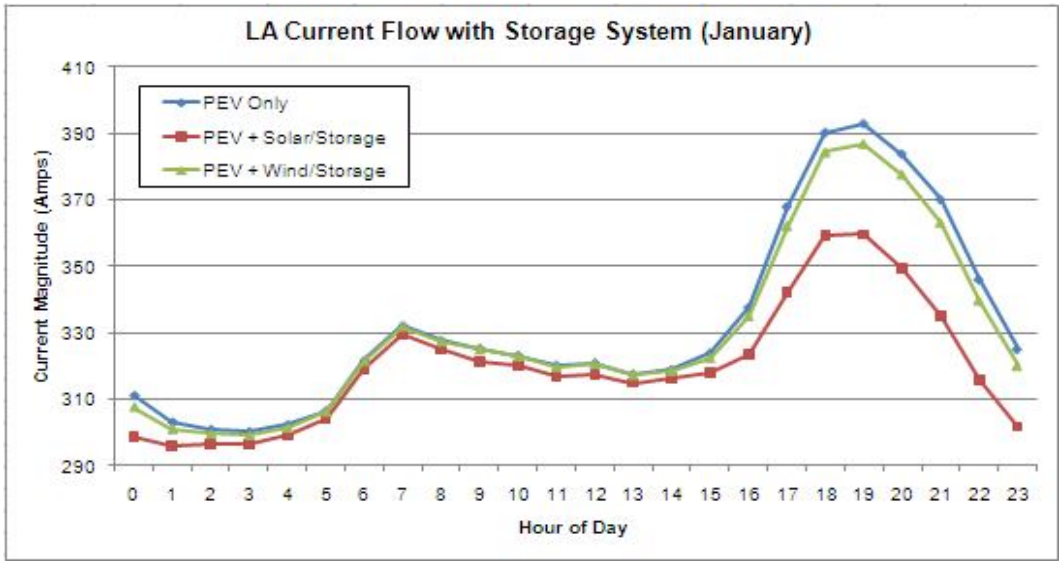

(b) System Current Flow with Storage System

Figure 2-13 System Current Flow for Los Angeles by DER Adoption in January

For the summer period shown in Figure 2-14, standalone solar and wind generation again have a negligible impact on the peak demand period, but essentially flattened the current flow when coupled with the storage system. In summer, both wind and solar generation are capable of reducing the peak demands induced by PEV charging.

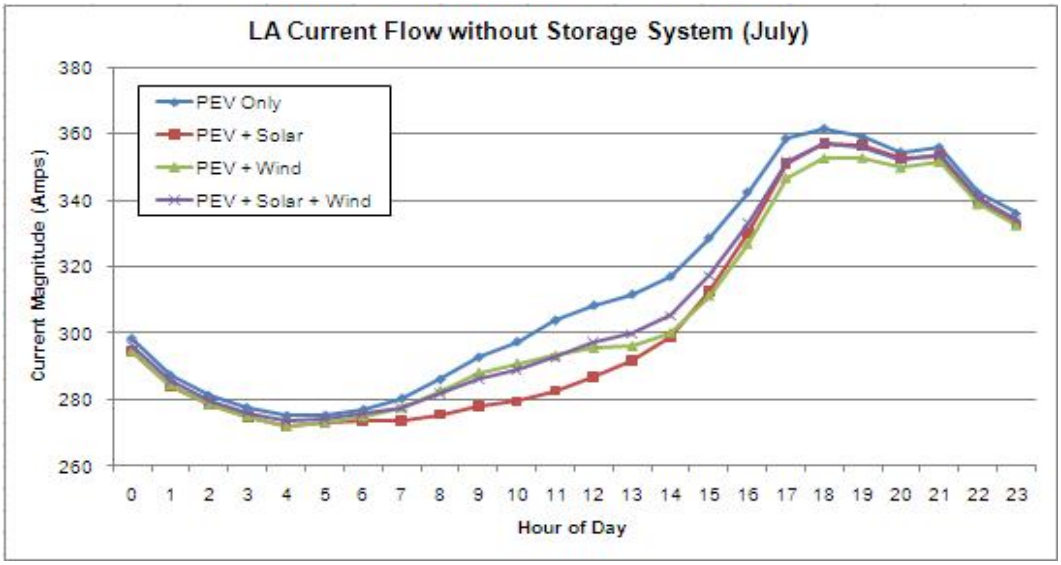

(a) System Current Flow without Storage System

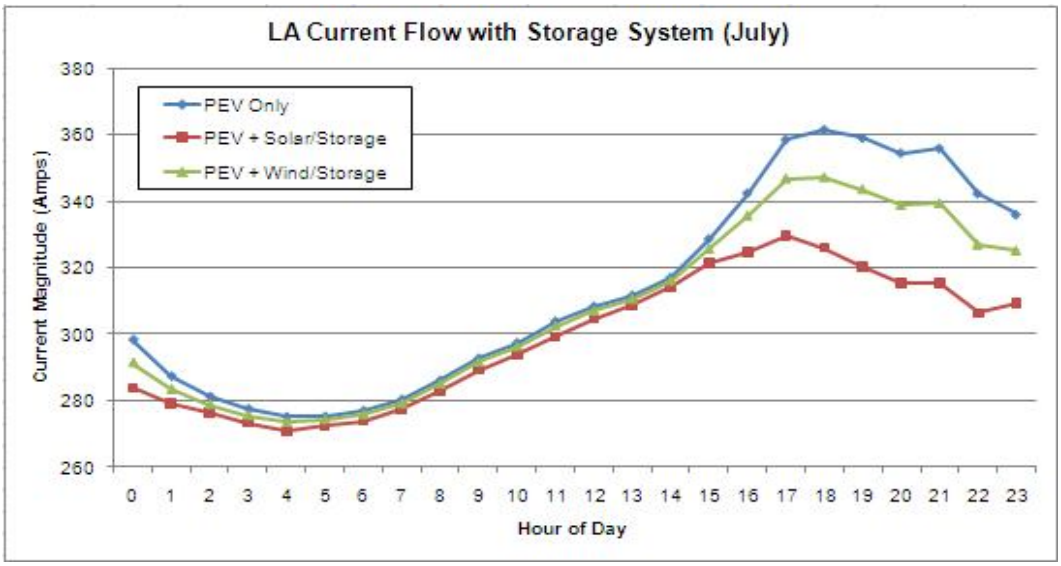

(b) System Current Flow with Storage System

Figure 2-14 System Current Flow for Los Angeles by DER Adoption in July

2.4.3. Orlando Case

Figure 2-15 and Figure 2-16 show current flow variations by system configuration in January and July in Orlando. Although standalone solar and wind generation are not available during the projected residential PEV market recharging period, in combination with the storage system can offset a growing PEV market demand for the winter period shown in Figure 2-15.

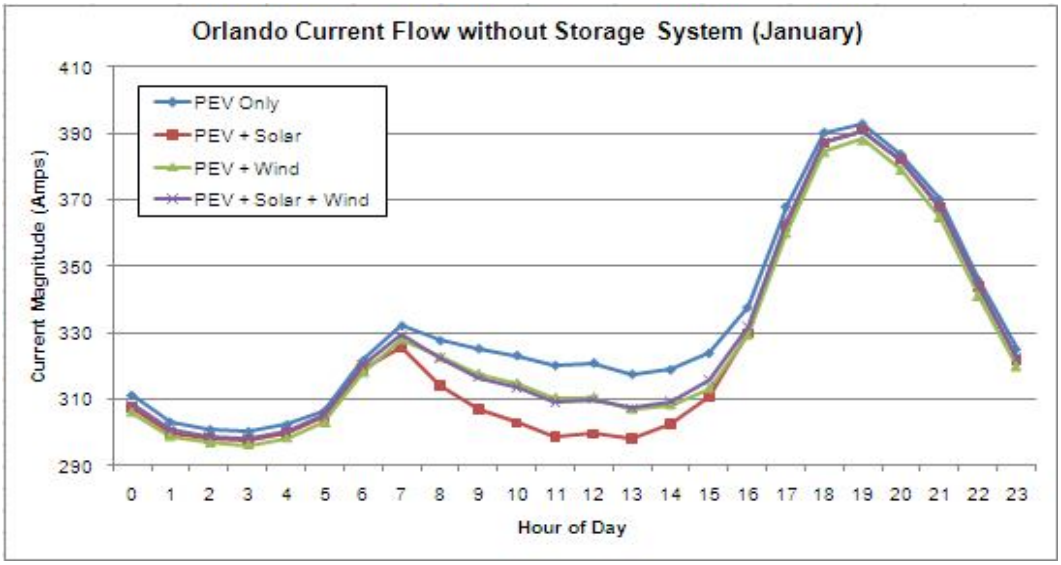

(a) System Current Flow without Storage System

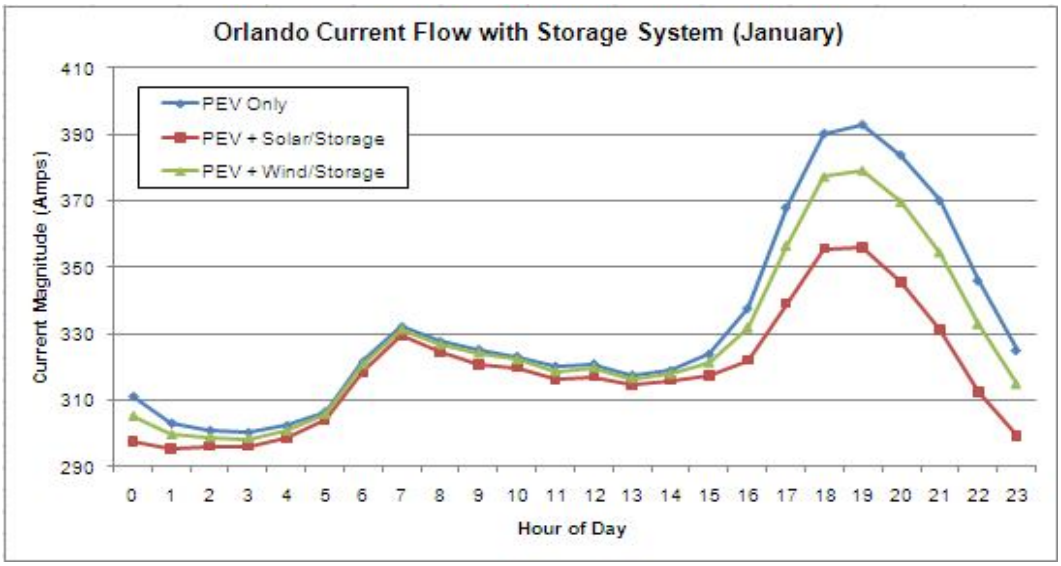

(b) System Current Flow with Storage System

Figure 2-15 System Current Flow for Orlando by DER Adoption in January

Figure 2-16 shows solar-storage impacts on the induced PEV demands during the summer period, when stored solar energy is recovered during the peak period. It also shows the diminished benefits of wind generation.

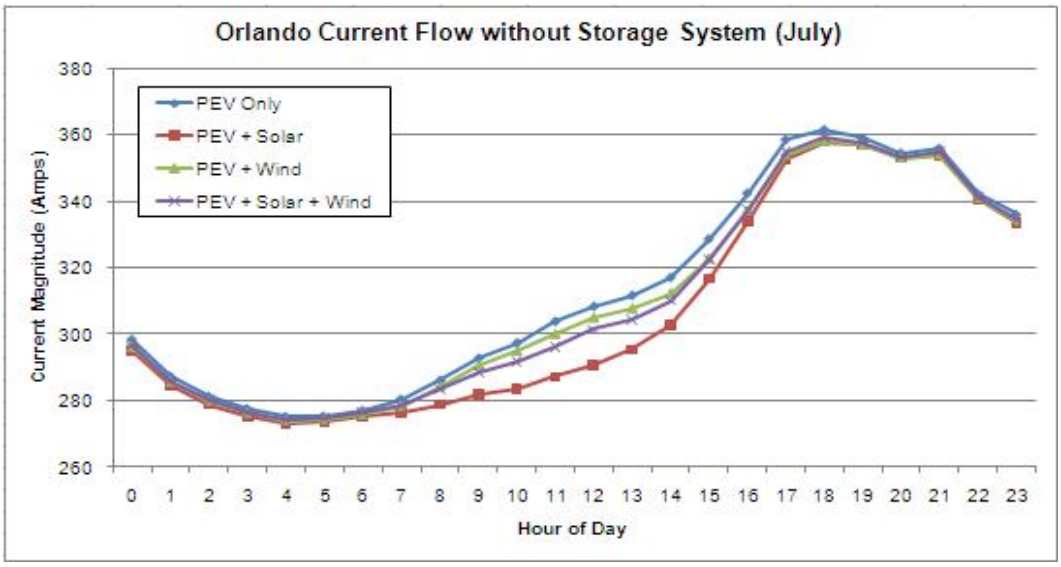

(a) System Current Flow without Storage System

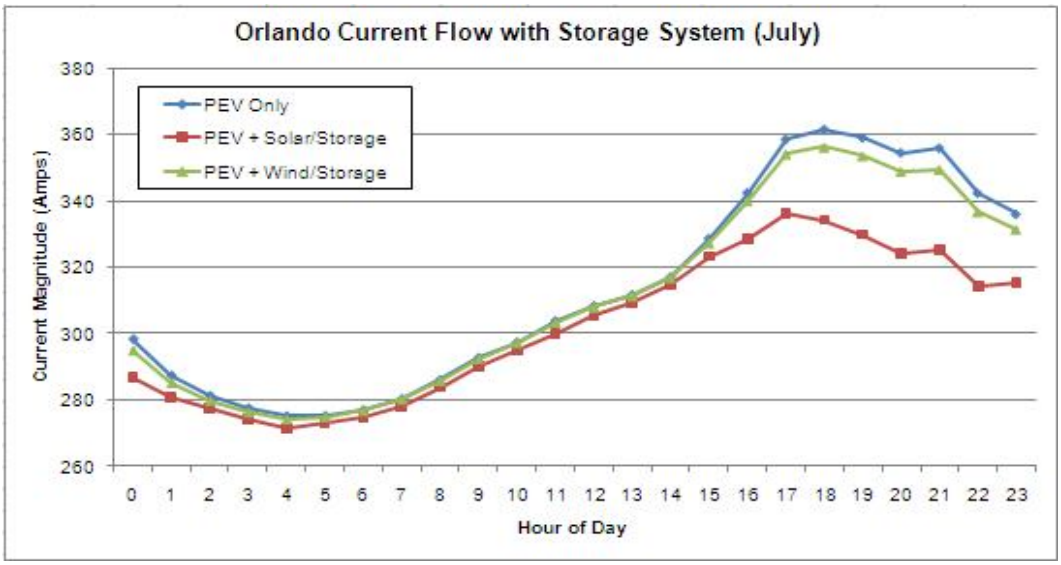

(b) System Current Flow with Storage System

Figure 2-16 System Current Flow for Orlando by DER Adoption in July

2.4.4. Case Study Comparison

Figure 2-17 summarizes peak current flow comparisons by location for the various scenarios. The results illustrate that a customer owned solar market could produce some significant impacts on current energy consumption profiles, primarily of benefit to utilities when coupled with an efficient battery storage device, which is needed to affect peak demands. The benefit of customer owned solar generation with battery storage is consistent for all locations during the summer analysis, where the applied solar generation is able to completely offset the added PEV loading. For the winter period, LA and Orlando are

comparable in reducing the PEV-induced demand, while the Detroit location shows significantly less benefit.

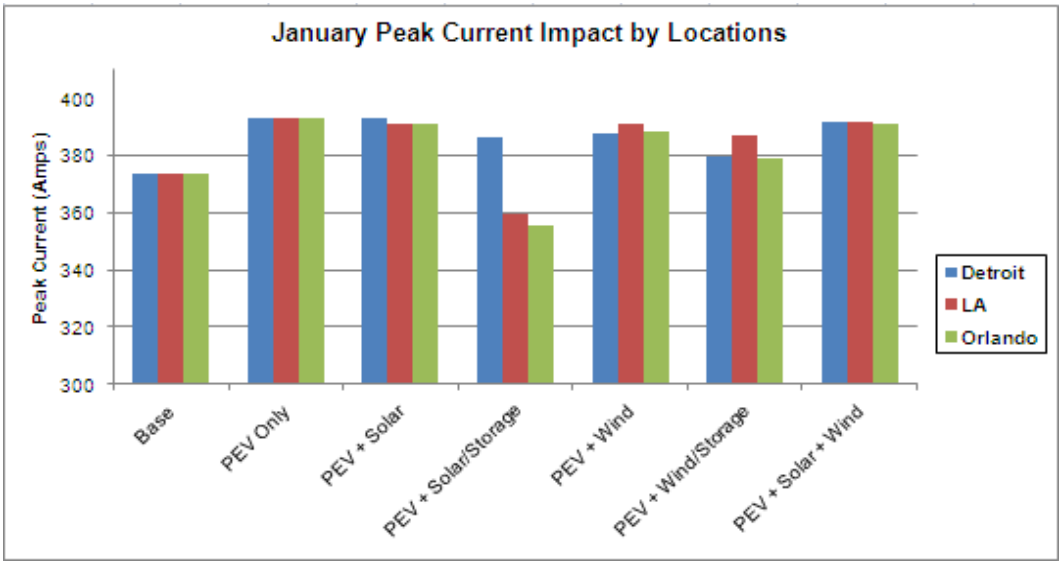

(a) Peak Current Comparison in January

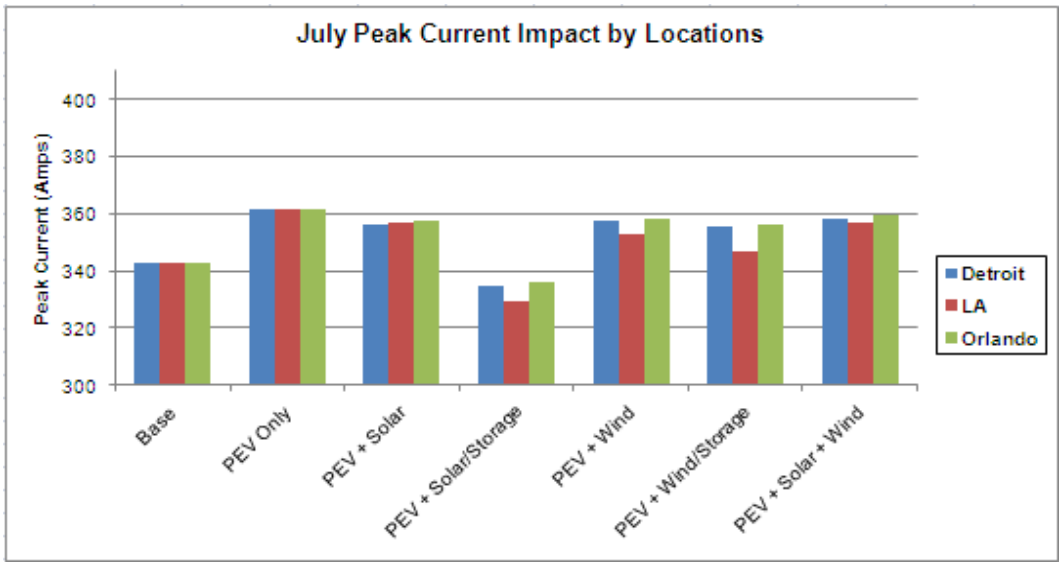

(b) Peak Current Comparison in July

Figure 2-17 Peak Current Comparison by Location

However, a customer owned wind market shows less benefit, even in combination with battery storage because there is less wind resource in the large, developed cities. Furthermore, standalone solar and wind generation have negligible impact on the peak demand period, as most of the generation occurs during the off-peak period for the predominantly residential feeder considered.

2.5. Conclusion

The results demonstrated that a maturing PEV market could produce significant impacts on peak demand, resulting in additional system overloading conditions. Thus, the study considers solar and wind generation, as well as in combination with battery storage system to control the associated peak demand growth driven by an emerging PEV market.

While the solar configuration produces more total energy, it has effectively no impact on the peak residential demands, which typically occur during times when solar generation is unavailable. However, when coupled with a battery storage system, the solar generation is able to significantly influence peak characteristics, especially during the peak growth scenario driven by an emerging PEV market. The study shows that in LA and Orlando, 30% adoption of solar generation could offset a 10% PEV adoption. This is also true in Detroit in the summer, but not the winter.

The "available at night" wind configuration shows less benefit, even in combination with battery storage system because of the lower total energy from the wind resource. The study shows that in the three selected cities, 30% adoption of wind generation could help to reduce the peak demands induced by 10% PEV adoption, but not offset the PEV loading.

Chapter 3 Monte Carlo Analysis of Plug-in Hybrid Vehicles and Distributed Energy Resource Growth with Residential Energy Storage in Michigan

3.1. Introduction

A PHEV is a hybrid electric vehicle which is designed to recharge its batteries by plugging into the power source. It is a potential solution to reduce vehicle emission and oil dependency. The Electric Power Research Institute (EPRI) quantified three distinct market PHEV adoption scenarios for the period 2010-2050 [8]. In these scenarios it takes some time to penetrate the market. However, PHEVs will have a significant share after some years. PHEVs reach a 20% of new vehicle market share in the low PHEV scenario, 62% in the medium PHEV scenario, and 80% in the high PHEV scenario.

Renewable energy as an alternative to fossil fuels offers a number of benefits. It reduces greenhouse emission and air pollutants during operation. Furthermore, it uses free, clean, and plentiful energy resources. Two representative energy resources are wind and solar energy. In some regions these are becoming increasingly significant sources of power system generation, and will become important energy resources in the future of energy supply. The U.S. Department of Energy (DOE) explores an energy scenario in which wind generation supplies 20% of power system generation by 2030 [9]. DOE also explores a future solar generation adoption scenario for the period 2010-2050 [10]. In this scenario, the contribution of solar generation is projected to be 14% of power system generation by 2020 and 27% by 2050.

The potential impact of PHEV on the existing power system has been studied in [11-24]. In these papers, PHEVs affect utility operations by adding additional electricity demand. Furthermore, large penetrations of PHEV result in reduced gas emissions, improved economics for utilities, and reduced oil dependencies. However, only effects of the addition of PHEVs into the existing power system are considered.

In previous work [25], the adoption level of solar and wind generation supplemented with storage are evaluated, and how these technologies may mitigate the effect of new electric vehicle loads are evaluated. However, the test scenarios considered are not based on future PHEV and DER projections. Furthermore, simulating one time point is not sufficient to evaluate the uncertainty of future PHEV load and DER

generation. In this chapter, using the 2020 and 2030 future scenarios [8-10], system effects due to the addition of PHEV, solar generation, and wind generation are considered, providing more realistic simulations. Furthermore, Monte Carlo simulation is used to evaluate adoption patterns of residential customers. The Monte Carlo simulation provides not only the expected average result, but also its uncertainty. Renewable energy growth coupled with storage systems that offset PHEV load growth is also considered.

The chapter is organized as follows. Section 3.2 presents the assumptions that are made regarding native system loads, PHEVs, DER, and storage. In Section 3.3 the adoption level of PHEVs and DERs in 2020 and 2030 are presented. In addition, the Monte Carlo simulation of the DER adoption analysis is introduced. In Section 3.4 the results of summer and winter analysis of an actual circuit with individual residential customers modeled are presented. Analysis results are then considered. Finally, findings of the study are summarized in Section 3.5.

3.2. Simulation Assumptions and Profile

3.2.1. Native Load Profile

For each hour, customer loads are estimated from averaged hourly SCADA measurements, hourly customer kWh load data, and monthly kWh load data processed by load research statistics to create hourly loading estimates for each customer [3, 4, 26-29]. From the available set of residential load measurements, winter (January) and summer (July) load profiles are selected to evaluate the seasonal effects. Figure 3-1 presents the kW measurements at the substation estimated from the native load profiles during winter and summer at the selected location in Michigan. The circuit considered (see Figure 3-12) has 2751 residential customers and 111 commercial customers. Due to the heavy residential load the circuit peaks later in the day, with the annual peak occurring during the summer. These load profiles provide a baseline condition prior to adopting the PHEVs and DERs.

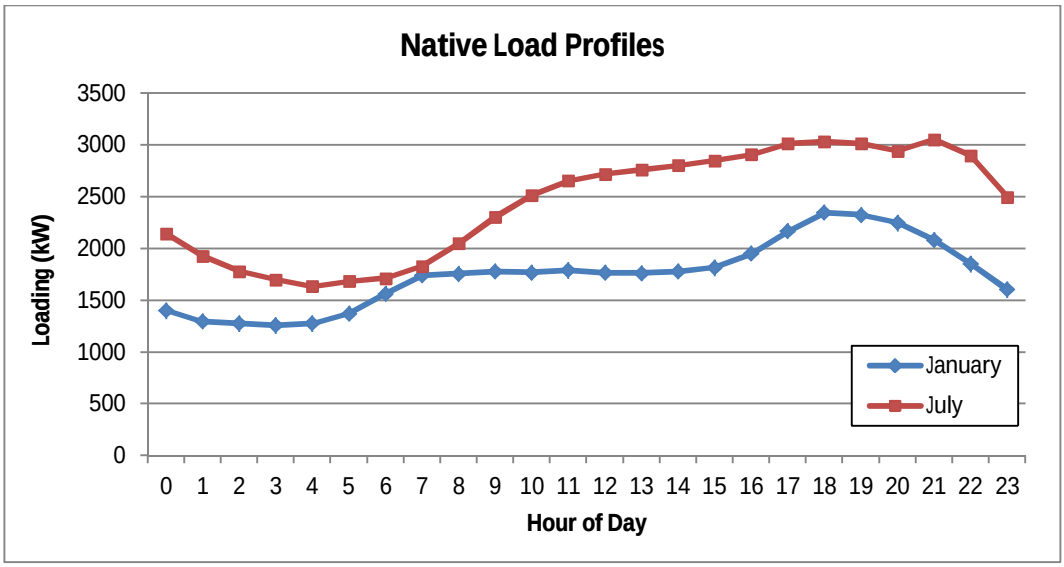

Figure 3-1 Native load profiles during summer and winter

3.2.2. PHEV Load Profile

Since PHEV technology is new to the mass market, information concerning how consumers will utilize the technology is not available. Therefore, several assumptions on PHEV usage are made in this study. It is assumed that the typical PHEV owner initiates recharging upon returning home from work. It is also assumed that the PHEV battery is charged from no charge to full charge when the charging occurs once a day. This assumption provides the worst case scenario. There are some likely PHEV charging profiles in [5]. This study uses a 120V/15A PHEV battery charger scenario. Figure 3-2 shows the typical 120V/15A charging profile for an 8kWh PHEV charger with an essentially constant demand of around 2kW for 5 hours.

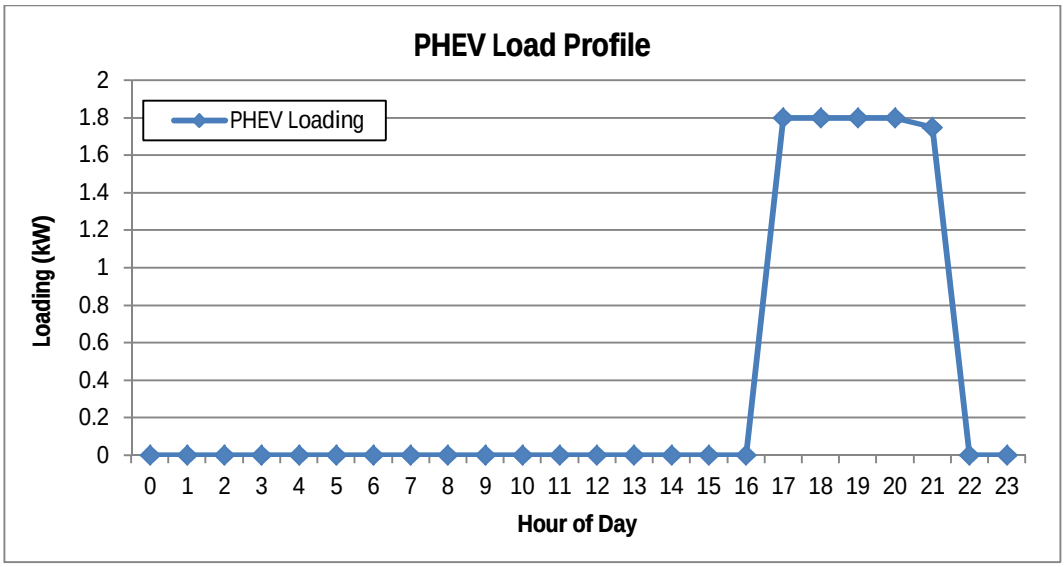

Figure 3-2 Typical 120V/15A charging profile for PHEV

3.2.3. Solar Generation Profile

For the simulation of solar generation, 4 kW solar generation units are used here. For a given geographical location, solar generation data from Clean Power Research (CPR) provides hourly solar generation data based on the defined solar generator parameters [30]. The solar generator parameters include system location information such as latitude and longitude, and solar generator specification such as the generator rating, efficiency, and tracking. The hourly average of the solar generation in January and July 2010 are used in this study. The resulting solar generation profile at a selected location in Michigan is shown in Figure 3-3. It is found that the solar generation in winter is noticeable less than summer at this location.

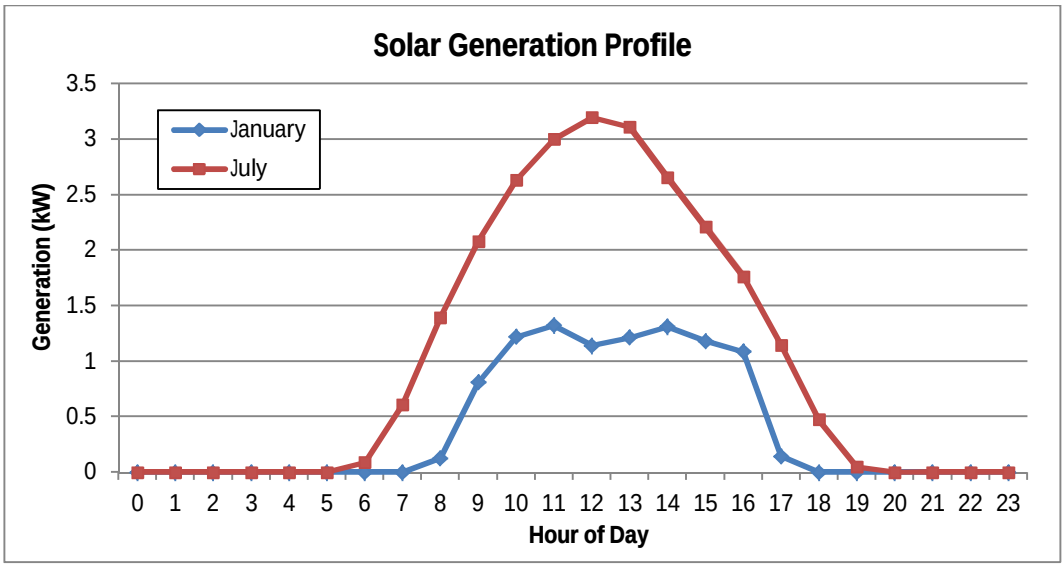

Figure 3-3 Solar generation profile during summer and winter

Before considering the effects of solar generation, verification of the solar generation profile used will be addressed. The data for comparison is obtained from the IMBY tool from NREL [1]. The comparison of solar generation profiles obtained from CPR and NREL is shown in Figure 3-4. As shown in this figure, the solar generation profile from CPR matches well with the reference profile from NREL during both winter and summer.

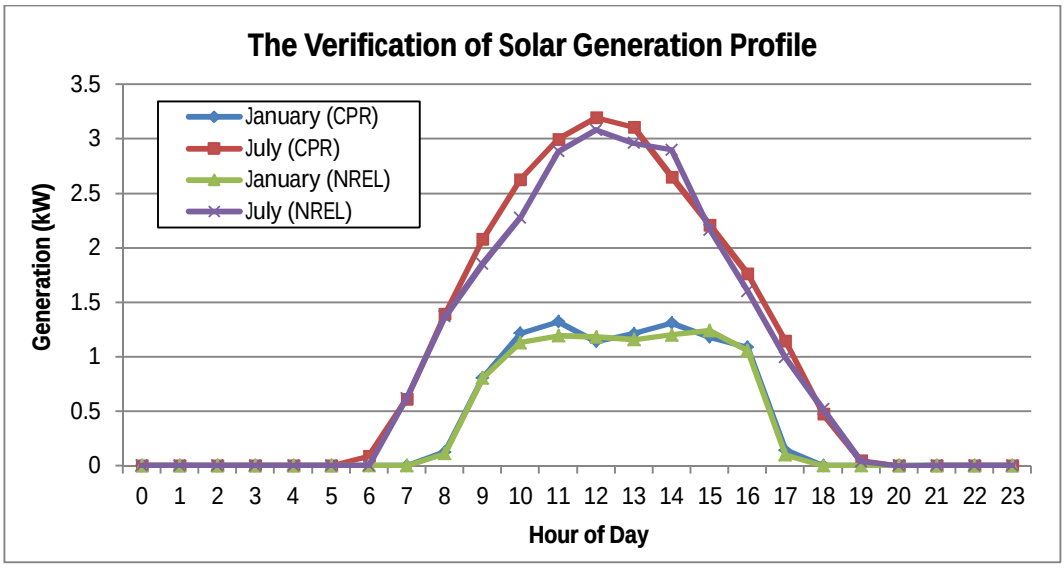

Figure 3-4 The verification of solar generation profile at the selected location

3.2.4. Wind Generation Profile

For the assessment of potential wind generation, a 4 kW wind generator is assumed. The hourly average wind speed is obtained from the NCDC for a given location in January and July 2010 [2]. Then, the wind generation is calculated by using the wind speed as:

$$P_{wind} = \frac{1}{2} \cdot \rho \cdot A \cdot v^3 \cdot c_p \tag{3-1}$$

where ρ is the air density, A is the area cleared by the rotor, v is the wind speed, and c_p is the efficiency of the turbine. In this study the wind generation is calculated at 15˚C and 1 atm pressure which is 1.225 kg/m^3 air density contained in a 5.0 m rotor with 40% efficiency. The hourly average of the wind generation at the selected circuit location in Michigan in January and July 2010 are shown in Figure 3-5. This figure indicates that wind generation fluctuates significantly, but the wind can produce energy during both day and night. Note that smaller amounts of wind generation are observed at this location because in general there is less wind resource available around large, developed cities.

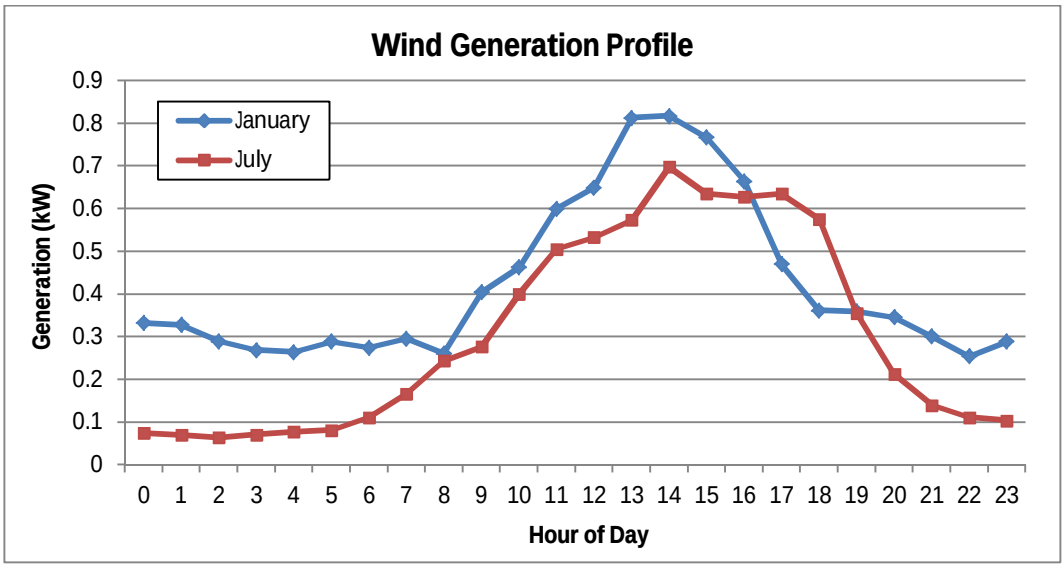

Figure 3-5 Wind generation profile during summer and winter

Before considering the effects of wind generation, a verification of the wind generation profile used will be performed. The wind speed used is based on actual measurements. The verification will be performed by comparing the calculated wind power using Eq. 3-1 with wind power calculations from a wind turbine manufacturer. The wind power curve of the UGE-4K wind turbine from Urban Green Energy is used for comparison [31]. The comparison of the wind generation profile obtained from Eq. 3-1 and the manufacturer's power curve is shown in Figure 3-6. As shown in this figure, the wind generation

profile from the model is quite well matched with the reference profile from the wind turbine power curve at the selected location during both winter and summer.

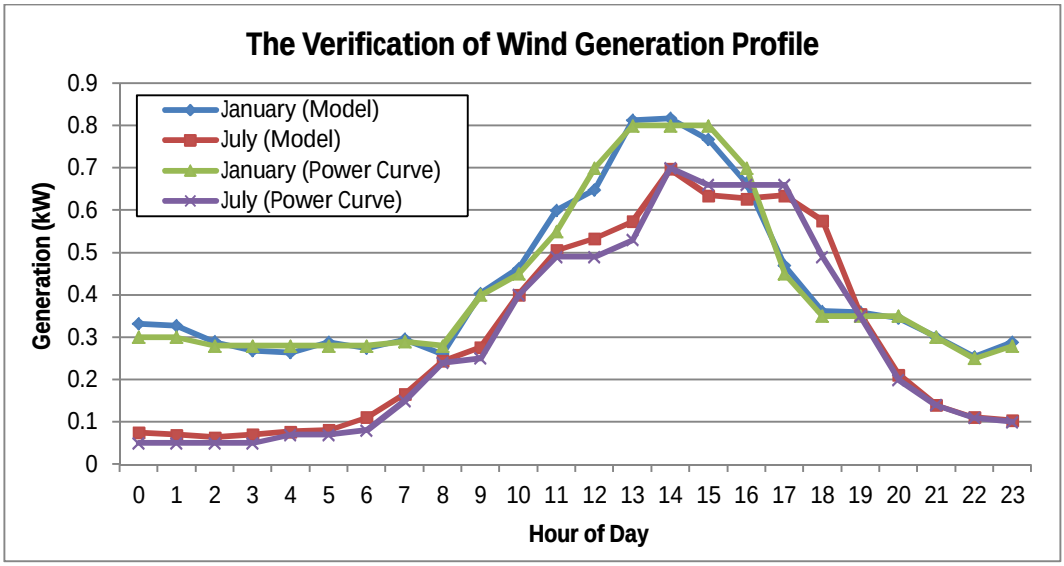

Figure 3-6 The verification of wind generation profile at the selected location

3.2.5. Storage Profile

While the real-time DER generation produces more total energy, it has effectively no impact on the peak residential demands which occur during times when the DER generation is off-peak. However, when coupled with an energy storage system, the DER generation can be used to influence the peak characteristic significantly, especially during the peak growth scenario driven by an emerging PHEV market. Therefore, this study considers a combination of DER generation with DER-storage, which stores DER generation for later retrieval. It is assumed that the size of the storage is limited to approximately 30% of the rated DER generation. Therefore, in the work here 1.2 kW of storage is coupled with 4 kW DER generation. It is also assumed that the energy storage system returns the stored energy to the electric distribution system during the 7 hour near-peak duration from 5 PM to 12 PM with 80% conversion efficiency.

3.3. Monte Carlo Simulation of DER Adoption Analysis

3.3.1. PHEV Penetration

To apply the PHEV adoption level determined by 2020 and 2030 future scenarios, market penetration of PHEVs from 2010 to 2030 are illustrated in Figure 3-7 [8]. As shown in this figure, the PHEVs could

reach a 36 % and 52% of new vehicle market share by 2020 and 2030, respectively. In this study, the number of customers who have PHEVs is decided based on these PHEV penetration estimates.

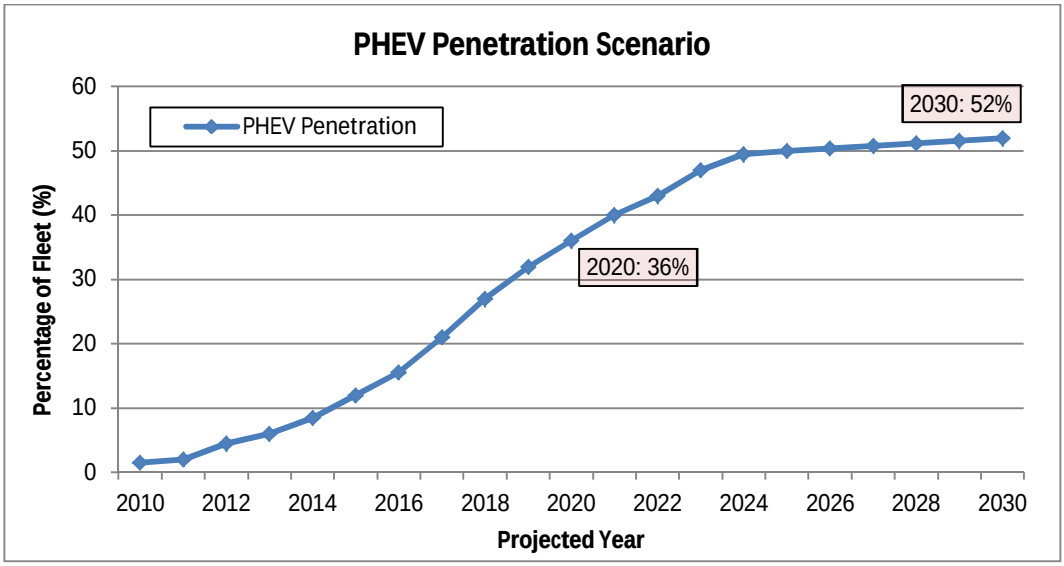

Figure 3-7 PHEV market share penetration scenario as a percent of vehicle market [8]

It is assumed that the PHEVs are charged in the house when the owners return home. Therefore, knowing the pattern of people arriving home from work can provide information when the PHEV charging will begin. A probability distribution of people arriving home from work is obtained by applying a Monte Carlo simulation to the census data and relating travel time to miles traveled as shown in Figure 3-8 [6]. Based on this distribution, it assumes that the PHEV owner initiates charging upon arriving home.

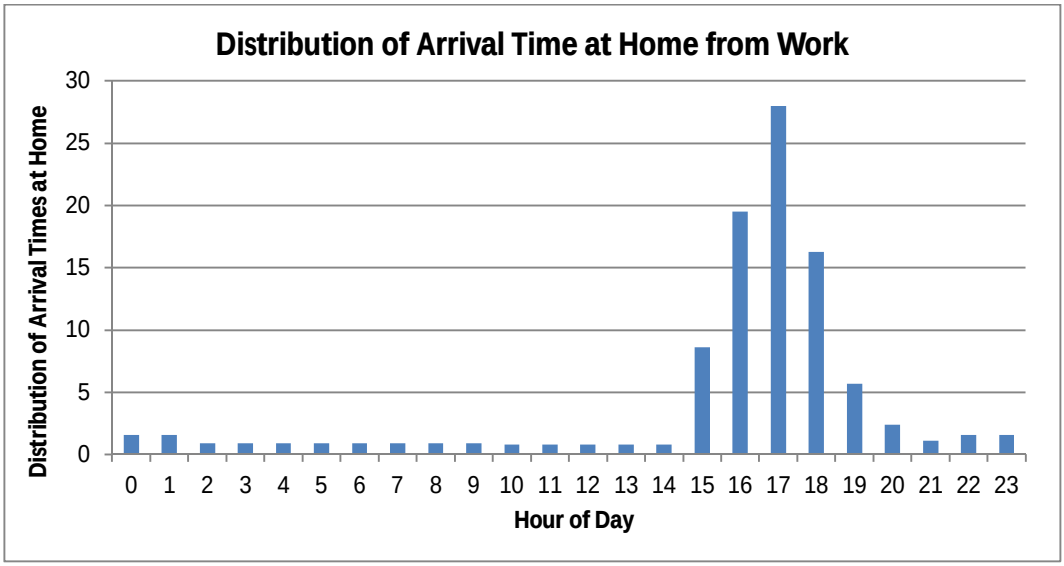

Figure 3-8 Distribution of arrival times at home from work

3.3.2. Solar Generation Penetration

The adoption level of solar generation in 2020 and 2030 are decided based on the future scenario shown in Figure 3-9 [10]. In this scenario, the contribution of solar generation is projected to be 3 % and 14 % of total electric demand by 2020 and 2030, respectively.

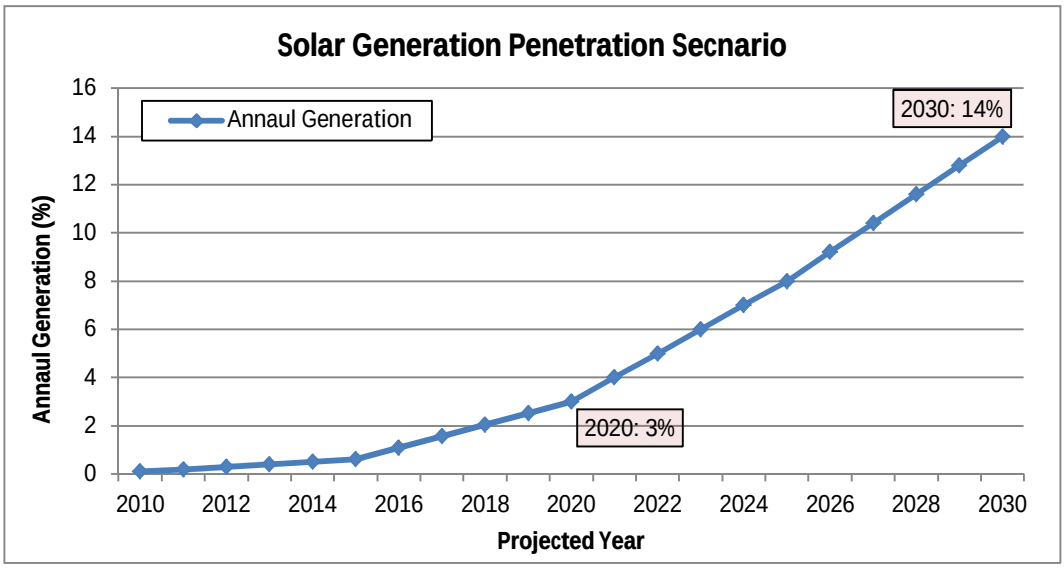

Figure 3-9 Solar generation penetration scenario as a percent of electricity demand [10]

In this study the DER adoption analysis is performed based on the number of customers who have solar generation. The number of customers associated with the projected adoption level of Figure 3-9 is calculated here as:

$$N_{customer} = \frac{l_{project} \cdot P_{total}}{P_{rating} \cdot CF \cdot (1 - l_{project})} \tag{3-2}$$

where $l_{project}$ is the projected adoption level of electric demand (%) from Figure 3-9, P_{total} is the annual average of generation at the substation (kW), P_{rating} is the DER generation rating (kW), and CF is the DER capacity factor representing the ratio between the actual generation and the rating (%). In this study, a 20 % capacity factor (CF) is used. The estimated adoption level of solar generation for DER adoption analysis in 2020 and 2030 is shown in Table 3-1.

Table 3-1 The estimated solar generation adoption level of customers

Projected year	Adoption level (%) of electric demand	Estimated adoption level (%) of customers
2020	3 %	6 %

2030	14 %	30 %

3.3.3. Wind Generation Penetration

The adoption level of wind generation in 2020 and 2030 is determined by the future scenario shown in Figure 3-10 [9]. In this scenario, wind generation capacity is capable of supplying 11 % and 20 % of electricity demand by 2020 and 2030, respectively. Based on this adoption level, Table 3-2 shows the estimated adoption level which is calculated by using Eq. 3-2 with 45 % capacity factor (CF) of wind generation.

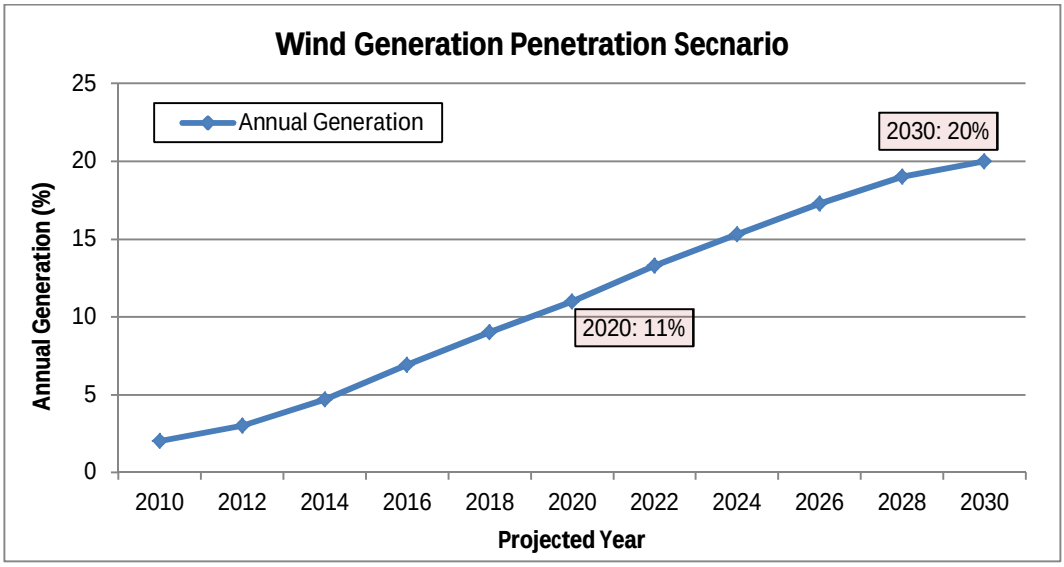

Figure 3-10 Wind generation penetration scenario as a percent of electricity demand [9]

Table 3-2 The estimated wind generation adoption level of customers

Projected year	Adoption level (%) of electric demand	Estimated adoption level (%) of customers
2020	11 %	10 %
2030	20 %	20 %

3.3.4. Simulation Methodology

A number of inputs are required for running the Monte Carlo DER adoption analysis as given by:

- The time point for analysis
- The PHEV load and DER generation profile at the selected location
- The adopted customer class and the percent adoption level

- The PHEV charging pattern
- The number of Monte Carlo iterations

The Monte Carlo DER adoption analysis is diagrammed in Figure 3-11. The steps in the algorithm are as follows:

Step 1) A random number seed for starting the placement of PHEVs and DERs is selected. The seed number is updated with each Monte Carlo iteration so that the placement of PHEVs and DERs are randomly updated. The seasonal load profile is selected, where either winter (January) or summer (July) load profiles are selected to evaluate the seasonal effects.

Step 2) PHEV Adoption

Step 2-1) The PHEV adoption level for the customer class is selected. In the study here 36 % and 52 % of residential customers have PHEVs in 2020 and 2030, respectively.

Step 2-2) The PHEV charging pattern is selected. The probability distribution of people arriving home from work, shown in Figure 3-8, is selected. The PHEVs will begin charging based on this distribution.

Step 2-3) PHEV adoptions are randomly placed at customer locations based on the selected PHEV adoption level in Step 2-1 and the PHEV charging pattern in Step 2-2.

Step 2-4) Steps 2-1 through 2-3 are repeated until the desired PHEV adoption level is achieved.

Step 3) DER Adoption

Step 3-1) The DER adoption level of the customer class is selected. In the study here the adoption levels of solar and wind generation presented in Table 3-1 and Table 3-2 are considered.

Step 3-2) DER adoptions are randomly placed at customers based on the selected DER adoption level in Step 3-1.

Step 3-3) Steps 3-1 through 3-2 are repeated until the desired DER adoption level is achieved.

Step 4) Load Estimation is performed. In this step, the loads are estimated for all customer classes of the selected circuit at the selected time point.

Step 5) Power Flow is performed. In this step, the voltage and current are calculated for the selected circuit at the selected time point.

Step 6) Steps 1 – 5 are repeated until the Monte Carlo simulation converges. For the circuit 1000 Monte Carlo iterations is required here. In this step, the current flow, the number of overload locations, and the number of undervoltage locations obtained from Step 5 is saved for each iteration.

After running the analysis, the following outputs are obtained from the Power Flow for each Monte Carlo run:

- The current flow at start-of-circuit
- The number of overload locations
- The number of undervoltage locations

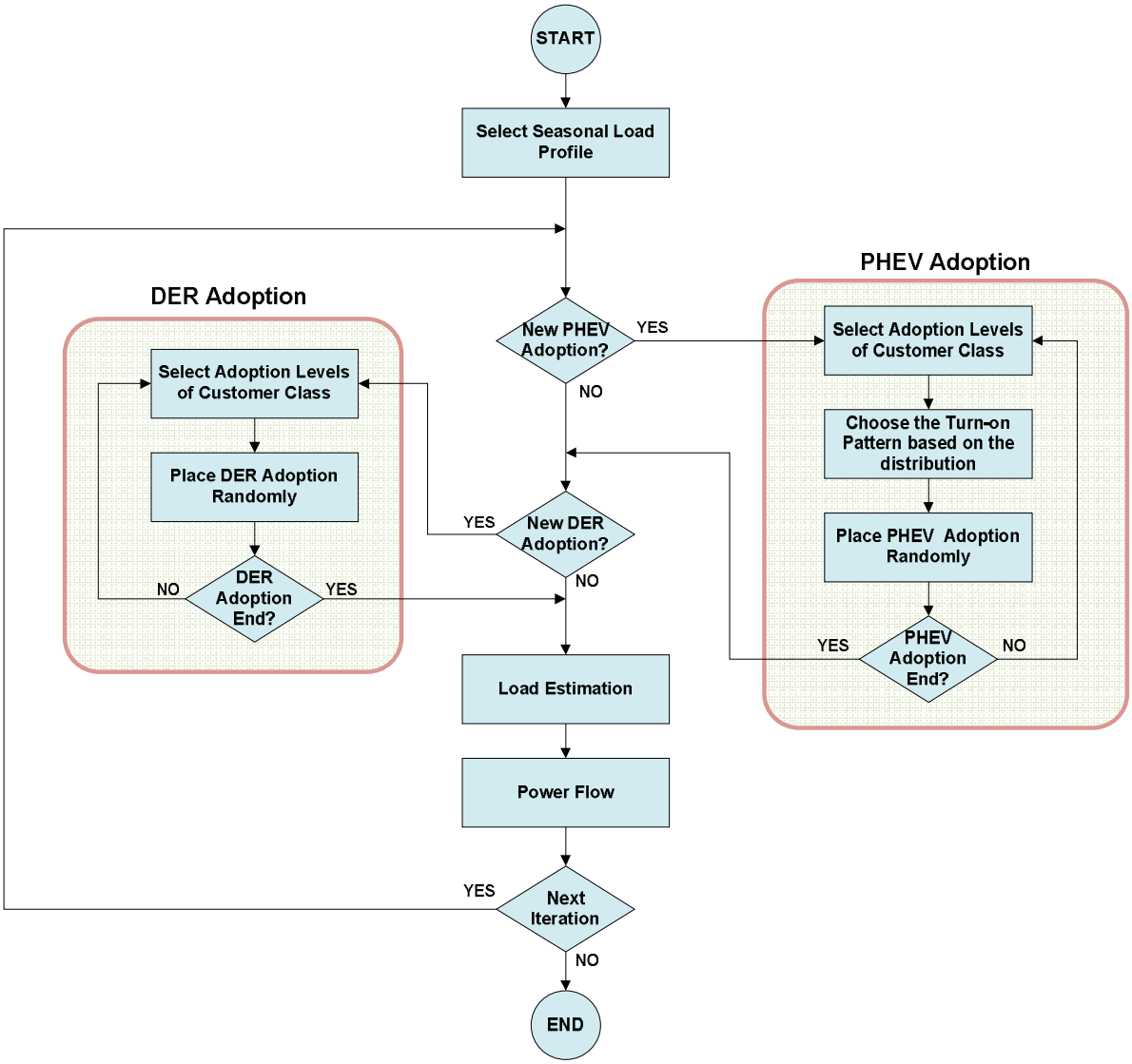

Figure 3-11 Flowchart of Monte Carlo DER adoption analysis

3.3.5. The Benefit of the Methodology

Monte Carlo simulation is employed to solve problems when it is difficult or impossible to compute a deterministic solution. Specifically, Monte Carlo simulation is useful in studying systems with significant uncertainty in inputs, such as future projection studies. Benefits of the Monte Carlo simulation include the following:

- It provides not only the expected average result, but also its uncertainty by creating the probability distribution of the results. Characteristics of the outputs may be estimated from the distributions.

- It allows several inputs to be used at the same time even though the inputs have different types of probability distributions. Here, two inputs having different distributions are used; customer's PHEV charging patterns and the random locations selected for PHEV and DER placements.

- The best and worst scenarios among the Monte Carlo iterations may be captured.

3.4. Test Results

The distribution circuit analyzed at the selected location in Michigan is shown in Figure 3-12. Its summer and winter load profiles are illustrated in Figure 3-1. In addition, the solar and wind generation profiles shown in Figure 3-3 and Figure 3-5 were derived for geographical locations along this circuit.

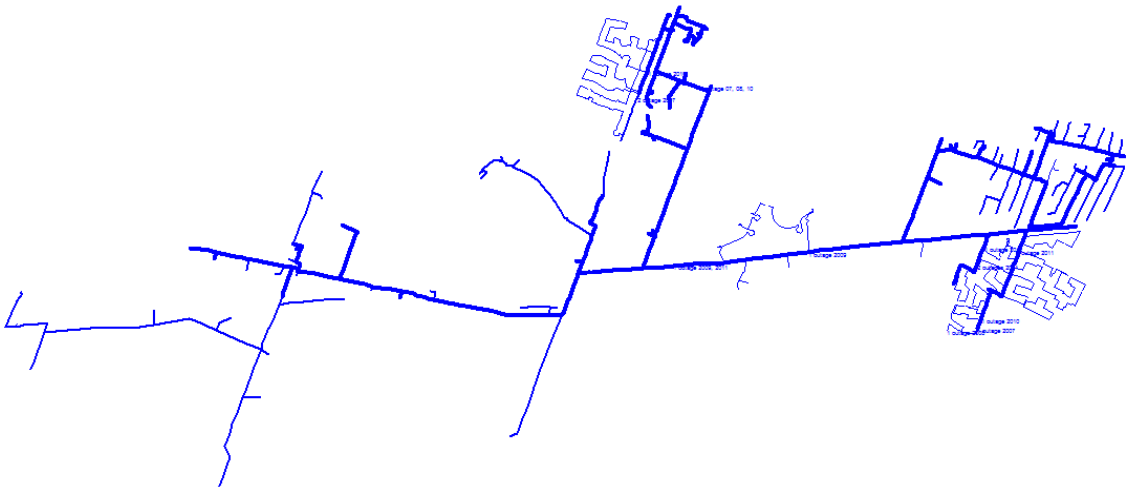

Figure 3-12 Distribution circuit analyzed

3.4.1. Monte Carlo Simulation Convergence

Monte Carlo simulation may be used to estimate expected values of random variables. One of the technical considerations in Monte Carlo simulation is to decide the number of samples to be drawn. For example, a sample size that is too small can affect the meaningfulness of results. Thus, it is important to check for the convergence of the statistical process. Here the average and variance of the results are checked after 1000 Monte Carlo iterations to insure that convergence has been reached. Figure 3-13 and Figure 3-14 show the average and variance of the results at 7 PM for the 2020 winter scenario without storage and with storage, respectively. As shown in these figures, both the cumulative average and variance of the current magnitude converge. Therefore, 1000 iterations are enough to show meaningful results.

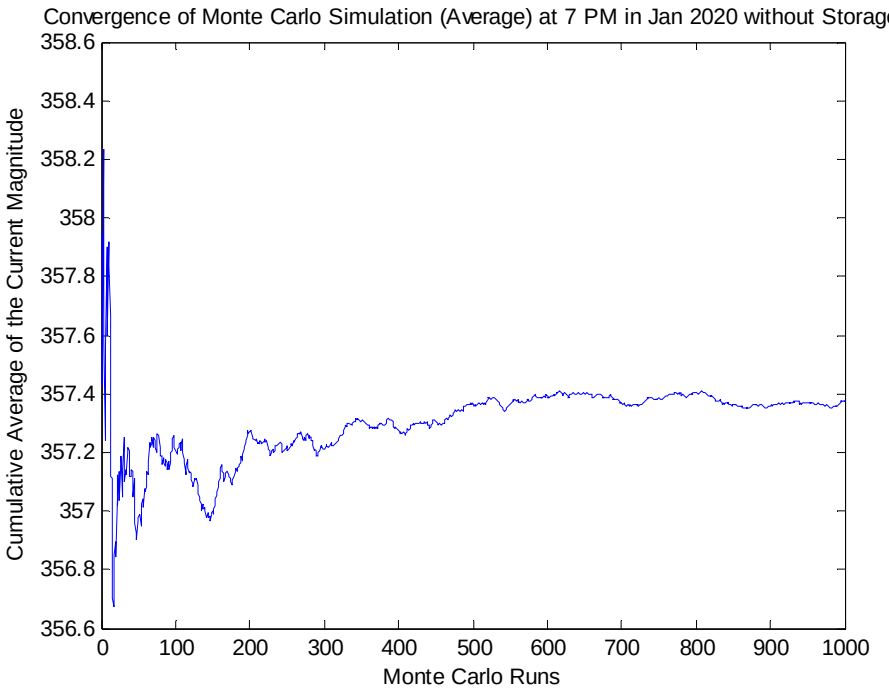

(a) Cumulative average of Monte Carlo runs

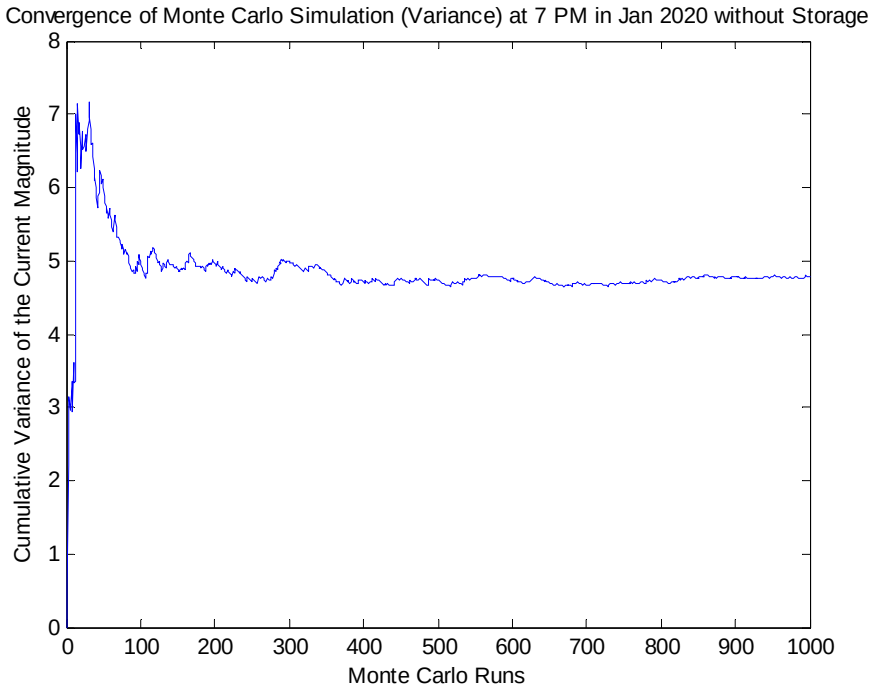

(b) Cumulative variance of Monte Carlo runs

Figure 3-13 Convergence of Monte Carlo simulation at 7 PM in 2020 winter scenario without storage

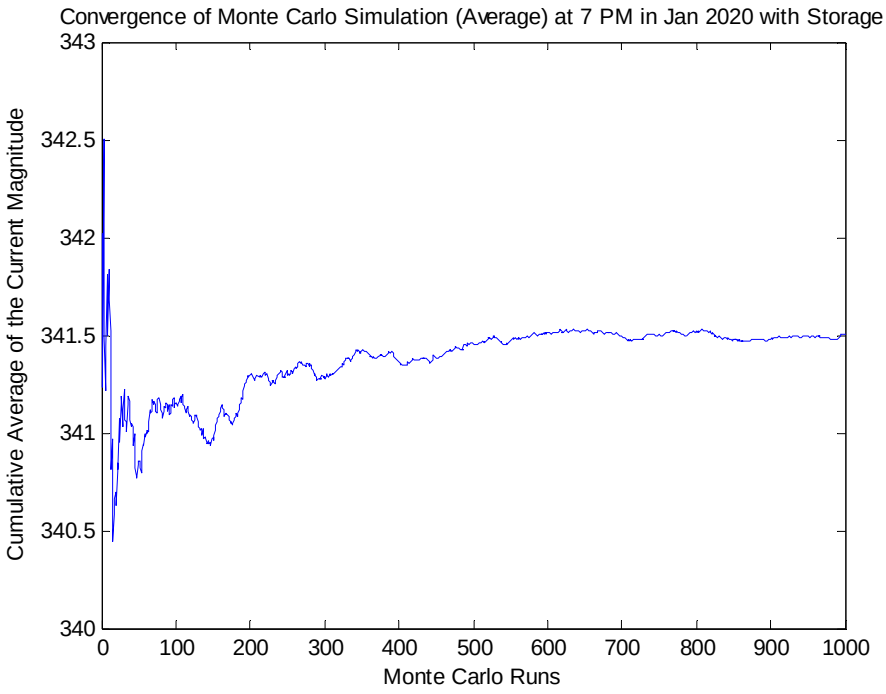

(a) Cumulative average of Monte Carlo runs

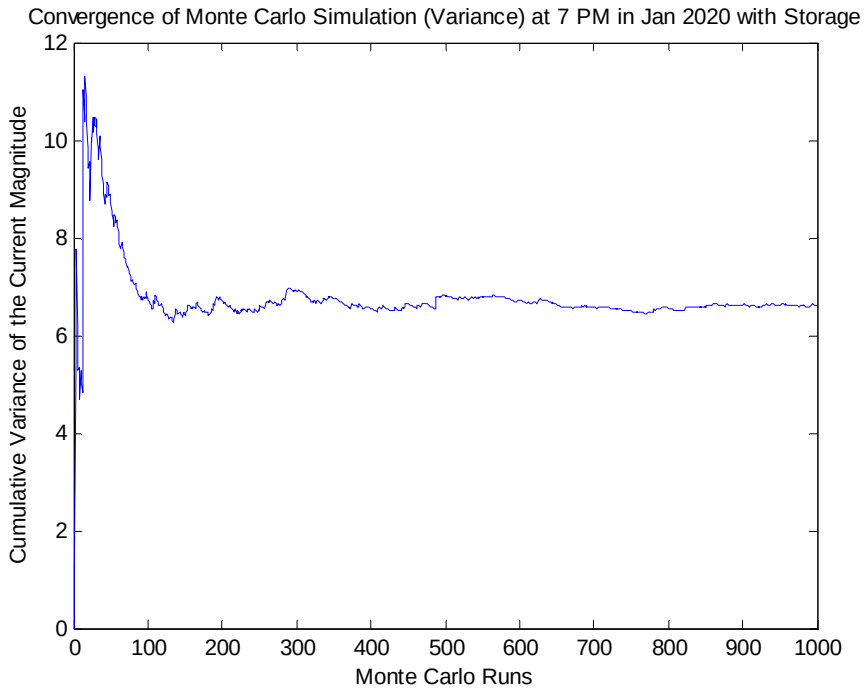

(b) Cumulative variance of Monte Carlo runs

Figure 3-14 Convergence of Monte Carlo simulation at 7 PM in 2020 winter scenario with storage

3.4.2. The Uncertainty of DER Adoption Analysis

Figure 3-15 and Figure 3-16 show the current flow obtained from the Monte Carlo simulation, measured at the substation for the 2020 winter and summer future scenarios, respectively. These figures provide not only the average of the results but also the extent of uncertainty that the results can have. The extent of uncertainty is represented by 10 quantile values which divide the samples into 10 equal parts so that each part represents 10 % of samples. These figures indicate that the scenario with the storage system shows more uncertainty during peak demand duration when the storage system returns the stored DER energy to the system. The average values show that the DER generation with the storage system helps offset the PHEV load growth during peak demand.

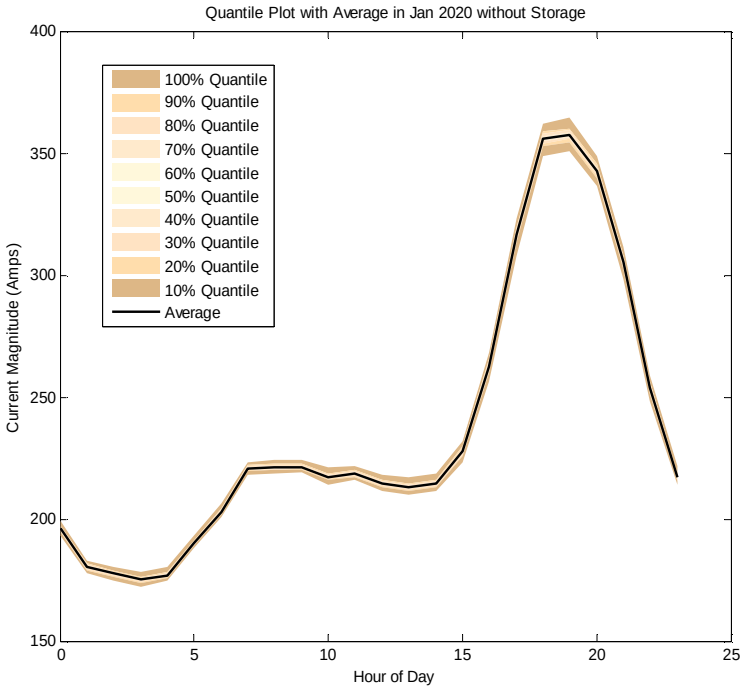

(a) Quantile plot in 2020 winter scenario without storage

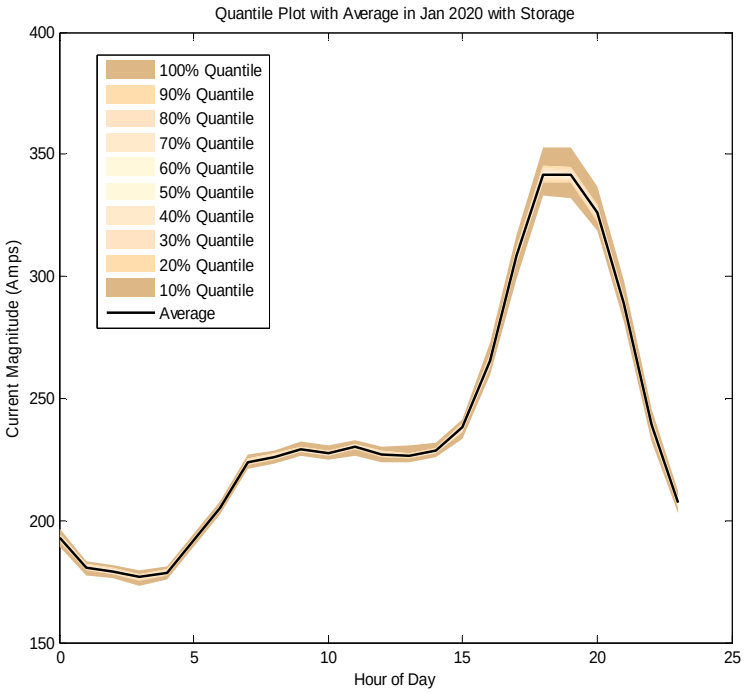

(b) Quantile plot in 2020 winter scenario with storage

Figure 3-15 Uncertainty estimation with expected value in 2020 winter scenario

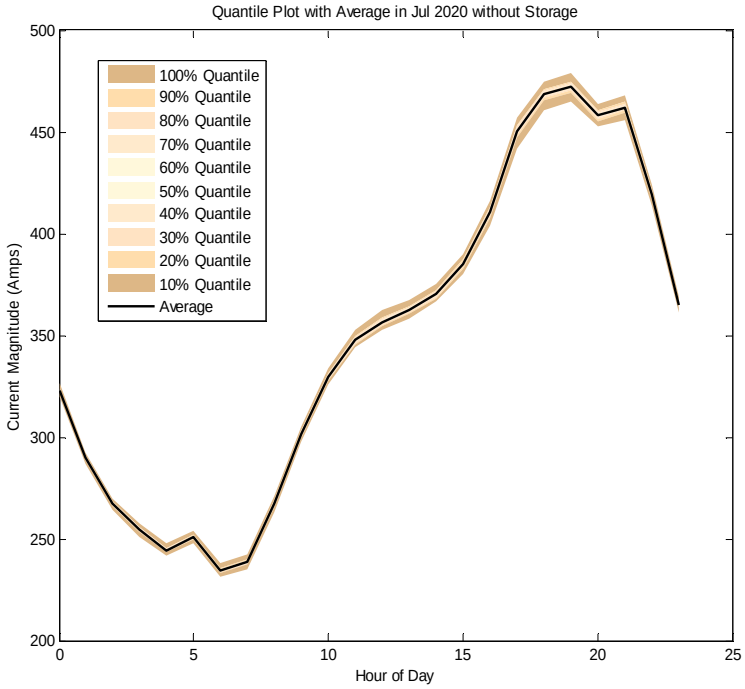

(a) Quantile plot in 2020 summer scenario without storage

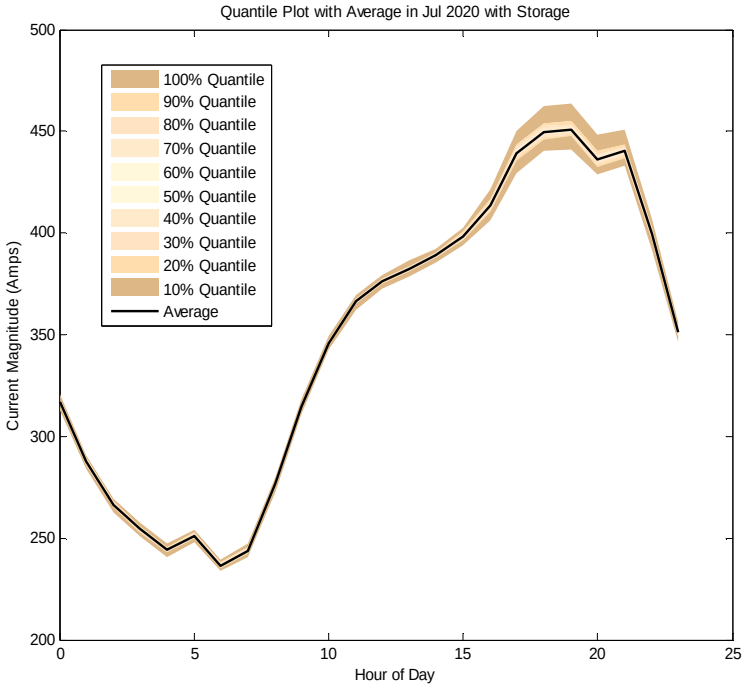

(b) Quantile plot in 2020 summer scenario with storage

Figure 3-16 Uncertainty estimation with expected value in 2020 summer scenario

Figure 3-17 and Figure 3-18 show the current flow measured at the substation for the 2030 winter and summer scenarios, respectively. In these figures, the scenario with the storage system shows more uncertainty during the peak demand duration. Furthermore, the extent of uncertainty is larger than the 2020 scenario. The increase in the uncertainty from the 2020 scenario to the 2030 scenario corresponds to the increase of the PHEV and DER adoptions. For the seasonal effects, the summer results indicate a larger uncertainty than winter.

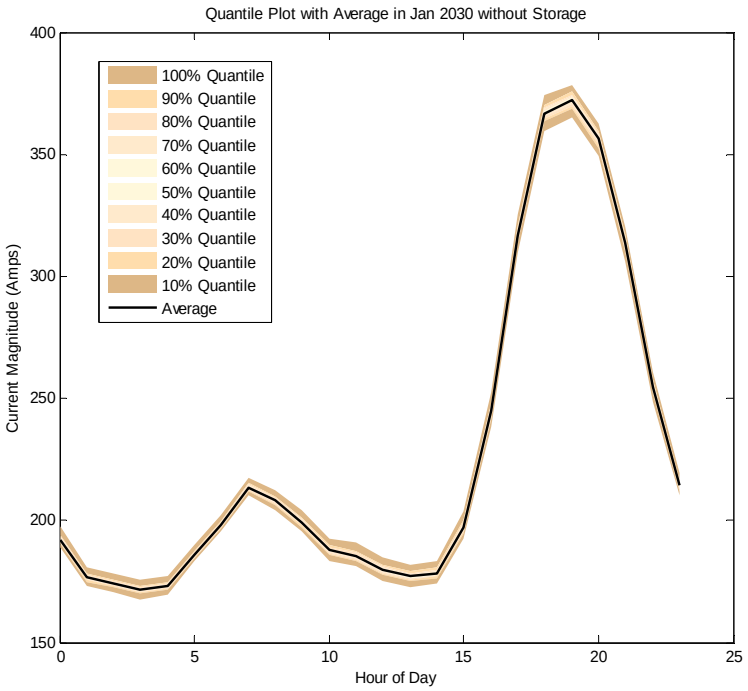

(a) Quantile plot in 2030 winter scenario without storage

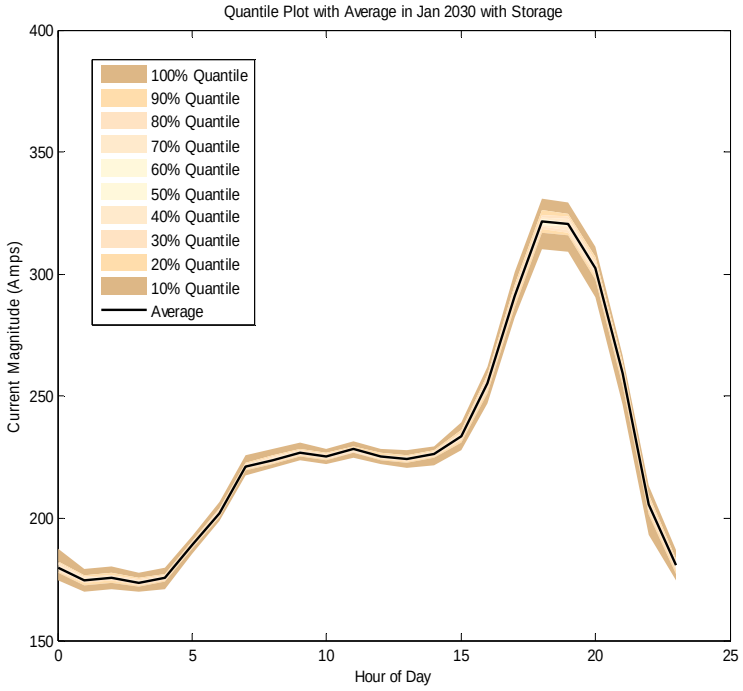

(b) Quantile plot in 2030 winter scenario with storage

Figure 3-17 Uncertainty estimation with expected value in 2030 winter scenario

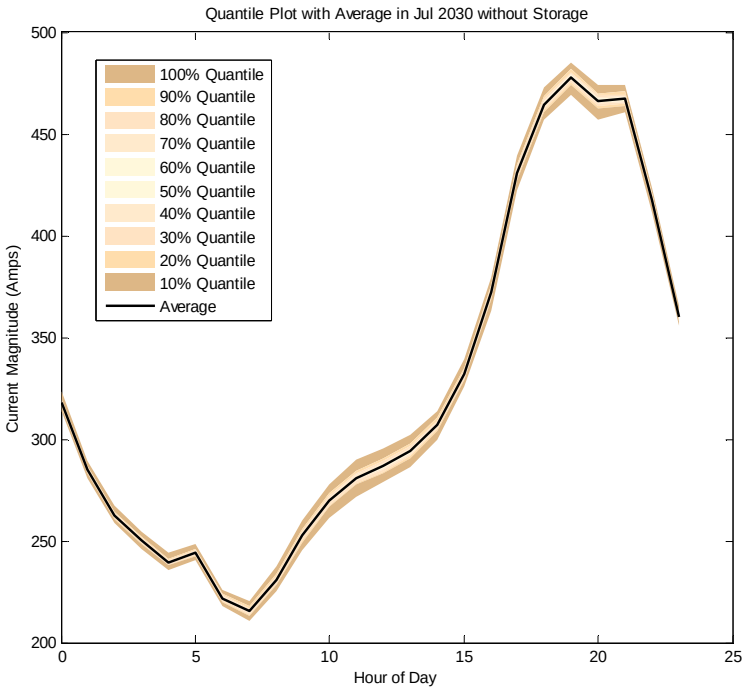

(a) Quantile plot in 2030 summer scenario without storage

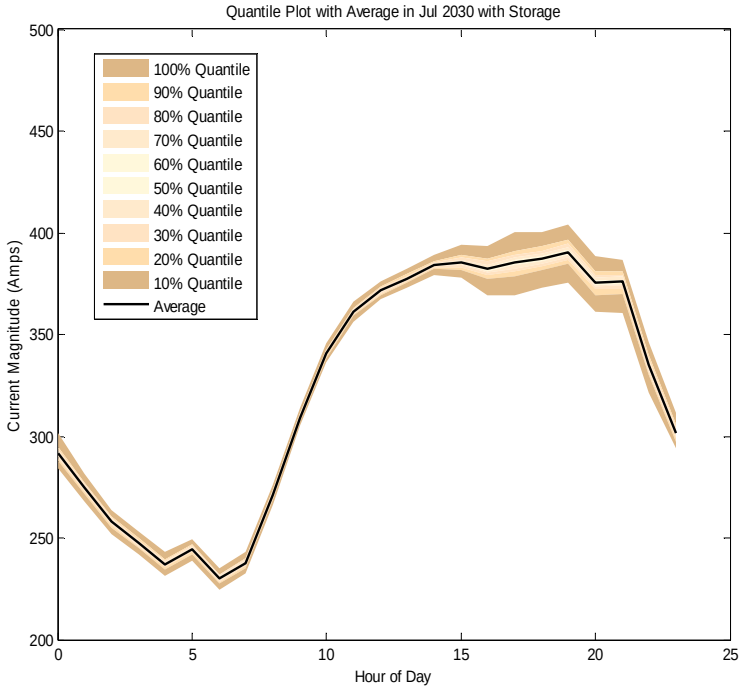

(b) Quantile plot in 2030 summer scenario with storage

Figure 3-18 Uncertainty estimation with expected value in 2030 summer scenario

In these figures, the average values are close to the 50% quantile values, which are median values, and the distribution is symmetric about the average. This is one of the properties of a normal distribution. To check that the samples follow a normal distribution, normal probability plots and histograms are evaluated. Figure 3-19 and Figure 3-20 show the normal probability plot and histogram with a normal distribution fit for the 7 PM 2020 winter scenario without storage and with storage, respectively. If the samples follow a normal distribution, the plot should be close to the red line. As shown in the figure, the samples obtained from the Monte Carlo simulation are close to the red line, indicating the samples come from a normal distribution. Therefore, the distribution at each hour can be estimated with mean and standard deviations.

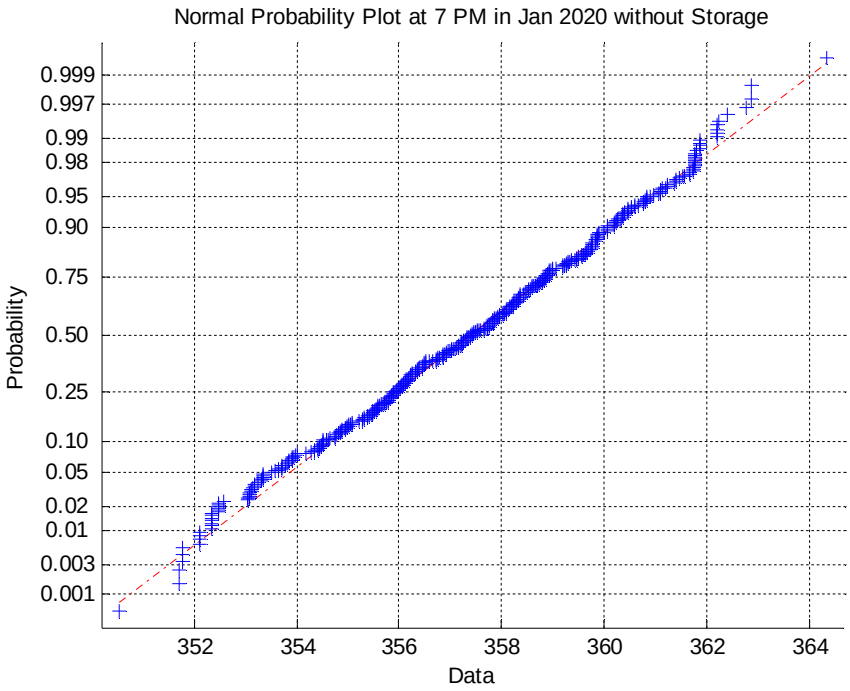

(a) Normal probability plot

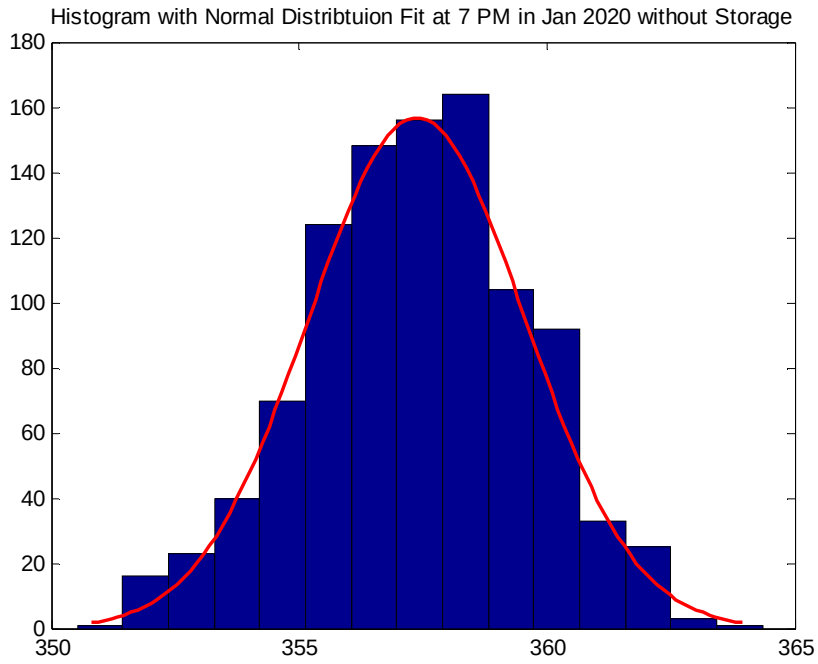

(b) Histogram with normal distribution fit

Figure 3-19 Normality of Monte Carlo simulation at 7 PM in 2020 winter scenario without storage

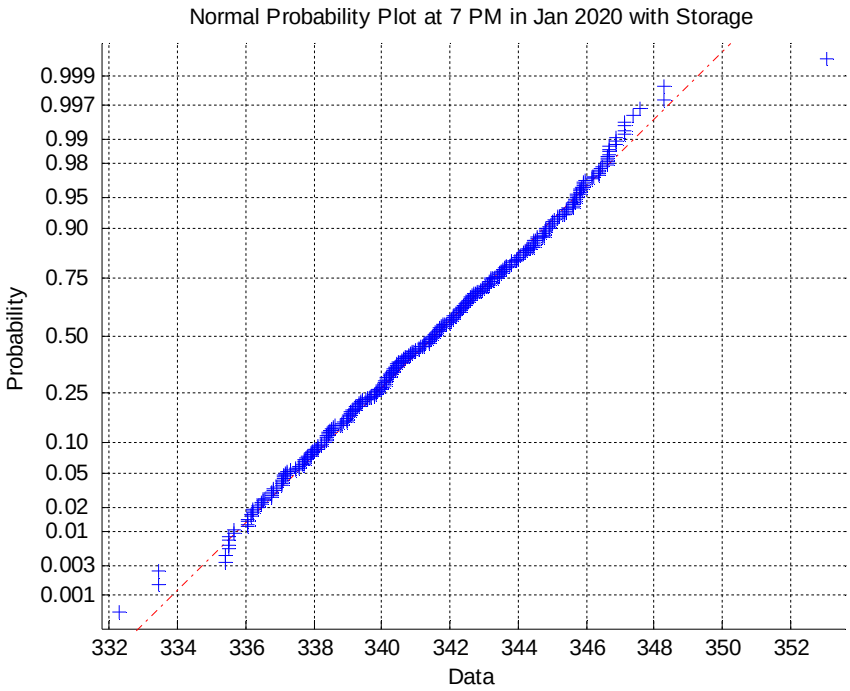

(a) Normal probability plot

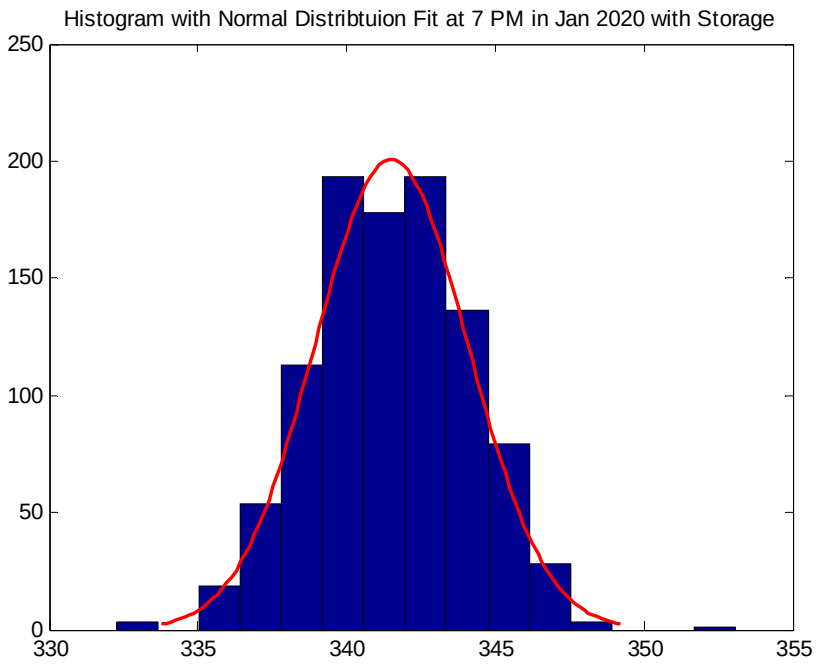

(b) Histogram with normal distribution fit

Figure 3-20 Normality of Monte Carlo simulation at 7 PM in 2020 winter scenario with storage

3.4.3. The Potential Impacts of New Technologies

To understand the capability of DER generation with storage technology offsetting a growing PHEV market demand and induced overload conditions, Figure 3-21 and Figure 3-22 show the average of the start-of-circuit current flow comparisons in 2020 and 2030 scenarios, respectively. As illustrated in Figure 3-21, none of the DER generation scenarios coupled with PHEV growth causes the current level to fall below the base system peak demand in 2020. However, the DER generation helps offset the new PHEV loads during winter and summer.

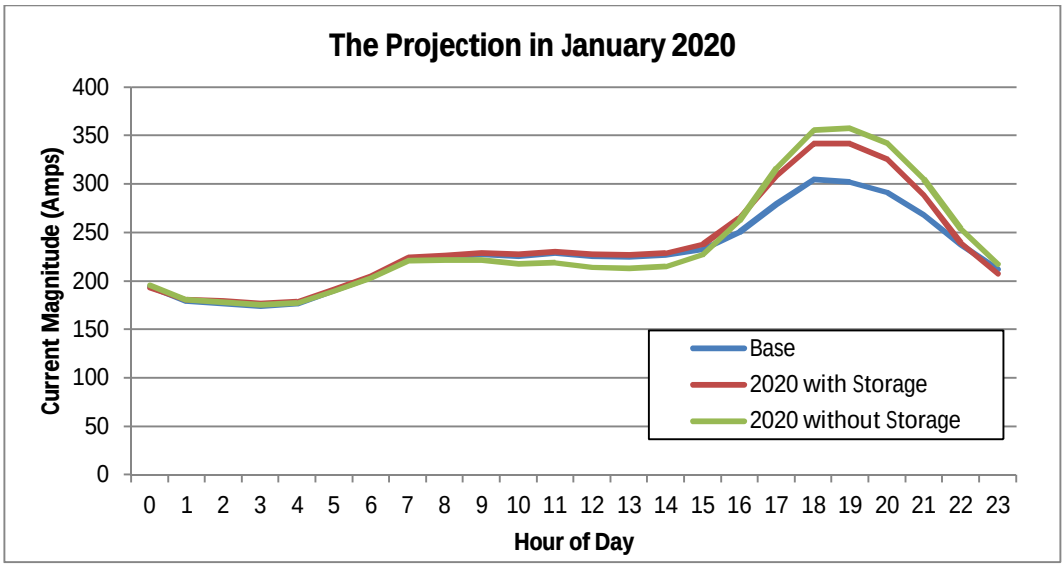

(a) Average system current flow in 2020 winter

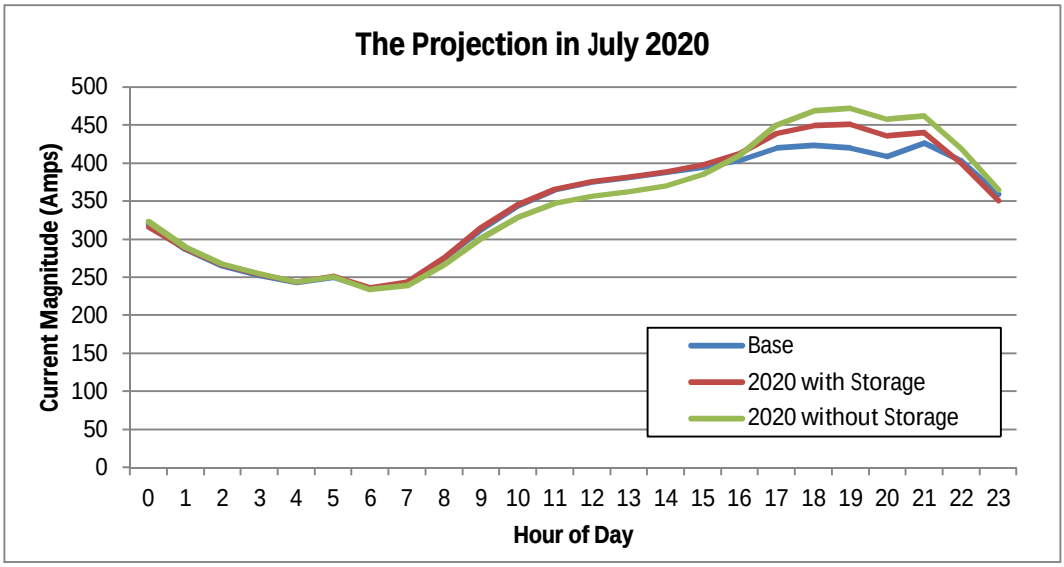

(b) Average system current flow in 2020 summer

Figure 3-21 Average system current flow in 2020 scenario

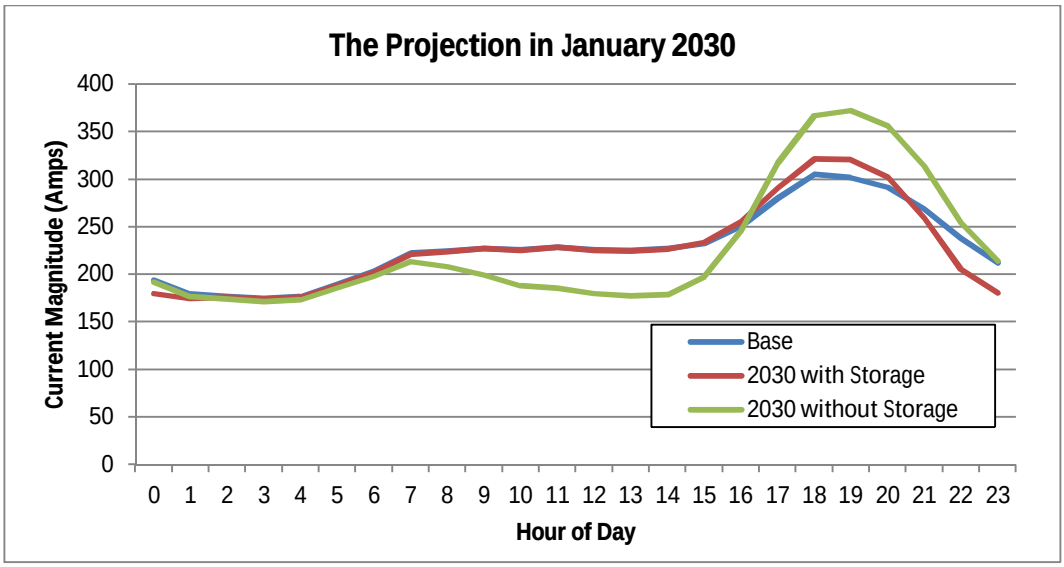

(a) Average system current flow in 2030 winter

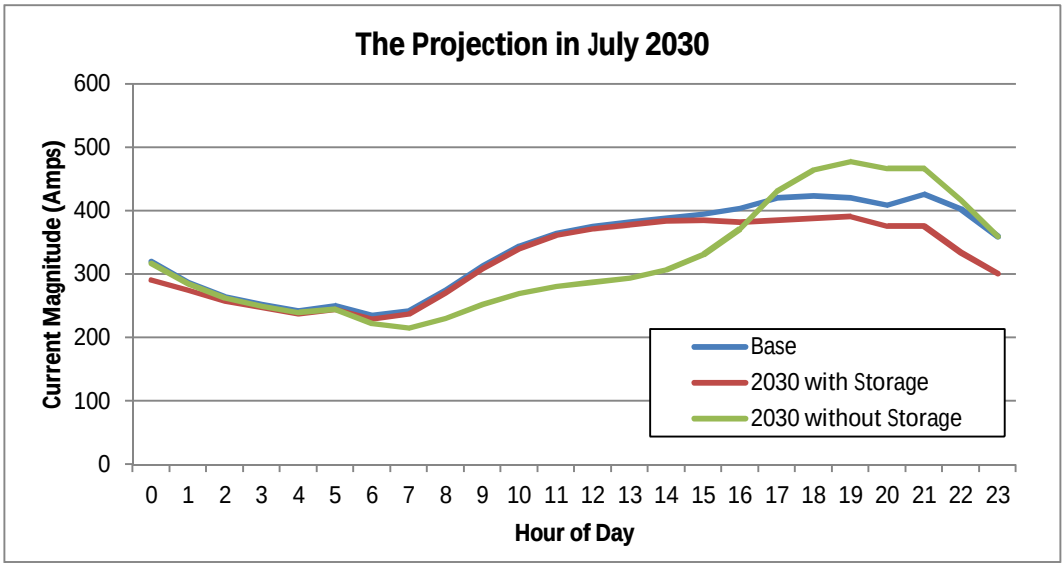

(b) Average system current flow in 2030 summer

Figure 3-22 Average system current flow in 2030 scenario

Figure 3-22 shows that DER generation without storage during winter and summer results in midday demand dips but has little impact on peak demands. However, with the projected PHEV recharging occurring during the existing peak, the DER generation with storage is able to clip the increased peak demand to a level below that of the base system during summer. During winter, the DER generation with storage reduces the peak current flow significantly, coming close to the base system.

Figure 3-23 shows the number of overloaded components resulting from the introduction of PHEV and DER. In this figure, the average, maximum, and minimum number of overloaded components from the Monte Carlo simulation are shown. The number of induced component overloads during winter is much smaller than during summer. Furthermore, the overloaded conditions occur much less when the DER generation is coupled with storage. The maximum number of overloaded components indicates the worst case, 6 overloaded components during winter, and 33 overloaded components during summer. As expected, the worst case occurs in the 2030 scenario without storage. In Figure 3-22, the DER generation with storage in the 2030 scenario reduced the peak demands induced by the PHEV load. It is also observed that the smallest number of overloaded components occurs when the DER generation is coupled with the storage in the 2030 scenario. The specific Monte Carlo iteration where the minimum number of overloads occurred provides DER generation adoption locations to be considered for minimizing overloads.

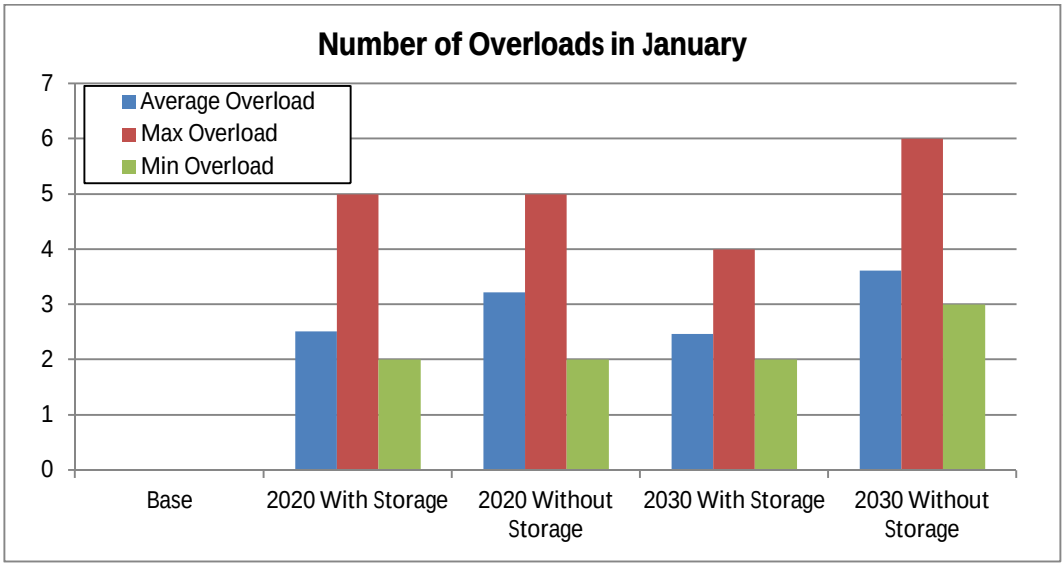

(a) Number of overload violations during winter

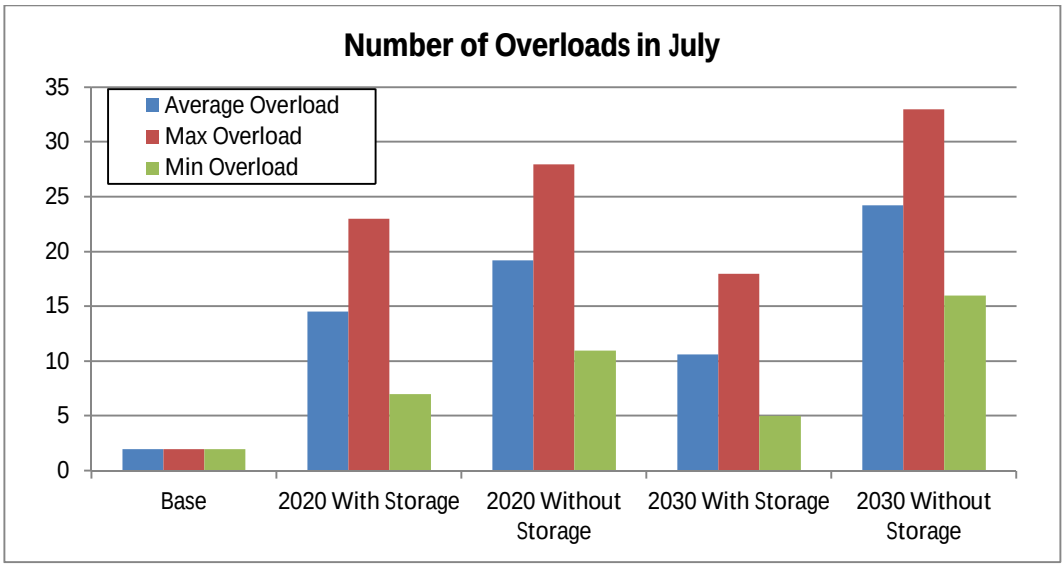

(b) Number of overload violations during summer

Figure 3-23 Number of PHEV-induced overloaded components

In summary, the results illustrate that the DER generation could produce some significant impacts on current energy consumption profiles, primarily of benefit to utilities when coupled with an efficient storage device, which can be used to affect peak demands. In the 2020 scenario, the DER generation with storage helps offset the new PHEV loads. In the 2030 scenario, the DER generation with storage is capable of reducing the peak demands induced by the PHEV loading. Therefore, more DER generation is required to offset the new PHEV load growth in 2020. However, the DER generation with storage is sufficient to manage the new PHEV load growth in 2030. Although the current flow at the start-of-circuit shows that the DER generation offsets the new PHEV load growth, the average number of overloaded components is still high. Thus, it is important to select the optimal locations of the DER generation to minimize the overloading conditions.

3.5. Conclusion

This chapter presents projected adoption levels of PHEV and DER generation for 2020 and 2030 future scenarios. Information on how consumer use of this technology will grow is projected. Several assumptions are presented that are used in the Monte Carlo DER adoption analysis.

A Monte Carlo DER adoption analysis has been introduced. It is shown that this analysis can evaluate the seasonal effects by selecting different load profiles and potential impacts from the addition of PHEV and DER generation with and without energy storage. Furthermore, this analysis provides not only the expected average results, but also its uncertainty.

Finally, the chpater presents the major findings from the Monte Carlo DER adoption analysis for an actual utility circuit where all individual customer loads are modeled: 1) the cumulative average and variance of the results obtained from 1000 Monte Carlo iterations converged well; 2) the analysis provides not only the average of the results but also the extent of uncertainty that the results can have. Furthermore, the distribution at each hour follows the normal distribution so that it can be estimated with mean and standard deviations; 3) the results demonstrate that a maturing PHEV market could produce significant impacts on peak demand, resulting in system overload conditions, which mainly occur in the secondary. The DER generation with storage is sufficient to manage the new PHEV load growth for the circuit in the 2030 scenario but not in the 2020 scenario. Locations for placing DER generation for possibly minimizing the number of overloads come from the specific Monte Carlo iteration where the adopted locations of DER generation minimize the overloading conditions.

Chapter 4 Local Steady-State and Quasi Steady-State Impact Studies of High Photovoltaic Generation Penetration in Power Distribution Circuits

4.1. Introduction

PV generation is one of the most rapidly growing renewable energy sources, and is regarded as an appealing alternative to conventional power generated from fossil fuel [10]. This is leading to significant levels of distributed PV generation being installed on distribution circuits. Although PV generation brings many advantages, circuit problems are created due to the intermittency of the PV generation, and overcoming these problems is a key challenge to achieving high PV penetration.

It is necessary for utilities to understand the impacts of PV generation on distribution circuits and operations. An impact study is intended to quantify the extent of the issues, discover any problems, and investigate alternative solutions.

An impact study can be divided into two categories; system wide and local [32]. A system wide study addresses growth impacts of new technologies on the circuit, including PHEV or PEV, DER generation, and energy storage systems. This study deals with the uncertainties and effects of new technology, including location, size, and operating characteristics [25, 33].

On the other hand, local impact studies address expected impacts of new technologies on a distribution circuit as it exists today. The native loading and PV generation data are available along with the location and characteristics of the PV generation. A local impact study is presented in this chapter.

The potential impact of PV generation on the existing distribution circuit has been discussed in [32, 34-41]. It is becoming apparent that local voltage issues are likely to precede protection, load, fault, harmonic, and stability issues as penetration increases. In addition, reverse power flow can negatively affect protection coordination and operation of voltage control and regulation equipment. Furthermore, PV generation induces changes in the circuit loss and imbalances of voltages and power flows.

In this chapter both local steady-state and quasi steady-state PV impact studies are presented. The steady-state impact study investigates impacts at extreme circuit conditions and the quasi steady-state

represents a series of steady-state studies over a set of time varying values. Thus, the quasi steady-state study evaluates a spectrum of impacts. In addition, PV generation power factor control for mitigating voltage variation problems is investigated.

This chapter is organized as follows. In Section 4.2 the most common expected impacts of PV on the distribution circuit are discussed. Section 4.3 presents simulation strategies addressing the impacts discussed in Section 4.2. In Section 4.4 the results obtained from existing circuits with individual customers modeled are presented. Finally, findings of the study are summarized in Section 4.5.

4.2. PV Impact Study

Some of the impacts from high PV penetration which should be considered in steady-state and quasi steady-state PV impact studies are discussed in this section.

4.2.1. Steady-State PV Impact Study

A steady-state PV impact study seeks to discover the worst case, or extreme impacts, on the distribution circuit. Circuit conditions that are considered include maximum loading, maximum PV generation, and maximum difference between PV generation and circuit load. The objective is to analyze extreme impacts by comparing circuit conditions before and after a change in PV generation. In these studies the effects of control actions are very important. Solar generation transients can be so rapid that traditional utility control devices cannot act sufficiently fast to correct circuit problems caused by the rapidly varying generation.

a) Customer voltage variation

Among the various technical challenges under high PV penetration, voltage variations caused by the intermittency of the PV generation are among the foremost concerns. The need to limit voltage variations resulting from rapidly varying PV generation can limit the amount of PV generation in the distribution circuit. The typical allowed variation in voltage is ±5% from a nominal voltage, but other concerns, such as causing excessive control motion of utility equipment, may place tighter restrictions on the allowable voltage variation [42].

It is important to maintain the voltage within allowable ranges at all components in the circuit. Many distribution circuits are radial and the voltage is controlled by automated devices (voltage regulators, switched capacitor banks, load tap changing transformers). Solar generation can vary rapidly up and down as clouds pass over, creating many voltage transients at the automated control devices. If typical utility

control equipment attempts to control all of the rapid variations in voltage, the equipment will require much more maintenance and have a shorter life span. However, typical utility control equipment is not fast enough to control the initial voltage variations due to PV generation transients.

b) Reverse power flow

High PV penetration can lead to reverse power flow conditions in distribution circuits which were originally designed for unidirectional power flow from the substation to the loads. Bidirectional power flow can be detrimental to the performance of some devices, including protective devices and automated control devices. Reverse power flow conditions can cause malfunctions in protection coordination and the operation of voltage regulation equipment.

c) Phase unbalance of power flow and customer voltage

Supplying unbalanced phase power flows and voltages results in degraded performance of three-phase motors and other three-phase utilization devices. If the unbalance is significant, the motors and devices may overheat or become inoperative. It is common to maintain the voltage unbalance within 2% [37]. In this chapter the IEEE definition of voltage unbalance, also known as the phase voltage unbalance rate (PVUR), is used [43]:

$$PVUR = \frac{\text{Maximum deviation from average phase voltage}}{\text{Average phase voltage}} \tag{4-1}$$

Similarily, the phase power flow unbalance rate (PFUR) is calculated as:

$$PFUR = \frac{\text{Maximum deviation from average phase real flow}}{\text{Average phase real flow}} \tag{4-2}$$

4.2.2. Quasi Steady-State PV Impact Study

The steady-state PV impact study evaluates impacts on the circuit at extreme circuit conditions, but does not show the spectrum of impacts between the extremes. The quasi steady-state PV impact study represents a series of studies run over a set of time varying values with some sample rate (i.e. one second, one minute, one hour). In this chapter the quasi steady-state PV impact studies use one hour measurements for evaluating the following concerns.

a) Customer voltage variation

The quasi steady-state study captures the effects of customer voltage variations within a given time frame. Information provided by the study includes how often overvoltage or undervoltage occur, and how voltages fluctuate throughout the day.

b) Circuit loss

PV generation can have significant impacts on circuit loss. PV generation affects both real and reactive circuit losses. The quasi steady-state study provides information on both real and reactive circuit losses over the time varying generation. Optimal control of PV generation is required to minimize the circuit loss.

c) Automated device steps

Voltage rise and variations caused by the intermittency of PV generation can lead to frequent utility control device step changes. These frequent step changes can shorten the expected life of the devices and increase maintenance costs. The quasi steady-state study counts the number of times control devices move over the time varying generation. Optimal control of PV generation should consider controlling PV generation so that the control motion of utility control devices is minimized.

4.3. Simulation Strategies

The variation in PV generation is due to changes in the cloud cover, which is the main reason for rapid solar generation changes. The power factor that the PV generation operates at has significant effects on the circuit response, and determining the optimal power factor can minimize the detrimental circuit effects.

4.3.1. Test Circuit

The distribution circuit to be analyzed is shown in Figure 4-1. The circuit model is derived from actual data. It is a 13.2kV, Y-connected circuit with 2751 residential customer and 111 industrial customers. The time varying customer loads are estimated from averaged hourly SCADA measurements, hourly customer kWh load data, and monthly kWh load data processed by load research statistics to create hourly loading estimates for each customer [3, 4].

The circuit contains two voltage regulators, two switched shunt capacitors, four protective devices, and numerous sectionalizing devices, with four sectionalizing devices illustrated in Figure 4-1. The voltage regulators operate based on voltage control using a 124 V base, +/- 1.0 volt bandwidth, and +/- 16

steps. The switched shunt capacitors operate based on voltage control with specified turn on and turn off voltage limits.

In the simulation 1000 kW PV generators are considered. Time-varying PV generation data are imported via the Internet using the IMBY application from the NREL [1]. For a given geographical location and size, the NREL interface provides hourly PV generation data for an entire year.

Four PVs, each with a 1000 kW rating, are randomly placed in the circuit. The PV penetration percentage is calculated based on the following equation:

$$\text{PV penetration (\%)} = \frac{\text{Max PV generation}}{\text{Native load at max PV generation time}} \tag{4-3}$$

The definition of PV penetration used in this chapter varies based on the selected time duration. The time varying PV generation and load for a day, July 15, is selected for analysis in this chapter and is shown in Figure 4-2. Due to heavy residential loading the circuit peaks late in the day, with the annual peak load occurring during the summer. The annual PV generation peak also occurs during the summer. Using Eq. 4-3, the PV penetration for the selected day for analysis is approximately 30%.

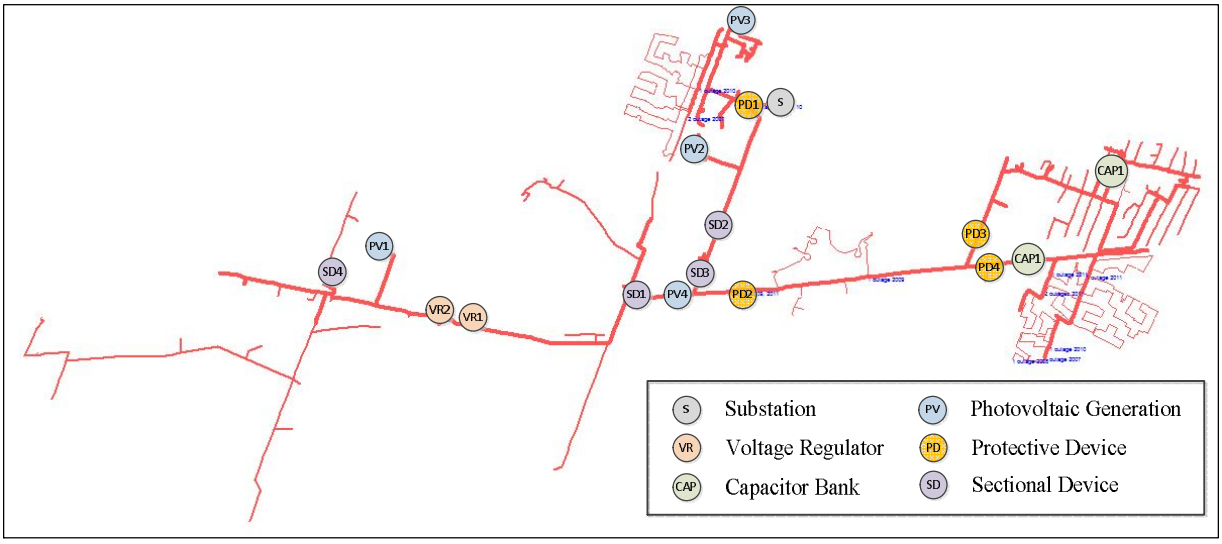

Figure 4-1 Distribution circuit to be analyzed

4.3.2. Time Point Selection

For the steady-state impact study, time points are determined for evaluating the worst impacts on the circuit. The maximum PV generation time point is selected to show the extreme effects on the circuit due to the largest amount of PV generation. The maximum load time point is selected to evaluate effects at the

extreme loading condition. The minimum load time is not selected here because this load occurs at night when PV generation does not impact the circuit operation. The time at which the maximum difference exists between the circuit load and the PV generation is also selected. The three time points selected for the steady-state PV impact study are illustrated in Figure 4-2 and are:

- Maximum PV generation: 01:00 PM
- Maximum circuit load: 04:00 PM
- Maximum difference between PV generation and circuit load: 07:00 PM

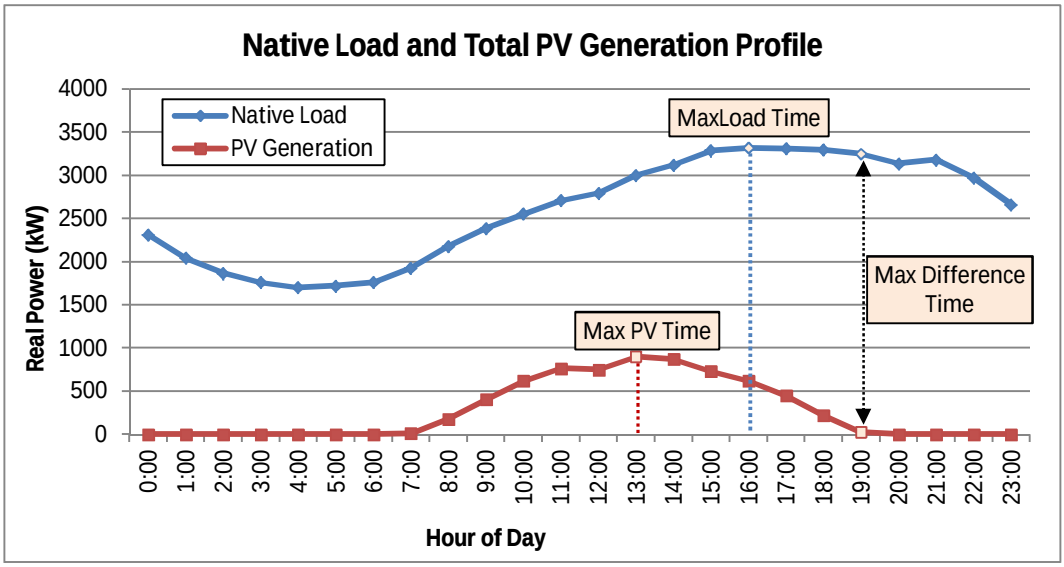

Figure 4-2 Native load and total generation profile

4.3.3. Cloud Cover Simulation

Changing cloud cover is the main reason for solar ramping producing rapid fluctuations in PV generation. Changing cloud cover has to be considered in dynamic PV impact studies. However, the cloud cover simulation is also used in the steady-state impact study. In the simulations here, four cloud cover cases are considered as:

- Study with 25% cloud cover resulting in 25% loss of PV generation
- Study with 50% cloud cover resulting in 50% loss of PV generation

- Study with 75% cloud cover resulting in 75% loss of PV generation
- Study with 100% cloud cover resulting in 100% loss of PV generation

4.3.4. Automated Device Control Simulation

Automated control devices act to regulate the voltage in the distribution circuit. The purpose of the steady-state impact study is to find the extreme impacts of PV generation. The automated utility control devices considered here have a slow response relative to the possible rates of change of solar generation. That is, large changes in solar generation can occur before the utility control devices can react. Therefore, the impact of PV generation changes is investigated in the following two ways:

- Study with automated control devices operating
- Study without automated control devices operating

4.3.5. Control of PV Generation Simulation

Voltage control capability of PV generation is studied in [44]. PV generation can use both active and reactive power injection for control. It is useful for utilities to provide the impacts of PV generation when they are controlled. There are many research efforts to develop optimal control strategies for PV generation [45-53]. It is out of scope to test these advanced control algorithms here. In this chapter, fixed power factor control is considered and used to provide insights into the effect of the power factor control, where the power factors considered in the simulations are given by:

- 0.8 leading power factor PV control
- 0.9 leading power factor PV control
- 1.0 power factor PV control
- 0.9 lagging power factor PV control
- 0.8 lagging power factor PV control

4.3.6. Simulation Cases

The steady-state PV impact studies for evaluating customer voltage variations performs power flow analysis runs associated with the loss and restoration of PV generation as given by the following, where the notation Vi, i = 1, 2, 3, 4, 5, indicates voltage values for the stated condition:

- V1: Base condition (without cloud cover)
- V2: Loss of generation without automated device operation
- V3: Loss of generation with automated device operation
- V4: Return of generation without automated device operation
- V5: Return of generation with automated device operation

After obtaining the voltages from the above power flow analysis runs, the variations in steady state voltage are calculated as:

- Case 1: the voltage difference between V2 and V1 (V2 – V1)
- Case 2: the voltage difference between V3 and V1 (V3 – V1)
- Case 3: the voltage difference between V4 and V3 (V4 – V3)
- Case 4: the voltage difference between V5 and V3 (V5 – V3)

The above cases are run for the selected extreme circuit condition time points and for the different specified PV generation power factor control values.

The steady-state PV impact study for evaluating reverse power flows, power flow phase unbalance, and customer voltage phase unbalance determines the time at which the maximum voltage variations occur with changing PV generation and PV generation power factor control.

The quasi steady-state PV impact study for customer voltage variations, circuit losses, and automated device steps performs a series of power flow analysis runs associated PV generation status on and off with PV generation power factor control.

4.4. Simulation Results

In this section, the simulation results of steady-state and quasi steady-state PV impact study cases are presented using the circuit and selected time periods discussed in the Section 4.3.

4.4.1. Steady-State Simulation Results

a) Customer voltage variation

Figure 4-3 and Figure 4-4 show the customer voltage variation at VR1 as a function of varying the power factor of the PV generation for 50% and 100% cloud cover. Each figure contains the results for the three different extreme circuit condition time points - maximum load, maximum PV generation, and the time at which the difference between the load and the PV generation is the greatest. The greatest voltage variation is observed at the time of maximum PV generation and the next at the time of the maximum load.

Cases 1 and 2 show a negative voltage variation, whereas cases 3 and 4 show a positive voltage variation at the VR1 location. It is also observed, as expected, that the voltage variation is less following the operation of the automated control devices.

These figures also include the limits of the voltage variation. ANSI C84.1 provides a guideline for voltage variations from 114 V to 126, V where the desired voltage is 120V [54]. In the work here a much smaller voltage variation (+/- 0.5V) is used for the voltage change limit. This limit is imposed so that the voltage regulator will not try to chase changes in the solar generation. The voltage variation at the maximum difference time is within the range for all cases because of the small amount of PV generation. A greater variation in voltage is observed for lagging power factor control of the PV generation than for leading power factor control. Therefore, in this case it is necessary to absorb reactive power to help mitigate the voltage variation caused by the rapidly varying PV generation. Most of the voltage variations at the 0.8 leading power factor control are within the 0.5 voltage change limit evaluated here.

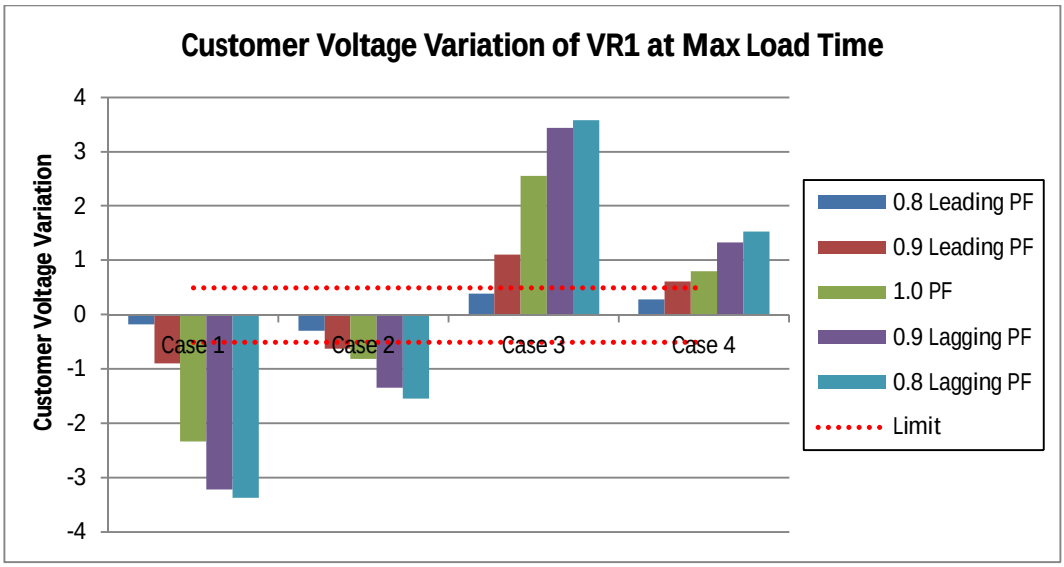

(a) Customer voltage variation of VR1 at max load time

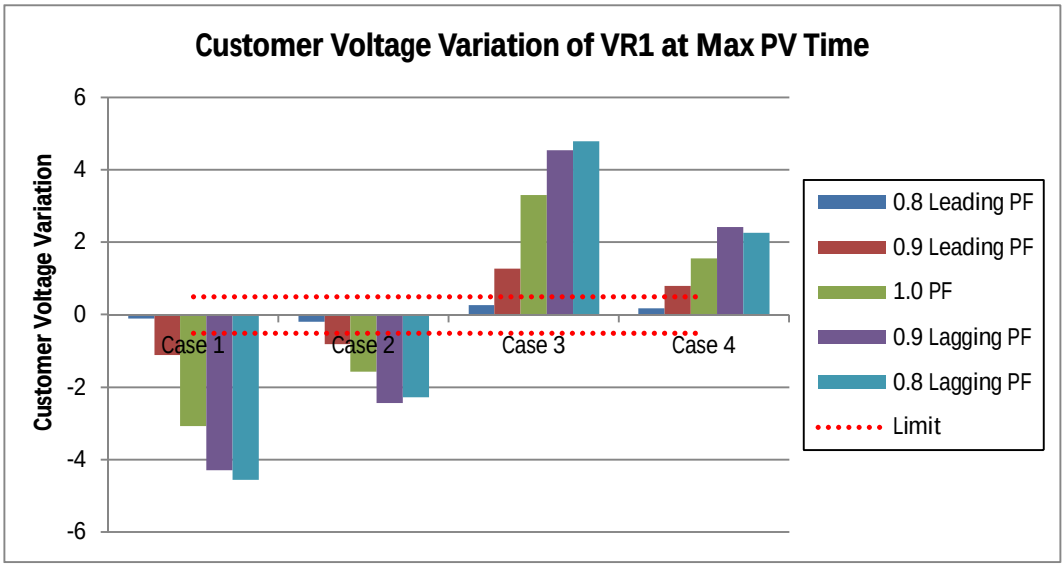

(b) Customer voltage variation of VR1 at max PV time

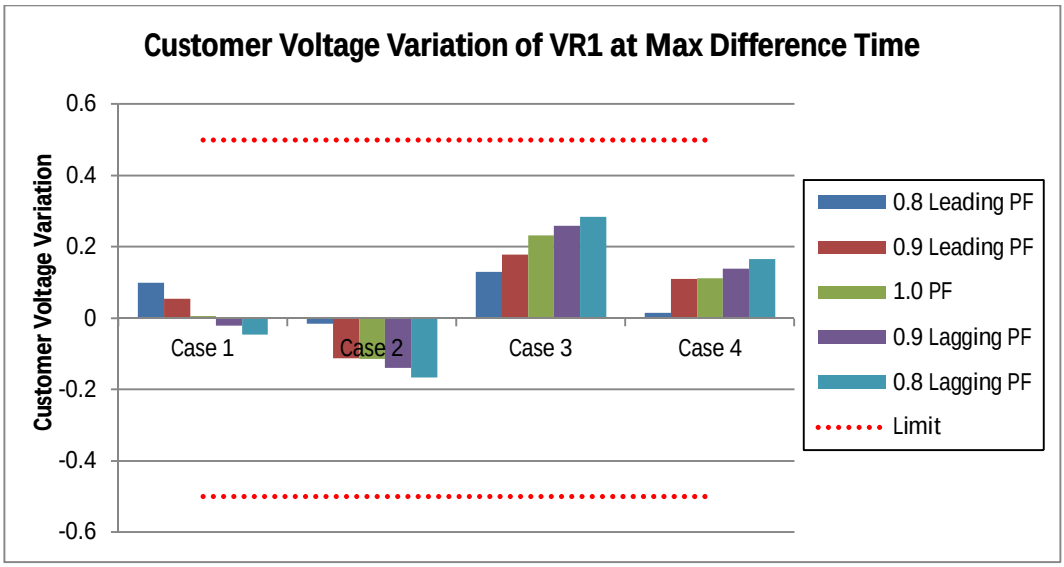

(c) Customer voltage variation of VR1 at max difference time

Figure 4-3 Customer voltage variation with 50% cloud cover

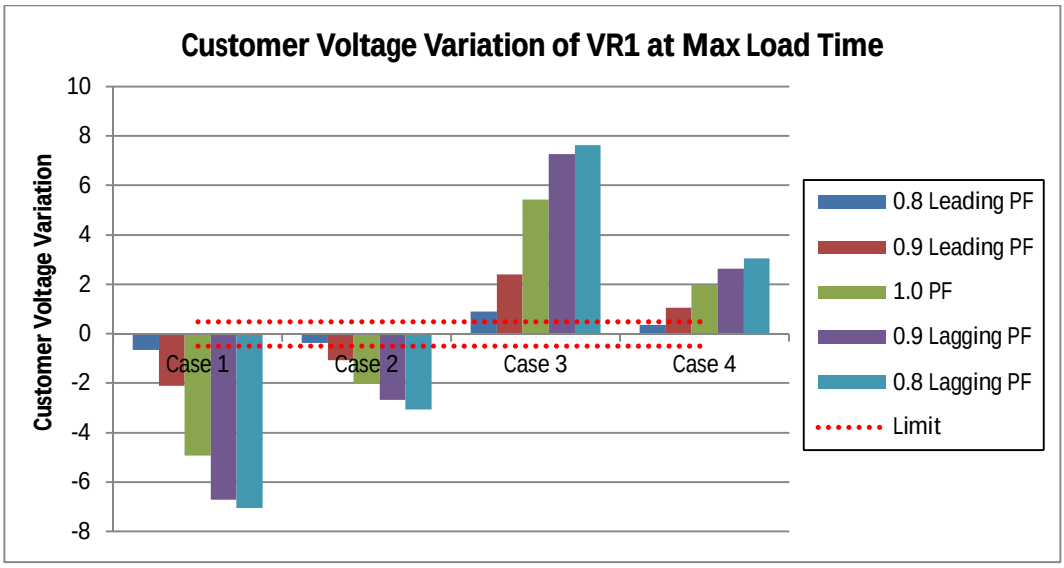

(a) Customer voltage variation of VR1 at max load time

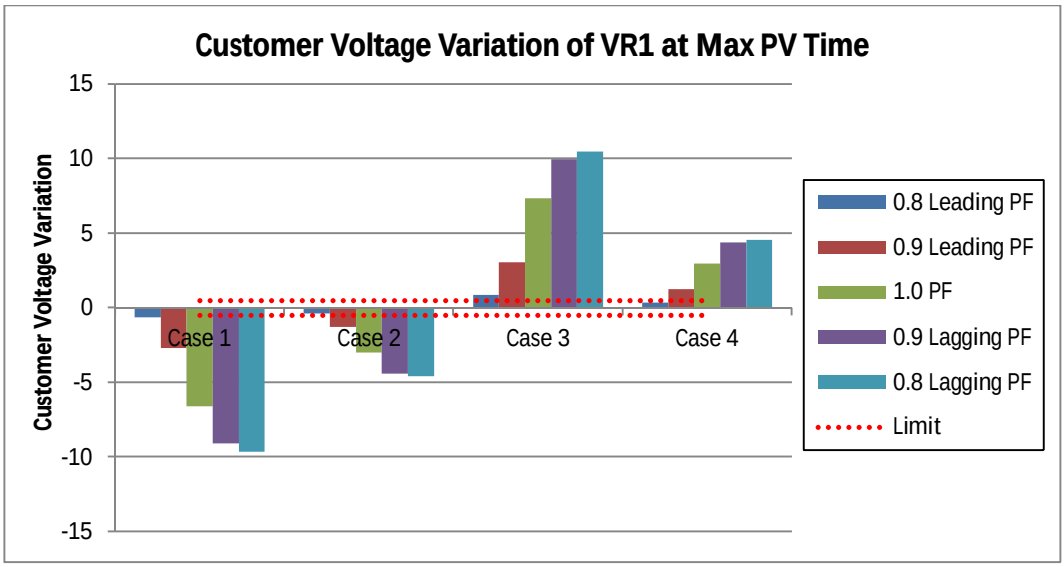

(b) Customer voltage variation of VR1 at max PV time

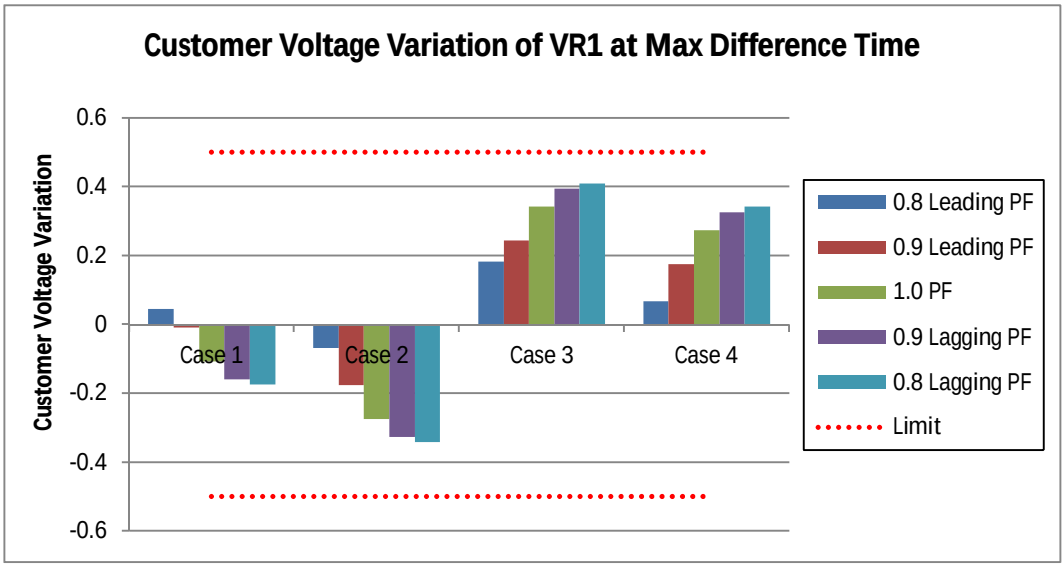

(c) Customer voltage variation of VR1 at max difference time

Figure 4-4 Customer voltage variation with 100% cloud cover

Figure 4-5 and Figure 4-6 show 3-D graphs as a function of PV generation power factor and cloud cover at VR1 for cases 1 and 3, respectively. Each figure contains the results of the three extreme circuit condition time points. This 3-D graph can be used to estimate voltage variations when the PV generation operates with some cloud cover and fixed power factor control. In Figure 4-5, voltage variation increases negatively for case 1 when cloud cover increases and the power factor varies from leading to lagging. On the other hand, voltage variation increases positively for case 3 when cloud cover increases, and the power factor varies from leading to lagging as shown in Figure 4-6. Hence, for optimal response the power factor control needs to change as a function of the generation.

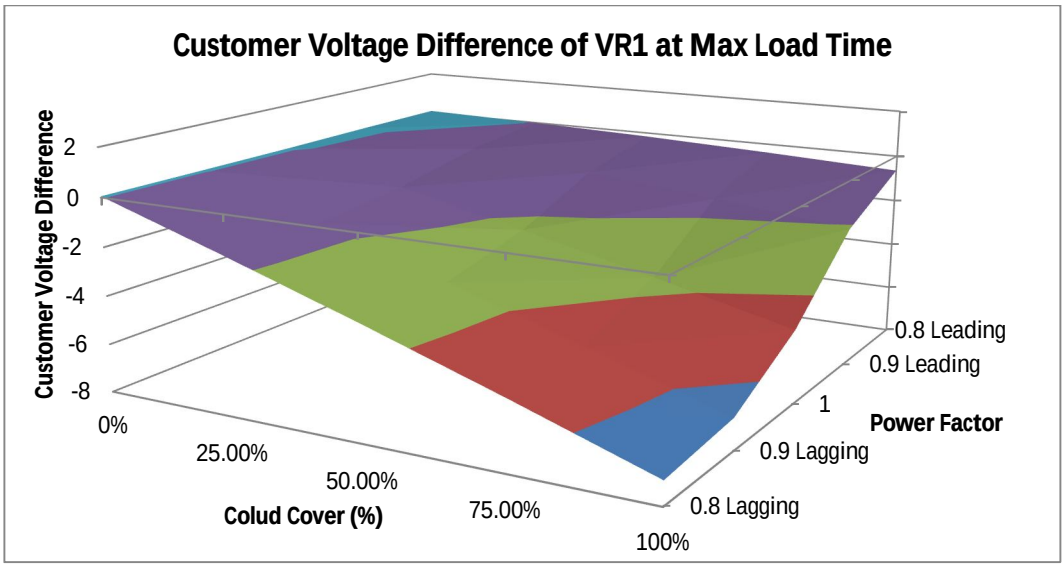

(a) 3-D Customer voltage variation at VR1 at max load time

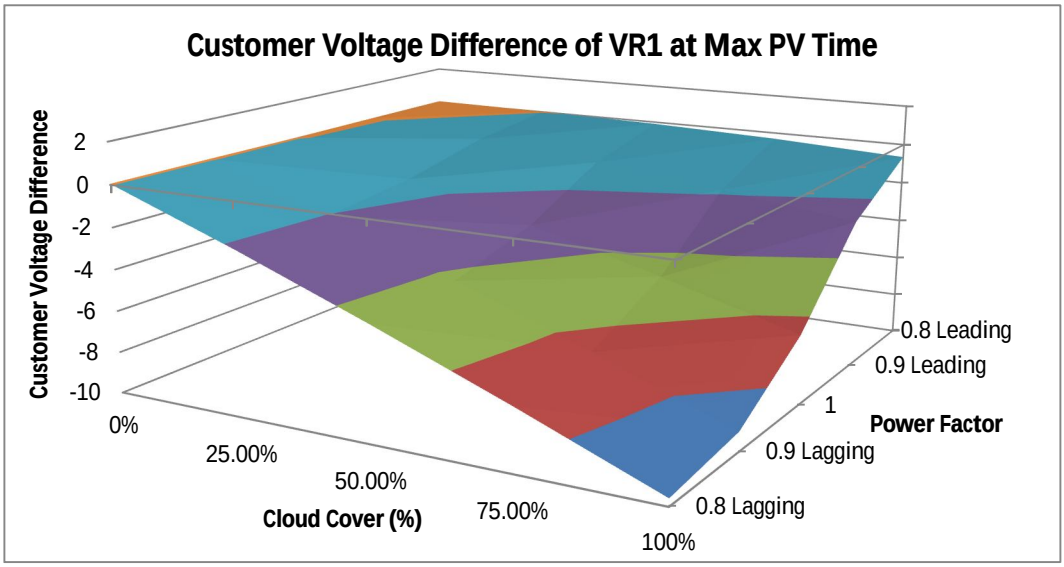

(b) 3-D Customer voltage variation at VR1 at max PV time

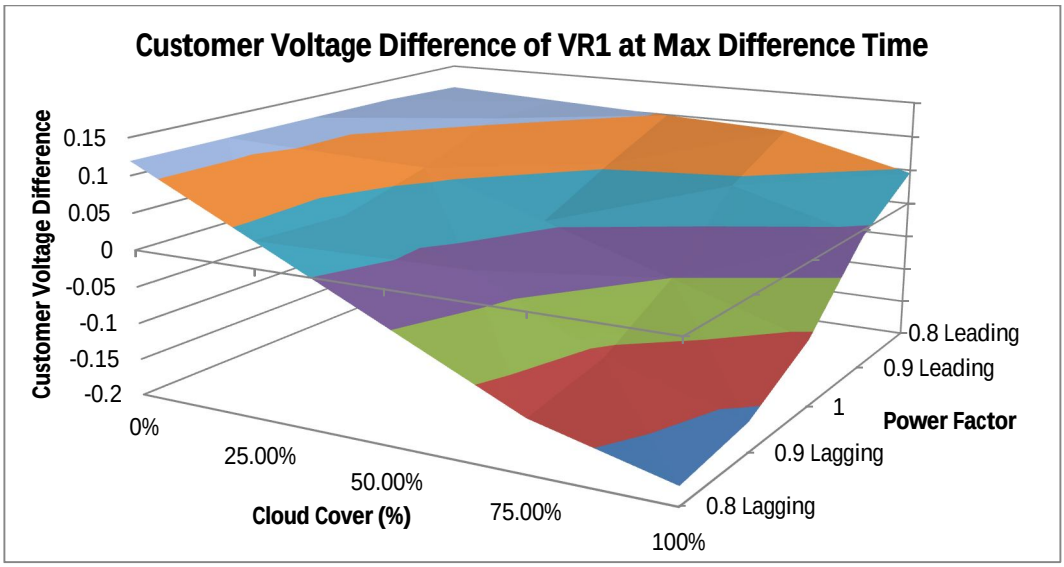

(c) 3-D Customer voltage variation at VR1 at max difference time

Figure 4-5 3-D Customer voltage variation for Case 1

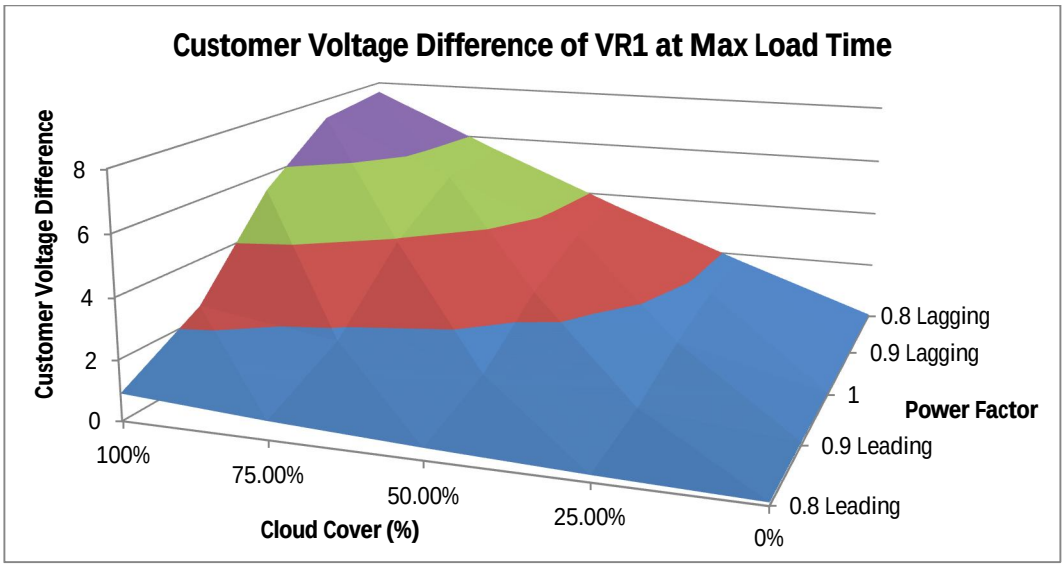

(a) 3-D Customer voltage variation at VR1 at max load time

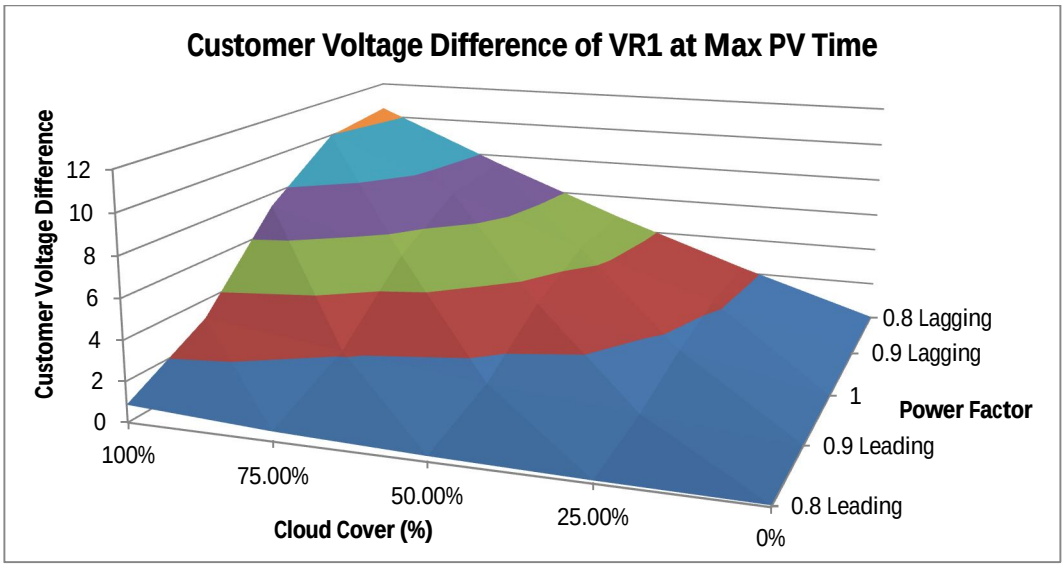

(b) 3-D Customer voltage variation at VR1 at max PV time

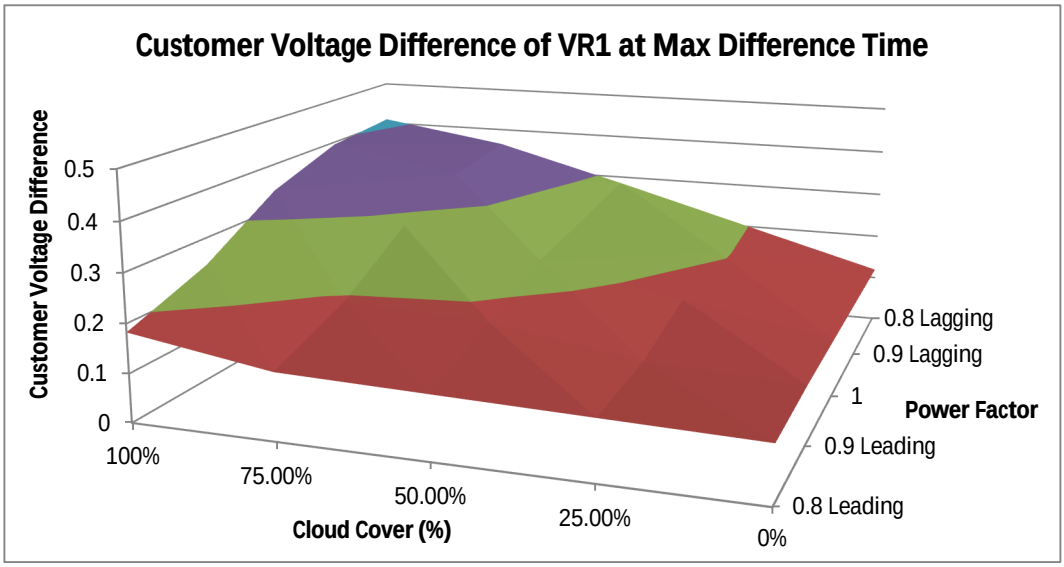

(c) 3-D Customer voltage variation at VR1 at max difference time

Figure 4-6 3-D Customer voltage variation for Case 3

b) Customer voltage variation by coloring the circuit

Figure 4-7 shows customer voltage variations by circuit color. This figure includes the results of phase A voltage difference when PV generation is on and off. The figure contains the results of the three different extreme circuit condition time points. The greater voltage variations are observed from PV4 to VR1 and downstream of SD4 at maximum circuit load and maximum PV generation times. The display of the results in this form shows the circuit locations that require some form of mitigation of the voltage problems created by the PV generation.

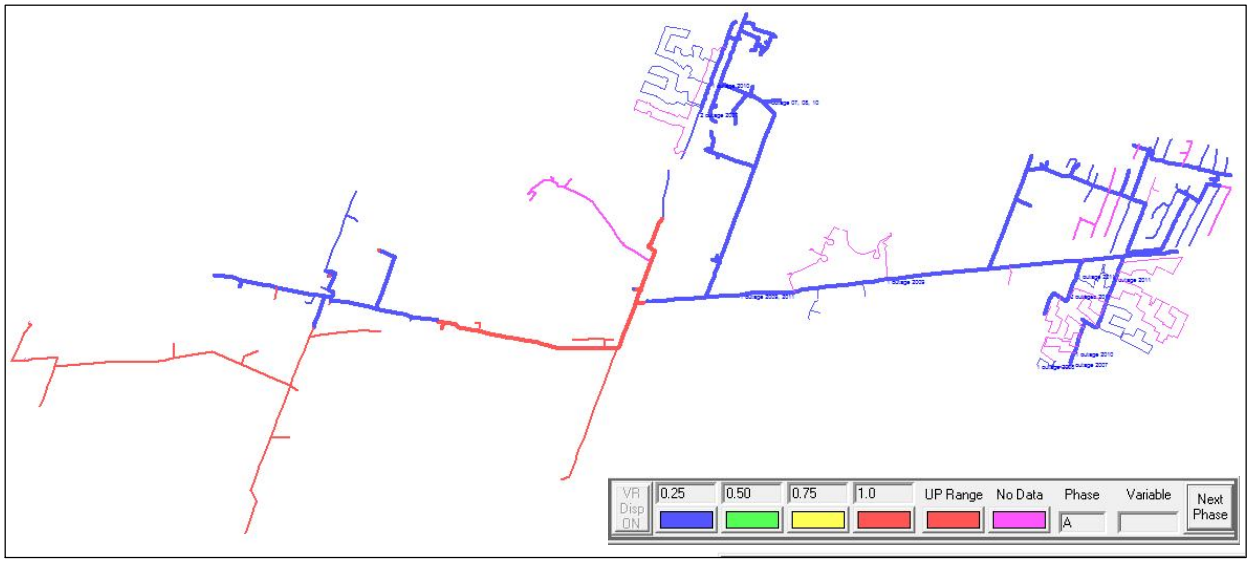

(a) Customer voltage variation by coloring the circuit at maximum circuit load time

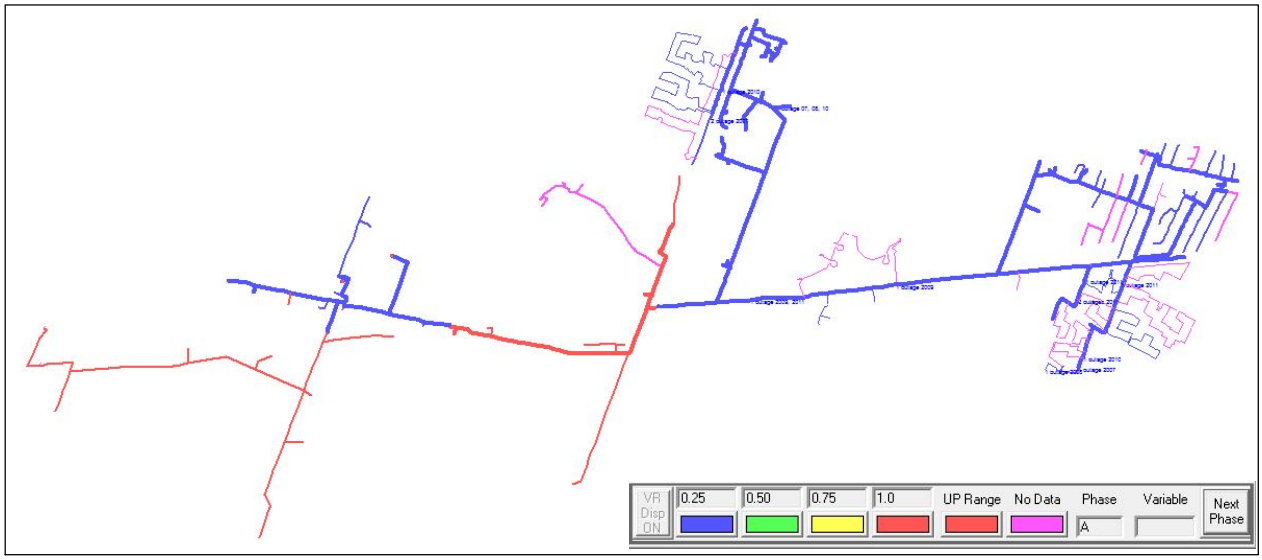

(b) Customer voltage variation by coloring the circuit at maximum PV generation time

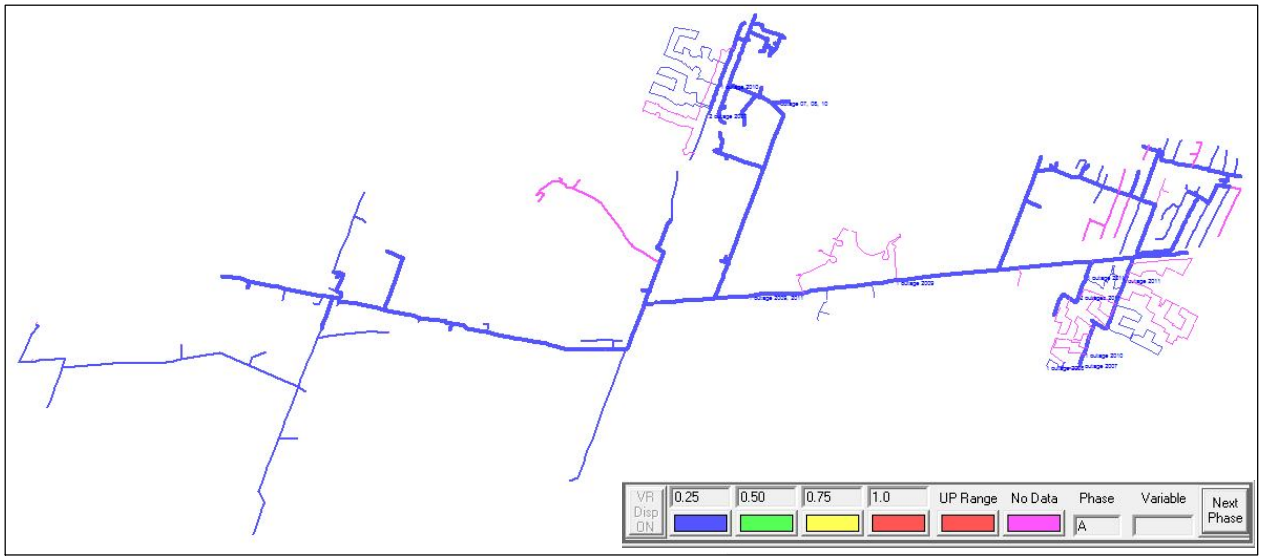

(c) Customer voltage variation by coloring the circuit at maximum difference between circuit load and PV generation

Figure 4-7 Customer voltage variation by coloring the circuit for Case 2 with 100% cloud cover

c) Customer voltage variation by distance

Figure 4-8 and Figure 4-9 show customer voltage variation as a function of distance from PV1 to the substation for both 50% and 100% cloud cover. In these figures V1 and V5 have the same values. Similar voltage variations are observed from the substation to SD1, but the voltage starts to vary after SD1 because of the loss of PV4 which is close to SD1. After VR1, distinct voltage variations are observed for the different cases. There is a greater variation from VR1 to PV1 in Figure 4-8 and Figure 4-9, but greater voltage variations are observed from SD1 to VR1 in Figure 4-7 due to automated device operations. In Figure 4-8 and Figure 4-9 it may also be observed that when the automated devices operate, the greatest voltage variation is observed from SD1 to VR1 for case 2 (V3-V1). This figure provides further information concerning where remedial actions are needed to reduce the voltage impacts.

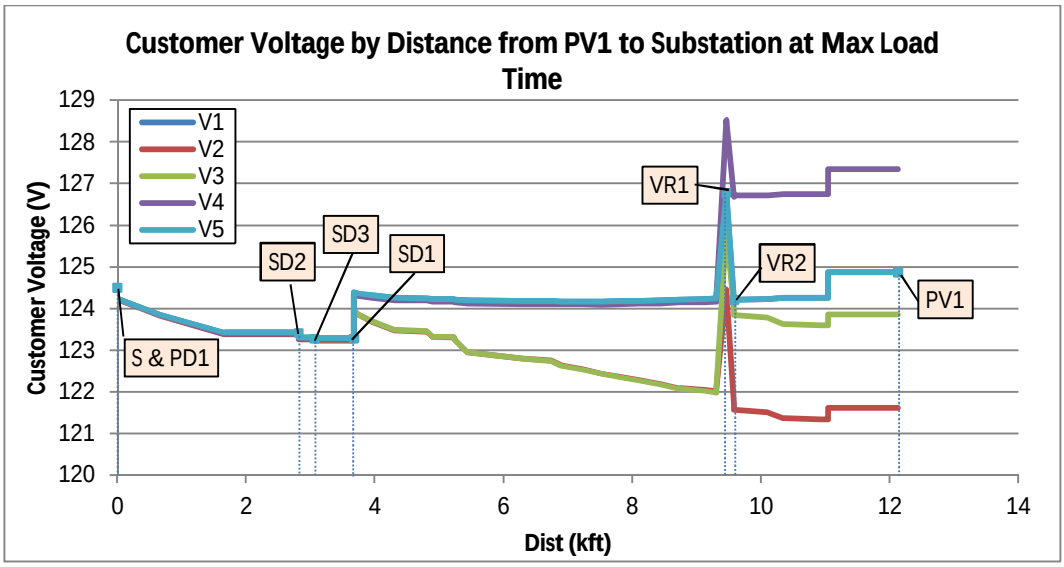

(a) Customer voltage by distance at maximum circuit load time

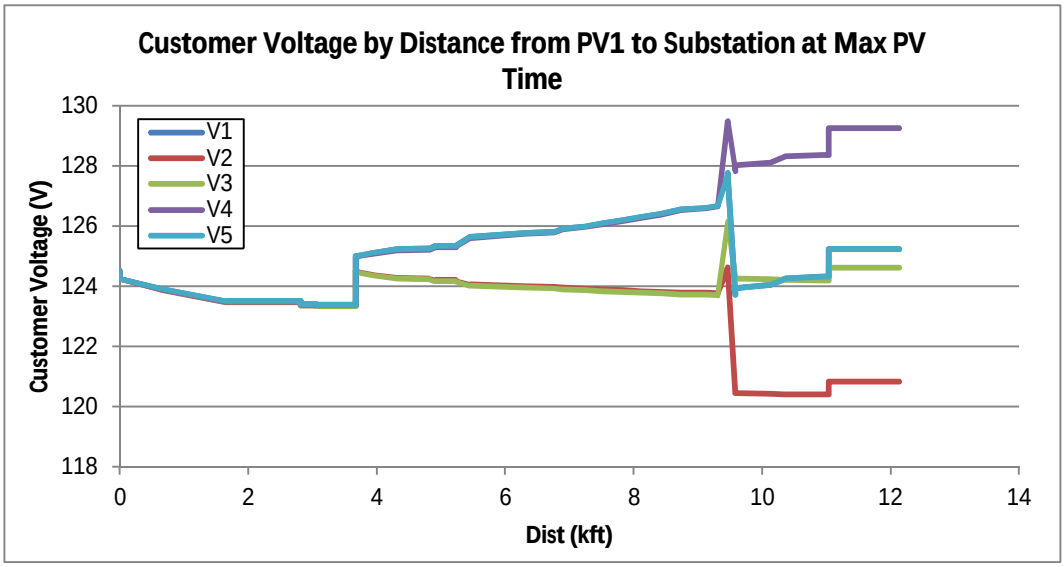

(b) Customer voltage by distance at maximum PV generation time

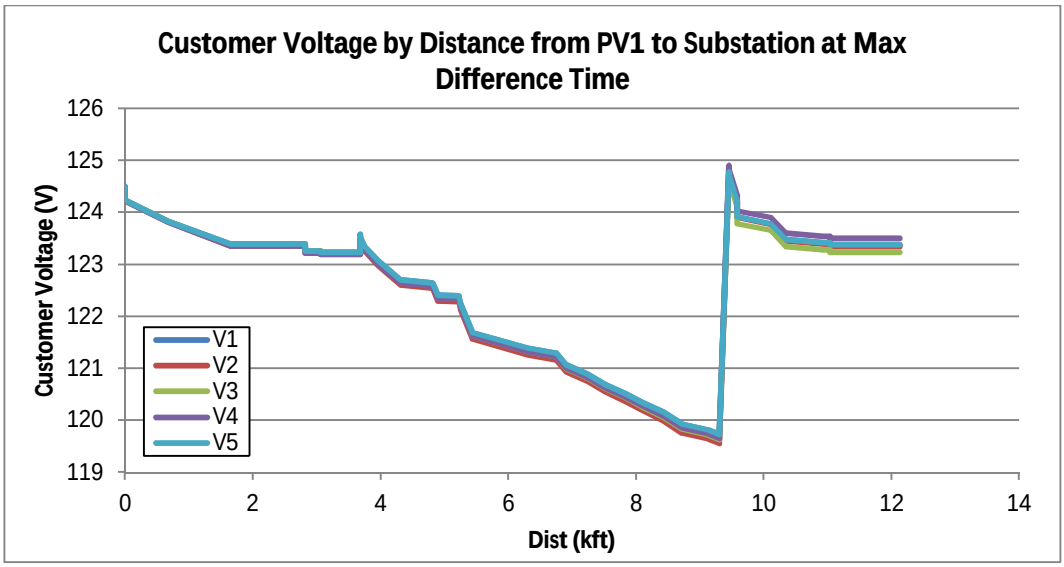

(c) Customer voltage by distance at maximum difference between circuit load and PV generation time

Figure 4-8 Customer voltage by distance with 50% cloud cover

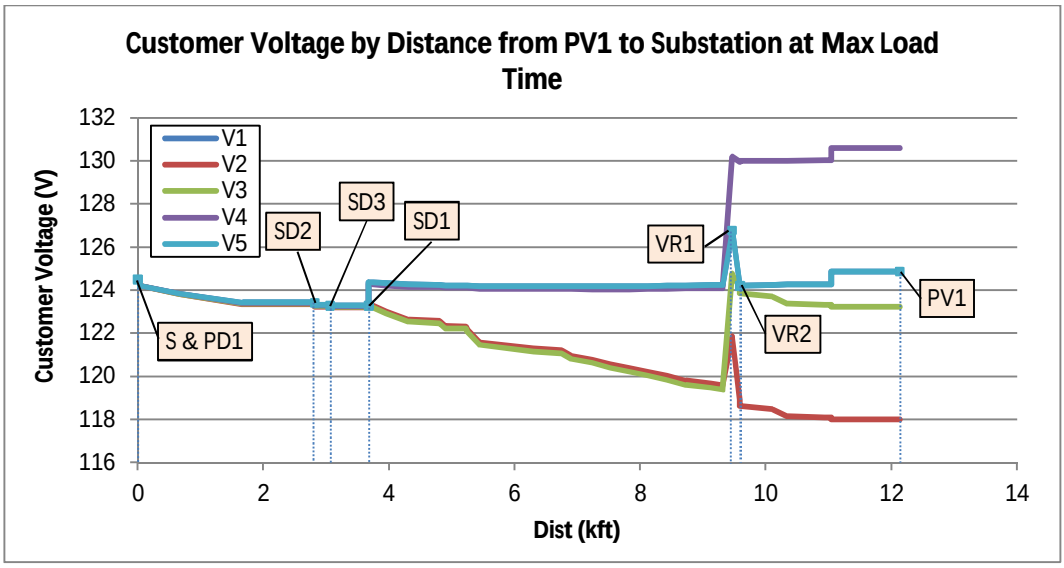

(a) Customer voltage by distance at maximum circuit load time

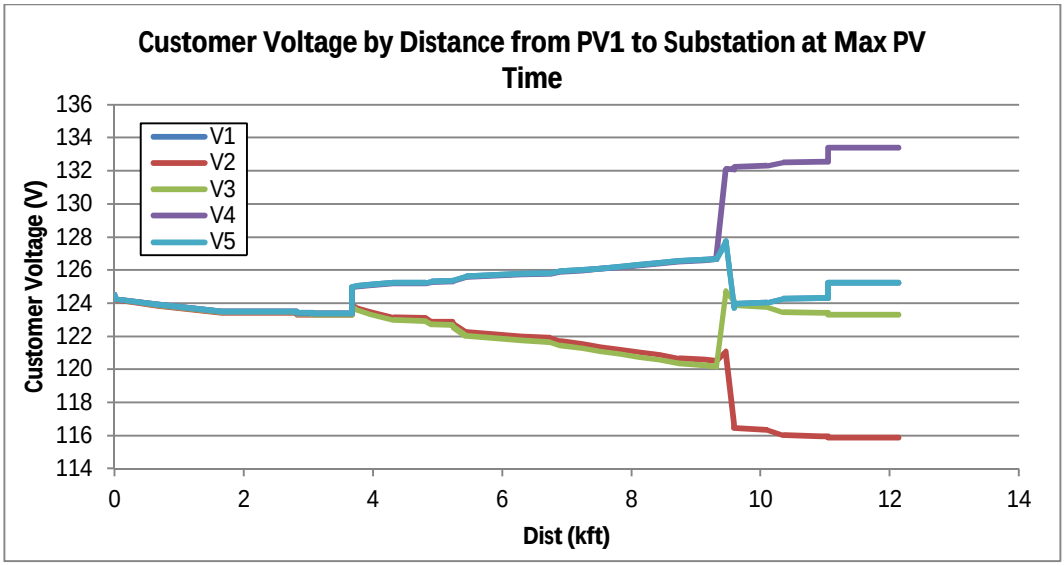

(b) Customer voltage by distance at maximum PV generation time

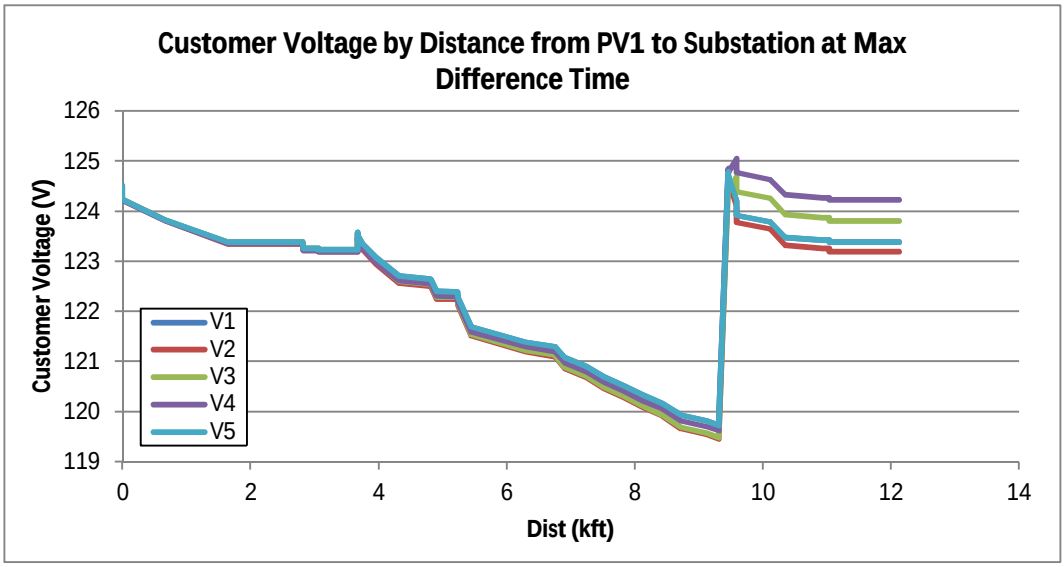

(c) Customer voltage by distance at maximum difference between circuit load and PV generation time

Figure 4-9 Customer voltage by distance when 100% cloud covers

d) Reverse power flow

Table 4-1 shows reverse power flow results for Case 2 involving 100% cloud cover. Results are shown at voltage regulators, capacitor banks, protective devices, and sectionalizing devices shown in Figure 4-1. Results are shown for the circuit with and without PV generation. The results show the maximum reverse flow and the time of occurrence of the maximum reverse flow. Reverse power flow occurs on phase A at VR1 and SD1 and on phase B at VR2 when PV generation is at its maximum (01:00 PM). Although reverse power flow does not occur, large power flow differences do occur at PD1, SD1,

and SD3 due to the PV generation. These results provide information as to where utility control and protection equipment need to be bidirectional.

Table 4-1 Reverse power flow results for Case 2 when 100% cloud covers

No.	Component Name	Max Difference Time	Phase	Flow Before (kW)	Flow After (kW)	Flow Difference
1	VR1	13:00	Phase A	156.19	***-77.19***	***233.38***
			Phase C	225.59	17.46	***208.13***
2	VR2	13:00	Phase B	54.59	***-163.90***	***218.49***
			Phase C	225.33	17.40	***207.92***
3	CAP1	14:00	Phase A	1285.15	1287.10	-1.96
			Phase B	1425.20	1426.66	-1.47
			Phase C	1218.64	1218.98	-0.34
4	CAP2	14:00	Phase A	234.53	234.88	-0.35
			Phase B	123.96	124.04	-0.08
			Phase C	17.78	17.79	-0.02
5	PD1	13:00	Phase A	3001.82	2096.34	***905.48***
			Phase B	2510.72	1613.99	***896.73***
			Phase C	2812.96	1916.43	***896.53***
6	PD2	14:00	Phase A	1508.92	1511.21	-2.29
			Phase B	1735.67	1737.31	-1.64
			Phase C	1553.27	1553.81	-0.54
7	PD3	13:00	Phase A	156.32	156.56	-0.24
			Phase B	156.67	156.76	-0.09
			Phase C	160.00	160.13	-0.12
8	PD4	14:00	Phase A	1285.86	1287.82	-1.96
			Phase B	1432.30	1433.77	-1.47
			Phase C	1219.08	1219.41	-0.33
9	SD1	13:00	Phase A	213.29	***-16.01***	***229.30***
			Phase B	277.20	53.89	***223.32***
			Phase C	365.98	145.05	***220.93***
10	SD2	13:00	Phase A	1939.35	1487.22	***452.13***
			Phase B	2225.76	1779.59	***446.17***
			Phase C	2134.45	1689.30	***445.15***
11	SD3	13:00	Phase A	1657.57	1205.48	***452.08***
			Phase B	1943.63	1497.67	***445.95***
			Phase C	1852.80	1407.81	***445.00***
12	SD4	13:00	Phase A	0.74	0.74	0.01
			Phase B	0.75	0.76	-0.01
			Phase C	0.68	0.73	-0.05

e) Customer Voltage Phase Unbalance

Table 4-2 shows customer voltage phase unbalance for Case 2 with 100% cloud cover. Results are given for voltage regulators, capacitor banks, protective devices, and sectionalizing devices shown in Figure 4-1. Results are shown for the circuit with and without the PV generation. The results show the maximum unbalance and the time of occurrence of the maximum unbalance. Note that a positive unbalance difference shown in the last column of the table indicates an improvement in the unbalance. This circuit has some excessive voltage unbalances (more than 2%) at VR1, VR2, and SD4 without the PV generation. Note that the voltage unbalance improves after the integration of PV generation (smaller

PVUR values). Overall the voltage unbalance is improved at all selected components except CAP2. This output provides information about where actions are needed to reduce voltage unbalance, especially if three-phase motor loads are present.

Table 4-2 Voltage phase unbalance for Case 2 with 100% cloud cover

No.	Component Name	Max Difference Time	Phase	PVUR Before	PVUR After	Unbalance Difference
1	VR1	13:00	Phase A	***0.0459***	0.0165	***0.0294***
2	VR2	14:00	Phase B	***0.0508***	0.0188	***0.0320***
3	CAP1	13:00	Phase A	0.0010	0.0005	0.0006
4	CAP2	16:00	Phase B	0.0071	0.0078	-0.0007
5	PD1	-	-	0.0000	0.0000	0.0000
6	PD2	11:00	Phase A	0.0008	0.0003	0.0005
7	PD3	13:00	Phase A	0.0009	0.0003	0.0006
8	PD4	13:00	Phase A	0.0009	0.0003	0.0006
9	SD1	13:00	Phase A	0.0006	0.0000	0.0006
10	SD2	13:00	Phase A	0.0005	0.0000	0.0005
11	SD3	14:00	Phase A	0.0005	0.0000	0.0005
12	SD4	13:00	Phase C	***0.0680***	***0.0203***	***0.0477***

f) Power Flow Phase Unbalance

Table 4-3 shows the power flow phase unbalance for Case 2 with 100% cloud cover. Results are given for voltage regulators, capacitor banks, protective devices, and sectionalizing devices shown in Figure 4-1. Results are shown for the circuit with and without PV generation. The results show the maximum unbalance and the time of occurrence of the maximum unbalance. Note that a positive power flow unbalance difference shown in the last column of the table indicates an improvement in the unbalance. Contrary to the voltage phase unbalance, the greater power flow unbalance is observed at VR1, VR2, and SD1 after integration of PV generation. Furthermore, the unbalance increases at most of the selected locations. The results here provide information about where actions need to be taken to help balance power flows.

Table 4-3 Power flow phase unbalance for Case 2 with 100% cloud cover

No.	Component Name	Max Difference Time	Phase	PFUR Before	PFUR After	Unbalance Difference
1	VR1	10:00	Phase A	0.1751	***7.1525***	***-6.9774***
2	VR2	16:00	Phase B	0.6169	***13.3801***	***-12.7633***
3	CAP1	07:00	Phase A	0.0164	0.0181	-0.0017
4	CAP2	16:00	Phase B	0.0228	0.0235	-0.0007
5	PD1	11:00	Phase B	0.1140	0.1641	-0.0501
6	PD2	07:00	Phase A	0.0292	0.0278	0.0014
7	PD3	13:00	Phase A	0.0085	0.0079	0.0006
8	PD4	07:00	Phase A	0.0148	0.0165	-0.0017
9	SD1	13:00	Phase A	0.2529	***1.2626***	***-1.0097***
10	SD2	13:00	Phase A	0.0764	0.0998	-0.0233
11	SD3	13:00	Phase A	0.0882	0.1203	-0.0320
12	SD4	13:00	Phase C	0.0680	0.0203	0.0477

4.4.2. Quasi Steady-State Simulation Results

a) Customer voltage variation

Figure 4-10 shows time-varying voltage at CAP1 as a function of the PV generation power factor. When the no PV generation case is compared to the case with PV generation, a voltage rise occurs at unity and lagging power factors. The analysis shows that leading power factor PV generation control mitigates the voltage rise. Note that 0.9 leading power factor control maintains the customer voltage level at CAP1 approximately at the value that existed before introducing the PV into the circuit. Furthermore, a 0.8 leading power factor control can reduce the voltage level below that which existed prior to the introduction of the PV generation. These results provide information on power factor control that can help mitigate voltage rise. Results for voltage regulator VR1 operation will be presented in automated device steps.

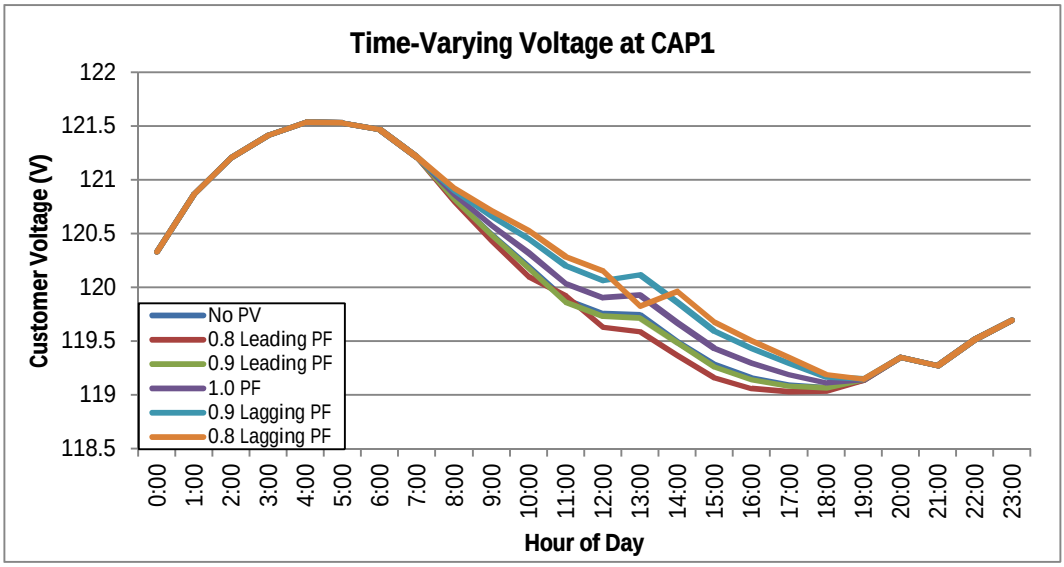

Figure 4-10 Time-varying voltage at CAP1 for Case 2 with 100% cloud cover

b) Circuit loss

Figure 4-11 and Figure 4-12 show time-varying real and reactive circuit losses, respectively, as a function of PV generation power factor. Both real and reactive circuit losses decrease after integration of PV generation operating with unity power factor. Lagging power factor control reduces the circuit loss further. A 0.9 leading power factor control has similar circuit losses as the no PV generation case, whereas a 0.8 leading power factor control increases the circuit loss. Therefore, PV generation leading power factor can help mitigate voltage rise problems, but such control causes the circuit losses to increase. Hence, a balance must be sought in the control of voltage and losses.

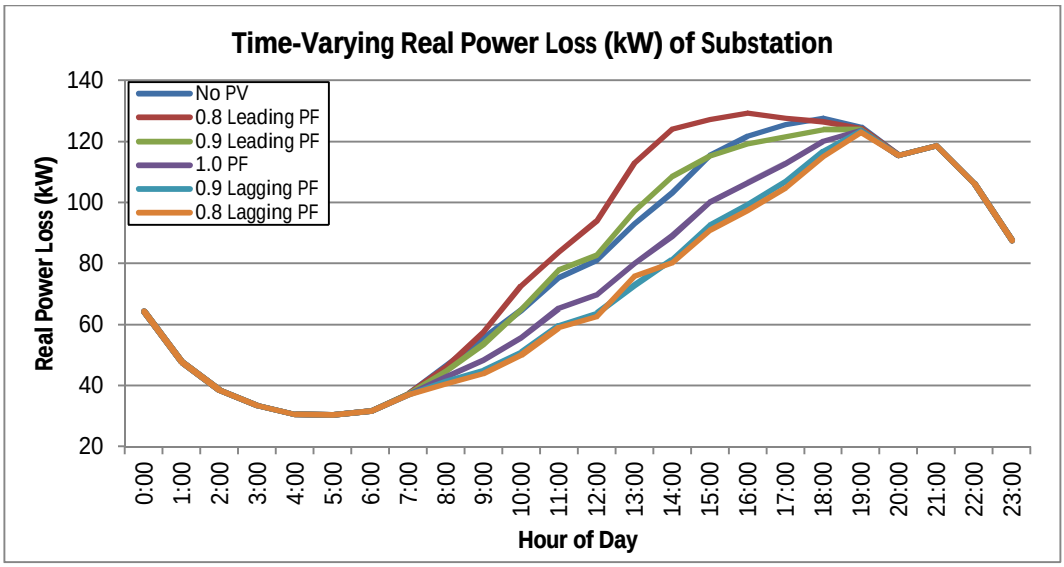

Figure 4-11 Time-varying real power circuit loss for Case 2 with 100% cloud cover

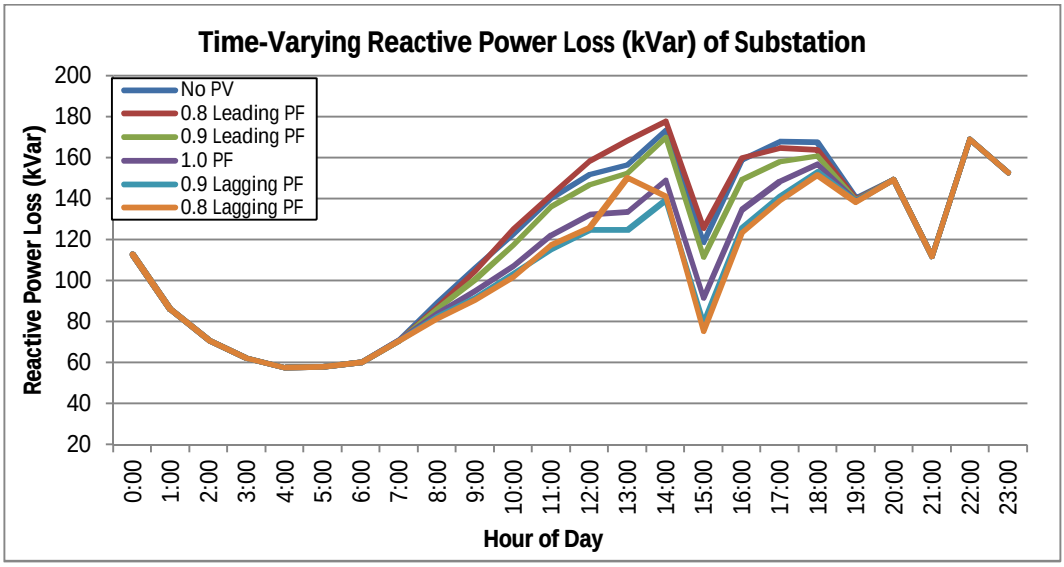

Figure 4-12 Time-varying reactive power circuit loss for Case 2 with 100% cloud cover

c) Automated device steps

Figure 4-13 shows the step variations of VR1 across the day as a function of PV generation power factor. Total steps variations are 20, 18, 18, 24, 36, and 40 steps for no PV generation, 0.8 leading, 0.9 leading, 1.0, 0.9 lagging, and 0.8 lagging power factors, respectively. With the PV generation operating at unity power factor, the total steps across the day increases by 4 steps over the no PV generation case. As can be seen, leading power factor control reduces the total steps and the lagging power factor control

increases the total steps significantly. The results here provide information that can be used to minimize maintenance activities and prolong life of utility control equipment.

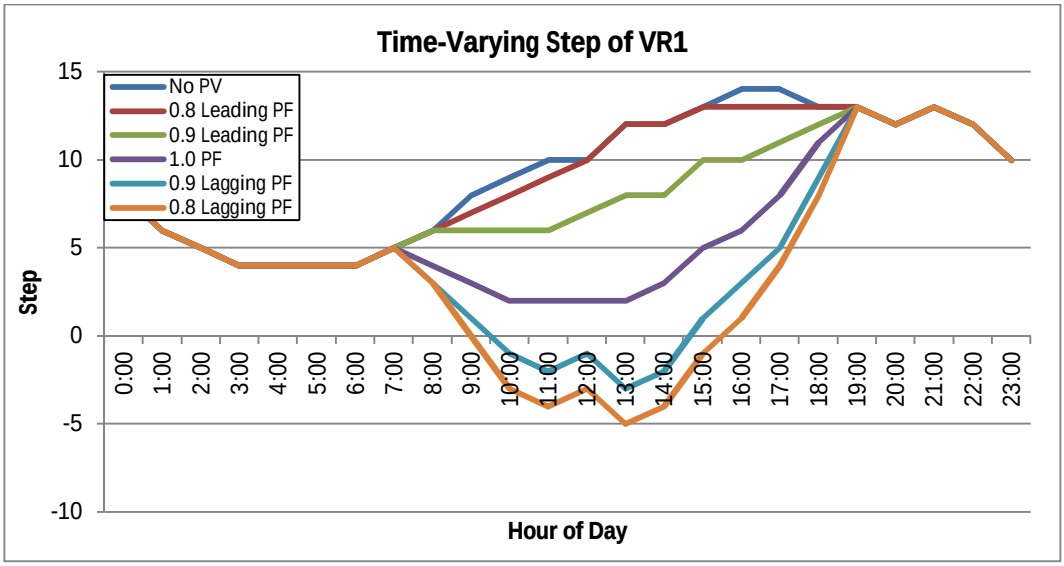

Figure 4-13 Time-varying steps of VR1 for Case 2 with 100% cloud cover

4.5. Conclusions

In this chapter the impacts of PV generation are investigated. Model data for a real distribution circuit is employed. Both steady-state and quasi steady-state impact studies are performed. In the studies changing cloud cover conditions and variations in PV generation power factor control are considered. Both improvements and adverse effects of PV generation on the circuit are discussed.

The steady-state impact studies consider voltage variations, reverse power flows, voltage phase unbalance, and power flow phase unbalance. In considering the voltage variations, several visualizations are provided, including 3-D voltage variation graphs, coloring the circuit model by voltage variations, and graphs of voltage variations versus distance. Each visualization provides information that is helpful in pursuing remedial actions needed to reduce voltage impacts. Reverse power flow, voltage phase unbalance, and power flow phase unbalance are also considered.

The quasi steady-state impact studies consider voltage variations, circuit losses, and automated device steps, across the time varying operation of the circuit. Voltage rise problems caused by the PV generation are observed in the simulation. In this particular simulation real and reactive losses are improved following the integration of PV generation. However, increases in automated control device steps are observed across the day. It is shown that PV generation power factor control can help to mitigate the

impacts. However, there are tradeoffs between controlling voltage variations, circuit losses, and motion of automated utility control devices.

Chapter 5 A Frequency Domain Approach to Characterize and Analyze Wind Speed Patterns

5.1. Introduction

Wind power has become an increasingly significant source of generation in power systems and will play an important role in the future of energy supply. This has led to an increase of the wind power/energy penetration level in the U.S. electricity market [9], for example. Despite its numerous advantages, the penetration of wind power is limited due to its uncertain and intermittent nature.

In order to fully benefit from wind power, accurate wind power forecasting is an essential tool in addressing this challenge [55]. This has motivated researchers to develop better forecast of the wind resources and the resulting power. Two mainstream approaches are the physical [56, 57] and the statistical approach [58-65].

The physical approach tries to refine the Numerical Weather Prediction (NWP) to take into account the local wind conditions by using downscaling models. These downscaling models require several physical considerations including; the description of the wind farm and the terrain. Then, local wind speed is transferred to wind power using the given power curve. This approach is useful at sites without wind measurements because it doesn't require the historical data. However, the approach is very complicated and acquiring the physical data is a major obstacle.

The statistical approach tries to find the relationship of how wind speed/power can be forecast using explanatory variables and online measured data. The time series model is applied in the paper [58-60]. In addition, Artificial Neural Networks (ANN) is used [61, 62]. Large sets of historical data are used for the training process, in order to learn the dependence of the output on input variables. The Fuzzy Logic is also used [63]. This approach is a nonlinear mapping of input variables into the output by using numerical and linguistic values. Data Mining and Bayesian methodology are applied to build time series models [64, 65]. Contrary to the physical approach, the statistical approach requires historical data.

The frequency domain approach is one of the statistical approaches and therefore, it requires historical data. In previous work [58-65], wind speed/power is forecast using the time domain data tainted by various noises. It is difficult to separate such noises. However, the frequency domain approach

characterizes and analyzes wind speed by using the pure data obtained by separating such noises. This benefit enables the improvement of forecasting accuracy.

It is critical to understand the characteristics of the wind resource in order to develop better wind speed forecasting. The power spectral density of a wind speed/power in the frequency domain provides information about the characteristics of wind variability [66-69]. These papers rely on frequency spectrum analysis to characterize the variations of wind speed.

The objectives of this chapter are (1) to formalize the frequency domain approach by addressing the major step and the prerequisite conditions for its application, and (2) to characterize and analyze wind speed patterns using this approach.

In conjunction with other factors, wind speed patterns are governed by weather and have a large range of variability daily and monthly, and from location to location as well. A detailed characterization of these patterns is fundamental in order to gain key insights and to fully realize potential improvements in wind power forecasting. Hence, wind speed patterns during different times are characterized by month and additionally, wind speed patterns at different locations are compared to characterize the patterns by physical geography. This study demonstrates that analysis and characterization of wind speed pattern in the frequency domain can reveal information that is difficult to obtain from the time domain.

The basic benefit of the frequency domain approach is that, under the right conditions, the original signal can be represented by using some of the harmonic components without losing significant accuracy. Therefore, knowing only the highest harmonic magnitude set (for example, DC, 1^{st}, 2^{nd} harmonics) can explain the characteristics of wind pattern. To analyze the harmonic components, a compact frequency-domain representation is offered to present the data in machine-readable format. This structured format helps simplify the diagnosis required to characterize and analyze wind speed patterns.

The chapter is organized as follows. Section 5.2 presents the frequency domain approach and introduces the technique and prerequisite conditions. In Section 5.3, the characterization of wind speed patterns is conducted to represent wind situations during different times and at different locations. In Section 5.4, this chapter continues to analyze the characterized dataset and shows that the new tool is a potentially useful indicator of wind speed patterns. Finally, findings of the study are summarized in Section 5.5.

5.2. Frequency Domain Approach

5.2.1. Methodology

Different locations have different wind strengths and patterns and it is therefore difficult to compare the characteristics of their patterns directly. The data normalization is used to analyze wind speed patterns at different locations. The dataset is scaled by its max value so that they fall within the range between 0.0 and 1.0:

$$x_n(t) = \frac{x_{original}(t)}{x_{peak}} \tag{5-1}$$

where $x_{original}(t)$ is the original wind speed and x_{peak} is the max value of this dataset.

Discrete Fourier Transform (DFT) is employed to decompose or separate the discrete waveform into a sum of sinusoids of different frequencies. Discrete time signal $x_n(t)$ in the range $0 \le n \le (N-1)$ is described in the frequency domain by X_k:

$$X_k = \sum_{n=0}^{N-1} x_n e^{-j2\pi nk/N}, \qquad k = 0,1,\cdots,(N-1) \tag{5-2}$$

where $e^{-j2\pi/N}$ is a primitive Nth root of unity. The complex number X_k represents the amplitude and phase of the frequency components.

The discrete time signal $x_n(t)$ can be calculated from X_k using the Inverse DFT (IDFT):

$$x_n(t) = \frac{1}{N}\sum_{k=0}^{N-1} X_k e^{j2\pi nk/N}, \qquad n = 0,1,\cdots,(N-1) \tag{5-3}$$

If $x_n(t)$ is real number, the DFT exhibits conjugate symmetry. Therefore, one obtains the complete information by only looking at half of X_k.

$$X_k = X^*_{N-k} \qquad \text{or} \qquad |X_k| = |X_{N-k}| \tag{5-4}$$

where X^*_{N-k} denotes complex conjugate of X_k. By using this property, the input signal $x_n(t)$ can be represented as:

$$x_n(t) = H_{DC} + \sum_{k=1}^{(N/2)-1} H_k \cdot \cos\left(\frac{2\pi n}{N} \cdot k + \theta_k\right) \quad (5\text{-}5)$$

where

$H_{DC} = \left(X_0 + X_{N/2}\right)/N$ is the DC component

$H_k = \left(2 \cdot \left|X_k\right|\right)/N$ is the k^{th} harmonic magnitude

$\left|X_k\right|$ and θ_k is the amplitude and phase of the complex number X_k respectively.

To exemplify the frequency approach, the monthly average of wind speed in July 2004 at San Gorgonio Pass is considered as shown in Figure 5-1. In Table 5-1, harmonic components and compact frequency-domain representations corresponding to the monthly wind speed data in 2004 at this location are represented.

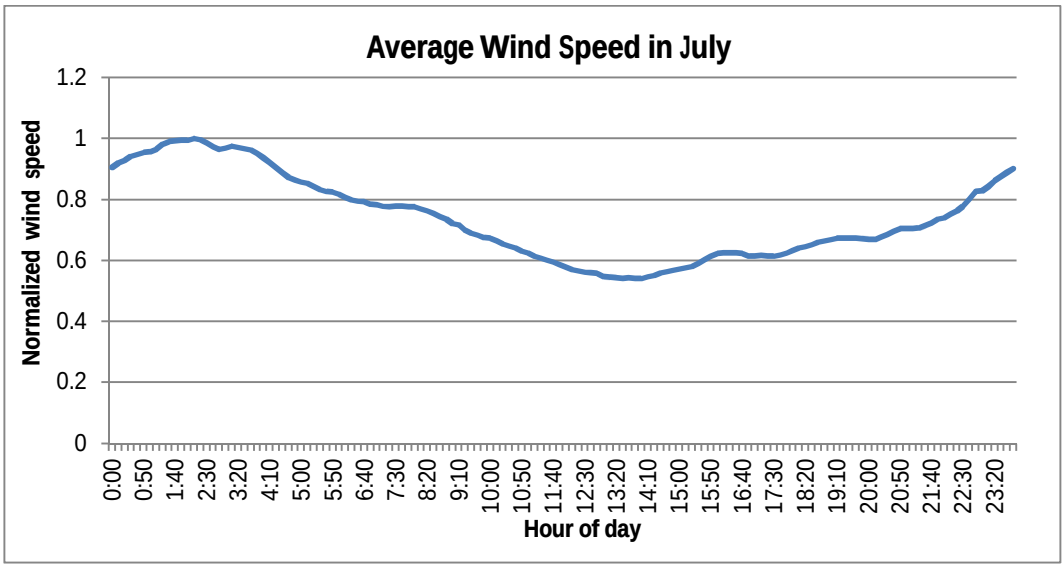

Figure 5-1 Average Wind Speed at San Gorgonio Pass in July 2004

Table 5-1 Harmonics and Their Compact Frequency-Domain Representations at San Gorgonio Pass in 2004

Month	M_{peak} (m/s)	K	Normalized Harmonic Magnitude H_K										
			H_{DC}	H_1	H_2	H_3	H_4	H_5	H_6	H_7	H_8	H_9	H_{10}
1	8.135	4	0.919	0.051	0.024	0.028	0.003	0.013	0.007	0.009	0.001	0.006	0.006
2	9.567	5	0.913	0.033	0.015	0.016	0.036	0.005	0.013	0.014	0.002	0.006	0.003
3	7.775	4	0.897	0.050	0.027	0.021	0.016	0.006	0.002	0.008	0.003	0.004	0.002
4	9.269	4	0.841	0.069	0.019	0.052	0.014	0.013	0.006	0.004	0.003	0.003	0.002
5	9.968	4	0.803	0.107	0.046	0.033	0.010	0.012	0.002	0.002	0.004	0.001	0.001
6	9.268	4	0.762	0.160	0.054	0.041	0.006	0.003	0.008	0.006	0.000	0.004	0.000
7	8.729	4	0.739	0.191	0.031	0.036	0.007	0.000	0.009	0.003	0.001	0.003	0.004

8	8.994	5	0.682	0.209	0.037	0.051	0.023	0.003	0.010	0.005	0.002	0.001	0.000
9	8.491	4	0.853	0.083	0.015	0.028	0.017	0.004	0.009	0.002	0.007	0.002	0.003
10	8.432	2	0.855	0.086	0.009	0.012	0.016	0.015	0.007	0.009	0.012	0.007	0.002
11	9.192	3	0.907	0.066	0.035	0.015	0.013	0.006	0.010	0.006	0.004	0.003	0.000
12	10.267	2	0.959	0.018	0.020	0.020	0.006	0.006	0.005	0.003	0.003	0.001	0.005

Month	Shape Descriptor (S)	Harmonic Angle θ_K (Deg)									
		θ_1	θ_2	θ_3	θ_4	θ_5	θ_6	θ_7	θ_8	θ_9	θ_{10}
1	4-92-5.065-2.051-3.334	65	51	334	276	329	181	181	341	94	8
2	5-91-3.056-2.029-2.206-4.230	56	29	206	230	189	221	211	149	196	239
3	4-90-5.036-3.151-2.279	36	151	279	345	354	270	183	105	160	89
4	4-84-7.321-2.003-5.268	321	3	268	277	227	314	287	252	8	92
5	4-80-11.341-5.253-3.276	341	253	276	301	222	130	89	125	265	127
6	4-76-16.320-5.281-4.313	320	281	313	273	104	11	55	259	24	201
7	4-74-19.321-3.279-4.296	321	279	296	216	314	25	145	225	344	121
8	5-68.322-21.304-4.271-5.283-2.251	322	304	271	283	251	329	92	88	347	103
9	4-85-8.008-2.312-3.262	8	312	262	314	311	250	4	173	303	43
10	2-86-9.004	4	74	318	309	246	186	215	151	93	96
11	3-91-7.082-4.038	82	38	73	298	287	340	67	26	296	64
12	2-96-2.140	140	81	65	53	315	13	62	135	35	49

This result shows that harmonic magnitude exhibits a trend that the first few are major components while the remaining components are negligibly small. Although it is difficult to find a trend in harmonic angle, the harmonic signal is composed of magnitude and angle so that high-order harmonic angles are also negligible. Thus, in the frequency domain, knowing a small number of low-order harmonics can explain the characteristics of wind speed.

To define the number of components required in order to obtain an acceptable range, Mean Absolute Percentage Error (MAPE) index is used:

$$MAPE = \frac{1}{n}\sum_{t=1}^{n}\left|\frac{A_t - F_t}{A_t}\right| \tag{5-6}$$

where A_t is the actual value, F_t is the estimated value by adding harmonic components sequentially. To obtain the number of components necessary, each iteration calculates times series data by adding a harmonic component sequentially until the resulting MAPE value is less than 2%. The out-of-range harmonic components are considered as noise in this chapter. Based on the experimental result, it is suitable to use 2% while preserving original nature of the signal.

Table 5-2 shows the results with included harmonic components and corresponding MAPE value. This indicates that DC and 3 harmonic components over most of the month are sufficient to explain the characteristics in the selected location. Furthermore, Figure 5-2 compares actual wind speed with estimated one using up to the 3rd harmonic component in July 2004. The figure shows that estimated wind speed matches well with actual one.

Table 5-2 MAPE Value by Adding Harmonic Components

	MAPE							
	DC	1st	2nd	3rd	4th	5th	6th	7th
Jan	0.0458	0.0270	0.0231	0.0136	0.0136	0.0105	0.0093	0.0078
Feb	0.0372	0.0311	0.0284	0.0274	0.0137	0.0137	0.0118	0.0072
Mar	0.0422	0.0257	0.0200	0.0140	0.0089	0.0082	0.0083	0.0056
Apr	0.0550	0.0412	0.0406	0.0147	0.0116	0.0069	0.0058	0.0050
May	0.0840	0.0388	0.0279	0.0116	0.0101	0.0055	0.0054	0.0052
Jun	0.1390	0.0536	0.0369	0.0111	0.0091	0.0088	0.0063	0.0048
Jul	0.1663	0.0371	0.0339	0.0110	0.0101	0.0101	0.0069	0.0066
Aug	0.1939	0.0518	0.0527	0.0243	0.0121	0.0121	0.0074	0.0058
Sep	0.0671	0.0268	0.0245	0.0152	0.0101	0.0097	0.0079	0.0077
Oct	0.0650	0.0192	0.0185	0.0180	0.0153	0.0127	0.0122	0.0114
Nov	0.0549	0.0283	0.0172	0.0133	0.0113	0.0106	0.0081	0.0071
Dec	0.0212	0.0181	0.0152	0.0086	0.0078	0.0067	0.0061	0.0060

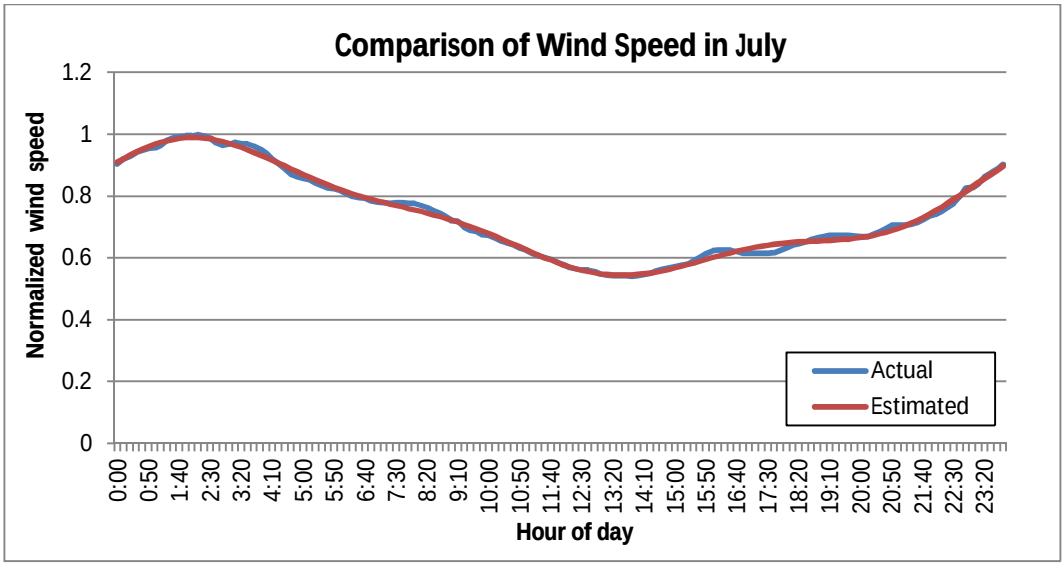

Figure 5-2 Comparison between Actual and Estimated Wind Speed including DC and 3 Harmonic components in July 2004

5.2.2. Prerequisite Condition

Prior to transforming the time domain dataset into the frequency domain, two prerequisite conditions have to be satisfied. The first condition is to check whether the time series data are stationary. When applying the DFT to a signal, we assume that the signal is stationary and that the signals in the sample continue into infinity [70]. The DFT performs poorly when this is not the case. To properly estimate all of the statistical properties in the frequency domain, the signal inside of the window of the DFT must be stationary in order that the outcome of the DFT is accurate. In this chapter, the augmented Dickey-Fuller (ADF) test is used to check the stationary [71]. In Eq. 5-7, it tests the null hypothesis of $\delta = 0$ against the alternative hypothesis of $\delta < 0$:

$$\Delta Y_t = \alpha_0 + \delta \cdot Y_{t-1} + \alpha_1 \cdot t + \sum_{i=1}^{m} \beta_i \cdot \Delta Y_{t-i} + \varepsilon_t \quad (5\text{-}7)$$

where ε_t is a white noise, α_0 is an intercept and δ, β_i, and α_1 are coefficients. Schwarz Bayesian Criterion (SBC) and Akaike Information Criterion (AIC) are used to determine the optimal lag length (m). Non-rejection of the null hypothesis implies that the series is non-stationary; whereas the rejection of the null indicates the time series is stationary. Greater detail is beyond the scope of this chapter [71]. The ADF test is performed using the wind speed data in San Gorgonio Pass during each month of 2004 and each year (2004, 2005, and 2006). Table 5-3 shows the results with optimal lag length (m) for the ADF test and corresponding test outputs. These results indicate that the data are stationary and therefore, they can be transformed into the frequency domain using DFT.

Table 5-3 Stationary Test using San Gorgonio Pass Wind Speed

	Optimal Lag	p-value	Decision
2004/01	98	0.0010	Passed Stationary Test
2004/02	96	0.0010	Passed Stationary Test
2004/03	98	0.0010	Passed Stationary Test
2004/04	97	0.0010	Passed Stationary Test
2004/05	98	0.0010	Passed Stationary Test
2004/06	97	0.0010	Passed Stationary Test
2004/07	98	0.0010	Passed Stationary Test
2004/08	98	0.0038	Passed Stationary Test
2004/09	97	0.0020	Passed Stationary Test
2004/10	98	0.0010	Passed Stationary Test
2004/11	97	0.0010	Passed Stationary Test
2004/12	98	0.0030	Passed Stationary Test
2004	181	0.0010	Passed Stationary Test
2005	181	0.0010	Passed Stationary Test
2006	181	0.0010	Passed Stationary Test

The second condition requires checking whether a band-limited signal is sampled at a rate higher than the Nyquist rate or not. If not, the shape of the Fourier transform of the sampled signal is distorted relative to the Fourier transform of the given signal. This is called aliasing [70]. The theory of Fourier transforms states that a signal of finite duration must have an infinite bandwidth in the frequency domain. However, the percentage of energy outside a certain frequency is negligibly small in Table 5-1 so that the bandwidth of a signal is practically finite in the frequency domain. Therefore, data sampled at a rate equal to twice the practical bandwidth is allowed since, in that case, the effect of aliasing will be negligible. The simple method to determine whether the given dataset is eligible to use the frequency domain approach is to check the value of the high-order harmonics. If the high-order harmonic is not negligibly small, this approach is not appropriate. In this case, the dataset must be re-sampled by raising the sampling rate. The wind speed data in this chapter are also sampled in finite duration, thus it is possible to have an aliasing error. But the high-order harmonic component is negligibly small as shown in Table 5-1.

5.2.3. Compact Frequency-Domain Representation

A compact frequency-domain representation scheme is developed that expresses any outcome in the same format. This representation reduces the complexity of the numeric outcome in the frequency domain and, further, includes all parameters created by performing the frequency domain approach. The wind pattern is described as:

$$\left(M_{peak}, S\right) \tag{5-8}$$

where

$$S = \left(K, H_{DC}, \left(H_1, \theta_1\right), \cdots, \left(H_K, \theta_K\right)\right)$$

and M_{peak} is the peak value of the period, x_{peak} in Eq. 5-1 and S is the shape descriptor. K indicates the number of harmonic components needed without losing much accuracy, $H_{DC}, H_1, \cdots, H_K$ and $\theta_1, \cdots, \theta_K$ represent the magnitudes and angles of the harmonic up to Kth harmonic respectively. Because the magnitude of harmonic is in a range between 0.0 and 1.0 with each interval 0.01 due to data normalization, it is expressed between 0 and 100 by multiplying 100 for simplicity. For the angle of harmonic only the integer value is used to represent the value between 0 and 360 degrees with each interval representing 1 degree. By connecting each parameter of shape descriptor, the compressed form is expressed as:

$$S = K - H_{DC} - H_1.\theta_1 - \cdots - H_K.\theta_K \tag{5-9}$$

The compact frequency-domain representation at San Gorgonio Pass is shown in Table 5-1. It shows that the each component in string can be independently analyzed. The results are expressed in machine-readable format so that this simple format can benefit from automated machine processing and analysis.

5.2.4. Additional Benefit

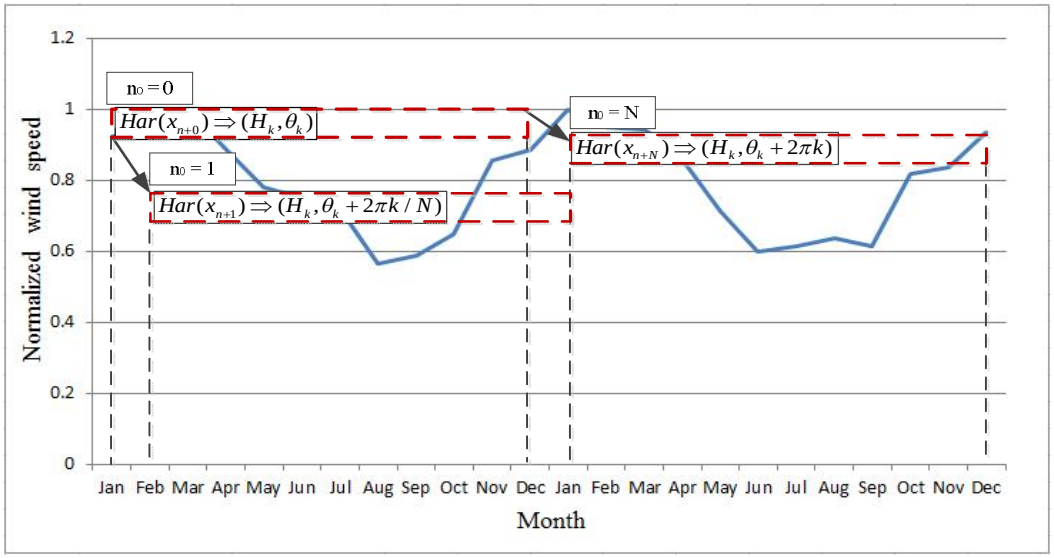

Figure 5-3 Annual Wind Speed Patterns at SanGorgonio Pass for Two Years

Table 5-4 Harmonics about the Shifted Wind Speed Patterns

	Harmonic Magnitude				Harmonic Angle		
	Current ($n_0 = 0$)	One time shifted ($n_0 = 1$)	One cycle shifted ($n_0 = N$)		Current ($n_0 = 0$)	One time shifted ($n_0 = 1$)	One cycle shifted ($n_0 = N$)
$H_{DC,n0}$	0.792	0.781	0.788	$\theta_{DC,n0}$	0	0	0
$H_{1,n0}$	0.195	0.195	0.198	$\theta_{1,n0}$	324	356	330
$H_{2,n0}$	0.028	0.025	0.024	$\theta_{2,n0}$	66	117	61
$H_{3,n0}$	0.046	0.034	0.015	$\theta_{3,n0}$	182	273	134
$H_{4,n0}$	0.011	0.015	0.030	$\theta_{4,n0}$	101	167	348
$H_{5,n0}$	0.013	0.018	0.026	$\theta_{5,n0}$	273	106	72

To show additional benefit of this approach, the annual wind speed patterns which are different time scale with this chapter are considered as shown in Figure 5-3 and the harmonics about the shifted wind speed patterns using 12 samples (N=12) are calculated in Table 5-4. If the wind speed data in the time domain is stationary, its original patterns, after noise removal, remain unchanged. Thus, the magnitude of low-order harmonics representing the original pattern is similar. However, it results in shifting the harmonic angle by DFT time-shifting property [70]. That is,

$$Har(x_n) \Rightarrow (H_k, \theta_k) \quad \text{then} \quad Har(x_{n\pm n_0}) \Rightarrow (H_k, \theta_k \pm 2\pi k n_0 / N) \tag{5-10}$$

when one cycle of the signal is shifted ($n_0 = N$), this equation states that the harmonic magnitude and angle are similar in the low-order harmonics. In this table, the harmonic magnitude and angle for the one cycle shifted patterns have values similar to the current harmonics. Using this implication, the annual wind speed patterns can be characterized by using similar low-order harmonic magnitude and angle. When one time is shifted ($n_0 = 1$), the harmonic angle in the low-order harmonics rotates in the

counterclockwise direction by the sampling angle ($2\pi k / N$). In the table, the harmonic magnitude has the similar values however, the harmonic angles have their sampling angle differences. This shows the potential to forecast future wind speed by using similar harmonic magnitude and shifted harmonic angle. In the high-order harmonics representing the noises, it is not same all the times. In this table, up to the 2nd harmonics are enough to represent the annual patterns determined by Eq. 5-6. The harmonics don't match well from 3rd harmonics. However, in the frequency domain approach, high-order harmonics are not used for characterizing and forecasting the wind speed patterns.

5.3. Characterization of Wind Speed Pattern

For a given wind location, the NREL interface provides 10-minute wind speed data [72]. The datasets for three years (2004, 2005, and 2006) are used in this analysis. The geographic location at 10 selected locations is given in Table 5-5. The investigation analyzes the inherent wind speed patterns in these locations which evenly include on-shore (LWS-1, LEN-1, LWS-2, LWS-3, and LCS-1) and off-shore (OCN-1, OEN-1, OEN-2, OEN-3, and OES-1), and current (LWS-1, LWS-2, and LWS-3) and mostly potential wind power locations (OCN-1, OEN-1, LEN-1, OEN-2, OEN-3, LCS-1, and OES-1).

Table 5-5 Information for 10 Selected Locations

No.	Location Name	Closest City/Town/Landmark	Latitude	Longitude
1	LWS-1	Altamont Pass, CA	37.81N	121.61W
2	OCN-1	Chicago, IL	42.02N	87.53W
3	OEN-1	Nantucket, MA	41.21N	69.89W
4	LEN-1	Harbor Beach, MI	43.86N	82.75W
5	OEN-2	Long Beach, NY	40.51N	73.56W
6	OEN-3	Erie ,PA	42.31N	80.28W
7	LWS-2	San Gorgonio Pass, CA	33.91N	116.77W
8	LWS-3	Tehachapi Pass, CA	35.14N	118.41W
9	LCS-1	Floydada, TX	34.06N	101.11W
10	OES-1	Weirwood, VA	37.43N	75.62W

Due to the circular nature of the harmonic angle, such directional data cannot be analyzed with commonly used statistical techniques which are used for harmonic magnitude. In circular distribution, the point 0° and 360° are identical. Circular statistics are employed in this chapter [73, 74].

5.3.1. Wind Speed Patterns during Different Times

To characterize the wind speed pattern during different times, Table 5-6 presents the compact frequency-domain representation for LEN-1 during 2004. The low-order harmonic is included only because the value of the high-order harmonic is negligibly small. All components are calculated for each day and then, the monthly mean ('1' to '12') is presented in the table. A much higher number of components (K) is observed than in the previous example, Table 5-1, which means daily wind speed has

greater fluctuation than monthly average one. Nevertheless, a lower number of components is needed in the frequency domain than in the time domain requiring all data points (144 in this case) to characterize the wind speed patterns.

Table 5-6 Compact Frequency-Domain Representations at LEN-1 during 2004

Month	M_{peak} (m/s)	Shape Descriptor (S)
1	12.545	16-72-15.242-9.296-5.321-5.125-…
2	10.682	16-69-19.329-9.006-5.344-5.081-…
3	12.456	23-67-20.254-10.056-6.082-5.139-…
4	12.468	25-63-19.275-11.260-7.265-5.046-…
5	11.978	34-57-14.299-11.024-7.222-5.105-…
6	10.347	27-65-12.319-11.128-6.241-5.090-…
7	9.899	28-63-17.326-11.129-7.267-5.121-…
8	10.51	26-62-14.311-11.143-6.282-6.078-…
9	10.431	20-64-19.318-9.121-6.174-6.037-…
10	11.463	18-67-15.311-10.015-6.006-4.179-…
11	11.412	18-68-16.297-10.299-6.295-4.069-…
12	13.476	23-70-17.088-10.193-6.019-4.135-…

A similar number of components are observed to be approximately 23. A consistent pattern in the harmonic magnitude is also observed. For example, the DC ranges from 0.57 to 0.72, the 1st harmonic magnitude ranges from 0.12 to 0.20, and 2nd harmonic magnitude ranges from 0.09 to 0.11. The narrow range for the harmonic magnitude indicates high consistency. In the case of the harmonic angle, it is not as obvious with harmonic magnitude but the low-order harmonic angle has little variation. For example, the 1st harmonic angle ranges from 242° to 88° with a mean equal to 339°.

Furthermore, some seasonal patterns are captured. During the summer (June-August), a greater number of components are observed. This indicates that the wind speed curve fluctuates more during the summer than during the winter (December-February). Also, smaller DC and 1st harmonic magnitude are observed in summer. However, the 2nd harmonic magnitude shows the opposite trend from DC and 1st harmonic in this location. With the harmonic angle, it is observed that summer has a similar harmonic angle value in all harmonics compared to winter. This seasonal pattern is also observed by the analyses in other years.

5.3.2. Wind Speed Patterns at Different Geographic Locations

To characterize the wind speed patterns at different geographic locations, all components are calculated for each day and then the three year average (2004, 2005, and 2006) of these daily components at 10 selected locations are compared in Table 5-7.

Table 5-7 Compact Frequency-Domain Representations at 10 Locations by Using the Average for Three Years (2004, 2005, and 2006)

Month	M_{peak} (m/s)	Shape Descriptor (S)
LWS-1	11.620	33-57-24.254-10.253-7.043-5.132-…
OCN-1	13.608	28-62-18.336-10.069-6.349-5.183-…
OEN-1	15.128	28-63-19.039-10.175-6.052-5.122-…
LEN-1	11.149	23-66-16.304-10.159-6.263-5.120-…
OEN-2	14.870	30-60-19.004-10.030-7.125-5.191-…
OEN-3	13.595	32-61-18.050-11.175-7.302-6.124-…
LWS-2	11.731	25-64-19.339-9.262-6.276-5.273-…
LWS-3	12.344	25-62-21.340-10.035-7.237-5.290-…
LCS-1	14.107	28-66-19.250-9.281-6.176-4.298-…
OES-1	14.365	34-60-19.359-11.144-7.024-5.108-…

A similar number of components are observed to be approximately 29. A consistent pattern in the harmonic magnitude is also observed; the range of DC around 0.62±0.05, 1st harmonic magnitude around 0.19±0.05, 2nd harmonic magnitude around 0.10±0.01. With the harmonic angle, it is not as obvious as harmonic magnitude but the low-order harmonic angle has little variation. For example, the 1st harmonic angle ranges from 250° to 50° with a mean equal to 338°. The narrower ranges in both harmonic magnitude and angle are observed in the analysis at different locations than in the analysis during different times. This suggests that the wind speed patterns at different locations have more consistent patterns in the frequency domain.

Furthermore, the geographical wind speed patterns can be captured using harmonic components. The smallest number of components is required in LEN-1 but the largest in OES-1. This indicates that the wind speed curve in LEN-1 is more stable than the others and, on the other hand, the curve in OES-1 has greater variability than the others. LCS-1 and LEN-1 have the highest DC value indicating highest wind speed average and, contrarily, a lower DC value is observed in LWS-1. Furthermore, each harmonic component represents the variability in a day. For example, the 1st harmonic explains 1 cycle variation per day and the 2nd harmonic represents 2 cycle variations per day and so on. The highest 1 cycle/day variation is observed in LWS-1 and the lowest in LEN-1. In other words, when considering only 1st harmonic components, the difference between max and min wind speed in a day is larger in LWS-1. For the 2nd harmonic, the difference of the magnitude between locations is very small so that the 2 cycle/day variation is similar in these locations.

5.4. Analysis of Wind Speed Pattern

5.4.1. Shape Consistency over Time

The shape descriptors during three years at LEN-1 are shown in Table 5-8. Harmonic components are calculated for each day and then, the annual average is presented. Similar values are observed for three years. DC (=0.66) and 1st (=0.16), 2nd (=0.10), 4th (=0.05), and 5th (=0.04) harmonic magnitude has same

values for three years. Even with the 3rd harmonic magnitude, it has only 0.01 difference in 2006 compared with other years. This shows that it can capture the common pattern readily and the observed patterns are well matched in the harmonic magnitude. In the case of the harmonic angle, it is not as obvious as with harmonic magnitude but it also has similar patterns in low-order harmonic. The harmonic is the combination of magnitude and angle. Even though the harmonic angle has a smaller consistency in the high-order harmonic, it has little value in harmonic magnitude indicating less effect on harmonic.

Table 5-8 Shape Descriptor at LEN-1 during 2004, 2005, and 2006

Year	Shape Descriptor (S)
2004	23-66-16.307-10.116-6.284-5.096-4.275-…
2005	23-66-16.304-10.169-6.283-5.141-4.256-…
2006	24-66-16.294-10.171-7.222-5.130-4.258-…

These observations indicate the potential to forecast future wind speed patterns in frequency domain using their historical patterns. These trends are also observed through analysis in different locations.

5.4.2. Certainty of Harmonic Patterns

For harmonic magnitude, the Coefficient of Variation (CV) is used. The CV is the ratio of the standard deviation σ_H to the mean μ_H representing a normalized measure of dispersion. It is a useful statistical measurement for comparing the degree of variation between datasets when the means are different from each other:

$$c_H = \frac{\sigma_H}{\mu_H} \tag{5-11}$$

The circular variance is used to evaluate the certainty of the harmonic angle. Circular variance provides a measure of how widely a set of directional data is spread. The value of the circular variance varies from 0.0 to 1.0, with the lower the value the higher the clustering of the values about the mean.

Table 5-9 CV and Variance for the Major Harmonic Components at LEN-1 during 2004

Month	CV				Variance		
	H_{DC}	H_1	H_2	H_3	θ_1	θ_2	θ_3
1	0.134	0.502	0.502	0.642	0.820	0.858	0.865
2	0.157	0.514	0.492	0.513	0.770	0.922	0.806
3	0.157	0.463	0.450	0.537	0.897	0.867	0.945
4	0.159	0.434	0.493	0.462	0.765	0.938	0.829
5	0.203	0.495	0.476	0.422	0.756	0.847	0.672
6	0.173	0.485	0.636	0.577	0.751	0.556	0.790
7	0.129	0.485	0.451	0.560	0.682	0.694	0.759
8	0.161	0.519	0.560	0.463	0.612	0.562	0.646
9	0.161	0.432	0.509	0.550	0.446	0.715	0.919
10	0.165	0.582	0.484	0.587	0.706	0.795	0.922

11	0.138	0.488	0.482	0.605	0.757	0.919	0.883
12	0.151	0.499	0.454	0.578	0.924	0.880	0.714

Table 5-10 CV and Variance for the Major Harmonic Components at 10 locations by Using the Average for Three Years (2004, 2005, and 2006)

Location	CV				Variance		
	H_{DC}	H_1	H_2	H_3	θ_1	θ_2	θ_3
LWS-1	0.230	0.402	0.521	0.605	0.472	0.726	0.851
OCN-1	0.195	0.482	0.556	0.566	0.707	0.878	0.965
OEN-1	0.184	0.486	0.530	0.578	0.819	0.837	0.957
LEN-1	0.170	0.506	0.533	0.545	0.831	0.866	0.891
OEN-2	0.195	0.459	0.532	0.555	0.630	0.846	0.887
OEN-3	0.203	0.477	0.534	0.574	0.823	0.807	0.915
LWS-2	0.232	0.536	0.639	0.623	0.662	0.928	0.785
LWS-3	0.202	0.467	0.558	0.586	0.543	0.852	0.896
LCS-1	0.179	0.457	0.565	0.604	0.594	0.865	0.923
OES-1	0.209	0.456	0.544	0.565	0.820	0.937	0.860

The CV of the major harmonic magnitude and variance of the major harmonic angle are presented in Table 5-9 at LEN-1 during 2004 and in Table 5-10 at 10 locations by using the three year average. The average of the major harmonic components and their compact frequency-domain representations are already given in Table 5-6 at LEN-1 during 2004 and Table 5-7 at 10 locations for three years. Figure 5-4 shows the CV during different times and at different locations in the time domain. The CV is calculated using their mean and standard deviation at each time point.

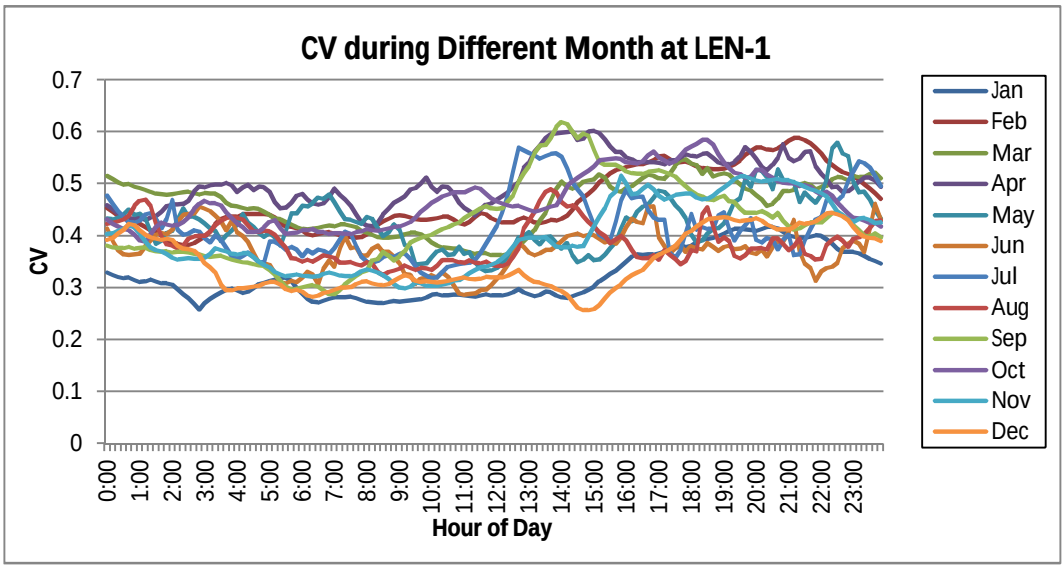

(a) CV in Time Domain during Different Month at LEN-1

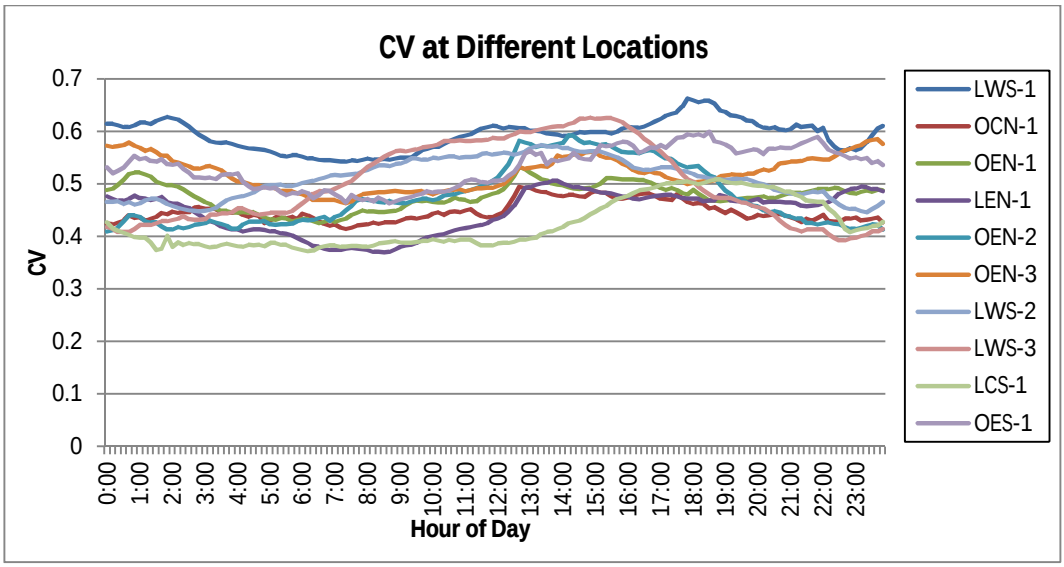

(b) CV in Time Domain at 10 Selected Locations

Figure 5-4 Plots of CV in Time Domain during Different Times and at Different Locations

In the frequency domain, most of the CV of the DC is less than 0.20 which is much smaller than the time domain. The CV for the rest of the harmonic is similar to the CV in the time domain but since the CV is in inverse proportion to the mean, the mean of the harmonic is much smaller than DC so that the impact of these increased levels of uncertainty is correspondingly smaller. Furthermore, the narrow range of CV is observed; DC around 0.16±0.03, 1st harmonic magnitude around 0.50±0.06 in Table 5-9 and DC around 0.20±0.03, 1st harmonic magnitude around 0.47±0.02 in Table 5-10. These ranges are much smaller than in the time domain; 0.42±0.18 in Figure 5-4 (a) and 0.49±0.15 in Figure 5-4 (b).

The smaller CV and its range indicate the higher certainty of the results. It will be easier to characterize the wind speed pattern in the frequency domain by taking advantage of a small number of components that are needed to represent the patterns with significant magnitude values and its high certainty of the results.

Unlike the harmonic magnitude, a higher value of the circular variance is observed, indicating a lower degree of certainty of the information. The value of the circular variance increases as the order of harmonics increase. Although the proposed approach can capture their harmonic magnitude patterns very well, further research is needed into the harmonic angle to improve the quality of the results in the frequency domain.

5.4.3. Shape Consistency over Locations

The results described thus far provide point estimation. These estimations give only a suggestion of the average characteristics of wind speed. Knowing not only the expected average characteristics, but also the uncertainty of results is important. In other words, it is necessary to know the extent of uncertainty the results can have. In this manner, the Uncertainty Range (UR) of the results is calculated as:

$$UR = \mu \pm \mu \times CV = \mu \pm \sigma \tag{5-12}$$

Figure 5-5 shows the average and its UR up to 2nd harmonic magnitude at 10 locations. Similar average of the harmonic magnitude among different locations is observed; DC is around 0.6, 1st harmonic magnitude is approximately 0.2, and 2nd harmonic magnitude is around 0.1. Furthermore, the UR in the 2nd harmonic magnitude is well overlapped at different locations. Even for the DC and 1st harmonic magnitude, the UR is partially overlapped. It means that the locations can have similar harmonic magnitudes by using the frequency domain approach even if they are located geographically far from each other, or located in on-shore or off-shore.

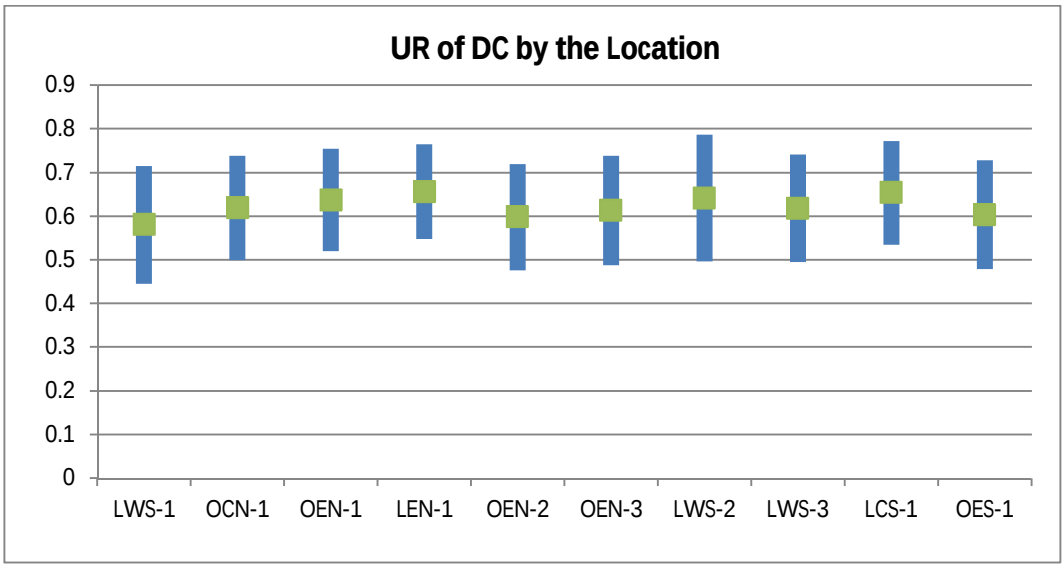

(a) Uncertainty of DC at 10 Locations

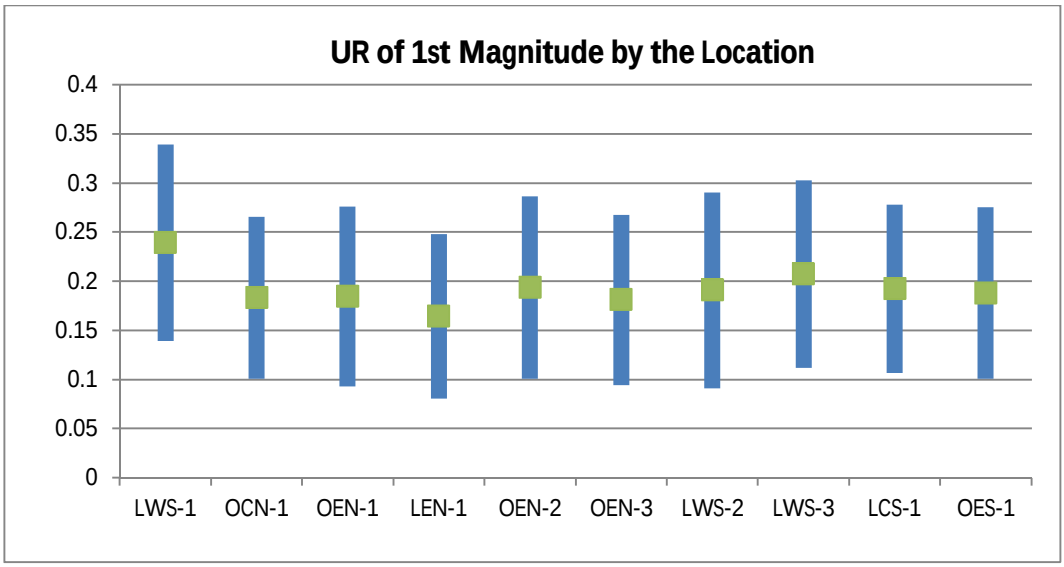

(b) Uncertainty of 1st Harmonic Magnitude at 10 Locations

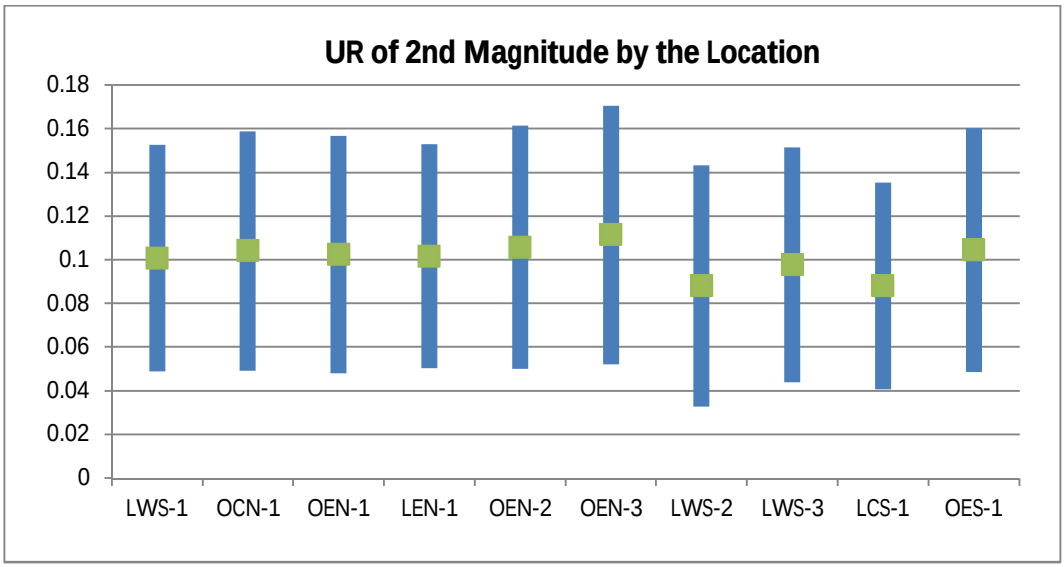

(c) Uncertainty of 2nd Harmonic Magnitude at 10 Locations

Figure 5-5 Uncertainty Quantification of Harmonic Magnitude at 10 Locations during 2004

These observations indicate the potential to estimate wind speed patterns at the new location with no physical measurements using available site data.

5.5. Conclusion

First, this chapter presents the methodology for the analysis and characterization of wind speed patterns in the frequency domain using DFT. It has shown that the dataset used is suitable for the frequency domain approach by satisfying its prerequisite conditions: 1) the wind speed dataset is

stationary; 2) their effect of aliasing is negligible. This chapter demonstrates that the time domain datasets can be transformed into frequency domain as a set of frequency components.

Second, compact frequency-domain representation is introduced. It has shown that its machine-readable format facilitates automated large-scale processing of wind speed data.

Third, this chapter proposes that wind speed patterns during different times can be characterized using the compact frequency-domain representation. A consistent pattern in shape descriptor is observed: similar number of components, harmonic magnitude, and harmonic angle during different months. In addition, it also allows for the capture of seasonal patterns. Such consistent and seasonal patterns help to estimate the wind speed patterns during different times in one location.

Fourth, this chapter also proposes that wind speed patterns at different geographic locations can be characterized using the compact frequency-domain representation. The shape descriptor has not only a similar value but also a narrower range of the values than the patterns during different times, which result in greater consistency. In addition, it allows for the capture of geographical wind speed patterns. Such consistent and geographical patterns help to estimate the wind speed patterns at different locations.

Finally, the chapter presents the major findings from analyzing the statistical results of the major harmonic components during different times and at different geographic locations: (1) the consistent harmonic component patterns for three years are captured. It shows a potential to forecast future wind speed patterns using historical data, (2) this approach is able to characterize wind speed patterns with higher certainty information of major harmonic components, (3) the UR is introduced to determine the level of uncertainty that the results can have. Similar UR in major harmonic components is obtained no matter how distant the locations are from each other, or whether the locations are in on- or off-shore. It shows the potential to estimate wind speed patterns for a new location using available site data.

The results of harmonic magnitude offer the benefit of characterizing and analyzing wind speed patterns but the results of harmonic angle show relatively less benefit. Further research is needed to be able to utilize the harmonic angle to improve the quality in the frequency domain. Furthermore, not only the shape descriptor (S) but also the max wind speed of the patterns (M_{peak}) in compact frequency-domain representation is needed to fully describe the patterns in the time domain. However, the shape of the patterns only is discussed in this chapter. Knowing the max wind speed is important in order to estimate and forecast wind speed patterns in the time domain. Thus, additional research concerning

estimating and forecasting the shape (S) and max wind speed (M_{peak}) of the patterns will be presented in the next using the frequency domain approach.

Chapter 6 Coordinated Control of Automated Devices and Photovoltaic Generators for Voltage Rise Mitigation in Power Distribution Circuits

6.1. Introduction

PV power generation is a rapidly growing renewable energy source, and is regarded as an appealing alternative to conventional power generated from fossil fuel. This has led to efforts to increase PV generation levels in the U.S. [10]. Although the integration of PV brings many advantages, high penetration of PV provides challenges in power system operations, mainly due to its uncertain and intermittent nature.

Among the various technical challenges under high PV penetration, voltage rise problems caused by reverse power flows are one of the foremost concerns [75]. The voltage rises due to the PV generation. Furthermore, the need to limit the voltage rise problem limits PV generators from injecting more active power into the distribution network. This can be one of the obstacles to high penetration of PVs into circuits.

Voltage control of PVs is studied in [44, 76]. These papers demonstrate the voltage control capability of the PV. PVs can use both active and reactive power injection for control. Based on this capability, many PV control strategies are presented in [45-53]. In [45-47], the reactive power injection of the PV is used to reduce voltage deviations caused by large PV penetrations. The control strategy minimizes circuit losses while maintaining the voltage within limits in [48-51]. An active curtailment strategy to reduce PV power injection is used to prevent voltage violations in [52, 53].

It is important to coordinate PV control with other controllable, automated devices, such as capacitor banks and voltage regulators. Optimal control of the automated devices is able to not only reduce circuit loss, but also improve the voltage profile [77, 78]. In these papers, different automated devices are coordinated to find optimal dispatch schedules.

This chapter introduces a control algorithm for maintaining the average customer voltage profile obtained before introducing the PV into the circuit. The control of automated devices, such as voltage regulators and switched capacitor banks, defines the optimal operating point or schedule by minimizing the circuit loss while simultaneously reducing the motion of the automated devices without considering

the PV. Then, the PV is controlled to maintain this operating point by controlling the active and reactive power. This is implemented with a centralized control algorithm which provides setpoints to both the automated devices and PVs that need to be adjusted [79, 80].

To evaluate the performance of the control algorithm, three penetration scenarios are considered, 10%, 20%, and 30% PV penetration into the distribution circuit. First, system effects due to the addition of PV are analyzed without the proposed coordinated control. Then, these effects are compared with those of using the coordinated control to show the effectiveness of the control.

The chapter is organized as follows. Section 6.2 presents the control strategy of the automated devices and the PV. In Section 6.3 the system effects due to the addition of large PV are analyzed for baseline conditions. In Section 6.4 the proposed control is analyzed. Its effectiveness is shown by comparing the results with the baseline conditions of Section 6.3. Finally, findings of the study are summarized in Section 6.5.

6.2. Control Strategy

The main objective of the control is to maintain the optimum operating profiles of the circuit established by automated devices without PV generation. Automated devices considered here are voltage regulators and switched capacitor banks. Then, the voltage profile of the circuit should not change when PV generation is introduced into the circuit. Thus, the PVs are controlled to maintain the optimal operating schedule established by the automated devices.

6.2.1. Control of Automated Devices

The objectives of the automated device control are to reduce the customer level voltage deviation from the desired value while minimizing the steps of the automated devices, and then to minimize the circuit loss. The control of the automated devices uses an iterative approach which involves adjusting the controllable single-step devices (switched shunt capacitors) and multiple-step devices (voltage regulators) to find the best operating point, as illustrated in Figure 6-1.

The total steps of the automated devices (M_n) are calculated by:

$$M_n = \sum_{k=1}^{K} m_{n,k} \tag{6-1}$$

where K is the total number of controllable automated devices and $m_{n,k}$ are the steps of device k at time n with the following constraint:

$$T_{n,k}^{\min} \le T_{n,k} \le T_{n,k}^{\max} \tag{6-2}$$

where $T_{n,k}$ is the step, and $T_{n,k}^{\min}$ and $T_{n,k}^{\max}$ are the limits of the step position. First, the number of possible steps having the same number of controllable device total steps (M_n) is calculated. The algorithm then selects the automated devices having the minimum total steps.

After the step positions (T_n) of the devices are determined, the average customer voltage throughout the circuit (V_n), the total steps of the devices (M_n), and the circuit loss (L_n) are calculated. The first priority is to maintain the average customer voltage (V_n) within a range of desired values ($V_{ref,n}$). The voltage deviation is calculated by:

$$\left|V_n - V_{ref,n}\right| < V_{tol,n} \tag{6-3}$$

where V_n is the average customer voltage of all customers ($V_n = avg\left(\sum v_{i,n}\right)$) and $V_{tol,n}$ is the acceptable voltage deviation at time n. This is defined as +/- 0.2% of the desired voltage ($V_{ref,n}$) in this chapter. In terms of volts it is +/- 0.24V, where the desired voltage is 120V. ANSI C84.1 provides a guideline for voltage variations from 114 V to 126 V [54]. In the work here a much smaller voltage variation is used for the average voltage limit.

The second priority is to minimize the steps taken by the automated devices. Some of the large number is used for the initial minimum total steps. The total steps (M_n) of the devices in Eq. 6-1 are compared with the saved minimum total steps ($M_{\min,n}$) as:

$$M_n \le M_{\min,n} \tag{6-4}$$

If the total steps are equal to or less than the saved minimum, the algorithm goes to the next step.

Lastly, it tries to reduce the circuit loss. The circuit loss is calculated as:

$$L_n = \sum \sqrt{P_{Loss,i,n}^2 + Q_{Loss,i,n}^2} \tag{6-5}$$

where $P_{Loss,i,n}$ is the real power loss and $Q_{Loss,i,n}$ is the reactive power loss of each component.

If the coordinated control algorithm finds a better operating point, it saves the results. Furthermore, if there are any possible steps having the same total steps, it goes to the first step to change the step of the devices. If the optimal operating point is not acquired in the same total steps, the total steps are increased.

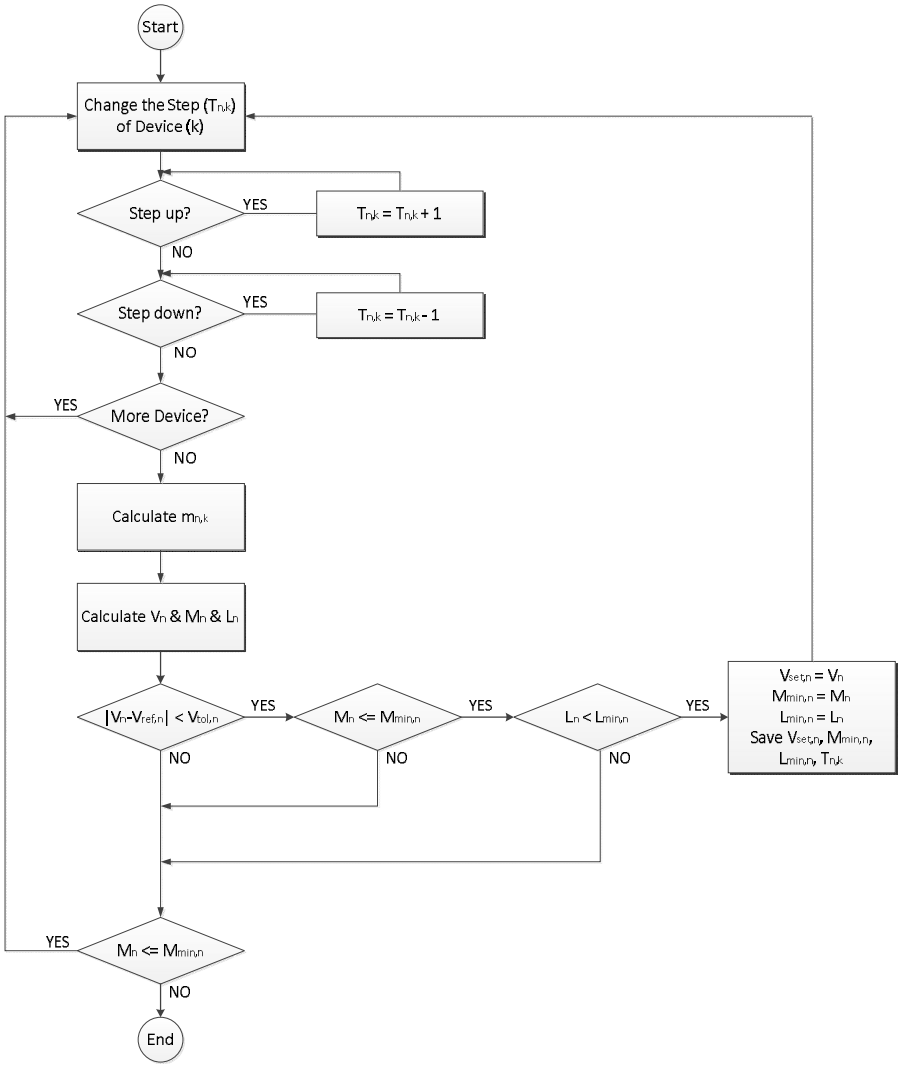

Figure 6-1 Flowchart of automated device control

6.2.2. Control of PV

The main objective of the PV control is to maintain the operating schedule or profiles established by the automated devices. The PV control algorithm uses an iterative approach by adjusting the power

factors of the controllable PV to reduce the customer level voltage deviations from the desired values ($V_{set,n}$). The PV control algorithm is illustrated in Figure 6-2.

If the set point of the desired customer voltage is greater than the current voltage, the power factor is adjusted to supply reactive power. Otherwise, the power factor is adjusted to consume reactive power. The algorithm first changes the power setpoint by increasing or decreasing it by steps of 0.1. Then, if the average customer voltage is within +/- 0.2% of the desired value, it tries to change the power factor by 0.01 steps with the following constraint:

$$PF_n^{\min} \le PF_n \le PF_n^{\max} \tag{6-6}$$

where PF = power factor.

After the power factors of all PVs are determined, the algorithm calculates the average customer voltage for the circuit (V_n). The objective is to reduce the voltage deviation from the desired set point ($V_{set,n}$) established by the automated devices. Next the voltage deviation is compared with the saved minimum deviation ($dV_{\min,n}$) as:

$$\left|V_n - V_{set,n}\right| < dV_{\min,n} \tag{6-7}$$

If the algorithm finds a better power factor for the controller, it saves the results. The algorithm then returns to the start to change the power factor of the PV and begin a new iteration. One hundred iterations are used as the maximum in this work. It should be noted that the power factor setpoints vary from one PV to another.

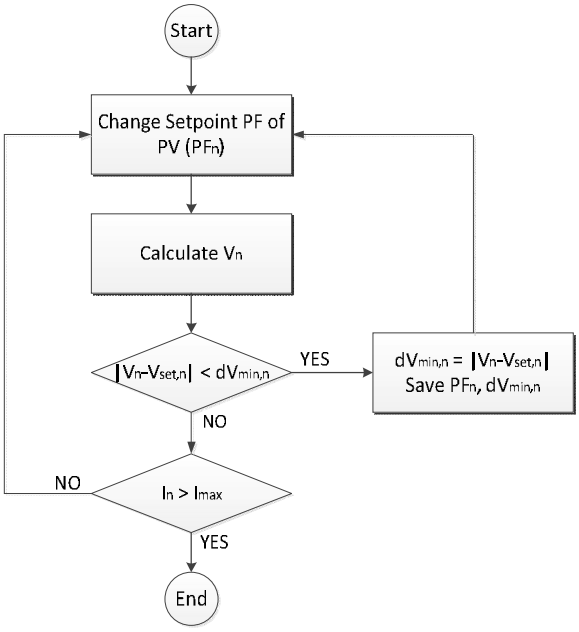

Figure 6-2 Flowchart for coordinated PV control

6.2.3. Control of Automated Devices and PVs

The overall control algorithm, including automated devices and PVs, is illustrated in Figure 6-3. The algorithm first finds the optimal operating schedule without considering the PV. In doing this it disconnects the PVs from the circuit. The algorithm then discovers all automated devices on the circuit. Once the PV are disconnected and the available automated devices are discovered, the initial average customer voltage ($V_{ref,n}$) is calculated. This initial value is used to find a better operating point by adjusting the automated devices as described in Section 6.2.1. When the solution is accepted, the new operating points ($V_{set,n}$), total number of device steps ($M_{\min,n}$), the circuit loss ($L_{\min,n}$), and the step of the automated devices (T_n) are obtained.

The algorithm then reconnects all PV to their original status and discovers all controllable PV on the circuit. That is, PVs that operate autonomously are not included in the controllable PV. Once the controllable PV are discovered, the step (T_n) previously calculated for the automated devices are implemented. Then, as PV generation is introduced, the PV control algorithm works to reduce the customer level voltage deviations from the desired value ($V_{set,n}$) by adjusting the power factors of the controllable PVs. When a solution is obtained, the power factor of the PV (PF_n) and the voltage deviation ($dV_{\min,n}$) from the desired value ($V_{set,n}$) are obtained.

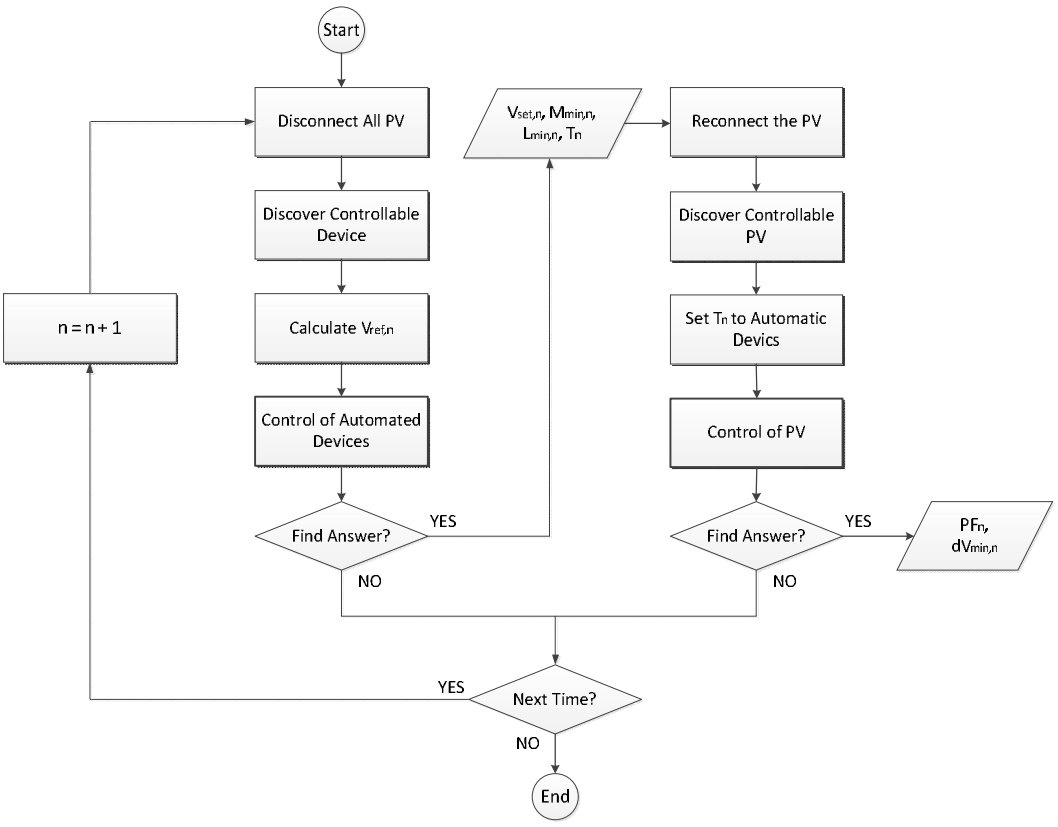

Figure 6-3 Flow chart of overall coordinated control

6.3. Effects of PV without Coordinated Control

To evaluate the performance of the coordinated control, different PV levels of adoption are analyzed. As more and more PV are connected to the circuit, the circuit voltages deviate further from nominal values. In this section the effects of various PV penetration levels are investigated without the coordinated control. This will establish a baseline condition that will be used in evaluating the coordinated control.

6.3.1. Test Circuit

The distribution circuit to be analyzed is shown in Figure 6-4. The circuit model is derived from actual data for a circuit in Michigan. It is a 13.2kV, Y-connected circuit with 2751 residential customer and 111 industrial customers. The time varying customer loads are estimated from averaged hourly SCADA measurements, hourly customer kWh load data, and monthly kWh load data processed by load research statistics to create hourly loading estimates for each customer [3, 4].

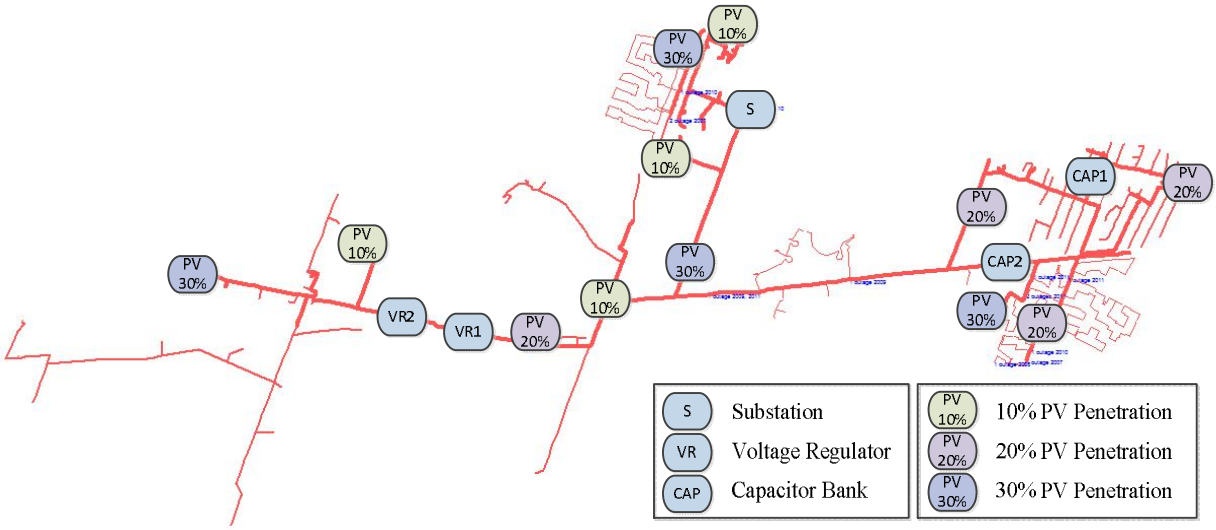

Figure 6-4 Distribution circuit to be analyzed

Representative circuit daily load profiles during winter (January 30) and summer (July 15) are shown in Figure 6-5. These hourly profiles are used in the simulation studies performed here. Due to heavy residential loading the circuit peaks late in the day, with the annual peak occurring during the summer.

The circuit contains two sets of voltage regulators and switched shunt capacitors as shown in Figure 6-4. The voltage regulators operate based on voltage control using a 124 V base, +/- 1.0 volt bandwidth, and +/- 16 steps. The switched shunt capacitors operate based on voltage control with specified turn on and turn off voltage limits.

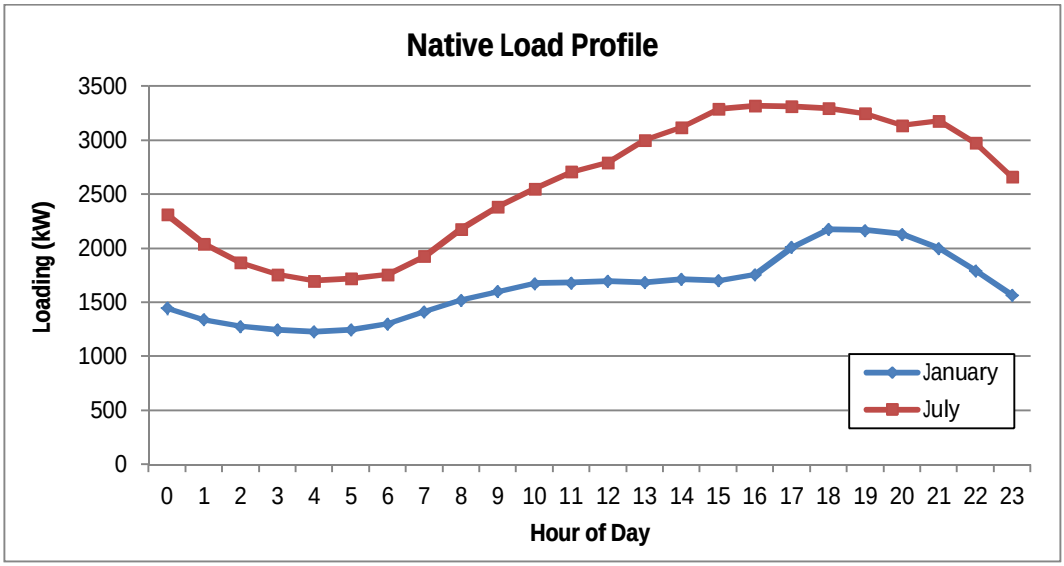

Figure 6-5 Native load profile at the substation during winter and summer

For the simulation of the PV control, 1000 kW PV generators are considered. Time-varying PV generation data are imported via the Internet using the IMBY application from the NREL [1]. For a given geographical location and size, the NREL interface provides hourly PV generation data for an entire year. The hourly PV generation profile obtained from the NREL interface for a representative day during winter and summer at a selected location on the circuit is shown in Figure 6-6. It is found that the generation during winter is noticeable less than summer at this location.

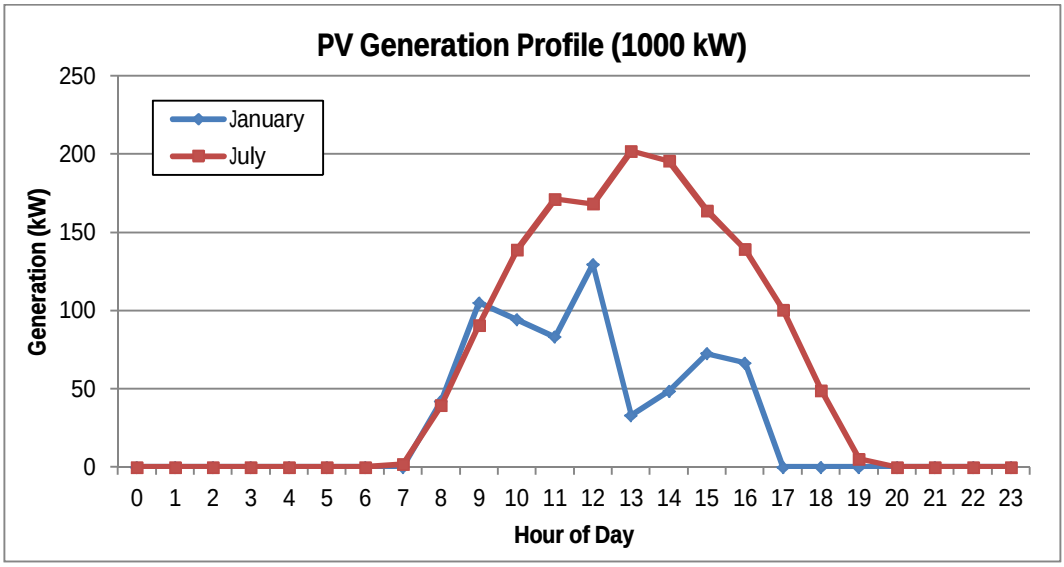

Figure 6-6 PV generation profile during winter and summer

To analyze PV penetration into the circuit, three penetration scenarios, 10%, 20%, and 30%, are considered here. The penetration level refers to the proportion of a power source on a system. There are several ways that this can be calculated [81]. In this chapter, the penetration is defined as the nominal capacity of a power source divided by peak demand. The nominal capacity of a PV generator is the expected generation from the PV. The following equation is used to calculate the PV generation required associated with each of the penetration levels:

$$PV_{Rating} = \frac{Max(P_{Demand}) \times 3}{CF} \times l_{penetration} \tag{6-8}$$

where $l_{penetration}$ is the penetration level of PV, $Max(P_{Demand})$ is the maximum electric demand (kW), and CF is the PV capacity factor representing the ratio between the actual generation and the generation rating (%). In this study a 25% capacity factor (CF) is used. Based on the above calculation, 4 PVs, 8 PVs, and 12 PVs, each with a 1000 kW rating, are randomly placed in the circuit for testing the 10%, 20%, and 30% penetration scenarios, respectively [25]. The locations of the PVs for the various penetration

scenarios are shown in Figure 6-4. Note that the 20% penetration scenario includes the generation for the 10% penetration scenario, and similarly for the 30% penetration scenario.

6.3.2. Baseline Investigation

Since the objective of the coordinated control is to reduce the average customer voltage deviation and to minimize the circuit loss, these aspects are investigated in this section to establish baseline conditions that exist without the coordinated controller. In this section the PV operate autonomously. Currently, the PVs in this circuit are operated with unity power factor.

a) Average Customer Voltage

Figure 6-7 shows the average customer voltage in January for the various PV adoption scenarios. In this figure, the voltage rise due to the PV generation occurs from 8 AM to 4 PM. The deviation is larger when the PV penetration increases. The maximum voltage deviations from the average customer voltage without PV are 0.13V, 0.71V, and 1.04V for 10%, 20%, and 30% penetrations, respectively.

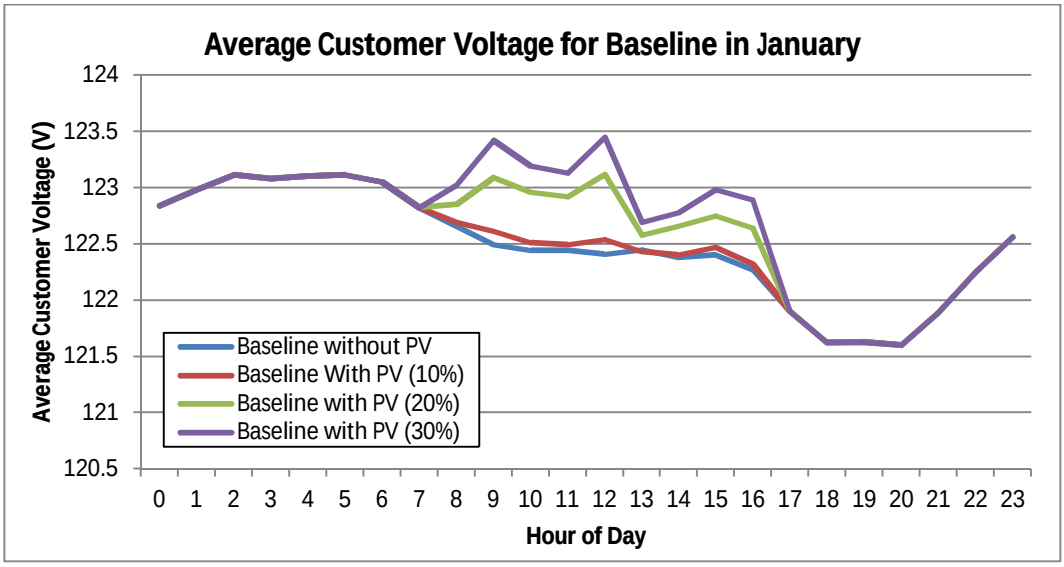

Figure 6-7 Average customer voltage in January for baseline

Figure 6-8 shows the average customer voltage in July for the various PV adoption scenarios. The voltage rise due to the PV generation is observed from 8 AM to 7 PM. The voltage deviation in the summer is larger than in the winter. The maximum voltage deviations are 0.25V, 1.10V, and 1.49V for 10%, 20%, and 30% penetrations, respectively.

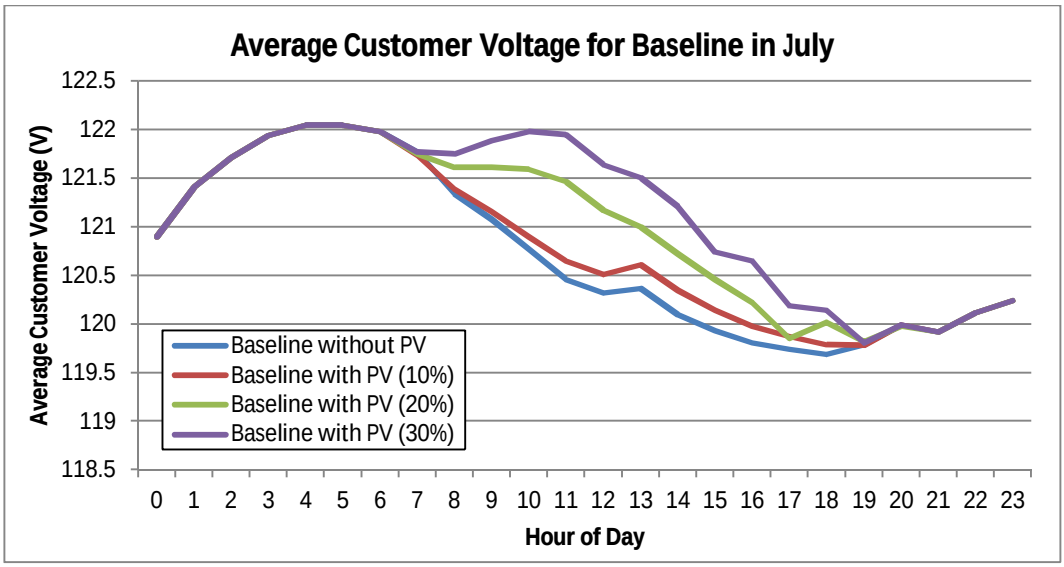

Figure 6-8 Average customer voltage in July for baseline

b) Circuit Loss

Figure 6-9 shows the real and reactive time-varying power losses in January for the case with no PV and then for the scenarios when PV are adopted into the circuit. In general, the circuit loss decreases for 10% PV adoption, and then decreases further for 20% PV adoption, but then starts to increase with 30% PV adoption. These trends also occur in July as illustrated in Figure 6-10. The results shown here are used to evaluate the performance of the coordinated control in the next section.

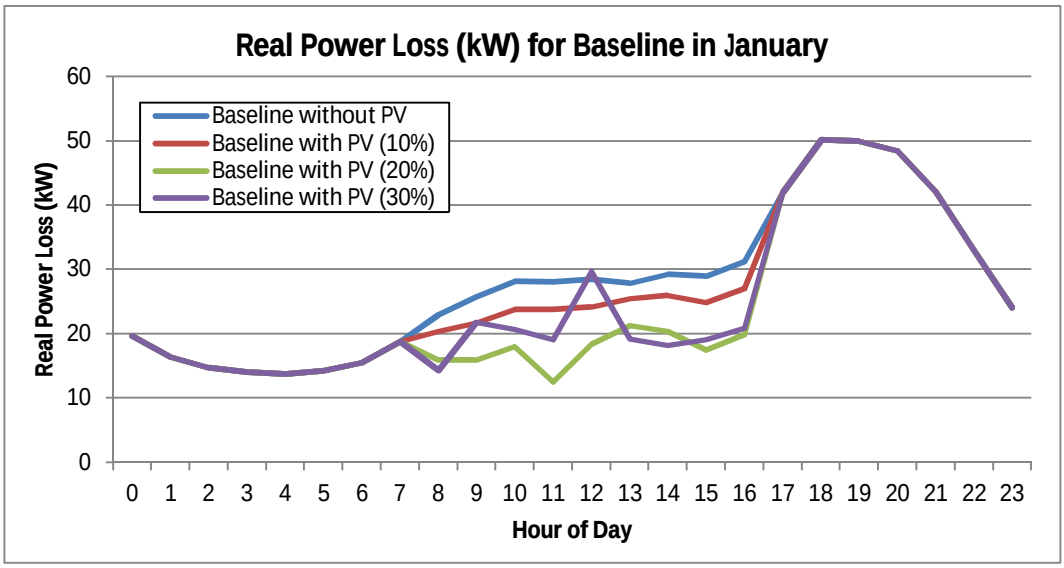

(a) Real power loss (kW)

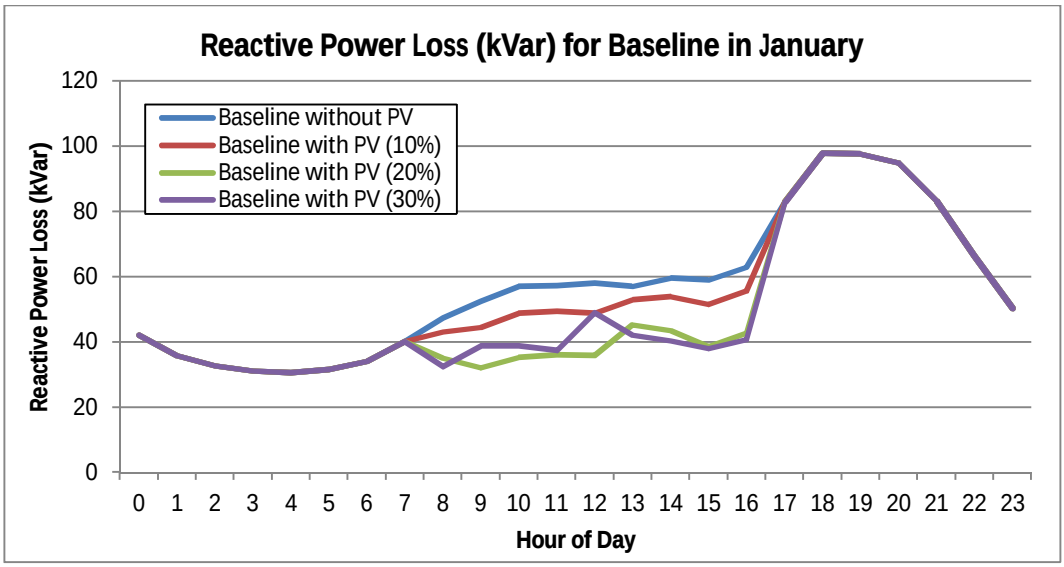

(b) Reactive power loss (kVar)

Figure 6-9 Circuit losses in January for baseline

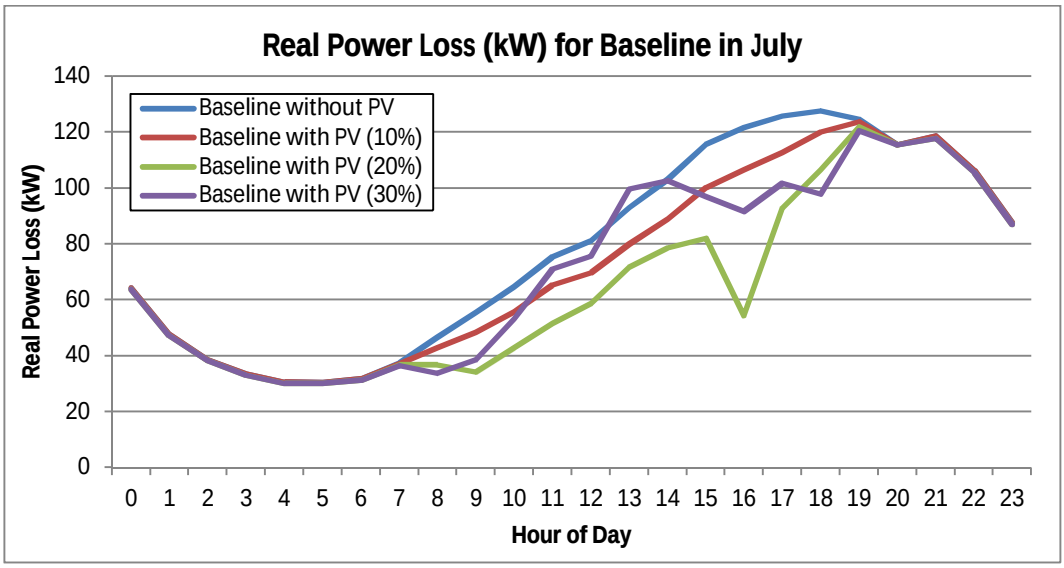

(a) Real power loss (kW)

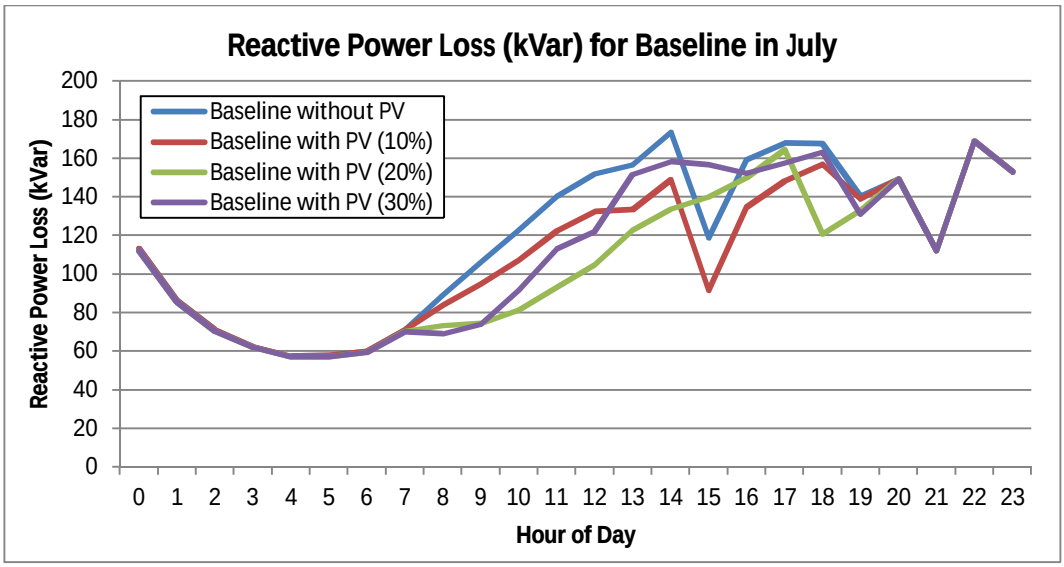

(b) Reactive power loss (kVar)

Figure 6-10 Circuit loss in July for baseline

6.4. Evaluation of Coordinated Control

In this section, the performance of the coordinated control is compared with the baseline conditions established in Section 6.3. First the automated devices used to implement the optimal operating schedule without PV in the circuit are evaluated. The performance of the automated device control is compared to the baseline conditions before PV is adopted into the circuit. Then, the performance of the coordinated PV control is evaluated for the various PV adoption scenarios.

6.4.1. Evaluation of Coordinated Automated Device Control

a) Average Customer Voltage

Figure 6-11 and Figure 6-12 show the average customer voltage obtained from the coordinated, automated device control without considering PV in January and July, respectively. The average customer voltage is calculated to reduce the circuit loss and minimize the automated device controller motion. In these figures, the average customer voltage is similar to the normal operating conditions before adopting the PV into the circuit in both January and July. The voltages ($V_{set,n}$) calculated here are used as inputs to the coordinated PV control. In summary, the automated device control maintains the average customer voltage within allowable ranges while reducing losses and minimizing device steps.

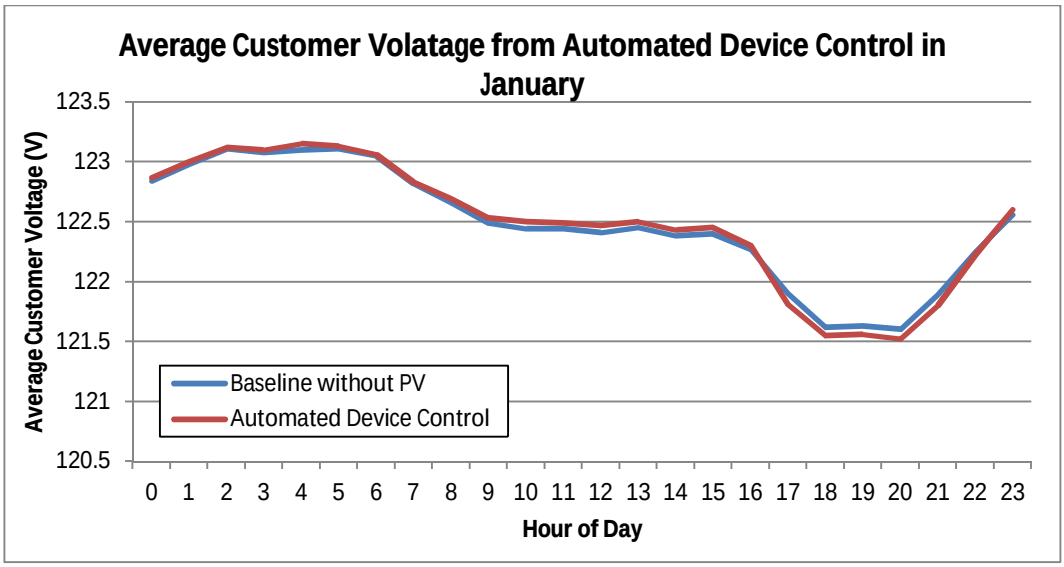

Figure 6-11 Comparison between coordinated automated device control and baseline of average customer voltage in January without PV

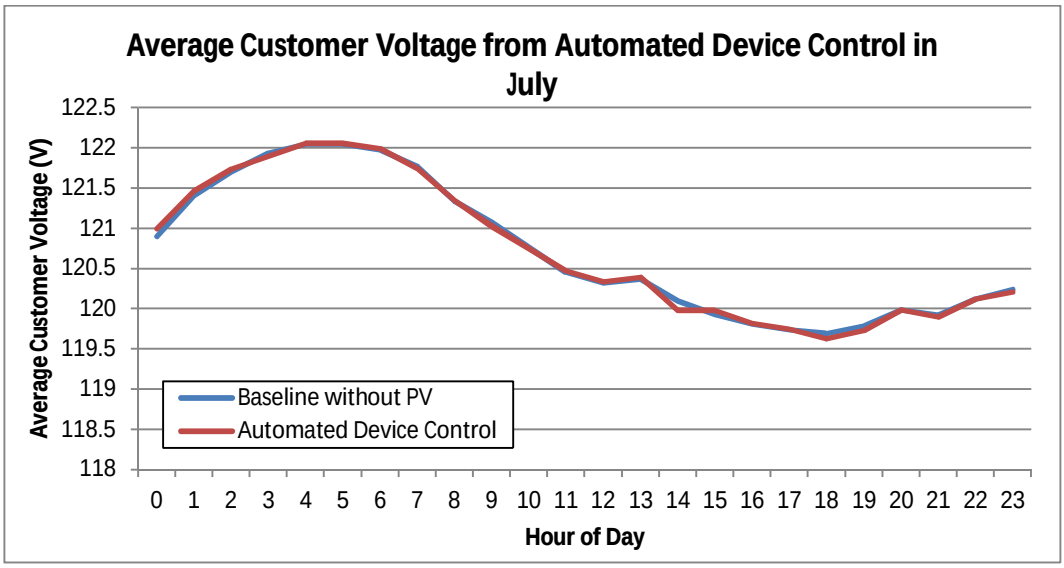

Figure 6-12 Comparison between coordinated automated device control and baseline of average customer voltage in July without PV

b) Circuit Loss

Figure 6-13 shows the reduction of real and reactive circuit losses from the automated device control in January. It should be noted that the reduction of the real power loss is greater when the reduction of the reactive power loss is less. The reduction of the reactive power loss is maximized during the first half of the day, and the reduction of the real power loss is maximized during the last half of the day.

Circuit loss summaries are shown in Table 6-1. For the entire day, the automated device control is able to improve the real and reactive power loss over the baseline by 6.53% and 2.74%, respectively.

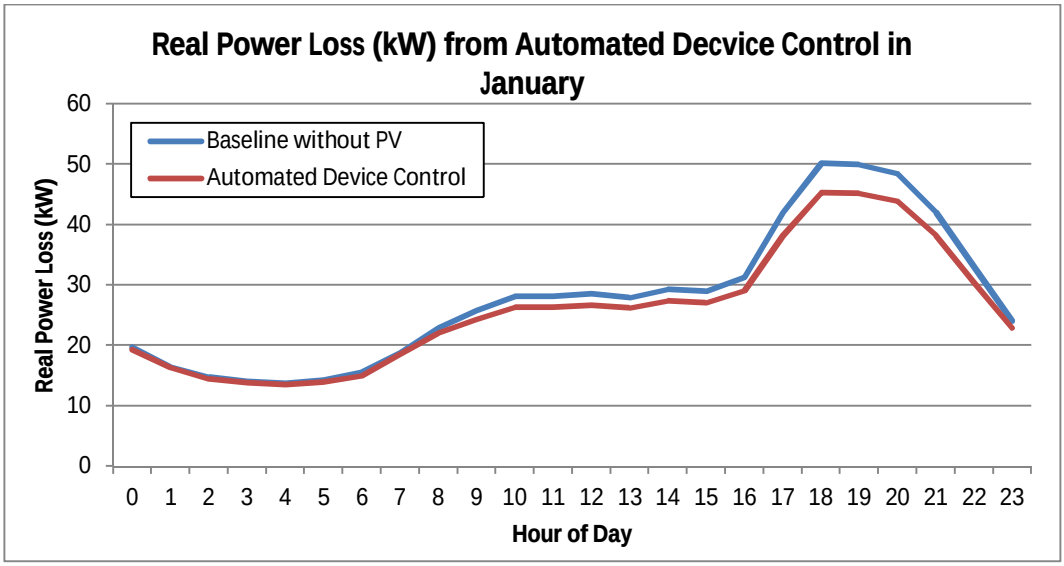

(a) Circuit real power loss (kW) comparison

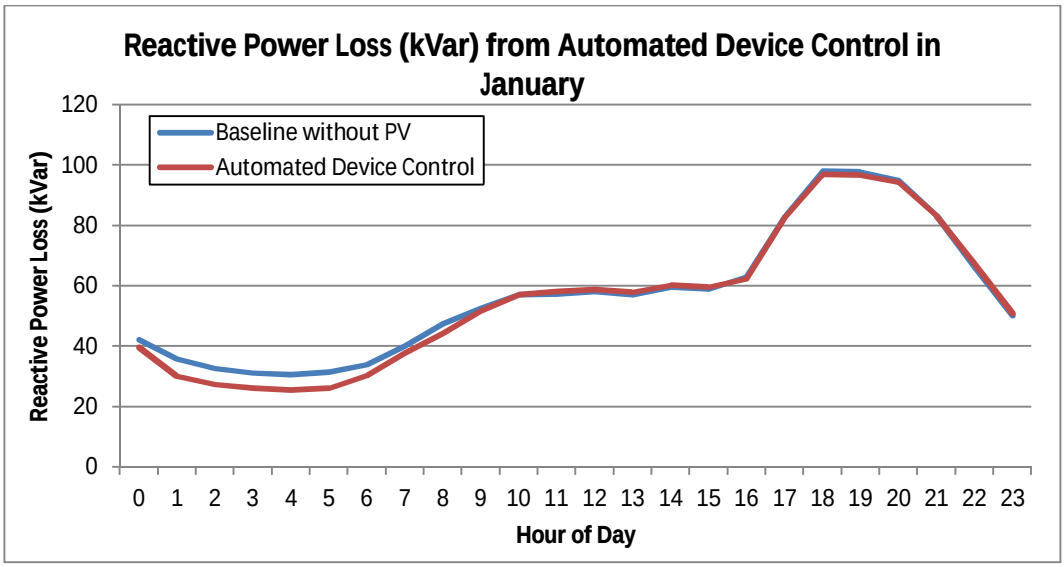

(b) Circuit reactive power loss (kVar) comparison

Figure 6-13 Circuit loss comparison between coordinated automated device control and baseline in January without PV

Table 6-1 Comparison of the circuit losses between the baseline and the coordinated automated device control over a representative day in January without PV

	Baseline Losses without PV	Coordinated Automated Device Control Losses	Improvement
Real Power Loss (kW-hr)	667.50 kW-hr	623.91 kW-hr	6.53 %
Reactive Power Loss (kVar-hr)	1362.76 kW-hr	1325.41 kW-hr	2.74 %

Figure 6-14 shows the reduction of the circuit loss with the automated device control in July. The power loss in July for the circuit is much higher.

Circuit loss summaries are shown in Table 6-2. For the entire day, the automated device control is able to improve the real and reactive power loss over the baseline by 9.57% and 9.63%, respectively. Higher improvement in July is obtained than January at this location. In summary, the coordinated, automated device control is able to reduce both the real and reactive power losses while maintaining the average customer voltage within tight limits.

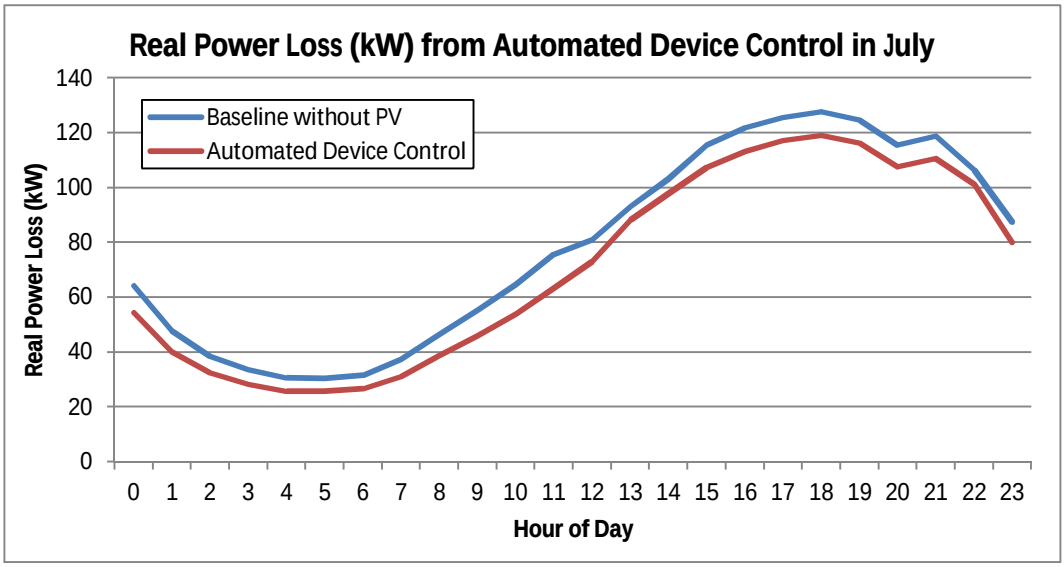

(a) Circuit real power loss (kW) comparison

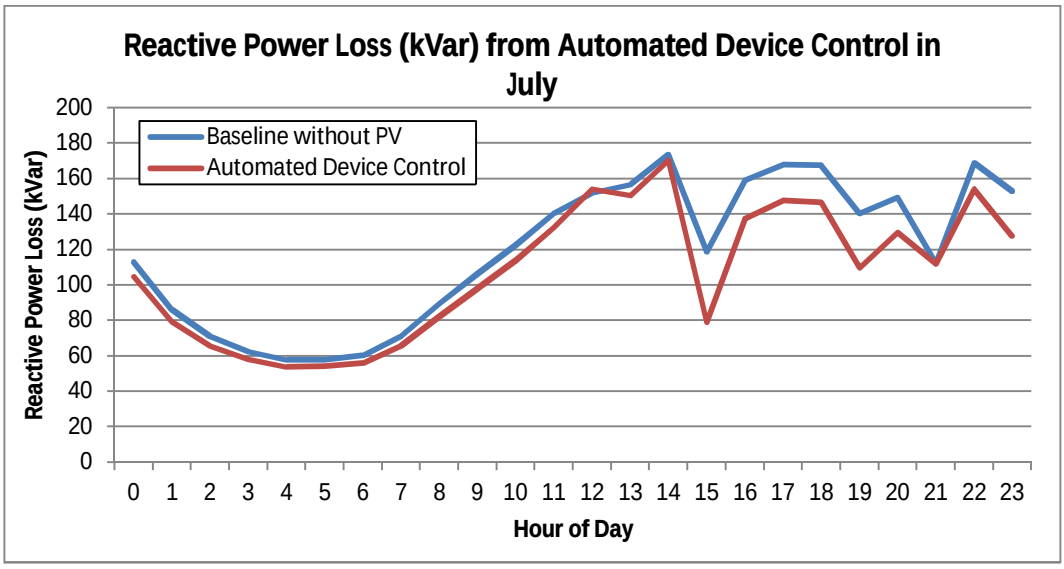

(b) Circuit reactive power loss (kVar) comparison

Figure 6-14 Circuit loss comparison between the coordinated automated device control and the baseline in July without PV

Table 6-2 Comparison of the circuit losses between the baseline and the coordinated automated device control over a representative day in July without PV

	Baseline Losses without PV	Coordinated Automated Device Control Losses	Improvement
Real Power Loss (kW-hr)	1877.03 kW-hr	1697.39 kW-hr	9.57 %
Reactive Power Loss (kVar-hr)	2857.54 kVar-hr	2582.39 kVar-hr	9.63 %

c) Steps of the Automated Devices

A control objective is to minimize the steps of the automated devices themselves. Figure 6-15 plots the step variations of VR1 across the day (see Figure 6-4) in January for four different cases, the coordinated, automated device control and the three baseline cases with PV. The step (T_n) obtained from the coordinated, automated device control should not change if the coordinated PV control works properly. From the figure it may be seen that with the baseline cases the number of steps increase as the PV generation increases, and that the coordinated automated devices result in significantly less steps.

Table 6-3 provides a summary of the steps across the cases of the 4 automated control devices (see Figure 6-4) in January.

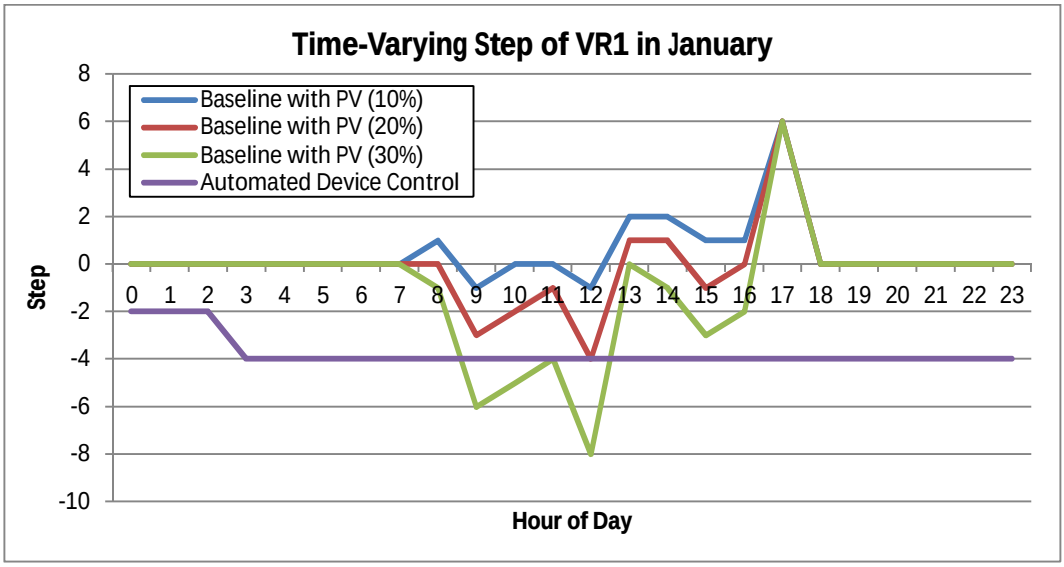

Figure 6-15 Comparison of time-varying step of VR1 between coordinated automated device control and baselines with PV in January

Table 6-3 Total steps of automated devices for a representative day in January

	VR1	VR2	CAP1	CAP2
Baseline with PV (10%)	20	14	0	0
Baseline with PV (20%)	28	16	0	0
Baseline with PV (30%)	38	24	0	0
Coordinated Automated Device Control	***2***	***1***	***0***	***0***

Figure 6-16 shows step variations of VR1 across the day in July. In July the device steps are much greater for all cases, but still are significantly less with the coordinated automated device control.

Table 6-4 provides a summary of the steps across the cases of the 4 automated control devices (see Figure 6-4) in July. It may be noted that capacitors move for the baseline cases but do not used in the coordinated automated device control. Again, for the baseline cases, the number of steps increases as the PV penetration level increases.

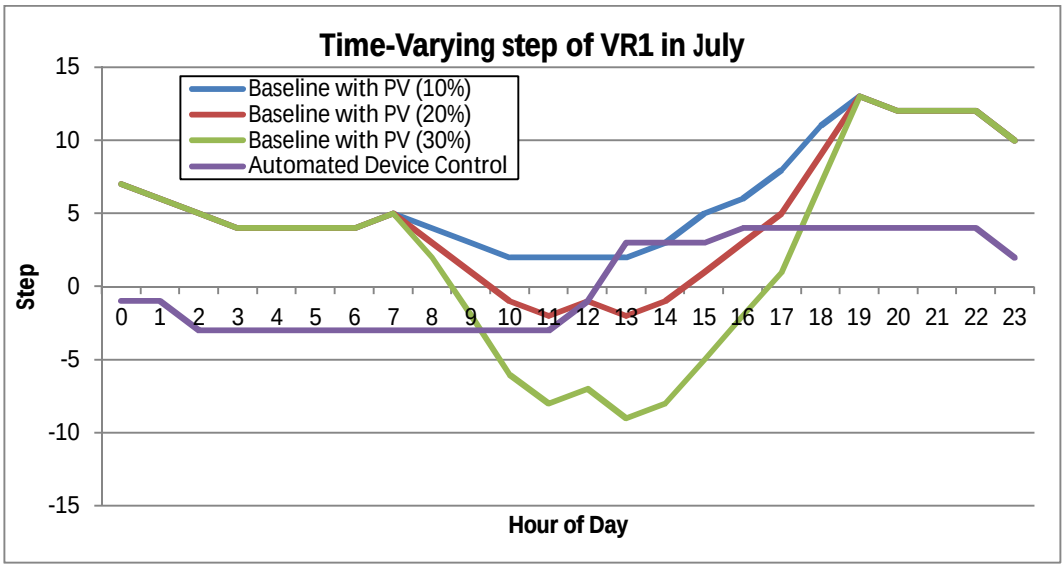

Figure 6-16 Time-varying step of VR1 using coordinated automated device control in July

Table 6-4 Total steps of the automated control device for a representative day in July

	VR1	VR2	CAP1	CAP2
Baseline with PV (10%)	21	16	2	0
Baseline with PV (20%)	31	14	2	0
Baseline with PV (30%)	45	22	2	0
Coordinated Automated Device Control	***11***	***6***	***0***	***0***

6.4.2. Coordinated Control of Automated Devices and PV

a) Average Customer Voltage

The objective of the coordinated PV control is to maintain the optimal operating voltage schedule established by the coordinated automated device control without PV generation. Figure 6-17 and Figure 6-18 show the average customer voltage ($V_{set,n}$) with its +/- 0.2% limit ($V_{set,n} \pm 0.002 \cdot V_{set,n}$) obtained from the coordinated automated device control in January and July respectively. These figures also show the average customer voltage obtained from the coordinated PV control for the various levels of PV penetration. It should be noted that the average customer voltage obtained from the coordinated PV control is maintained within the limits during both January and July. Thus, the coordinated control is able to mitigate the voltage rise caused by PV penetration.

Table 6-5 and Table 6-6 compare the maximum voltage deviation for the baseline cases and coordinated control cases for January and July, respectively. The maximum voltage deviations are significantly reduced with the coordinated control for the 20% and 30% PV penetration levels.

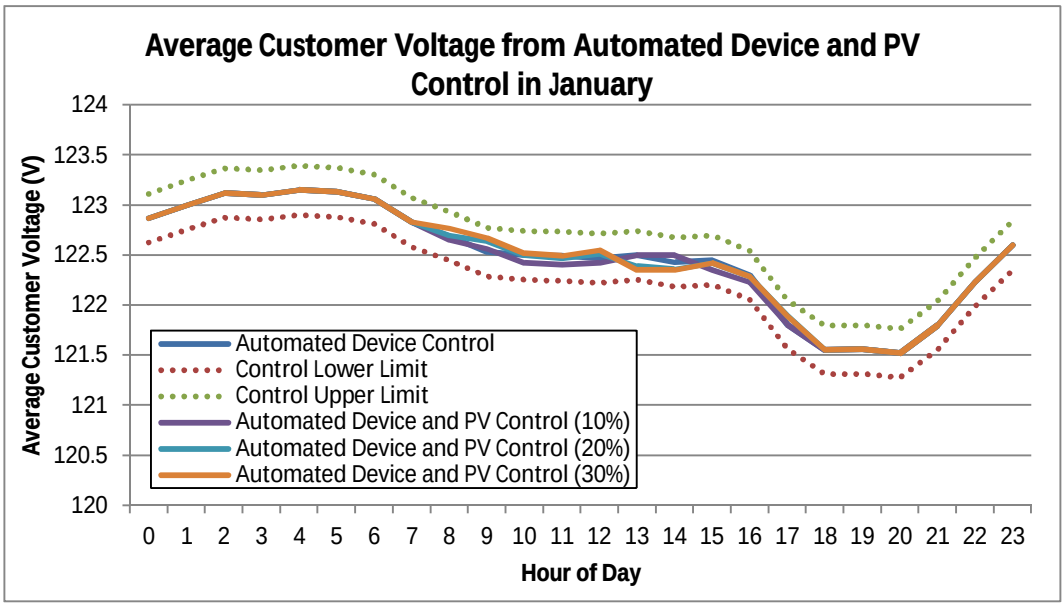

Figure 6-17 Average customer voltage with coordinated automated devices and PV control for three adoption scenarios in January

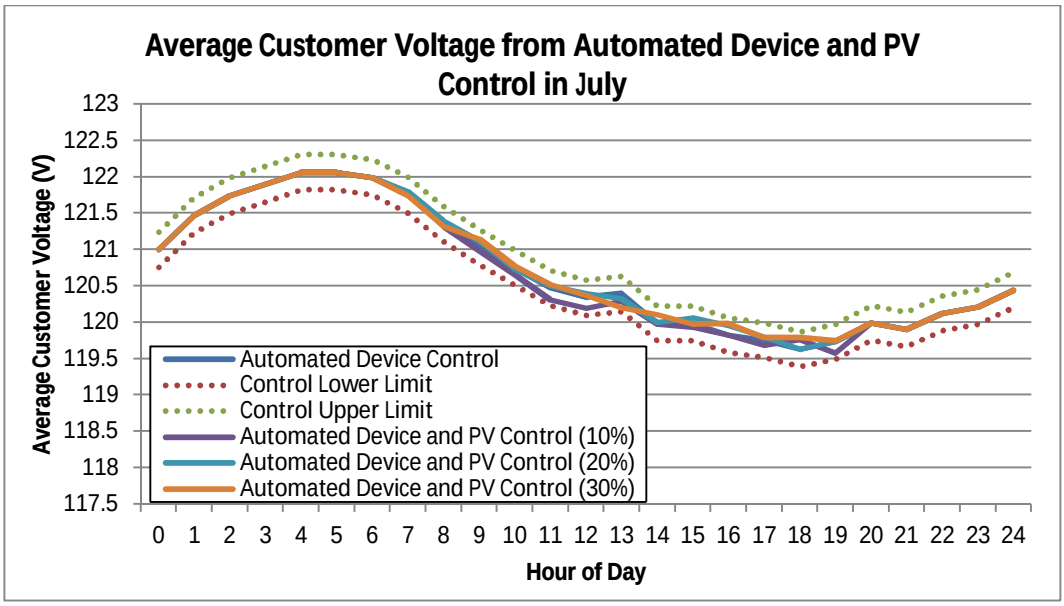

Figure 6-18 Average customer voltage with coordinated automated devices and PV control for three adoption scenarios in July

Table 6-5 Maximum voltage deviation comparison for January

	Baseline Condition (V)	Coordinated Automated Device and PV Control (V)
10% PV Penetration	0.13	0.12
20% PV Penetration	0.71	0.15
30% PV Penetration	1.04	0.18

Table 6-6 Maximum voltage deviation comparison for July

	Baseline Condition (V)	Coordinated Automated Device and PV Control (V)
10% PV Penetration	0.25	0.21
20% PV Penetration	1.10	0.14
30% PV Penetration	1.49	0.17

b) Circuit Loss

Table 6-7 and Table 6-8 compare the real and reactive circuit power losses of the coordinated PV control with the baseline conditions in January. The real power loss is reduced by 3.65%, 2.31%, and 2.46% corresponding to 10%, 20%, and 30% PV penetration levels, respectively. The reactive power loss is reduced by 1.19%, 1.30%, and 1.20% corresponding to 10%, 20%, and 30% PV penetration levels, respectively. Therefore, the coordinated control is able to maintain the voltage operating schedule while minimizing the circuit losses.

Table 6-7 Summation of the real power loss (kW-hr) during the day in January

	Baseline Circuit Losses (kWHr)	Circuit Losses with Automated Device and PV Control (kWHr)	Improvement of Automated Device and PV Control
10% PV Penetration	633.91	610.80	3.65 %
20% PV Penetration	576.54	563.22	2.31 %
30% PV Penetration	599.61	584.88	2.46 %

Table 6-8 Summation of the reactive power loss (kVar-hr) during the day in January

	Baseline Circuit Losses (kVarHr)	Circuit Losses with Automated Device and PV Control (kVarHr)	Improvement of Automated Device and PV Control
10% PV Penetration	1300.43	1284.98	1.19 %
20% PV Penetration	1196.10	1180.58	1.30 %
30% PV Penetration	1209.30 r	1194.73	1.20 %

Table 6-9 and Table 6-10 compare the real and reactive power circuit losses of the coordinated PV control and baseline cases for July. Similar to the automated device results of Table 6-2, the improvement obtained with the coordinated PV control is greater in July.

Table 6-9 Summation of the real power loss (kW-hr) during the day in July

	Baseline Circuit Losses (kWHr)	Circuit Losses with Automated Device and PV Control (kWHr)	Improvement of Automated Device and PV Control
10% PV Penetration	1756.14	1697.39	3.35 %
20% PV Penetration	1568.55	1511.99	3.61 %
30% PV Penetration	1719.60	1654.25	3.80 %

Table 6-10 Summation of the reactive power loss (kVar-hr) during the day in July

	Baseline Circuit Losses (kVarHr)	Circuit Losses with Automated Device and PV Control (kVarHr)	Improvement of Automated Device and PV Control
10% PV Penetration	2657.42	2514.02	5.40 %
20% PV Penetration	2550.40	2453.92	3.78 %
30% PV Penetration	2698.50	2581.04	4.35 %

c) Aggregated PV Output

Figure 6-19 shows the aggregated power from coordinated PV control of all PV in January for the three adoption scenarios. Note that the reactive power increases as the real power increases. Furthermore, the reactive power increases as the penetration level of the PV increases. The power factor of the PV is controlled to consume reactive power for mitigating the voltage rise. Each PV may operate at a different power factor, but the overall PV generation is controlled around 0.90 leading when there is sufficient irradiance available for generation.

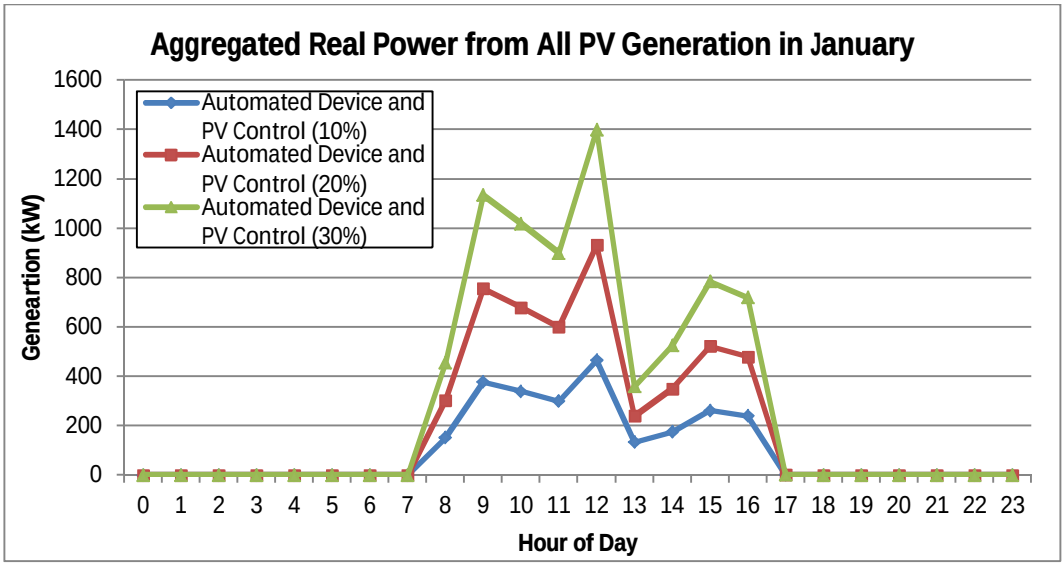

(a) Aggregated real power (kW) from all PV

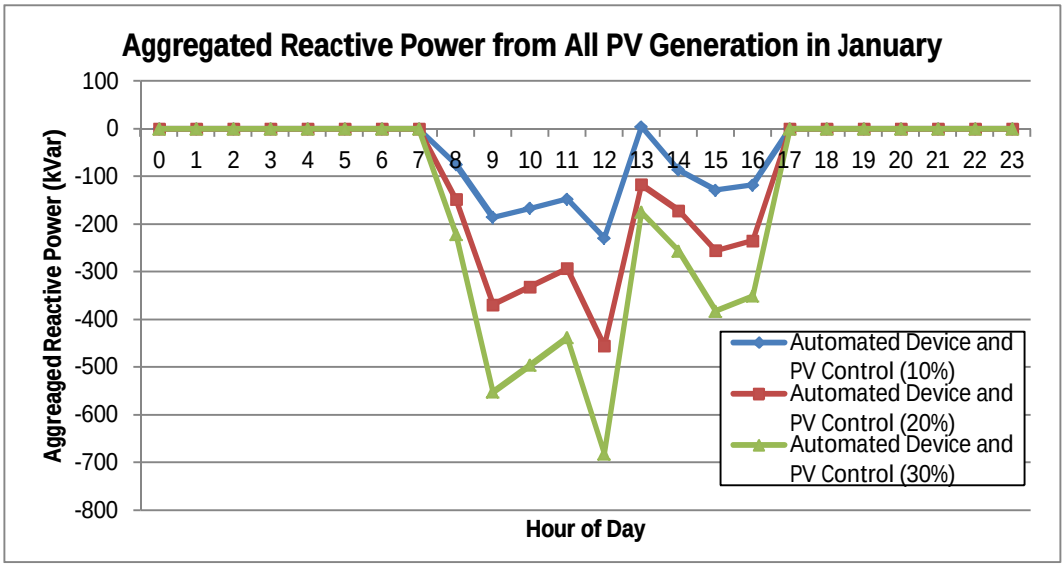

(b) Aggregated reactive power (kVar) from all PV

Figure 6-19 Aggregated power output from all PV for three penetration scenarios in January

Figure 6-20 shows the aggregated power from the coordinated PV control of all PV in July for the three adoption scenarios.

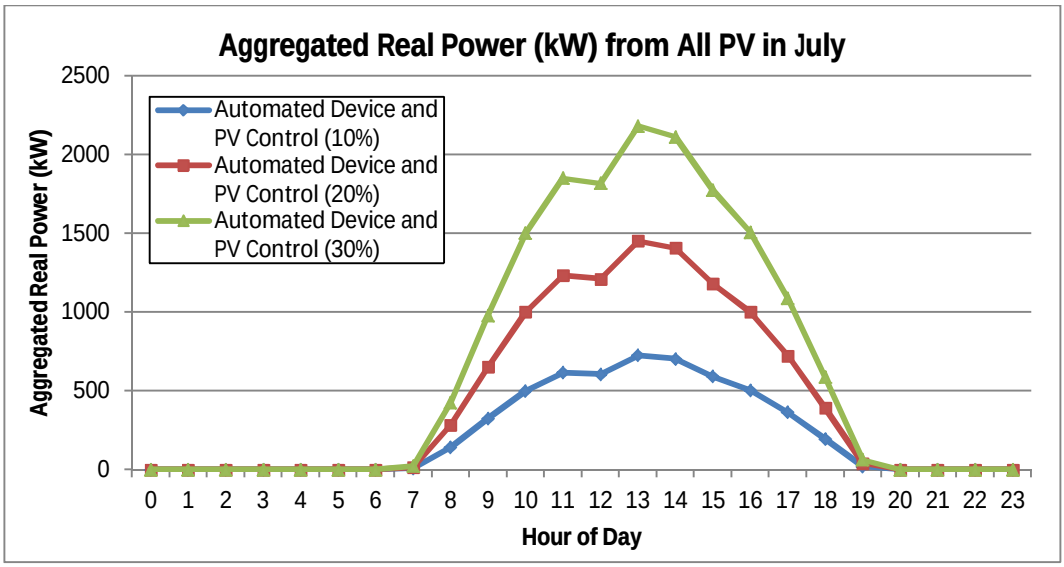

(a) Aggregated real power (kW) from all PV

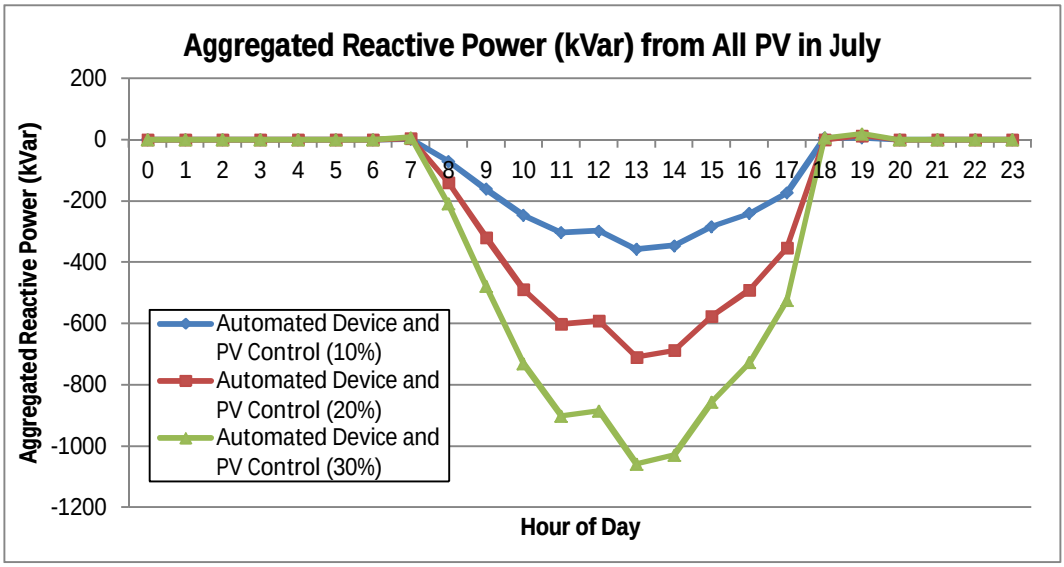

(b) Aggregated reactive power (kVar) from all PV

Figure 6-20 Aggregated power output from all PV for three penetration scenarios in July

6.5. Conclusion

Coordinated control algorithms for automated devices, such as automated voltage regulators and capacitors, and PV generators are investigated to mitigate voltage rise problems caused by high PV penetration. The control strategy involves using the automated devices to establish an optimum voltage schedule that does not consider the PV generation. The voltage that is controlled is the average customer voltage, and it is controlled with very tight limits. The optimum schedule minimizes circuit losses while reducing automated device movement. The optimum voltage schedule is used as an input to the

coordinated PV control algorithm, which seeks to adjust the real and reactive PV power generation to maintain the optimum voltage schedule.

A large scale, real distribution circuit is considered in the analysis. Three PV adoption scenarios are considered, 10%, 20%, and 30% penetration. Baseline conditions that do not consider coordinated control are established for all scenarios and used in comparisons with scenarios that do consider coordinated control. For all scenarios the coordinated control is able to maintain a voltage schedule that eliminates voltage rise problems and that significantly reduces losses and automated device controller movement.

Chapter 7 Configurable, Hierarchical, Model-based, Scheduling Control with Photovoltaic Generators in Power Distribution Circuits

7.1. Introduction

Photovoltaic (PV) generation is one of the most rapidly growing renewable energy sources, and is regarded as an appealing alternative to conventional power generated from fossil fuel. This has led to efforts to increase PV generation levels in the U.S. [10]. Although the integration of PV brings many advantages, high penetration of PV provides a number of challenges in power system operation, mainly due to its uncertain and intermittent nature.

A major research challenge is optimized control of high PV penetration within the existing power system. In a power distribution circuit that contains a high level of PV generation that is not combined with rapidly acting storage, a sudden change of PV generation can create voltage problems, which in turn may limit the amount of PV generation that can be added to the circuit.

A control algorithm that dispatches real and reactive PV generator power can be used to address this problem, keeping voltages and power factors at desired levels. PV generator control structures can be classified into three categories; local, hierarchical, and decentralized control [80, 82-88]. In all of these control paradigms it is assumed that each PV generator has its own local controller.

Local PV generation inverter control is primarily used today, which aims to control PV operating points using local measurements. Local control is typically low cost and simple to operate and maintain. However, as PV penetration levels increase, it becomes more and more difficult to tune PV inverter and distribution circuit voltage control device settings to meet requirements. Also, with local control only, it is difficult to handle the multitude of failure scenarios that are possible.

Here, hierarchical control collects circuit-wide information, and uses this big picture view to make supervisory level decisions that are used to better coordinate local device actions to meet system level objectives. Under this strategy, local control is still used to insure safety and to protect equipment from damage. If communications are lost between local controllers and the hierarchical control, the local control can continue to work similar to the control that is used today. An advantage of hierarchical control

is that multi-objective optimization solutions can be achieved. If the hierarchical control is model based, then the control can handle all scenarios that are reflected in the model solution.

Many PV hierarchical control strategies are presented in [45, 47-53, 89]. In [45, 47, 89] reactive power injection of the PV is used to reduce voltage deviations caused by large PV penetrations. The control strategy minimizes circuit loss while maintaining the voltage within limits in [48-51]. An active curtailment strategy to reduce PV power injection is used to prevent voltage violations in [52, 53]. Other work has investigated optimal coordination of control devices. In [77, 78, 90] different automated control devices are coordinated to find optimal dispatch schedules. Optimal control of the automated control devices is able to reduce circuit loss and improve the voltage profile [77, 78, 90]. In these papers different automated control devices are coordinated to find optimal dispatch schedules.

This chapter introduces a hierarchical control algorithm referred to as Configurable, Hierarchical, Model-based Scheduling Control (CHMSC) for maintaining the average customer voltage profile obtained before introducing the PV into the circuit. The CHMSC algorithm first looks at the operation of control devices owned by the utility, such as voltage regulators and switched capacitor banks, and uses time-series based simulation to determine a control schedule that works to minimize circuit loss while simultaneously reducing the motion of the automated control devices. This control schedule is created without considering PV generation. The CHMSC algorithm then generates coordinated PV inverter control set-points that work to maintain the system operating conditions established by the utility control devices. Thus, the CHMSC algorithm provides time varying set-points to local controllers for both the automated control devices and PV controllers.

The chapter is organized as follows. Section 7.2 presents the CHMSC algorithm and its coordination. In Section 7.3 the proposed control is analyzed. In Section 7.4 the effectiveness is shown by comparing the CHMSC performance with the performance of local control. Findings of the study are summarized in Section 7.5.

7.2. Configurable, Hierarchical, Model-based, Scheduling Control

The main objective of CHMSC is to determine the optimum operating circuit voltage profiles and control schedule prior to introducing PV into the circuit, then use hierarchical PV controller set-point adjustment to help maintain this schedule as PV generated power is injected into the system. The approach reduces losses and voltage control device movement, while minimizing the impact that PV will have on circuit operation, which was most likely designed without any consideration given to installation of PV. CHMSC works to have the PV generation support the optimum voltage profiles and control

schedule. The term *optimum* is associated here with discrete searches based upon the CHMSC prioritized objectives.

7.2.1. CHMSC Outline

Circuit measurements are sent to a control center where CHMSC is located and makes decisions on control actions based on all measurements and the control objectives, as shown in Figure 7-1. As illustrated in Figure 7-1, optimum profiles determined by CHMSC are sent to automated control devices and PVs that have communications. CHMSC, using load and solar forecasts, will take into account the expected actions of control devices and PV generators that do not have communications and are controlled solely by their own local controller. Two such local controllers are illustrated in Figure 7-1. The CHMSC control algorithm can be used on any distribution circuit topology, including radial, lightly meshed, and heavily meshed.

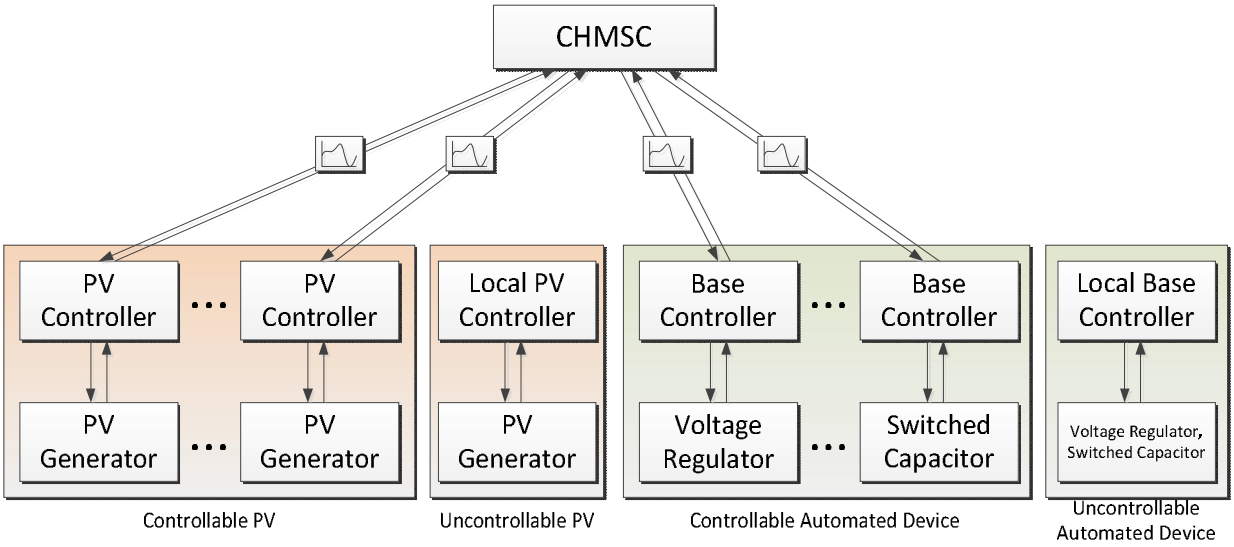

Figure 7-1 Control system architecture

CHMSC calculates schedules as illustrated in Figure 7-2. Using the load forecast, CHMSC first calculates the optimal schedules for the automated control devices in the absence of PV generation, referred to here as Base Controller Schedule. The Base Controller Schedule provides a time varying schedule for utility control devices and also optimum voltage schedules to be followed throughout the circuit. That is, the optimum voltage schedule varies from circuit location to circuit location. At a given circuit location, the optimum voltage schedule varies as a function of time. Next, using the solar forecast and the optimum voltage schedules, the optimal schedules for the PV generators are determined. The PV Controller Schedule provides a time varying power factor schedule for each PV Controller. The time varying power factor schedule can vary from PV controller to PV controller. Then, based upon the set-

point type required for each local controller, such as voltage, power factor, or other, optimal set-point schedules are determined and provided to individual local controllers, whether they be utility owned or not. Thus, the set-point schedules are time varying and vary from one local controller to another. The algorithms used to determine the base controller and PV controller schedules are presented in sections 7.2.2 and 7.2.3, respectively.

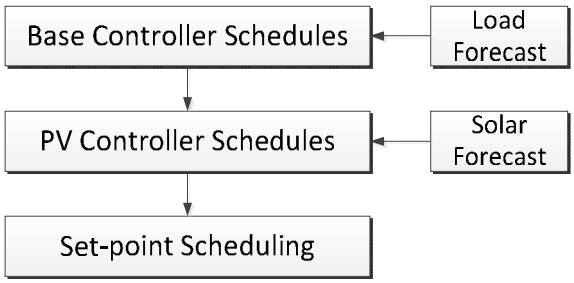

Figure 7-2 CHMSC architecture

Based upon circuit and PV generation measurements, the CHMSC updates its calculations every five minutes. If the optimal set-point schedules for a base or PV controller have changed significantly from the ones currently being used, then the set-point schedules are updated for the local controllers. This update cycle is similar to that used in real-time energy markets [91].

If a PV generator is lost or a circuit reconfiguration occurs, the CHMSC immediately recalculates optimal schedules based upon the new situation. Note that if a communication failure occurs, the local controllers can continue to work against the optimal schedule previously provided as long as the variable being controlled, such as voltage, stays within the allowable range. If the locally measured variable goes out of bounds, then the local control will override the use of the optimal schedule.

7.2.2. Base Controller Schedule

Controller schedules represent the planned operation of the controllers over a period of time. Here the controller schedules are eventually determined in terms of control variable set-points, such as power factor or voltage set-points, as a function of time. However, in this section the schedules will initially be determined in terms of control device step positions.

The base controller schedules are determined by performing a search over controllable single-step (often switched shunt capacitors) and multi-step device (often voltage regulators) positions to find one or more sets of device positions that satisfy three prioritized objectives [78, 90]. That is, there may be multiple control solutions that satisfy one or more of the objectives, where each control solution is represented by a set of device positions.

The highest priority control objective is to maintain the average customer voltage within a desired bandwidth of a set-point without violating voltage operating constraint limits. If more than one set of device positions satisfy the highest priority objective, the set with the smallest number of total device steps, or least device motion, is selected. If two or more sets of device positions satisfy the voltage criteria and have the same total device motion, then a set with the least circuit loss is selected.

A flowchart of the algorithm used for determining the base controller schedules is illustrated in Figure 7-3. Let M_n represent the total number of allowable device steps at time n. M_n is related to the individual control device steps by

$$M_n = \sum_{k=1}^{K} m_{n,k} \tag{7-1}$$

where K is the total number of controllable devices and $m_{n,k}$ are the number of steps of device k at time n subject to the constraint

$$T_k^{\min} \le T_{n,k} \le T_k^{\max} \tag{7-2}$$

where $T_{n,k}$ is the step at time n, and $T_k^{\min}$ and $T_k^{\max}$ are the limits of the step position.

The first priority is to maintain the average customer voltage V_n within a range of a desired value $V_{ref,n}$. This is the average customer voltage that would exist without PV generation in the circuit at time n. The voltage deviation is calculated by

$$\left|V_n - V_{ref,n}\right| < V_{tol,n} \tag{7-3}$$

where

$$V_n = avg\left(\sum v_{i,n}\right) \tag{7-4}$$

$V_{tol,n}$ is the acceptable voltage deviation at time n

$v_{i,n}$ is the customer voltage of the component i at time n.

$V_{tol,n}$ is defined as +/- 1% of the desired voltage ($V_{ref,n}$) in this chapter. If any operating constraint limits are violated, such as

$$v_i^{\min} \le v_{i,n} \le v_i^{\max} \tag{7-5}$$

where $v_i^{\min}$ and $v_i^{\max}$ are lower and upper limits, respectively, on customer voltage, then the reference voltage is modified until either the constraint violation is eliminated or the controllers reach their limits. Note that the voltage control limits can change depending upon the type of customer.

If more than one control solution exists that satisfies the voltage criteria, then the second priority, minimize the steps taken by the control devices, is evaluated.

Finally, if more than one control solution exists which satisfies both the voltage and minimum controller motion criteria, the CHMSC algorithm works on the third priority, to reduce the circuit loss, where the circuit loss is calculated as

$$L_n = \sum \sqrt{P_{Loss,i,n}^2 + Q_{Loss,i,n}^2} \tag{7-6}$$

where $P_{Loss,i,n}$ is the real power loss and $Q_{Loss,i,n}$ is the reactive power loss of each component.

If a control solution that satisfies the highest priority is not acquired in M_n steps, the total allowable steps M_n is increased and the search repeated.

For each device k, a set of step positions $\{T_{n,k}\}$ as a function of time step n is thus determined, and this defines the schedule for device k in terms of actual step positions. Then, for each device k, a schedule of optimum voltage set-points $\{Vop_{n,k}\}$ is created. The optimum voltage schedules are then used in determining the optimum schedules for the PV generator controls, which is addressed in the next section.

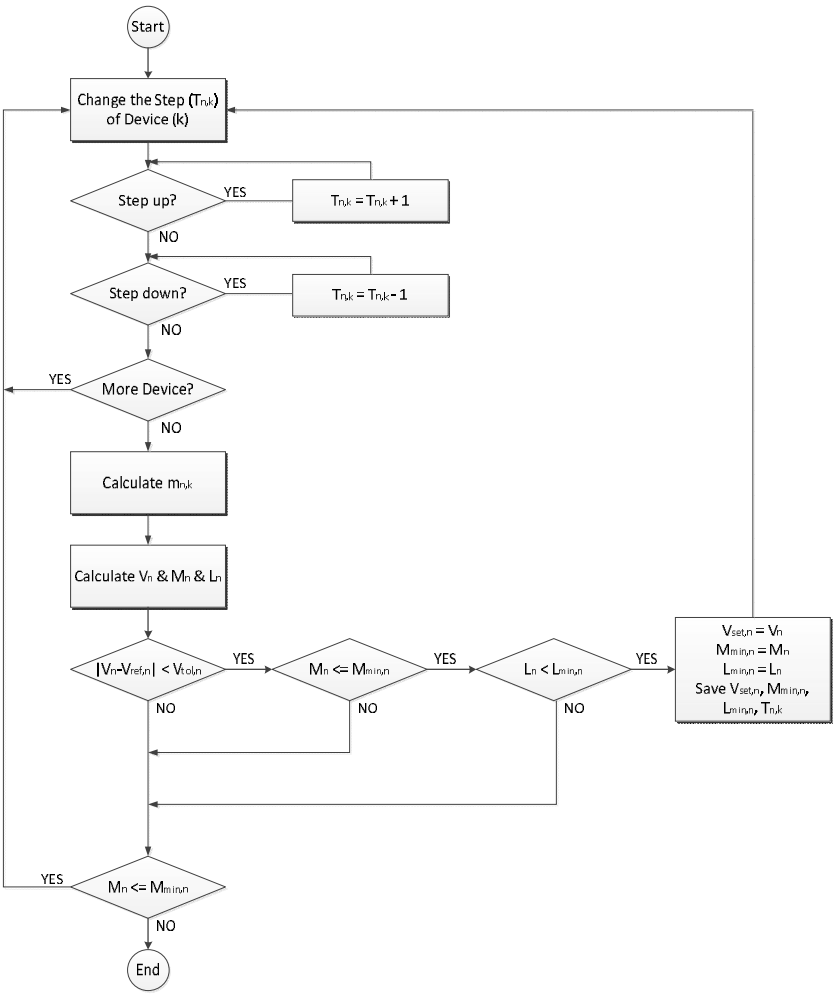

Figure 7-3 Flowchart for base controller schedule

7.2.3. PV Controller Schedule

The PV control algorithm uses an iterative approach to adjusting the power factors of the controllable PV to minimize the customer level voltage deviations from the optimum voltage profile obtained from the Base Controller schedules, as illustrated in Figure 7-4. Again note that for a given time point the voltage set-points determined in the base controller schedule may vary from PV generator to PV generator. Also, note that at different time points for a given PV generator the voltage set-point may vary.

If the optimum set-point is greater than the current voltage, the power factor is adjusted to supply reactive power. If the optimum set-point is less than the current voltage, the power factor is adjusted to consume reactive power. Discrete power factor steps are used by the algorithm. The algorithm first changes the power factor for a PV generator by increasing or decreasing the power factor in steps of 0.1. If the average customer voltage falls within +/- 0.5% of the optimum set-point, the algorithm changes the power factor by 0.01 steps with the following constraint:

$$PF_n^{\min} \le PF_n \le PF_n^{\max} \tag{7-7}$$

where PF = power factor.

After the power factors of all PVs are determined, the algorithm calculates the average customer voltage for the circuit (V_n). The objective is to reduce the voltage deviation from the optimum set-point ($V_{set,n}$) established by the automated control devices. Next the voltage deviation is compared with the saved minimum deviation ($dV_{\min,n}$) as:

$$\left|V_n - V_{set,n}\right| < dV_{\min,n} \tag{7-8}$$

If the algorithm finds a better power factor for the controller, it saves the results. The algorithm then returns to the start to change the power factor of the PV and begin a new iteration. One hundred iterations are used as the maximum in this work.

Individual local controllers may not work directly in terms of voltage and power factor set-points. Thus, the CHMSC controller finally performs set-point scheduling, as illustrated in Figure 7-2, based upon the individual controller needs.

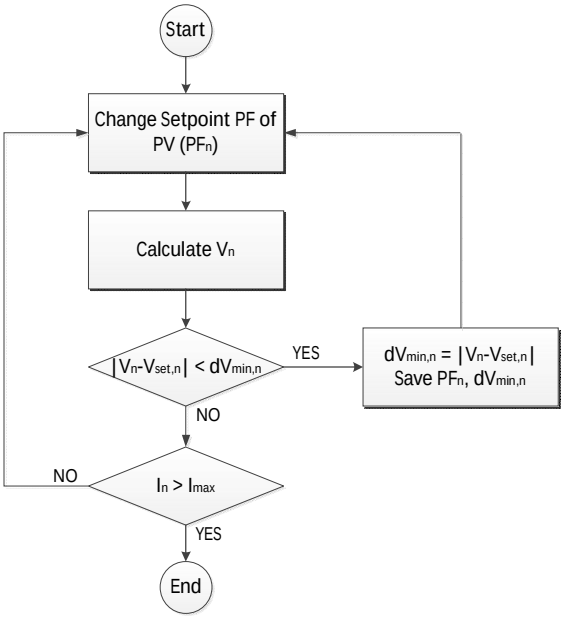

Figure 7-4 Flowchart for PV controller schedule

7.2.4. Local Controller

For optimum operation, the optimum voltage and power factor schedules would be transmitted to all local controllers, as illustrated in Figure 7-1, and all local controllers would work directly with the optimum schedules. However, most existing PV controllers are not designed to take such schedules. Here we will use a common PV local control scheme, but assume that the voltage set-point of the local PV controller can be varied.

For local control of PVs, voltage-reactive power droop control is used in the work here, as shown in Figure 7-5 [46]. This control provides voltage regulation support by supplying reactive power if the line voltage drops below the selected voltage set-point and by consuming reactive power if the line voltage is higher than the selected voltage set-point. The reactive power that can be supplied is limited, as illustrated in Figure 7-5. Note that here the maximum reactive power is limited at 70% of the PV MVA rating. The gain used for the droop control is 2500 var/volt. This gain and the maximum reactive power limits are used for both the local control and CHMSC simulations described in the following sections. The major difference between the local control and the CHMSC control is that the voltage set-point to the local control changes with CHMSC and the set-point does not change when CHMSC is not used (i.e., the voltage set-point is fixed when just local control is used).

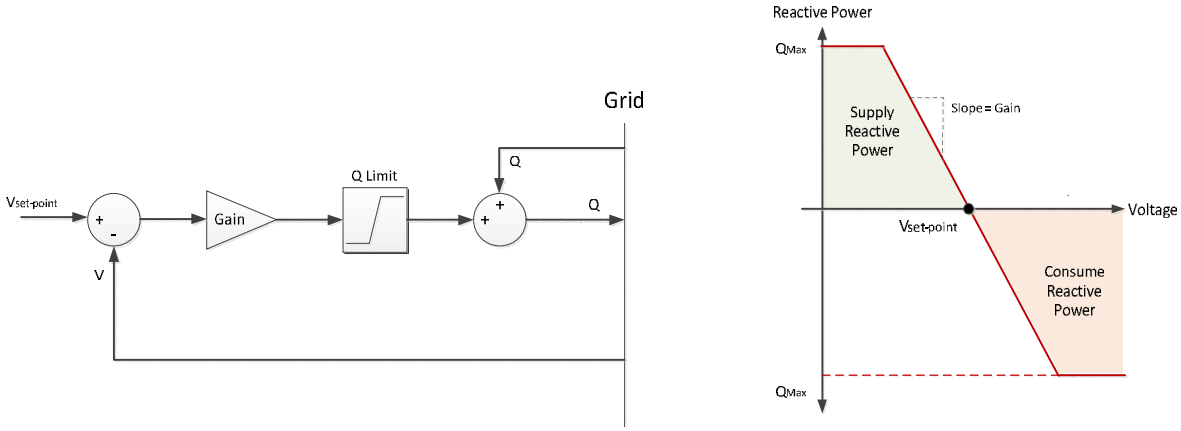

(a) voltage-reactive power control block diagram **(b) voltage-reactive power characteristics**

Figure 7-5 Voltage-reactive power droop control

Utility control devices considered here are voltage regulators and switched shunt capacitors. Voltage regulators provide the output voltage to be regulated from 90% to 110%. For example, each step in a 32 multi-step voltage regulator having a 20% voltage range of regulation represents a 0.625% voltage change. Therefore, one step change of a voltage regulator is seen to result in a voltage change of 0.75 V based on a 120V base.

Switched shunt capacitors are equipped with controllers that use local measurements to determine when to switch the capacitors on and off. For example, when the measured voltage is higher than the desired voltage, the controller opens the switch to remove the capacitor from service. When the voltage drops below the desired voltage, the controller closes the switch to place the capacitor in service.

7.3. Evaluation of Configurable, Hierarchical, Model-based, Scheduling Control

To evaluate the performance of the CHMSC, different PV adoption levels are analyzed. As more and more PVs are connected to the system the system behavior is affected. In this section the performance of CHMSC is compared with local control. When just local control is used, the voltage set-points are not updated.

7.3.1. Simulation Study

The distribution circuit to be analyzed is shown in Figure 7-6. The circuit model is derived from data for an actual circuit. It is a 13.2 kV, Y-connected circuit. The time varying customer loads are estimated from averaged hourly SCADA measurements, hourly customer kWh load data, and monthly kWh load data processed by load research statistics to create hourly loading estimates for each customer [3, 4].

The circuit studied contains 21 voltage regulators and 8 switched shunt capacitors. The voltage regulators operate on voltage control with a 1.0 volt bandwidth and +/- 16 steps. The switched shunt capacitors also operate to control voltage with specified turn on and turn off voltage limits.

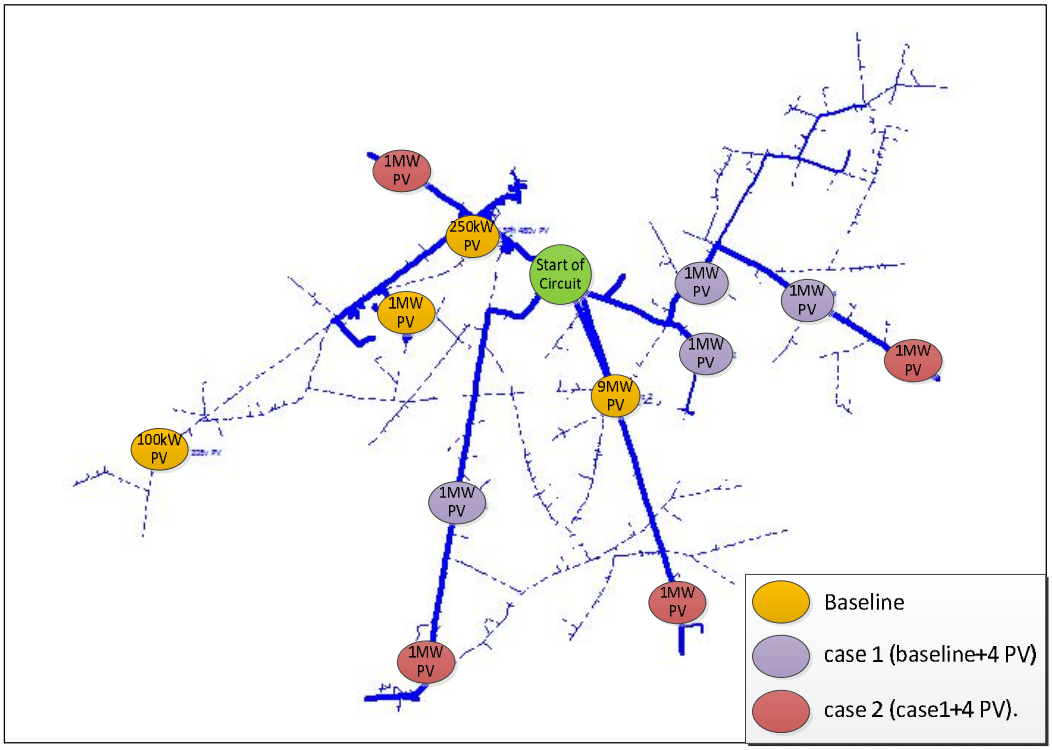

Figure 7-6 Distribution circuit to be analyzed with baseline, case 1, and case 2 PV penetration levels

This circuit has 4 existing PV generators, referred to as baseline generators, as marked in Figure 7-6. The existing baseline PV generators are now controlled in the field to unity power factor and have 1 second resolution real power measurements available. Here the simulation uses these 1 second measurements in a quasi-steady state power flow. For the simulation of the higher PV penetrations, 1 MW PV generators are used. The generation from the added PV generators considered in cases 1 and 2 is based on the baseline PV generator measurements. The locations of the added PV generators were randomly selected [25, 33].

April 2 from 14:00 to 16:00 contains the time of maximum PV generation for the existing generation, or baseline. This 2 hour time period is used in the case studies to be presented. The PV generation data for the 9 MW PV on April 2 from 14:00 to 16:00 is shown in Figure 7-7. In this chapter 3 levels of PV penetration are analyzed and used in the controller comparisons, as indicated in Figure 7-6: baseline case with existing generation; case 1 (baseline + four 1 MW PVs added to the circuit); and case 2 (case1 + four 1 MW PVs added to the circuit). The rated PV generation for the baseline case is 10.35 MW, for case 1, 14.35 MW, and for case 2, 18.35 MW.

The PV penetration percentage is calculated based on the following equation:

$$\text{PV penetration (\%)} = \frac{\text{Max PV generation}}{\text{Native load at max PV generation time}} \quad (7\text{-}9)$$

Thus, the definition of PV penetration used in this chapter varies based on the selected time duration. The PV penetration for the selected day for analysis is approximately 69%, 96%, and 123% for the baseline case, case 1, and case 2, respectively.

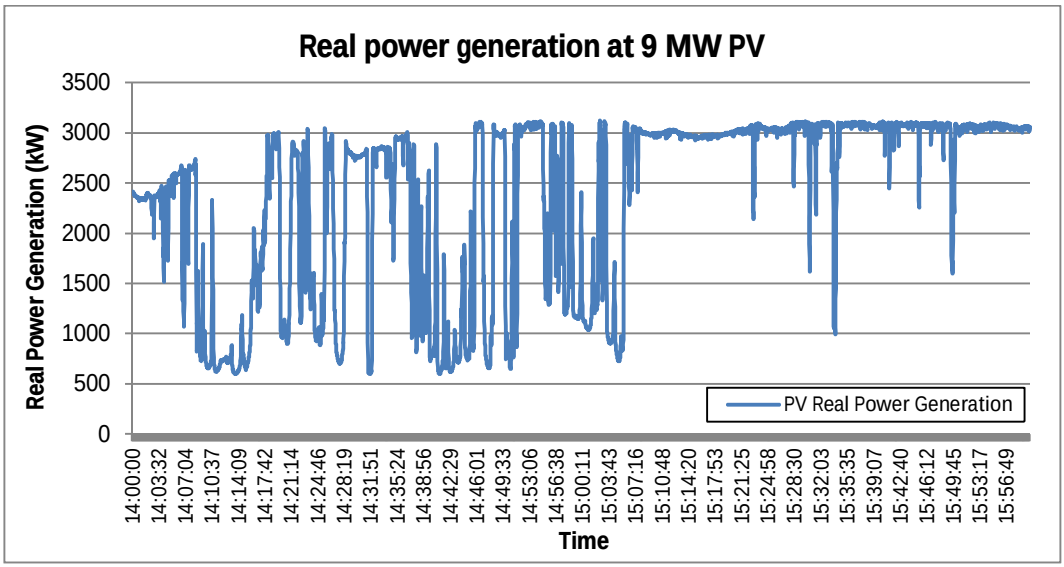

Figure 7-7 Real power generation data at 9 MW PV on April 2 from 14:00 to 16:00

High PV penetration often leads to reverse power flow conditions in distribution circuits. Bidirectional power flow can be detrimental to the performance of automated control devices. Figure 7-8 shows the reverse power flow by circuit color on April 2 at 14:00 for the baseline. For case 2, representing a PV penetration level of 123%, the entire circuit would be colored with the reverse power flow (not shown in Figure 7-8).

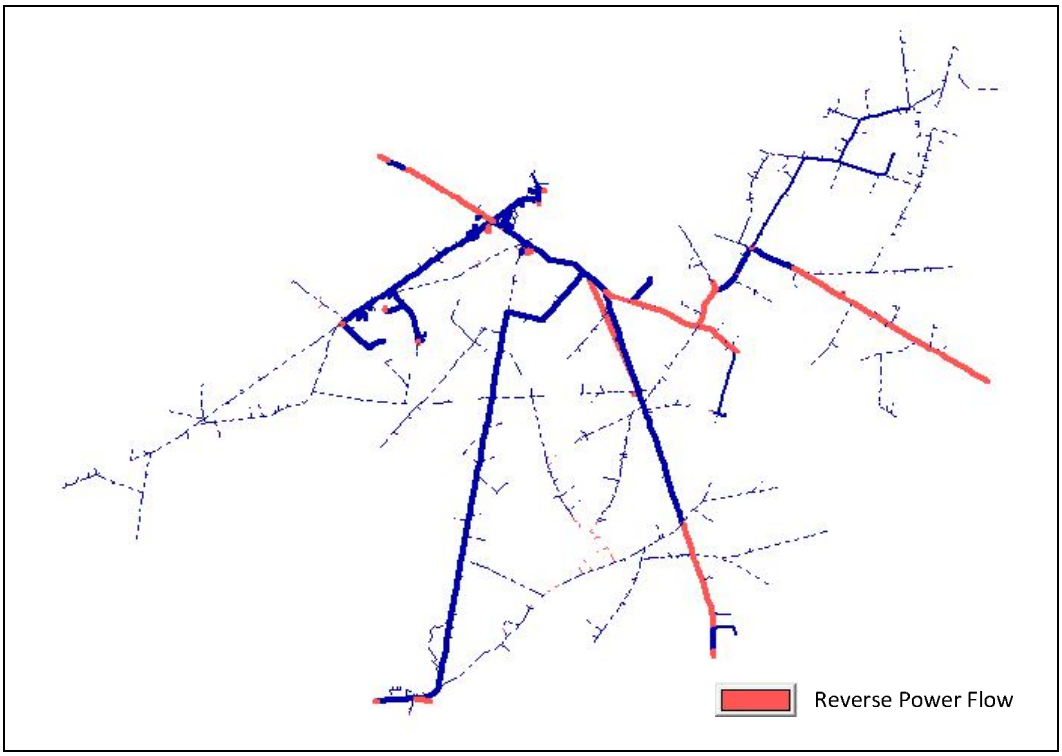

Figure 7-8 Reverse power flow on April 2 at 14:00 corresponding to case 2

In order to evaluate control performance, PV generation changes are considered at the time of maximum PV generation [34]. For the baseline, Figure 7-9 illustrates how voltage variations are observed as a function of loss of PV generation. From the figure it may be seen that a 1% voltage variation, based on a 120V volt base, is observed when 20% of the PV generation is lost, where the generation loss occurs at maximum generation. Since one of the objectives here is to control the voltage variation to within 1%, the CHMSC will be re-run when a 20% variation of PV generation is observed. In Figure 7-7 there are four times at which the PV generation varies more than 20%, which are: 2:48:13 PM, 2:48:14 PM, 2:51:00 PM, 2:51:16 PM. Furthermore, in the CHMSC simulations the loss of communication is also tested at 2:25:00 PM and 3:55:00 PM.

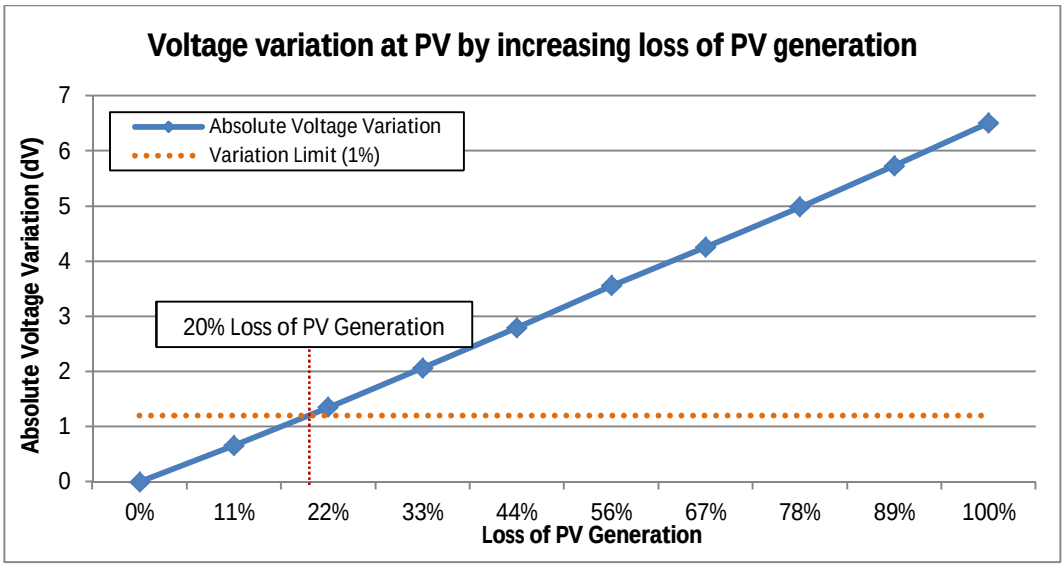

Figure 7-9 Voltage variations by increasing levels of loss of generation for baseline condition

When local control is not coordinated by CHMSC, the local control uses the nominal voltage as a set-point. Here the local PV controllers are modeled in Matlab, and then Matlab coder is used to convert the Matlab file to a dynamic link library file that is used in the power system simulation [92].

7.3.2. Comparison between Local Control and CHMSC for Case 1

In this section the CHMSC simulation results are compared with the results of local control for case 1. Case 1 includes the existing 4 PV generation sites and 4 additional 1 MW PV generation sites, representing a PV penetration of 96%, as illustrated in Figure 7-6. Five variables are used here in comparing CHMSC with local control, which are average customer voltage, circuit losses, steps of automated control devices, PV reactive power generation, and the voltage variation at the 9 MW PV generator.

a) Average Customer Voltage

Figure 7-10 shows the optimal average customer voltage as a function of time obtained from CHMSC. In CHMSC the average customer voltage is calculated to reduce the circuit loss and minimize the automated control device motion. Actual optimal voltage set-points for PV generators will vary from PV generator to PV generator. Here the optimal set-points are updated every 5 minutes or when 20% changes in PV generation are observed. In Figure 7-10, the optimal average customer voltage is shown at which the PV generation varies more than 20% and when the simulated loss of communication occurs.

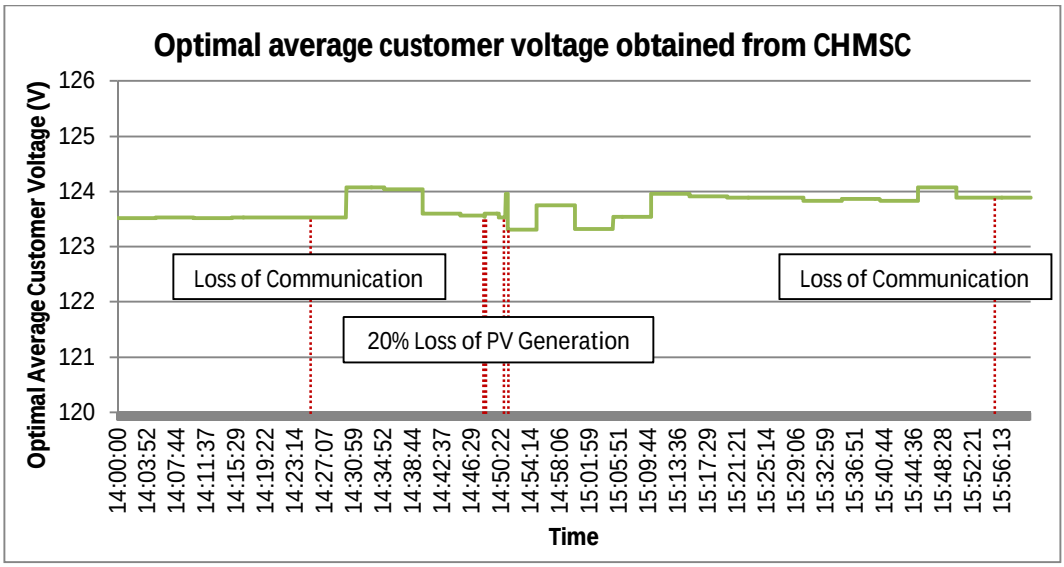

Figure 7-10 CHMSC optimal average customer voltage

Figure 7-11 compares the average customer voltage obtained from CHMSC with that obtained from local control. From the figure both CHMSC and the local control maintain the average customer voltage within allowable ranges. However, as will be shown below, local control is not able to maintain voltages at specific locations within the allowable range.

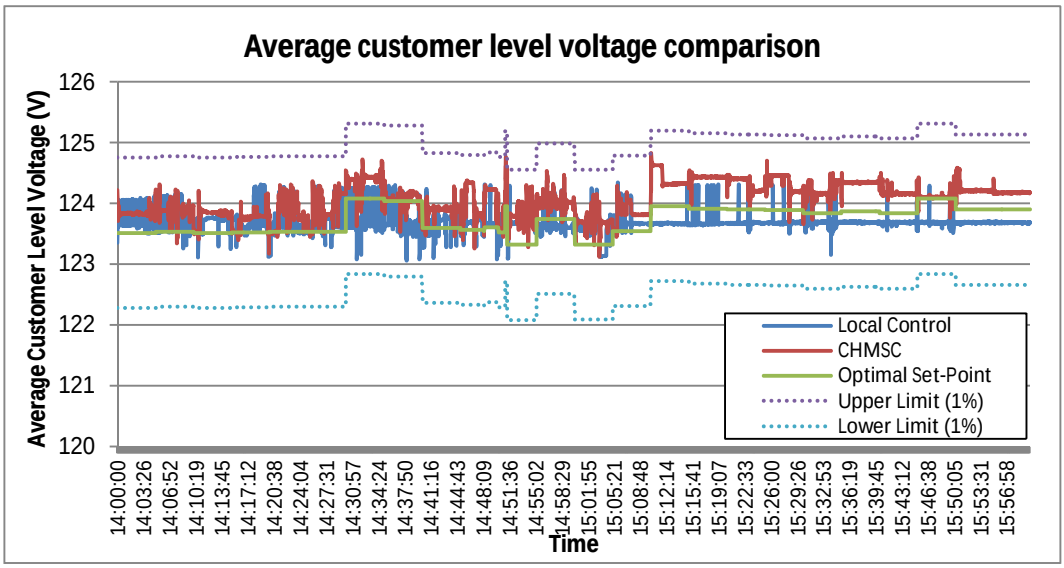

Figure 7-11 Average customer level voltage comparison between local control and CHMSC for case 1

b) Circuit Loss

Figure 7-12 and Figure 7-13 show the real and reactive circuit loss comparisons, respectively. Both the real and reactive circuit losses are significantly reduced with CHMSC. Circuit loss summaries are

shown in Table 7-1. For the two hour simulation CHMSC is able to improve the real and reactive power loss over the local control by 38.06% and 45.83%, respectively.

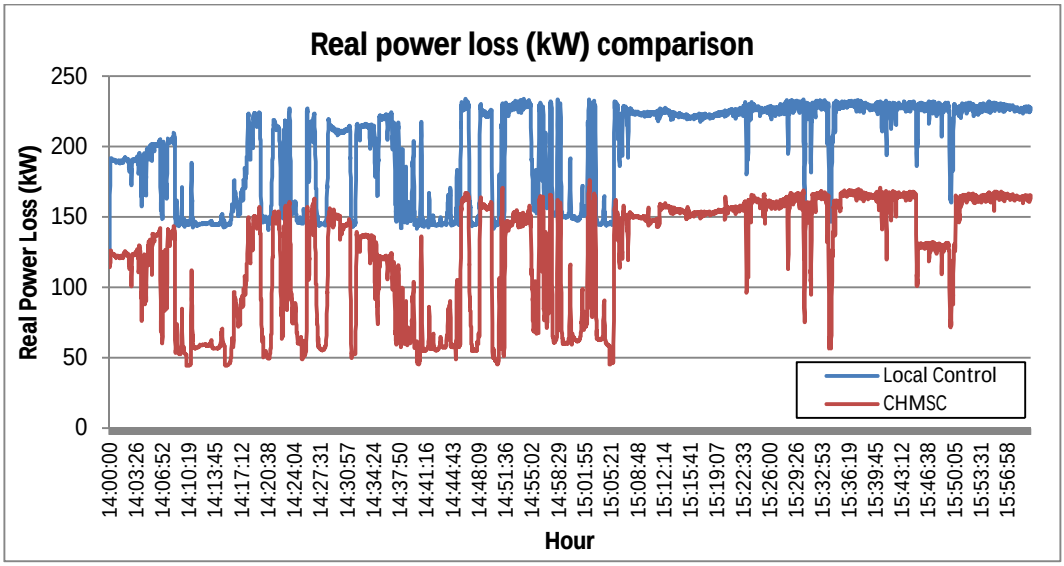

Figure 7-12 Real power loss (kW) comparison between local control and CHMSC for case 1

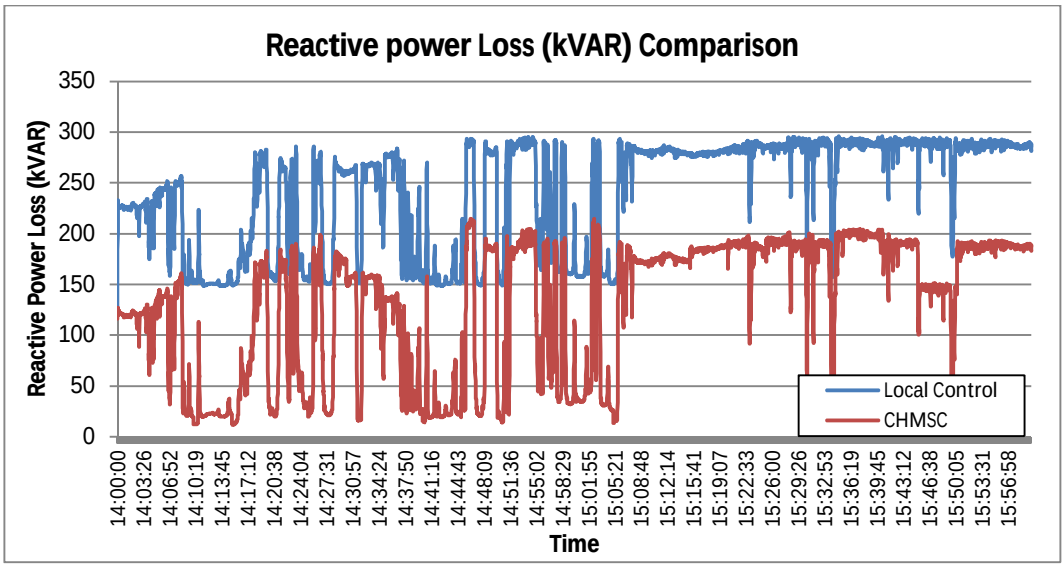

Figure 7-13 Reacitve power loss (kVAR) comparison between local control and CHMSC for case 1

Table 7-1 Comparison of the total circuit losses between local control and CHMSC for case 1

	Local Control	CHMSC	Improvement
Real Power Loss (kW-hr)	198.98 kW-hr	123.25 kW-hr	38.06%
Reactive Power Loss (kVAR-hr)	240.69 kVar-hr	130.38 kVar-hr	45.83%

c) PV Reactive Power Generation

Figure 7-14 show the reactive power generation at the largest PV generator, the 9 MW generator. Note that in all local control the maximum reactive power is limited at 70% of the PV MVA rating. As shown in Figure 7-14, at the 9 MW generator the local control is always limited at the maximum reactive power injection. The CHMSC controls the reactive power to maintain the optimal voltage set-point, which is shown in the next section where the voltage variation is considered. With CHMSC the reactive power generation never reaches its limit. This is due to the participation of the other coordinated generators in the reactive power control.

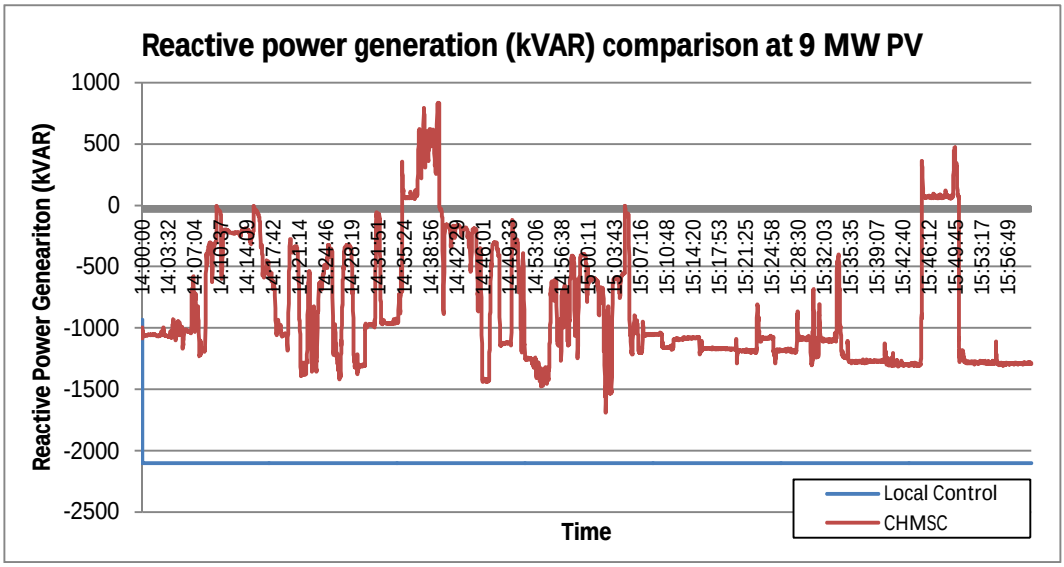

Figure 7-14 Reactive power generation (kVAR) comparison at 9 MW PV between local control and CHMSC for case 1

d) Voltage Variation

Figure 7-15 and Figure 7-16 show the primary system voltage variations with local control and CHMSC, respectively, at the 9 MW generator. The local control is not able to maintain the voltage set-point within the 1% variation limits because the reactive power generation is clamped at its limit. However, the CHMSC is able to maintain the voltage within the allowable range due to the coordination with other generators.

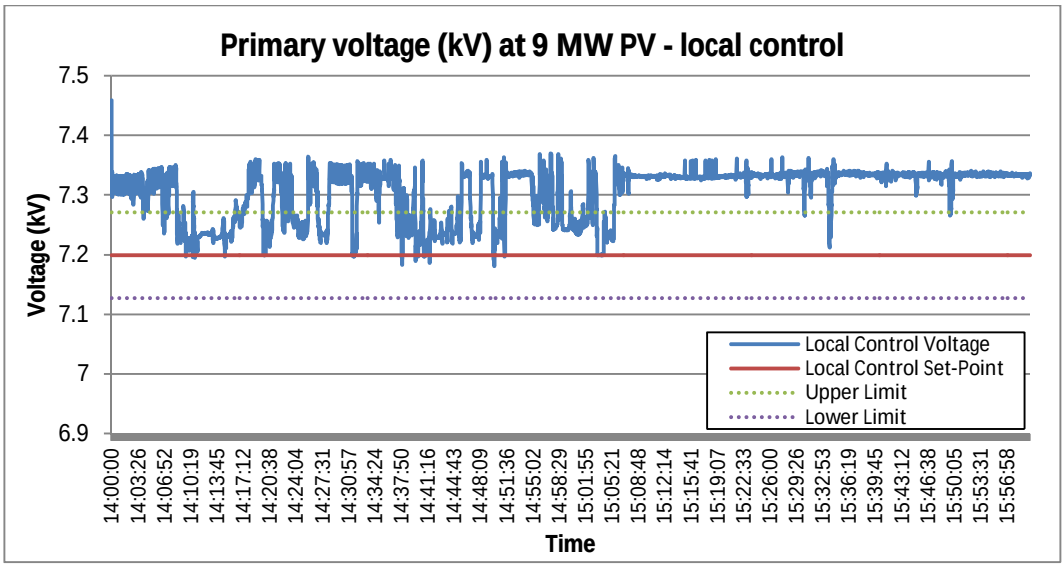

Figure 7-15 Voltage at 9 MW PV using local control for case 1

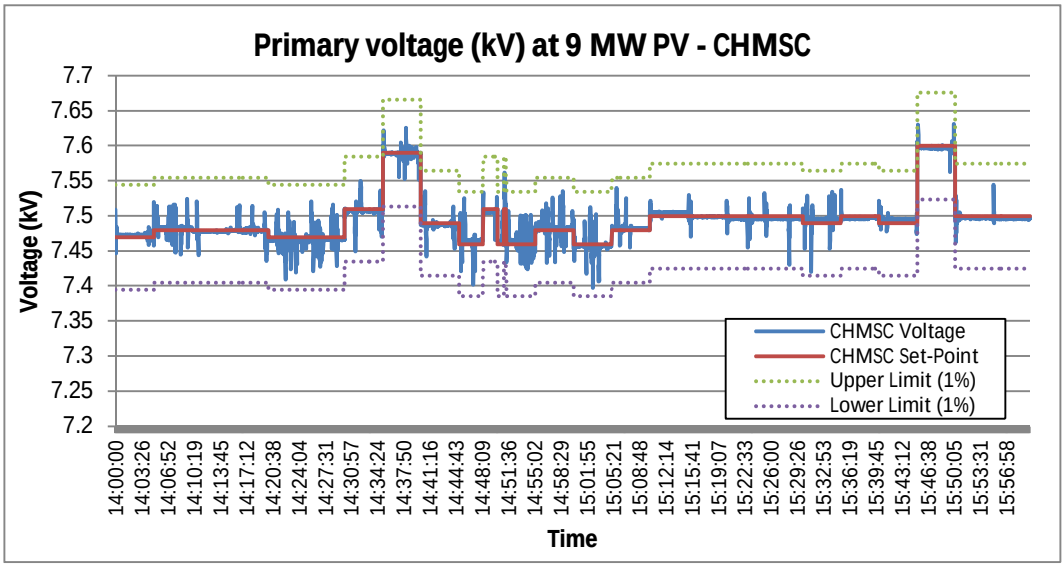

Figure 7-16 Voltage at 9MW PV using CHMSC for case 1

e) Steps of Automated Control Devices

One of the CHMSC control objectives is to minimize the steps of the automated control devices themselves. The circuit studied has 21 voltage regulators and 8 switched shunt capacitors. Table 7-2 provides a summary of the control device steps and compares the local control with CHMSC for the two hour simulation period. From the table it may be seen that the CHMSC results in significantly fewer steps than local control.

Table 7-2 Total steps comparison of automated control devices for 2 hours between local control and CHMSC for case 1

	Local Control	CHMSC	% Reduction in Controller Motion with CHMSC
All Voltage Regulators	2374	1559	34 %
All Switched Shunt Capacitors	1070	684	36 %

7.3.3. Control Performance Comparisons for Baseline, Case 1, and Case 2

In this section further comparisons of CHMSC with local control are presented for the baseline case, case 1, and case 2, where the cases are illustrated in Figure 7-6. Circuit losses, automated device motion, voltage violations, and overload violations will be considered.

a) Circuit Loss

Figure 7-17 and Figure 7-18 compares total real and reactive power losses as the level of PV generation increases from the baseline case to case 2. Both real and reactive circuit losses increase with increasing PV generation, but in all cases CHMSC has significantly lower losses.

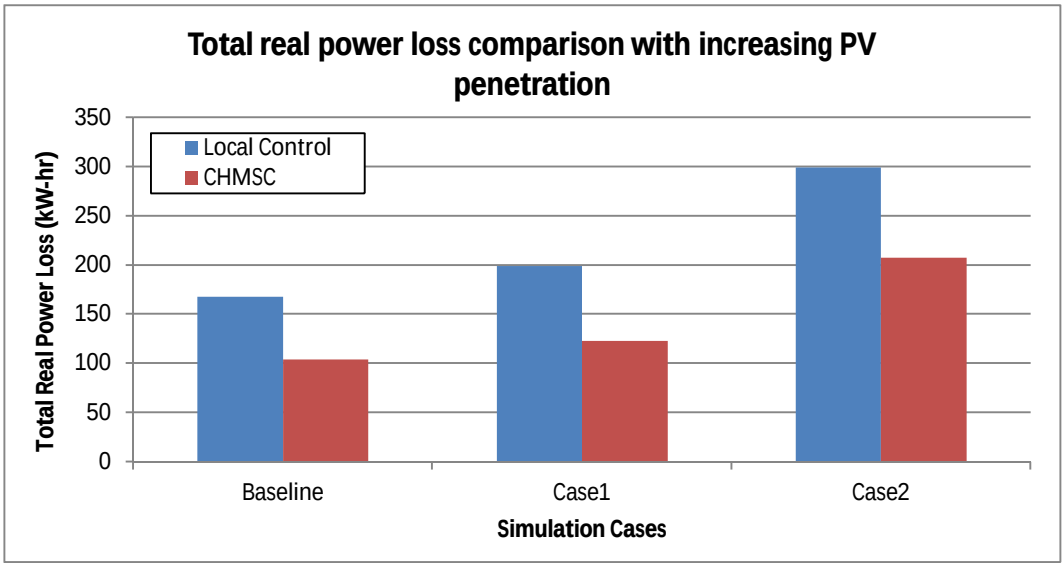

Figure 7-17 Total real power loss comparison for 2 hour simulation by increasing PV penetration

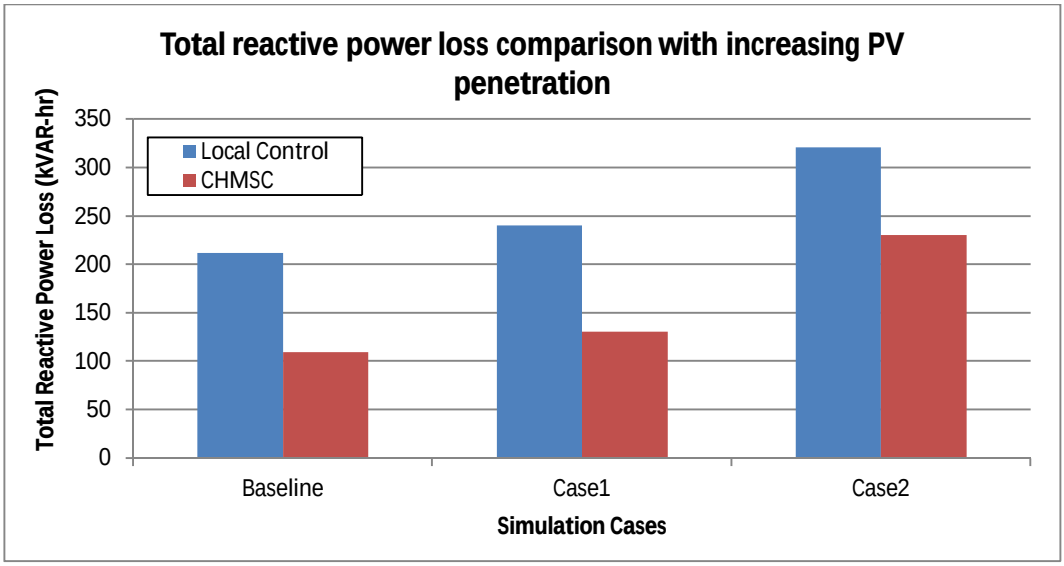

Figure 7-18 Total reactive power loss comparison for 2 hour simulation by increasing PV penetration

b) Steps of Automated Control Devices

Figure 7-19 compares the control motion, in terms of percent reduction of CHMSC over local control, as the level of PV penetration increases. As shown in the figure, the percent reduction ranges from a little over 20% to over 40%. And, as the PV penetration level increases, the improvement of CHMSC over local control continues to increase. It may be noted that CHMSC has a slightly larger improvement for switched capacitors.

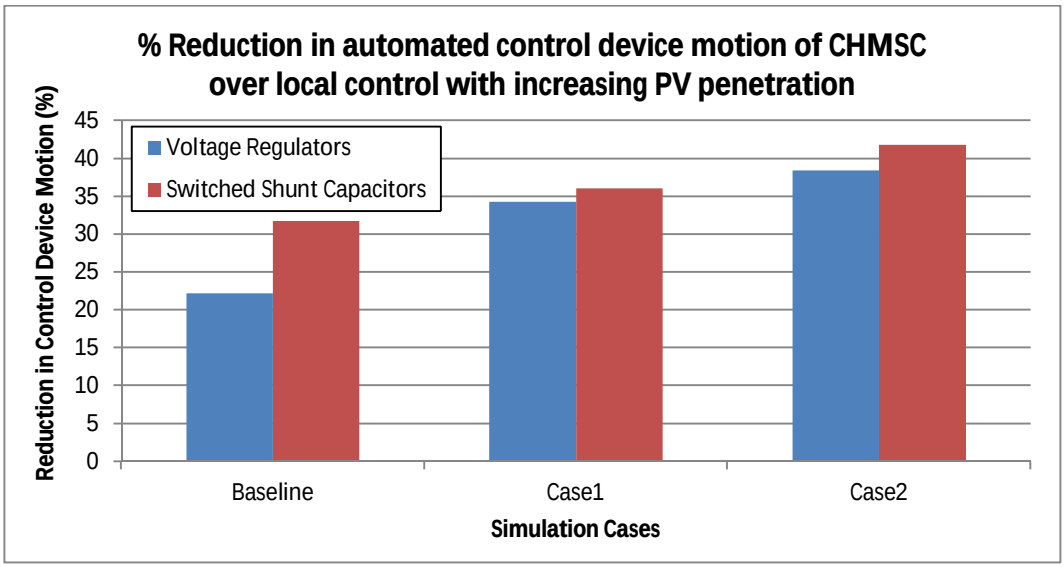

Figure 7-19 Reduction in control device movement with CHMSC with increasing PV penetration

c) Number of Voltage Violation

Figure 7-20 shows how the number of customer voltage violations, low and high, increase as the level of PV generation increases. It may be noted that local control has more than four times the violations of CHMSC. Customer voltage violations are only reported at load busses, and there are 1109 load busses in the model. Since there are 7200 power flow runs performed over the 2 hour period, there are 7,984,800 voltage calculations (7200 x 1109) that are checked for low or high voltage at load busses during the simulation. Hence, approximately 1600 voltage violations (worst case in Figure 7-20) represent approximately 0.02% violations.

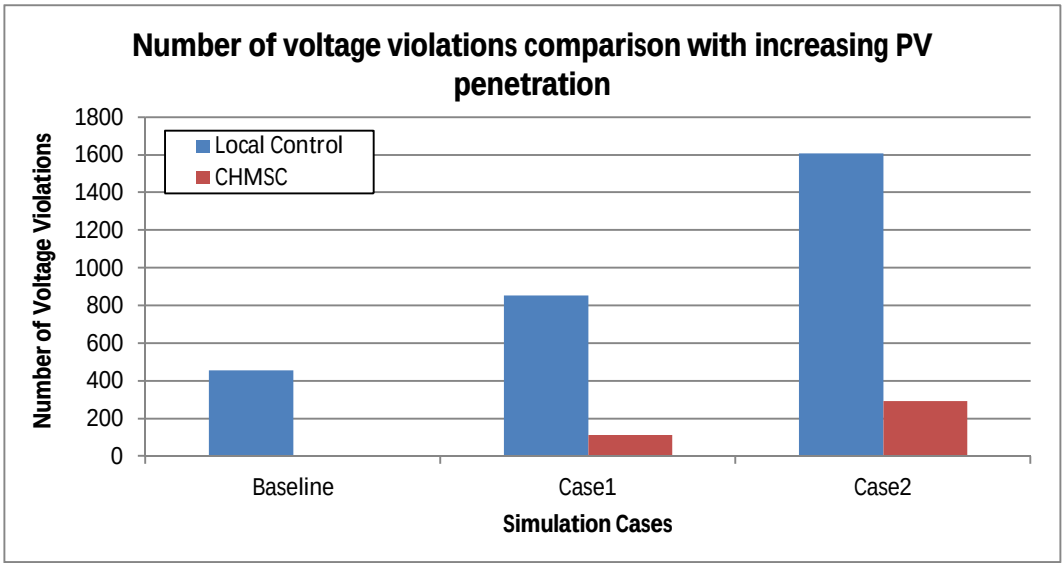

Figure 7-20 Number of voltage violations during 2 hour period with increasing PV penetration

d) Number of Overloading Violation

Figure 7-21 shows how the number of overloads increases as the level of PV generation increases. CHMSC has 93% and 54% fewer overloads for cases 1 and 2, respectively. Note that the circuit has 4883 components. Thus, there are 35,157,600 calculations (4883×7200) that are checked at individual components for an overload condition during the simulation. Hence, approximately 15500 overload violations (worst case in Figure 7-21) represent approximately 0.044% violations.

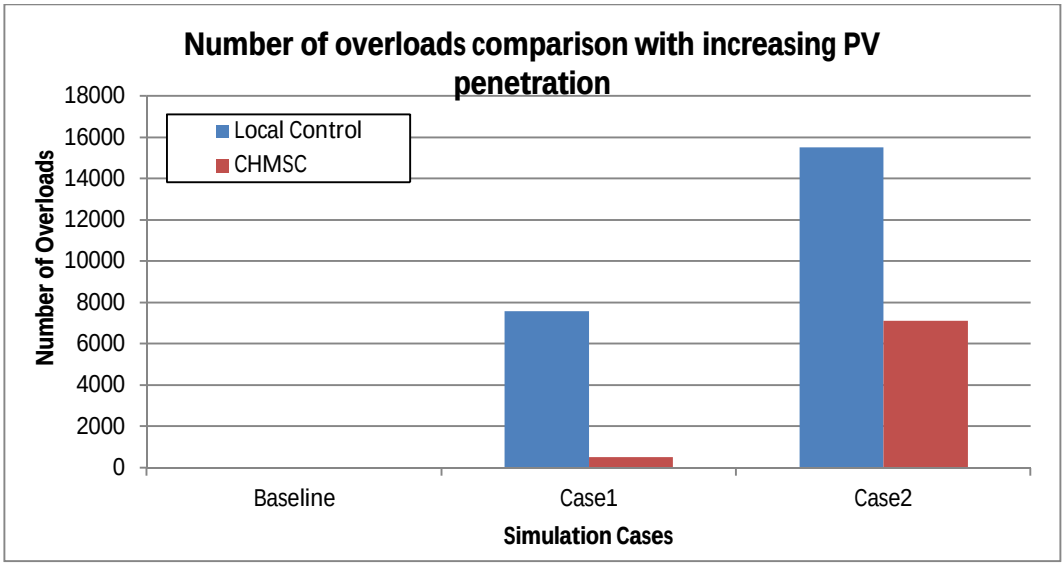

Figure 7-21 Number of overloads during 2 hour period with increasing PV penetration

7.4. Conclusions

The Configurable, Hierarchical, Model-based, Scheduling Control presented uses utility automated control devices to establish an optimum voltage schedule, where the optimum voltage schedule varies with time-of-day and with circuit location. The optimum voltage schedule calculation does not consider PV generation. PV generators that have communications are then requested to help maintain the optimal voltage schedule. If a PV generator controller does not have communications, then CHMSC studies can be used to help determine reasonable PV controller gains that support the power system operation.

A model of an existing circuit with high PV penetration (69%) was used as a starting point for the comparison of CHMSC with local control only. In performing the analysis one second PV generation measurement data from the existing solar generators was used. In the comparison CHMSC used the same local controllers, but varied the voltage set-points of the local controllers. The comparison of the performance between CHMSC and local control only was performed for three levels of PV penetration – 69%, 96%, and 123%. Comparisons included real losses, reactive losses, voltage violations, overload violations, motion of utility owned automated control devices, and the control of voltage. The CHMSC outperformed the local control only, and often the difference in performance increased as the level of PV penetration increased.

Existing distribution systems and their associated controls have been around for decades. Most distribution circuits have capacity to accommodate some level of PV generation, but the question is how

much can they handle without creating problems. The control approach presented seeks to accommodate very high levels of PV penetration with the least impact on the system operation.

Chapter 8 Conclusions and Future Work

8.1. Conclusions

Today's power system is facing growing challenges in maintaining a secure and reliable energy supply. Part of the growing challenge is the possibility of significant levels of uncertain renewable generation being installed in the power system. This brings new challenges involving the management of intermittent generation. Understanding the impacts of renewable generation on the power system and its operations is necessary to meeting these challenges. Investigating solutions to mitigate these impacts is important to achieving high penetration levels of renewable generation in the power system.

This dissertation focuses on two different aspects of renewable energy applications in distribution networks. It starts with system wide and local impact studies to address the expected impacts of new technologies in current distribution circuits. Then, optimal solutions to utilizing high penetrations of renewable generation are proposed: 1-a frequency domain approach for wind generation; 2-an optimal control algorithm for PV generation.

A DER adoption analysis for system wide impact studies is presented in Chapter 2. This work is the first effort to simultaneously consider the effects of adopting PEV, DER generation, and energy storage. This is work is important because this is closer to the real-world problems that must be considered. The results demonstrated that a maturing PEV market could produce significant impacts on peak demand, resulting in system overloading conditions. While the solar configuration produces more total energy, it has effectively no impact on the peak residential demands, which typically occur during times when solar generation is unavailable. However, when coupled with a battery storage system, the solar generation is able to significantly influence peak characteristics, especially during the peak growth scenario driven by an emerging PEV market. Furthermore, the "available at night" wind configuration shows less benefits, even in combination with battery storage systems, because of the lower total energy from the wind resource.

A Monte Carlo DER adoption analysis for advanced system wide impact studies is presented in Chapter 3. This work is the first effort to make up for uncertain future impact from DER adoption analysis because simulating one time point is not sufficient to evaluate the uncertainty of future PHEV load and DER generation. Monte Carlo simulations are used to evaluate adoption patterns of residential customers. This work is also important because it applies projected adoption levels of PHEV and DER generation for 2020 and 2030 future scenarios based on DOE reports. The results demonstrated that this

analysis can evaluate the seasonal effects by selecting different load profiles and potential impacts from the addition of PHEV and DER generation with and without energy storage. Furthermore, this analysis provides not only the expected average results, but also its uncertainty. The major findings from the Monte Carlo DER adoption analysis, which used an actual utility circuit where all individual customer loads are modeled, were: 1) The cumulative average and variance of the results obtained from 1000 Monte Carlo iterations converged well; 2) The analysis provides not only the average of the results but also the extent of uncertainty that the results can have. Furthermore, the distribution at each hour follows the normal distribution so that it can be estimated with mean and standard deviations; 3) The results demonstrate that a maturing PHEV market could produce significant impacts on peak demand, resulting in system overload conditions, which mainly occur in the secondary distribution. This would require utilities to upgrade many secondary systems where PHEVs were installed.

A DER impact study for evaluating local impacts is presented in Chapter 4. This work is the first effort to standardize the impact study when utilities consider installing new DER generation into their existing distribution circuit. This work is important for utilities to understand the impacts of DER generation on distribution circuits and operations. Both steady-state and quasi steady-state impact studies are performed. In the studies changing cloud cover conditions and variations in PV generation power factor control are considered. Both improvements and adverse effects of PV generation on the circuit are discussed. The steady-state impact studies consider voltage variations, reverse power flows, voltage phase unbalance, and power flow phase unbalance. Furthermore, the quasi steady-state impact studies consider voltage variations, circuit losses, and automated device steps across the time varying operation of the circuit.

A frequency domain approach is proposed as a solution for wind generation in Chapter 5. This work is the first effort to characterize and analyze the wind speed patterns in frequency domain. This work is important because accurate characterization of wind speed patterns is the foundation for accurate wind forecasting so that it provides the solution for uncertain and intermittent wind generation. This chapter presents the methodology for the analysis and characterization of wind speed patterns in the frequency domain using DFT. A compact frequency-domain representation is introduced. This representation has shown that the machine-readable format facilitates automated large-scale processing of wind speed data. It is proposed that wind speed patterns during different times can be characterized using the compact frequency-domain representation. It is also proposed that wind speed patterns at different geographic locations can be characterized using the compact frequency-domain representation. Major findings from analyzing the statistical results of the harmonic components during different times and at different geographic locations are: (1) the consistent harmonic component patterns for three years are captured. It

shows a potential to forecast future wind speed patterns using historical data, (2) this approach is able to characterize wind speed patterns with higher certainty information of major harmonic components, (3) the UR is introduced to determine the level of uncertainty that the results can have. Similar UR in major harmonic components is obtained no matter how distant the locations are from each other, or whether the locations are in on- or off-shore.

In Chapter 6, ***coordinated control of automated devices and PV generators*** is investigated to mitigate voltage rise problems caused by high PV penetration. This work is the first effort to coordinate the automated device with PV generators. In addition, this work is the first to look at using utility controls to set an optimum control schedule, and then providing a schedule to non-utility controls, in this case PV inverters, that supports the optimum control schedule. Furthermore, this control provided a unique set of prioritized objectives that had not been considered together in any previous work. This work is important because the coordinated control is essential to achieving a high penetration of PV generators. The control strategy involves using the automated devices to establish an optimum voltage schedule that does not consider the PV generation. The voltage that is controlled is the average customer voltage, and it is controlled with very tight limits. The optimum schedule minimizes circuit losses while reducing automated device movement. The optimum voltage schedule is used as an input to the coordinated PV control algorithm, which seeks to adjust the real and reactive PV power generation to maintain the optimum voltage schedule. For all simulations the coordinated control is able to maintain a voltage schedule that eliminates voltage rise problems and that significantly reduces losses and automated device controller movement.

Then, ***a Configurable, Hierarchical, Model-based, Scheduling Control (CHMSC)*** is proposed in Chapter 7. This work is the first effort to coordinate centralized control with local control. This work is important because it shows that the centralized control performs well in the existing environment where most PV generators are operated by local control. A model of an existing circuit with high PV penetration was used as a starting point for the comparison of CHMSC with local control only. In performing the analysis one second PV generation measurement data from existing solar generators was used. In the comparison CHMSC used the same local controllers, but varied the voltage set-points of the local controllers. The comparison of the performance between CHMSC and local control was performed for three levels of PV penetration – 69%, 96%, and 123%. Comparisons included real losses, reactive losses, voltage violations, overload violations, motion of utility owned automated control devices, and the control of voltage. The CHMSC outperformed the local control only, and often the difference in performance increased as the level of PV penetration increased.

8.2. Future Work

Several topics of interest arise from the completion of this study. Areas that would help progress toward a better understanding of the feasibility and implementation of the proposed methodologies are as follows:

- In the system wide impact study in Chapter 2 the smaller amounts of wind generation are observed in the three selected cities because of the lack of wind resources in large cities. Therefore, the "available at night" wind configuration shows less benefit, even in combination with battery storage system. It is necessary to study the wind generation in the rural area where wind resources are not affected by large buildings.

- Solar generation can vary rapidly up and down as clouds pass over. In a local impact study in Chapter 3, changing cloud cover is considered from 25% to 100% cloud cover resulting in from 25% to 100% loss of PV generation. However, PV generation does not vary so much. For example, the maximum PV generation variability during the day is often around 20~30%. Therefore, it is necessary to study PV variability with realistic variability estimates.

- In Chapter 5 frequency domain approach shows potential for forecasting wind speed patterns with better accuracy than the time domain. It also shows potential to accurately estimate the wind speed patterns for a target location using available data from the reference site. However, a forecasting system using the frequency domain approach does not exist yet.

- The optimal set-points in the coordinated control algorithms in Chapter 6 and 7 are determined to maintain the average customer voltage profile obtained before introducing the PV into the circuit. However, utilities sometimes desire to run different existing feeder voltage profiles during solar production hours. Investigating different set-points, such as set-points for providing voltage headroom during solar production hours, is needed.

References

[1] National Renewable Energy Laboratory (NREL). In My Backyard (IMBY). [Online]. Available: http://www.nrel.gov/eis/imby/

[2] National Climatic Data Center (NCDC). Climate Data Online (CDO). [Online]. Available: http://www.ncdc.noaa.gov/oa/climate/climatedata.html

[3] R. P. Broadwater, A. Sargent, A. Yarali, H. E. Shaalan, and J. Nazarko, *Estimating substation peaks from load research data*, Power Delivery, IEEE Transactions on, vol. 12, pp. 451-456, 1997.

[4] A. Sargent, R. P. Broadwater, J. C. Thompson, and J. Nazarko, *Estimation of diversity and kWHR-to-peak-kW factors from load research data*, Power Systems, IEEE Transactions on, vol. 9, pp. 1450-1456, 1994.

[5] J. Taylor, A. Maitra, M. Alexander, D. Brooks, and M. Duvall, *Evaluation of the impact of plug-in electric vehicle loading on distribution system operations*, in Power & Energy Society General Meeting, 2009. PES '09. IEEE, 2009, pp. 1-6.

[6] U.S. Census Bureau 2000 Data. [Online]. Available: http://www.census.gov/

[7] NREL: Solar Radiation Data Manual for Flat-Plate and Concentrating Collectors. [Online]. Available: http://rredc.nrel.gov/solar/pubs/redbook/

[8] *Environmental Assessment of Plug-In Hybrid Electric Vehicles, Volume 1: Nationwide Greenhouse Gas Emissions*, Electric Power Research Institute, 1015325, July 2007.

[9] *20% wind energy by 2030*, United States Department of Energy, DOE/GO-102008-2567, May 2008.

[10] *SunShot Vision Study*, United States Department of Energy, DOE/GO-102012-3037, February 2012.

[11] K. Schneider, C. Gerkensmeyer, M. Kintner-Meyer, and R. Fletcher, *Impact assessment of plug-in hybrid vehicles on pacific northwest distribution systems*, in Power and Energy Society General Meeting - Conversion and Delivery of Electrical Energy in the 21st Century, 2008 IEEE, 2008, pp. 1-6.

[12] C. Roe, A. P. Meliopoulos, J. Meisel, and T. Overbye, *Power System Level Impacts of Plug-In Hybrid Electric Vehicles Using Simulation Data*, in Energy 2030 Conference, 2008. ENERGY 2008. IEEE, 2008, pp. 1-6.

[13] Y. Xiaolong, *Impacts assessment of PHEV charge profiles on generation expansion using national energy modeling system*, in Power and Energy Society General Meeting - Conversion and Delivery of Electrical Energy in the 21st Century, 2008 IEEE, 2008, pp. 1-5.

[14] K. Clement, E. Haesen, and J. Driesen, *Coordinated charging of multiple plug-in hybrid electric vehicles in residential distribution grids*, in Power Systems Conference and Exposition, 2009. PSCE '09. IEEE/PES, 2009, pp. 1-7.

[15] R. T. Doucette and M. D. McCulloch, *Modeling the prospects of plug-in hybrid electric vehicles to reduce CO2 emissions*, Applied Energy, vol. 88, pp. 2315-2323, 7// 2011.

[16] S. Huang, B.-M. S. Hodge, F. Taheripour, J. F. Pekny, G. V. Reklaitis, and W. E. Tyner, *The effects of electricity pricing on PHEV competitiveness*, Energy Policy, vol. 39, pp. 1552-1561, 3// 2011.

[17] X. Cui, H. K. Kim, C. Liu, S.-C. Kao, and B. L. Bhaduri, *Simulating the household plug-in hybrid electric vehicle distribution and its electric distribution network impacts*, Transportation Research Part D: Transport and Environment, vol. 17, pp. 548-554, 10// 2012.

[18] C. Weiller, *Plug-in hybrid electric vehicle impacts on hourly electricity demand in the United States*, Energy Policy, vol. 39, pp. 3766-3778, 6// 2011.

[19] S. Huang, H. Safiullah, J. Xiao, B.-M. S. Hodge, R. Hoffman, J. Soller, *et al.*, *The effects of electric vehicles on residential households in the city of Indianapolis*, Energy Policy, vol. 49, pp. 442-455, 10// 2012.
[20] M. Khan and K. M. Kockelman, *Predicting the market potential of plug-in electric vehicles using multiday GPS data*, Energy Policy, vol. 46, pp. 225-233, 7// 2012.
[21] R. Sioshansi, R. Fagiani, and V. Marano, *Cost and emissions impacts of plug-in hybrid vehicles on the Ohio power system*, Energy Policy, vol. 38, pp. 6703-6712, 11// 2010.
[22] W. Su and M.-Y. Chow, *Computational intelligence-based energy management for a large-scale PHEV/PEV enabled municipal parking deck*, Applied Energy, vol. 96, pp. 171-182, 8// 2012.
[23] M. Stadler, M. Kloess, M. Groissböck, G. Cardoso, R. Sharma, M. C. Bozchalui, *et al.*, *Electric storage in California's commercial buildings*, Applied Energy, vol. 104, pp. 711-722, 4// 2013.
[24] N. Juul and P. Meibom, *Road transport and power system scenarios for Northern Europe in 2030*, Applied Energy, vol. 92, pp. 573-582, 4// 2012.
[25] J. Jung, H. Asgeirsson, T. Basso, J. Hambrick, M. Dilek, R. Seguin, *et al.*, *Evaluation of DER adoption in the presence of new load growth and energy storage technologies*, in Power and Energy Society General Meeting, 2011 IEEE, 2011, pp. 1-8.
[26] T. Räsänen, D. Voukantsis, H. Niska, K. Karatzas, and M. Kolehmainen, *Data-based method for creating electricity use load profiles using large amount of customer-specific hourly measured electricity use data*, Applied Energy, vol. 87, pp. 3538-3545, 11// 2010.
[27] J. Widén and E. Wäckelgård, *A high-resolution stochastic model of domestic activity patterns and electricity demand*, Applied Energy, vol. 87, pp. 1880-1892, 6// 2010.
[28] R. A. R. Kilpatrick, P. F. G. Banfill, and D. P. Jenkins, *Methodology for characterising domestic electrical demand by usage categories*, Applied Energy, vol. 88, pp. 612-621, 3// 2011.
[29] L. Baringo and A. J. Conejo, *Correlated wind-power production and electric load scenarios for investment decisions*, Applied Energy, vol. 101, pp. 475-482, 1// 2013.
[30] Clean Power Research (CPR) Solar Anywhere [Online]. Available: http://www.cleanpower.com/
[31] Urban Green Energy UGE-4K [Online]. Available: http://www.urbangreenenergy.com/products/uge-4k
[32] F. Katiraei, Agu, x, and J. R. ero, *Solar PV Integration Challenges*, Power and Energy Magazine, IEEE, vol. 9, pp. 62-71, 2011.
[33] J. Jung, Y. Cho, D. Cheng, A. Onen, R. Arghandeh, M. Dilek, *et al.*, *Monte Carlo analysis of Plug-in Hybrid Vehicles and Distributed Energy Resource growth with residential energy storage in Michigan*, Applied Energy, vol. 108, pp. 218-235, 8// 2013.
[34] S. Eftekharnejad, V. Vittal, G. T. Heydt, B. Keel, and J. Loehr, *Impact of Increased Penetration of Photovoltaic Generation on Power Systems*, Power Systems, IEEE Transactions on, vol. 28, pp. 893-901, 2013.
[35] R. Viral and D. K. Khatod, *Optimal planning of distributed generation systems in distribution system: A review*, Renewable and Sustainable Energy Reviews, vol. 16, pp. 5146-5165, 9// 2012.
[36] M. A. Eltawil and Z. Zhao, *Grid-connected photovoltaic power systems: Technical and potential problems—A review*, Renewable and Sustainable Energy Reviews, vol. 14, pp. 112-129, 1// 2010.
[37] P. Mitra, G. T. Heydt, and V. Vittal, *The impact of distributed photovoltaic generation on residential distribution systems*, in North American Power Symposium (NAPS), 2012, 2012, pp. 1-6.
[38] M. Thomson and D. G. Infield, *Impact of widespread photovoltaics generation on distribution systems*, Renewable Power Generation, IET, vol. 1, pp. 33-40, 2007.
[39] J. Widén, E. Wäckelgård, J. Paatero, and P. Lund, *Impacts of distributed photovoltaics on network voltages: Stochastic simulations of three Swedish low-voltage distribution grids*, Electric Power Systems Research, vol. 80, pp. 1562-1571, 12// 2010.
[40] J. A. P. Lopes, N. Hatziargyriou, J. Mutale, P. Djapic, and N. Jenkins, *Integrating distributed generation into electric power systems: A review of drivers, challenges and opportunities*, Electric Power Systems Research, vol. 77, pp. 1189-1203, 7// 2007.

[41] K. Fekete, Z. Klaic, and L. Majdandzic, *Expansion of the residential photovoltaic systems and its harmonic impact on the distribution grid*, Renewable Energy, vol. 43, pp. 140-148, 7// 2012.
[42] *IEEE Application Guide for IEEE Std 1547, IEEE Standard for Interconnecting Distributed Resources with Electric Power Systems*, IEEE Std 1547.2-2008, pp. 1-207, 2009.
[43] P. Pillay and M. Manyage, *Definitions of Voltage Unbalance*, Power Engineering Review, IEEE, vol. 21, pp. 49-51, 2001.
[44] K. Nara, S. Ishizu, and Y. Mishima, *Voltage control availability of distributed generators in power distribution system*, in Power Tech, 2005 IEEE Russia, 2005, pp. 1-6.
[45] Y. Miyamoto and Y. Hayashi, *Evaluation of generation efficiency and voltage deviation in residentail clustered PV voltage control*, in Photovoltaic Specialists Conference (PVSC), 2011 37th IEEE, 2011, pp. 002391-002396.
[46] H. Alatrash, R. A. Amarin, and L. Cheung, *Enabling Large-Scale PV Integration into the Grid*, in Green Technologies Conference, 2012 IEEE, 2012, pp. 1-6.
[47] P. M. S. Carvalho, P. F. Correia, and L. A. F. Ferreira, *Distributed Reactive Power Generation Control for Voltage Rise Mitigation in Distribution Networks*, Power Systems, IEEE Transactions on, vol. 23, pp. 766-772, 2008.
[48] L. Xiaohu, A. Aichhorn, L. Liming, and L. Hui, *Coordinated Control of Distributed Energy Storage System With Tap Changer Transformers for Voltage Rise Mitigation Under High Photovoltaic Penetration*, Smart Grid, IEEE Transactions on, vol. 3, pp. 897-906, 2012.
[49] H. Ying-Yi and L. Yi-Feng, *Optimal VAR Control Considering Wind Farms Using Probabilistic Load-Flow and Gray-Based Genetic Algorithms*, Power Delivery, IEEE Transactions on, vol. 24, pp. 1441-1449, 2009.
[50] A. Cagnano, F. Torelli, F. Alfonzetti, and E. De Tuglie, *Can PV plants provide a reactive power ancillary service? A treat offered by an on-line controller*, Renewable Energy, vol. 36, pp. 1047-1052, 3// 2011.
[51] T. Niknam, *A new HBMO algorithm for multiobjective daily Volt/Var control in distribution systems considering Distributed Generators*, Applied Energy, vol. 88, pp. 778-788, 3// 2011.
[52] W. Yang, Z. Peng, L. Wenyuan, X. Weidong, and A. Abdollahi, *Online Overvoltage Prevention Control of Photovoltaic Generators in Microgrids*, Smart Grid, IEEE Transactions on, vol. 3, pp. 2071-2078, 2012.
[53] L. Chia-Hung, H. Wei-Lin, C. Chao-Shun, H. Cheng-Ting, and K. Te-Tien, *Optimization of Photovoltaic Penetration in Distribution Systems Considering Annual Duration Curve of Solar Irradiation*, Power Systems, IEEE Transactions on, vol. 27, pp. 1090-1097, 2012.
[54] *American National Standard for Electric Power Systems and Equipment – Voltage Ratings (60 Hertz)*, American National Standard Institute, Inc., ANSI C84.1, Dec. 2006.
[55] D. Corbus, D. Lew, G. Jordan, W. Winters, F. Van Hull, J. Manobianco, *et al.*, *Up with wind*, Power and Energy Magazine, IEEE, vol. 7, pp. 36-46, 2009.
[56] L. Landberg, *Short-term prediction of the power production from wind farms*, Journal of Wind Engineering and Industrial Aerodynamics, vol. 80, pp. 207-220, 3/1/ 1999.
[57] J. Tambke, M. Lange, U. Focken, J.-O. Wolff, and J. A. T. Bye, *Forecasting offshore wind speeds above the North Sea*, Wind Energy, vol. 8, pp. 3-16, 2005.
[58] H. Liu, E. Erdem, and J. Shi, *Comprehensive evaluation of ARMA–GARCH(-M) approaches for modeling the mean and volatility of wind speed*, Applied Energy, vol. 88, pp. 724-732, 3// 2011.
[59] E. Erdem and J. Shi, *ARMA based approaches for forecasting the tuple of wind speed and direction*, Applied Energy, vol. 88, pp. 1405-1414, 4// 2011.
[60] C. Gallego, P. Pinson, H. Madsen, A. Costa, and A. Cuerva, *Influence of local wind speed and direction on wind power dynamics – Application to offshore very short-term forecasting*, Applied Energy, vol. 88, pp. 4087-4096, 11// 2011.
[61] D. A. Fadare, *The application of artificial neural networks to mapping of wind speed profile for energy application in Nigeria*, Applied Energy, vol. 87, pp. 934-942, 3// 2010.

[62] G. Li and J. Shi, *On comparing three artificial neural networks for wind speed forecasting*, Applied Energy, vol. 87, pp. 2313-2320, 7// 2010.
[63] I. G. Damousis, M. C. Alexiadis, J. B. Theocharis, and P. S. Dokopoulos, *A fuzzy model for wind speed prediction and power generation in wind parks using spatial correlation*, Energy Conversion, IEEE Transactions on, vol. 19, pp. 352-361, 2004.
[64] A. Kusiak, Z. Haiyang, and S. Zhe, *Short-Term Prediction of Wind Farm Power: A Data Mining Approach*, Energy Conversion, IEEE Transactions on, vol. 24, pp. 125-136, 2009.
[65] M. S. Miranda and R. W. Dunn, *One-hour-ahead wind speed prediction using a Bayesian methodology*, in Power Engineering Society General Meeting, 2006. IEEE, 2006, p. 6 pp.
[66] J. Apt, *The spectrum of power from wind turbines*, Journal of Power Sources, vol. 169, pp. 369-374, 6/20/ 2007.
[67] S. Singh, T. Bhatti, and D. Kothari, *A Review of Wind-Resource-Assessment Technology*, Journal of Energy Engineering, vol. 132, pp. 8-14, 2006.
[68] T. Ackermann, *Wind power in power systems*: John Wiley & Sons, Ltd., 2005.
[69] E. Eggleston and R. Clark, *WIND SPEED POWER SPECTRUM ANALYSIS FOR BUSHLAND, TEXAS, USA*, Wind Engineering vol. 24, pp. 49-52, 2000.
[70] B. Porat, *A course in digital signal processing*: John Wiley & Sons, Inc., 1997.
[71] S. G. Makridakis, S. C. Wheelwright, and R. J. Hyndman, *Forecasting: Methods and Applications*: John Wiley & Sons, Inc., 1998.
[72] National Renewable Energy Laboratory. Eastern and western wind integration dataset [Online]. Available: http://www.nrel.gov/wind/integrationdatasets/
[73] P. Berens, *CircStat: A MATLAB Toolbox for Circular Statistics*, Journal of Statistical Software, vol. 31, pp. 1-21, 2009.
[74] S. R. Jammalamadaka and A. Sengupta, *Topics in Circular Statistics*: World Scientific, 2001.
[75] C. L. Masters, *Voltage rise: the big issue when connecting embedded generation to long 11 kV overhead lines*, Power Engineering Journal, vol. 16, pp. 5-12, 2002.
[76] M. Braun, *Reactive Power Supplied by PV Inverters – Cost-Benefit-Analysis*, in 22nd European Photovoltaic Solar Energy Conference and Exhibition, Milan, Italy, 2007.
[77] P. Jong-young, N. Soon-Ryul, and P. Jong-Keun, *Control of a ULTC Considering the Dispatch Schedule of Capacitors in a Distribution System*, Power Systems, IEEE Transactions on, vol. 22, pp. 755-761, 2007.
[78] J. Hambrick and R. P. Broadwater, *Configurable, Hierarchical, Model-Based Control of Electrical Distribution Circuits*, Power Systems, IEEE Transactions on, vol. 26, pp. 1072-1079, 2011.
[79] M. Moradzadeh, R. Boel, and L. Vandevelde, *Voltage Coordination in Multi-Area Power Systems via Distributed Model Predictive Control*, Power Systems, IEEE Transactions on, vol. 28, pp. 513-521, 2013.
[80] M. S. Carmeli, F. Castelli-Dezza, M. Mauri, G. Marchegiani, and D. Rosati, *Control strategies and configurations of hybrid distributed generation systems*, Renewable Energy, vol. 41, pp. 294-305, 5// 2012.
[81] *The Costs and Impacts of Intermittency: An assessment of the evidence on the costs and impacts of intermittent generation on the British electricity network*, UK Energy Research Centre, ISBN 1-903144-04-3, Mar. 2006. Available: http://www.uwig.org/0604_Intermittency_report_final.pdf
[82] R. Zamora and A. K. Srivastava, *Controls for microgrids with storage: Review, challenges, and research needs*, Renewable and Sustainable Energy Reviews, vol. 14, pp. 2009-2018, 9// 2010.
[83] E. Planas, A. Gil-de-Muro, J. Andreu, I. Kortabarria, and I. Martínez de Alegría, *General aspects, hierarchical controls and droop methods in microgrids: A review*, Renewable and Sustainable Energy Reviews, vol. 17, pp. 147-159, 1// 2013.
[84] S. K. Pandey, S. R. Mohanty, and N. Kishor, *A literature survey on load–frequency control for conventional and distribution generation power systems*, Renewable and Sustainable Energy Reviews, vol. 25, pp. 318-334, 9// 2013.

[85] M. H. Nehrir, C. Wang, K. Strunz, H. Aki, R. Ramakumar, J. Bing, *et al.*, *A Review of Hybrid Renewable/Alternative Energy Systems for Electric Power Generation: Configurations, Control, and Applications*, Sustainable Energy, IEEE Transactions on, vol. 2, pp. 392-403, 2011.

[86] J. Lagorse, D. Paire, and A. Miraoui, *A multi-agent system for energy management of distributed power sources*, Renewable Energy, vol. 35, pp. 174-182, 1// 2010.

[87] M. Dakkak, A. Hirata, R. Muhida, and Z. Kawasaki, *Operation strategy of residential centralized photovoltaic system in remote areas*, Renewable Energy, vol. 28, pp. 997-1012, 6// 2003.

[88] X. Huanhai, Q. Zhihua, J. Seuss, and A. Maknouninejad, *A Self-Organizing Strategy for Power Flow Control of Photovoltaic Generators in a Distribution Network*, Power Systems, IEEE Transactions on, vol. 26, pp. 1462-1473, 2011.

[89] P. N. Vovos, A. E. Kiprakis, A. R. Wallace, and G. P. Harrison, *Centralized and Distributed Voltage Control: Impact on Distributed Generation Penetration*, Power Systems, IEEE Transactions on, vol. 22, pp. 476-483, 2007.

[90] A. Onen, D. Cheng, R. Arghandeh, J. Jung, J. Woyak, M. Dilek, *et al.*, *Smart Model Based Coordinated Control Based on Feeder Losses, Energy Consumption, and Voltage Violations*, Electric Power Components and Systems, vol. 41, pp. 1686-1696, 2013/12/10 2013.

[91] A. L. Ott, *Experience with PJM market operation, system design, and implementation*, Power Systems, IEEE Transactions on, vol. 18, pp. 528-534, 2003.

[92] Matlab Coder [Online]. Available: http://www.mathworks.com/products/matlab-coder/